



LEAD-FREE SOLDERING ALLOYS: MICROSTRUCTURE OPTIMIZATION FOR ELECTRONIC APPLICATIONS

Thesis submitted for the degree of
Master of Philosophy
at the University of Leicester

by

SERGEY BELYAKOV

Engineering Department
University of Leicester

August 2009

ABSTRACT

LEAD-FREE SOLDERING ALLOYS: MICROSTRUCTURE OPTIMIZATION FOR ELECTRONIC APPLICATIONS

Sergey Belyakov

As a result of environmental issues, manufacturing of lead-free electronics has become a global trend since July 1, 2006. Due to the considerable toxicity of lead leading to health and environmental concerns, new legislations have been imposed in its use. Efforts have been made to replace the traditional soldering alloys with new compositions, but the reliability of the new materials requires further investigation.

The purpose of this work is investigations of:

1. Growth of intermetallic phases (IMCs) during soldering and service life.
2. Investigation of effects of solder compositions, cooling kinetics and ultrasound vibration on the microstructure of crystallizing solders.
3. Nucleation and growth of bulk intermetallic precipitates and interfacial intermetallic layer in the “solder-joint” system.
4. Mechanisms of solder-joint failure.
5. Stability of microstructures over time.
6. Crystallographically-faceted void formation phenomenon.

The solder alloy compositions used: SAC405 (Sn95.5–Ag4.0–Cu0.5), SAC305 (Sn96.5–Ag3.0–Cu0.5), CASTIN (Sn96.2–Ag2.5–Cu0.8–Sb0.5) and SN100C (Sn–Cu0.7–Ni0.05+Ge) were chosen due to their preferability for lead-free electronics applications.

Investigations carried out revealed a strong dependence of the lead-free alloy microstructure on composition and solidification conditions (cooling rates, ultrasound). Lower amounts of alloying elements (< 2.5% of Ag) result in an increase in solder microstructural integrity. Cooling rates and ultrasound modify phase size and distribution. For instance, a cooling rate of 24 °C/sec (SAC405 alloy) lowered the maximum IMC needles length to 2µm compared to 44 µm at 1 °C/sec. Ultrasound of 30 kHz increases the microstructural homogeneity of bulk solders and lowers the amount of undercooling (from 24 °C to 7 °C for SAC 405 alloy). However, it deteriorates the strength characteristics of a solder-joint due to intensification of interfacial diffusional process, causing more intensive growth of the interfacial IMC layer. It was shown that solder-joint tensile strength is highly dependent on the IMC layer which has an optimal width of about 2µm. Thermal-cycling revealed differences in evolution of solder-joints and an average 7% strength reduction was obtained for samples subjected to 100 thermal cycles. Ageing resulted in rapid coarsening of a solder-joint microstructure and preferable IMC growth along the β-Sn grain boundaries. The interfacial IMC layer separates into two strata: Cu₃Sn and Cu₆Sn₅ as it develops into the solder. Crystallographically-faceted voiding was observed in solder-joints in the ‘as soldered’ state and during subsequent ageing. The voids were found to be strongly dependent on the width of Cu substrate.

A fundamental goal of this research is to help to meet the future requirements of reliable lead-free electronic products.

Acknowledgement

First of all, I would like to acknowledge my supervisors Professor Helen V. Atkinson and Doctor Simon Gill for their kind guidance and help with every aspect of the project. Special thanks go to Mr. Graham Clark, Mr. Barry Kirkland and Mr. Paul Williams for their patient help in the laboratory and technical advice. Acknowledgements to the Engineering Department for kindly provided equipment and facilities and to the Russian Ministry of Education for the scholarship provided.

TABLE OF CONTENTS

1. INTRODUCTION	8
2. LITERATURE SURVEY AND THEORETICAL BACKGROUND	14
2.1. Potential lead-free alloys	14
2.2. Microstructures of Pb-free solder joints	20
2.2.1. Microstructure of eutectic solders.....	20
2.2.2. Near-eutectic Sn-Ag-Cu alloy microstructure: dependence on cooling rate	25
2.2.3. Near-eutectic Sn-Ag-Cu alloy microstructure: dependence on alloying elements	27
2.3. Mechanical properties of lead-free solders	29
2.4. Thermal-fatigue properties of lead-free solders.....	32
2.5. Interfacial reactions in lead-free solder joints.....	35
2.5.1. During soldering	35
2.5.2. During annealing.....	37
2.6. Alloy composition optimization	38
2.6.1. Minor alloying element additions	38
2.6.2. Tin pest	39
2.7. Ultrasound modification of crystallizing alloy microstructure	40
2.8. Voiding	43
3. MICROSCOPY TECHNIQUES	46
3.1. Reflected light microscopy	46
3.2. Cross-polarized light microscopy	46
3.3. Scanning electron microscopy	46
3.4. Electron Backscattered Diffraction.....	49
3.5. Energy Dispersive X-Ray Analysis	51

4. MATERIALS AND EXPERIMENTAL METHODS	53
4.1. Materials	53
4.2. Metallographic specimen preparation.....	54
4.2.1. Mounting.....	54
4.2.2. Grinding.....	55
4.2.3. Polishing	56
4.2.4. Metallographic etching	57
4.3. Bulk solder specimen preparation for microstructural investigation.....	58
4.4. Cooling experiment.....	58
4.5. Image analysis.....	59
4.6. Ultrasonic experimental methods	60
4.6.1. Application of an ultrasonic field into bulk solders.....	60
4.6.2. Ultrasonic introduction into solder-joints	64
4.7. Tensile strength experimental setup	65
4.8. Solder-joint sample preparation for the IMC layer investigation	67
4.9. Thermal-cycling experimental method	67
4.10. Ageing experiments	69
4.11. Sample preparation for investigation of crystallographically-faceted voids	69
5. EXPERIMENTAL RESULTS	72
5.1. Microstructural investigation of lead-free solders	72
5.1.1. Alloy composition influence on microstructural features.....	72
5.1.2. Cooling rate influence on solder microstructure.....	81
5.1.3. Ultrasound modification of solder microstructure	84
5.1.3.1. Crystallization of bulk solders	84
5.1.3.1.1. Dependence of amount of undercooling on ultrasonic field.....	84

5.1.3.1.2. Dependence of the solder microstructure on the ultrasonic field	86
5.1.3.2. Crystallization of a solder-joint system within an ultrasonic field	88
5.2. Dependence of solder-joint tensile strength on IMC layer width.....	90
5.3. Microstructural transformations within solder joints	94
5.3.1. Microstructural transformations due to thermal-cycling	94
5.3.2. Tensile strength testing of cycled samples	100
5.3.3. Microstructural transformations during solid state annealing	102
5.3.3.1. In solder bulk	102
5.3.3.2. On the substrate-solder interface	104
5.4. Voiding and phenomenon of crystallographically-faceted voids formation....	106
5.4.1. Crystallographically faceted voids in ‘as soldered’ state.....	107
5.4.1.1. Solder joints with ‘massive’ copper substrate (substrate thickness	
> 10 000 μm)	107
5.4.1.2. Solder joints with ‘thin’ copper substrate (substrate thickness	
< 50 μm)	113
5.4.1.3. Pure bulk Tin (Sn) without substrate	114
5.4.1.4. Bulk SAC, CASTIN and Sn100C solders without substrate.....	115
5.4.2. Faceted void evolution during solid-state annealing	115
5.4.2.1. Solder-joints with ‘massive’ copper substrate (substrate thickness	
> 10 000 μm)	115
5.4.2.2. Solder joints with ‘thin’ copper substrate (< 50 μm).....	120
5.4.2.3. Bulk solders without substrate	121
6. DISCUSSION	126
7. CONCLUSION	144
8. FUTURE WORK.....	148

APPENDIX 1	150
APPENDIX 2	156
APPENDIX 3	162
9. REFERENCES	165

1. INTRODUCTION

The foundation of the transition to lead-free technologies in the electronics industry was laid in 1992, when an American senator, Albert Arnold Gore, submitted for USA congress consideration the administration bill named “Restriction of Lead Contaminations”, well known as “The Reid Bill”. A big list of lead-containing materials and products, including materials for electronic production, was attached to the bill. Moreover, in 1993 the “lead tax act” was passed, according to which every pound of lead in imported goods or produced within the country is subjected to tax charging. Lead was banned from use in electronic products selling on the European market after July 1st, 2006.

There are four main reasons for the transition to lead-free technologies in the electronics industry.

Impact on human health and environment. Lead is considered to be one of the most dangerous toxic materials. It is able to imitate biologically important metals in the body metabolism (such as iron and calcium) binding and interacting with the same essential proteins and molecules. Having displaced the original chemical elements in the molecules, lead terminates their functions essential for certain biological processes. Accumulation of lead in the body metabolism destroys the circulatory system, the central nervous system and damages reproductive function [1].

High temperature impact on solder joint mechanical stability. There is a tendency in the automotive electronics industry towards placing all the electronic parts in the engine compartment to avoid unnecessary wiring. But the working temperatures of electronic control units can exceed 150°C there. It is known that the strength characteristics of Sn6xPb3x solders become critical under temperature cycling conditions with a peak temperature over 125°C [2]. The higher temperatures lead to plastic deformation, diffusion,

recrystallization and grain growth inside of a solder joint. Investigations carried out by different research institutions such as JEIDA (Japan Electronics Industry Development Association) proposed the most suitable solder alloy for Sn₆xPb₃x replacement in automotive electronic industry is Sn/Ag/Cu [3].

Legislation. The laws that actively ban lead in electronic solders are the European Union's Reduction of Hazardous Substances (RoHS) Directive [4] and the Waste Electrical and Electronic Equipment Directive (WEEE Directive) [5]. Currently, aerospace/military and communications applications are exempt from this directive, which primarily covers consumer electronics, handheld devices and personal computers.

Competitive environmentally-friendly products. The first lead-free portable player MiniDisc MJ30 was produced in 1998 by the Panasonic company which straight away increased sales volume from 4.7% to 15%. In high-volume manufacturing there must be a negligible difference in the price of a lead-free device and a conventional one.

Problems caused by lead-free technology implementation

As a result of the issues highlighted above, lead-free electronics manufacturing has become a global trend. Traditional lead-based alloys have a considerable history and there has been extensive investigation of their microstructural stability and reliability. New solder materials proposed as replacements have ternary or quaternary compositions [2] which result in a drop in microstructural homogeneity (intermetallic phase formation) and a deterioration in reliability of solder joints and, consequently, reliability of a piece of electronic equipment. Another issue which brings a great deal of concern is the high melting temperature of the new lead-free soldering alloys [2]. Elevated soldering temperatures can damage component packaging and the materials of printed circuit boards (PCBs), leading to higher stress accumulation within the soldered interconnections due to

CTE (coefficient of thermal expansion) mismatch of the materials involved. Figure 1 explains the problem of melting temperature elevation from a technological point of view: the figure depicts the technological window of the soldering process, where the upper line delineates the maximal allowed temperatures while soldering (exceeding these in different stages can damage either the ability of the soldering paste to wet the metallization pads or damages the components to be soldered); the lower line delineates the minimal temperatures while soldering (not reaching those will result in poor wetting and even lead to failure to reflow a soldering paste). The soldering process is divided into two stages: preheating and reflow, both of these are of high importance. The first serves for flux activation and dissolution of oxidized layers from the surfaces to be soldered, whereas the second stage should provide proper wetting of the soldered pads and deliver all the necessary interfacial reactions with an intermetallic layer formed in order to create a strong bond [6].

While implementing lead-free solders in surface mount technology (SMT), problems caused by the soldering process window contraction can be faced: the lead-free solder melting temperatures are up to about 210 — 230 °C instead of 183 °C for the traditional tin-lead eutectic ($\text{Sn}_{63}\text{Pb}_{37}$), whereas components to be mounted are very sensitive to the process peak temperatures (maximal allowed temperature for most SMT components is 260 °C). Consequently, there is a narrower range of temperatures allowed during the reflow process (figure 1), deviation from which could bring defects and lower reliability of electronic products.

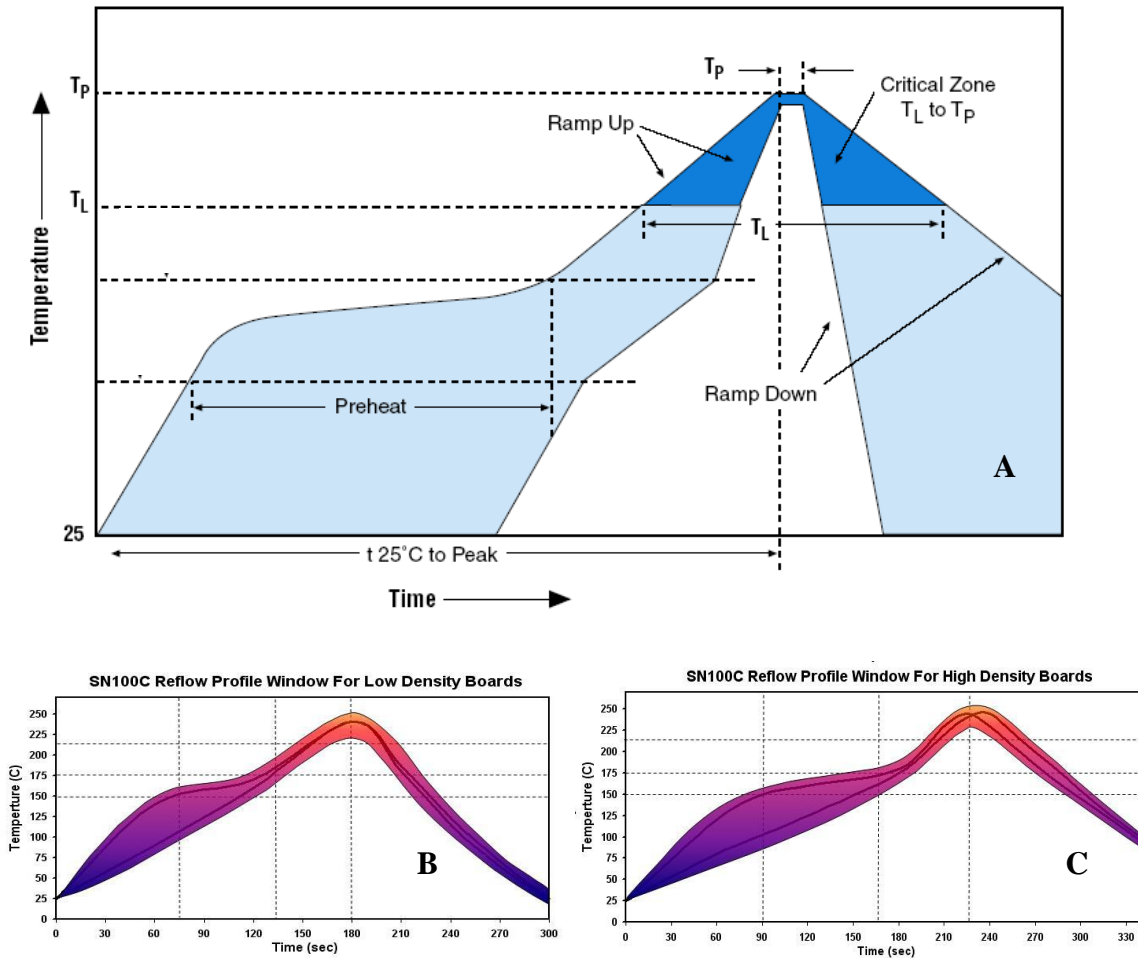


Figure 1. (A): Soldering process window: difference between T_L (solder melting temperature) and T_p (allowed peak temperature). The zone between T_L and T_p is very critical in terms of delivering a solder-joint of high quality [7]; (B,C): recommended reflow profile for the soldering paste SN100C for high- and low-density PCBs [taken from manufacturer (AIM Ltd.) technical datasheet].

In order to produce a reliable lead-free electronic device, the following aspects firstly need to be comprehensively investigated and understood [2]:

- microstructural stability of new lead-free soldering material;
- process of intermetallic phase formation;
- voiding processes in new materials;

- lead-free solder joint corrosion resistance;
- lead-free solder alloy compatibility with printed circuit boards (PCB) and surface mount component finishing metallization;
- lead-free solder alloy wettability of soldering pads and component metallization;
- property modification of boards and components under high temperatures;
- flux and washer fluid compatibility with lead-free technologies.

In the view of the above, the present work is devoted to microstructure optimization of new lead-free soldering materials. It includes investigations of:

7. growth and stability of intermetallic phases (which affect reliability) during soldering and service life;
8. factors which can affect soldering processes to improve the integrity of the solder-joint microstructure, namely, thermodynamic (investigation of effect of solder compositions), kinetic (cooling rates) and energetic (ultrasound vibration) influence on solidifying lead-free soldering alloy. The challenge of the ultrasound vibration investigation has arisen from a lack of information concerning the ultrasound influence on solidification processes in solders, but there is a vast amount of information about ultrasound microstructure optimization in the casting industry;
9. bulk intermetallic precipitates and interfacial intermetallic layer development in the “solder-joint” system;
10. mechanisms of solder-joint failure;
11. stability of microstructures over time (ageing experiments);
12. crystallographically-faceted void formation and evolution during the solidification process and following ageing.

This work is of particular interest as it aims to contribute original experimental data into the lead-free soldering knowledge bank and, consequently, to improve lead-free solder-joints long-term stability and reliability.

2. LITERATURE SURVEY AND THEORETICAL BACKGROUND

2.1. Potential lead-free alloys

Lead-containing alloys for soldering applications have been widely used in the microelectronics industry for the last decades. They not only provide the electrical contact between metallization of components and printed circuit boards, but at the same time, they also serve as a mechanical support for the components and deliver heat dissipation from the active ones. These alloys were used as a solderable surface finish layer of the component lead frames and printed circuit boards. Lead-based alloys have a long history and there has been extensive investigation of solder-joint microstructural stability and reliability. Nevertheless, the worldwide trend towards elimination of toxic materials from the electronics industry and customer demand for environmentally-friendly electronic devices has caused implementation of the new lead-free technologies. It is noteworthy, that the total amount of lead, used for electronic solders is less than 1% of the total lead consumption in different industries worldwide [3].

There are a many different lead-free alloys available nowadays. They can be categorized by parameters such as melting point, toxicology, cost, availability and chemical resistance. The preference is given to the Sn-Ag-Cu (SAC) alloy family, followed by alloys containing bismuth, antimony, indium, zinc and aluminum [8].

A solder alloy which is being proposed for the replacement of the traditional Sn-Pb eutectic composition should have its melting point as close as possible to the tin-lead eutectic temperature, and should have a narrow melting range to avoid ‘tombstoning’ of small components (the ‘tombstoning’ of an electronic component occurs due to non-simultaneous reflowing of soldering paste on metallization pads when the component can stand up on end due to surface tension of the molten solder). New lead-free soldering

alloys should be compatible with existing infrastructure and materials (many materials used in SMT will be damaged if exposed to 260 °C peak temperature even for a small period of time) [2].

At the moment, there are more than one hundred engineering solutions protected by patents for lead-free solder alloy compositions. However, there is not enough data on their long-term reliability in different environmental conditions. The preferred alloy for the Sn-Pb eutectic replacement is considered to be SAC family; however, this issue needs further investigation. The main types of lead-free alloys are shown in Table 1.

Alloy type	Composition, mass %	Meting temperature, °C
Lead-Free solders with low-melting temperature		
Sn/Bi (tin/bismuth)	Sn42/Bi58	138 (eutectic)
Sn/In (tin/indium)	Sn48/In52	118 (eutectic)
Bi/In (bismuth/indium)	Bi67/In33	107...112
Lead-Free solders with low-melting temperature for the traditional eutectic Sn-Pb replacement		
Sn/Zn (tin/zinc)	Sn91/Zn9	195...200
Sn/Bi/Zn (tin/ bismuth/zinc)	Sn89/Zn8/Bi3	189...199
Sn/Bi/In (tin/ bismuth/indium)	Sn70/Bi20/In10	143...193
Lead-Free solders with average-melting temperature for the traditional eutectic Sn-Pb replacement		
Sn/Ag (tin/silver)	Sn96,5/Ag3,5	221 (eutectic)
Sn/Cu (tin/copper)	Sn99,3/Cu0,7	227 (eutectic)
Sn/Ag/Bi (tin/silver/bismuth)	Sn93,5/Ag3,5/Bi3	206...213
Sn/Ag/Bi (tin /silver/bismuth)	Sn90,5/Ag2/Bi7,5	207...212
Sn/Ag/Cu (tin/silver/copper)	Sn95,5/Ag3,8/Cu0,7	217 (eutectic)
Sn/Ag/Cu/Sb (tin/copper/antimony)	Sn96,7/Ag2/Cu0,8/Sb0,5	216...222
Lead-Free solders with high-melting temperature		
Sn/Sb (tin/antimony)	Sn95/Sb5	232...240
Sn/Au (tin/gold)	Au80/Sn20	280 (eutectic)

Table 1. Lead-free alloys compositions and their melting temperatures [2]

Every single alloy presented in the table has its unique set of properties. The lead-free solders with low-melting temperature have quite limited application. They cannot be used in electronic devices operating in higher-temperature environments (over 100 °C) [2]. Most

of the lead-free alloys with average-melting temperature for the eutectic Sn-Pb solder replacement are alloys based on tin with small additions of copper, silver, bismuth or antimony. The most popular composition in electronics production nowadays is the ternary eutectic of the SAC (Sn-Ag-Cu) alloy family [8]. The Sn_{95,5}/Ag_{3,8}/Cu_{0,7} alloy has physical and mechanical properties which are the most closest to those of eutectic Sn₆₃Pb₃₇ [2]. Solders with high-melting temperature are commonly used in production of ball grid array packages (BGA). This technology named ‘flip-chip’ was developed to produce active components (memory etc.) with high-density interconnection. It includes two-level interconnects. The solder joints of the first level serve to attach flip-chips to a ceramic carrier. This type of interconnects was usually produced from Pb-rich solders with a melting temperature of 350 °C [9]. The second-level interconnects serving to attach the ceramic modules to a PCB were usually produced from Sn-Pb eutectic. Thus, a hierarchy was established of solders with melting points between two levels with a gap of more than 100 °C. In the situation of transition to the lead-free technologies, this hierarchy is being distorted since proposed lead-free solders can provide a maximum possible separation of less than 50 °C between the melting points of any two solders (table 1). This situation becomes quite challenging, since a great attention should be paid in order to prevent the first-level assembly from melting during the subsequent second-level assembly operations. The eutectic compositions shown in the table are more preferable since they crystallize at one fixed temperature preventing the components being soldered from displacement, and providing higher reliability and quality of the solder joints.

It is important to note that most of the candidates for lead-based alloy replacement typically contain Sn in considerable amounts (around 90%). Consequently, the mechanical, physical and chemical properties of these solders will be strongly influenced by the properties of pure Sn to a much greater extent than in the case of the lead-based solders [9].

Pure Sn is polymorphic and, depending on pressure and temperature, capable of existing in three allotropic modifications: α , β , γ [10]. The β -phase (white tin) has the body-centered tetragonal crystal structure, whereas, pure Pb has the face-centered cubic structure, which means that its mechanical and physical properties are more isotropic than those of β -Sn phase. The β -Sn phase has more restricted crystal symmetry and as a result it is more difficult to deform mechanically than Pb [9]. One of the remarkable features of β -Sn crystals is their ability to double refract the incident polarized light beam. The degree of the polarized light rotation strongly depends on the reflecting surface crystallographic orientation.

As a result of the research work concerning lead-free alloys [3], some quite promising candidates for the traditional lead-based alloys replacement have been proposed. They have different applications and different concerns, which are listed in Table 2.

Composition, wt%	Melting point, °C	Applications	Concerns
Sn–3.5Ag	221	SMT, flip chip	Cu dissolution, excessive IMCs, voids
Sn–3.8Ag–0.7Cu	217	SMT, PTH, BGA	Cu dissolution, excessive IMCs, voids
Sn–3.5Ag–3Bi	208 - 215	SMT	Cu dissolution, fillet lift, low mp phase
Sn–0.7Cu	227	PTH, flip-chip	Cu dissolution, wetting, excessive IMCs
63Sn–37Pb	183	PTH, SMT, BGA	Pb toxicity
97Pb–3Sn	317	Flip-chip	Pb toxicity
IMC - intermetallic compound; mp - melting point; SMT – surface mount technology; PTH - plated-through holes; BGA – ball grid array			

Table 2. Examples of Pb-free candidate solders and former Pb-containing solders [3]

The phase equilibrium diagrams (Figures 2 - 5) can explain the difficulty in obtaining a homogenous solder joint with stable mechanical properties while transiting to lead-free technologies. Near-eutectic Sn-Pb alloy (figure 5) has a homogeneous microstructure comprising of Pb-rich and Sn-rich phases, whereas lead-free solder systems (figure 4) tend to produce intermetallic precipitates (IMCs) during solidification. The IMCs will deteriorate the microstructural integrity of a solder joint and, consequently, deteriorate its long-term stability.

The eutectic temperature in the tin-silver-copper system is 217°C [9], higher than eutectic tin-lead by 34°C. The higher the melting point, the more serious problems it may cause in terms of the performance of materials to be assembled and reliability of solder joints. Consequently, the soldering process control becomes more challenging and the process parameters impact on the lead-free solder joint properties.

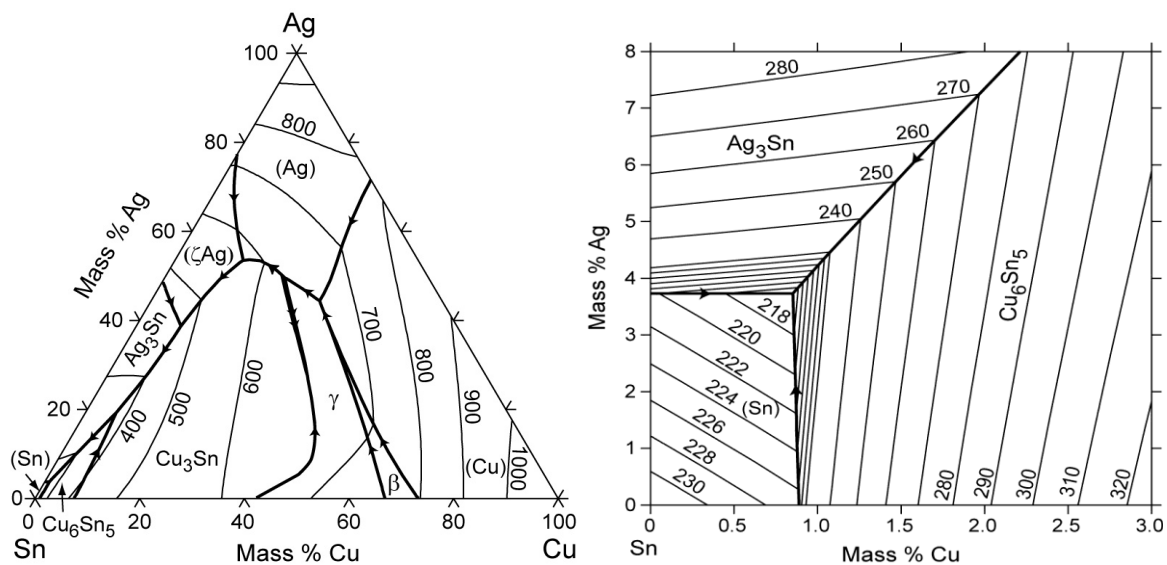


Figure 2. Sn-Ag-Cu phase equilibrium diagram [11]

The lines on the plot are the lowest temperatures in (°C) where Sn-Ag-Cu alloys of the compositions given by specific points on the graph have no remaining solid

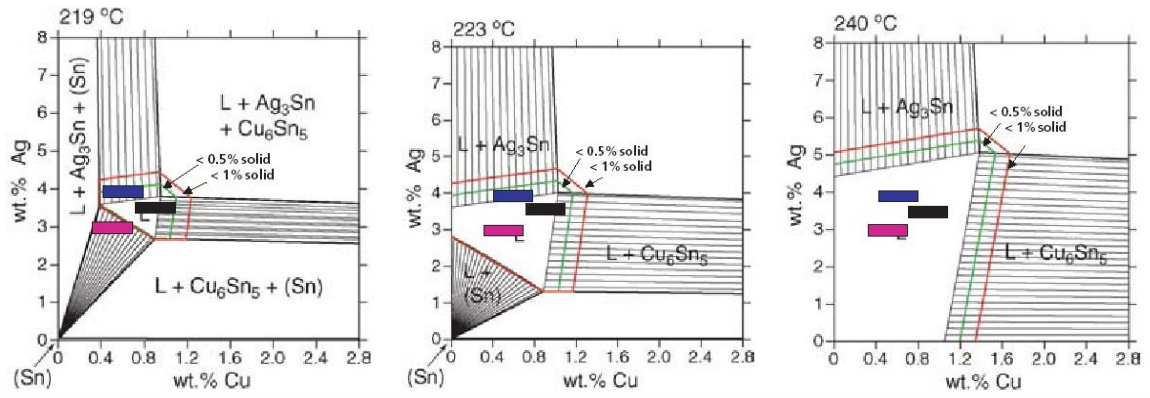


Figure 3. The Sn-Ag-Cu phase diagram shown at specific temperatures: (a) 219°C, (b) 223°C and (c) 240°C [8]. The colored rectangles correspond to the alloy ranges recommended by NEMI (International Electronics Manufacturing Initiative): blue and JEIDA (Japan Electronics Industry Development Association): purple; black rectangle shows the eutectic [8]. The region bounded by the green line contains less than 0.5% solid; the region bounded by the red line corresponds to less than 1% solid [8]

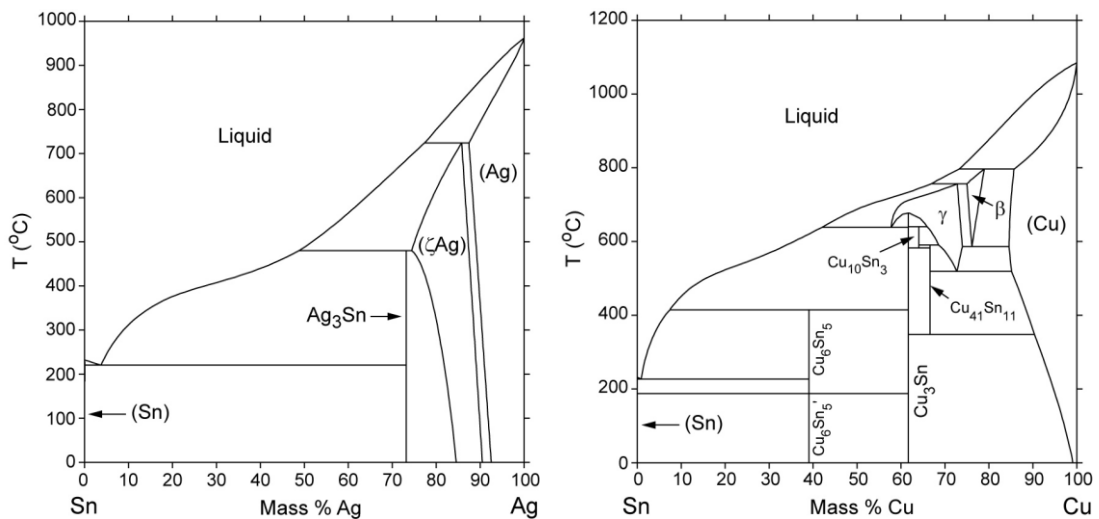


Figure 4. Sn-Ag [12] and Sn-Cu [13] phase equilibrium diagram

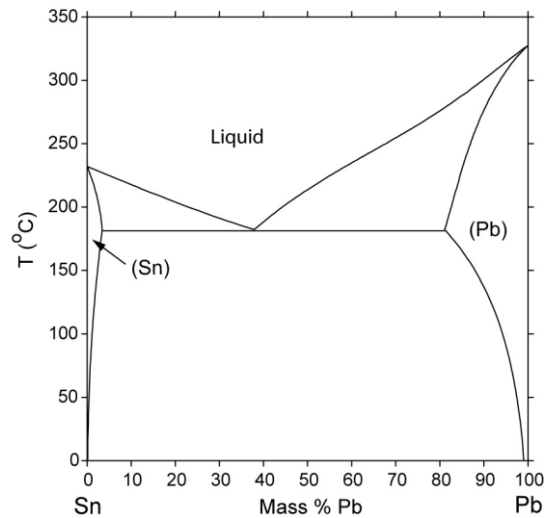


Figure 5. Sn-Pb phase equilibrium diagram [14]

2.2. Microstructures of Pb-free solder joints

2.2.1. Microstructure of eutectic solders

As was shown in Table 1, most of the potential lead-free alloys for lead-containing solder replacement have a binary or ternary eutectic composition. The eutectic composition provides benefits such as: (i) lowest melting point of a ternary system, (ii) the system melts at a single temperature (which is not always true for crystallization due to the undercooling required). The melting point of the traditional eutectic Sn-Pb composition is 183 °C. And the typical microstructure of this alloy can be described as a mixture of two phases: Sn-rich and Pb-rich (figure 6). The volume fraction of each phase is a function of the alloy composition. The size and shape of these phases are strongly influenced by the soldering process conditions. Fast cooling rates result in a finer structure. These are the microstructural features (phase morphology, phase distribution etc.), which determine the physical and mechanical properties of a solder joint.

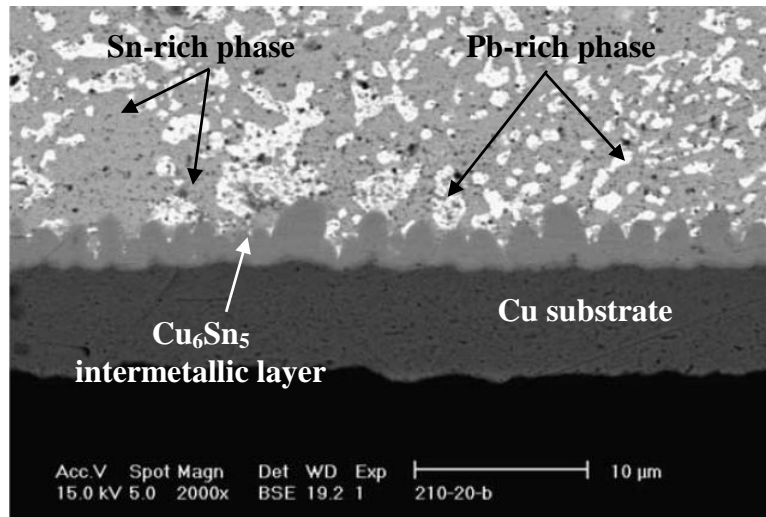


Figure 6. Typical microstructure of a Sn-Pb solder-joint [15].

According to the phase diagram, the equilibrium microstructure for the ternary near-eutectic Sn–Ag–Cu system should be a mixture of three phases — Ag₃Sn, Cu₆Sn₅ and β-Sn [16]. A typical microstructure observed in a SAC solder-joint is shown in figure 7. The microstructure is represented by β-Sn dendritic arms surrounded by ternary eutectic composition: β-Sn matrix with Ag₃Sn and Cu₆Sn₅ intermetallics entrapped [9].

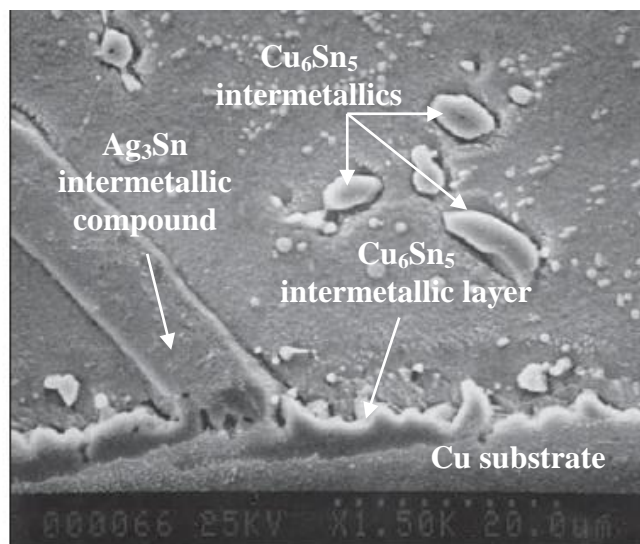


Figure 7. Typical microstructure of a Sn–Ag–Cu solder-joint [9]

Attempts to investigate the crystallization behavior as well as to define the ternary eutectic composition and ternary eutectic reaction in the Sn-Ag-Cu system have been undertaken by different researchers.

In 1959, Gebhardt and Petzow [17] investigated the entire liquidus for the Sn-Ag-Cu system. They described the transition reaction as follows: $L + \text{Cu}_6\text{Sn}_5 \rightarrow \beta\text{-Sn} + \text{Ag}_3\text{Sn}$ at 225 °C with the composition of the liquid of 4.0 wt % Ag and 0.5 wt % Cu.

In 1960, Fedorov [18] reported three isopleths. It is evident from those that the ternary eutectic reaction takes place at 218 °C.

In 1994, Miller et al. [19], by means of differential thermal analysis (DTA), discovered the ternary eutectic at 217 °C and described its composition as 4.7 wt % Ag and 1.7 wt % Cu. Based on these results a patent was issued [20].

Not long time ago, Loomans and Fine [21], using DTA, specified the composition of the ternary eutectic as 3.5 wt % Ag and 0.9 wt % Cu and described the transition reactions: $L \rightarrow \beta\text{-Sn} + \text{Cu}_6\text{Sn}_5$ and $L \rightarrow \beta\text{-Sn} + \text{Ag}_3\text{Sn}$.

There is still no agreement achieved about the exact eutectic composition of the system Sn-Ag-Cu and about the temperature of the eutectic reaction. The data obtained varies, which shows the complexity of ternary alloy system investigations and possible difficulties in prediction of exact behavior in different conditions.

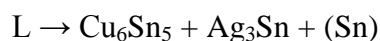
Nevertheless, the solidification behavior of the Sn-Ag-Cu is well investigated and understood. During the solidification of near-eutectic Sn-Ag-Cu alloys from the fully molten state, the equilibrium eutectic transformation is kinetically inhibited (due to comparatively fast cooling rates while soldering in production). The intermetallics (IMCs) Cu_6Sn_5 and Ag_3Sn tend to nucleate with minimal undercooling, whereas, the β -Sn phase requires from 15 to 30 °C of undercooling in order to start the nucleation process [22]. In contrast, Pb-rich solders require a very small undercooling before crystallization, as

illustrated in Table 3 [9]. Given this inequality in the required undercooling, Ag₃Sn and Cu₆Sn₅ intermetallic precipitates can grow to a considerable size in the liquid phase, in case of slow cooling rate of a solder joint. Having started to nucleate, the β-Sn phase grows by the dendritic growth mechanism with very rapid growth kinetics because of large amount of undercooling achieved [23]. On average, a solder joint can fully solidify in less than one second after the β-Sn phase starts to nucleate [22]. The very fast β-Sn dendrite formation and the associated release of latent heat of fusion raises the temperature of the solder joint suppressing the further nucleation of all three phases. Since the IMCs are not observed inside of the β-Sn dendrites, it is likely that most of the nucleation and growth of these phases occur in the supersaturated liquid phase. During the final stages of solidification, the rapidly growing dendrites impinge on each other, decorated with the IMC particulates.

Solder composition (wt.%)	Melting temp. during heating, T1 (°C)	Solidification temp. during cooling, T2 (°C)	Required undercooling, ΔT (T1 - T2) (°C)
Sn-3.8Ag-0.7Cu (SAC)	217.0	187.2	29.8
SAC + 0.1Zn	217.7	213.3	4.4
SAC + 0.7Zn	217.2	213.6	3.6
Sn-8Zn-3Bi	193.7	191.8	1.9
100Sn	232.6	217.5	15.1
95Pb-5Sn	305.6	302.4	3.2
100Pb	328.5	324.1	4.4

Table 3. The amount of undercooling required for the solidification of typical solders [9]

Thus, the crystallization process of the near-eutectic Sn-Ag-Cu system can be divided into three stages:



The first two stages occur in a certain temperature range, whilst the third stage takes place under certain fixed temperature, depending on amount of undercooling required [24].

The typical near-eutectic Sn-Ag-Cu microstructure is shown in Figure 8. The light colored regions of the optical image identify the β -Sn phase, the dark regions, surrounding the β -Sn dendrite arms, are represented by β -Sn matrix with intermetallic compound particulates Cu_6Sn_5 and Ag_3Sn entrapped [24].

It is worthy of note that the composition of the interdendritic regions exceeds the eutectic one in terms of Ag and Cu concentrations. Consequently, one may note that eutectic transformation occurs only during the final stages of the alloy solidification, i.e. the interdendritic liquid solidifies at the supreme moment [25]. During the pro-eutectic IMC phase formation the Cu and Ag atoms deplete from the surrounding Sn-rich liquid phase. Thus, the composition of the remaining liquid phase starts to deviate from its original one, which prevents the alloy's equilibrium solidification.

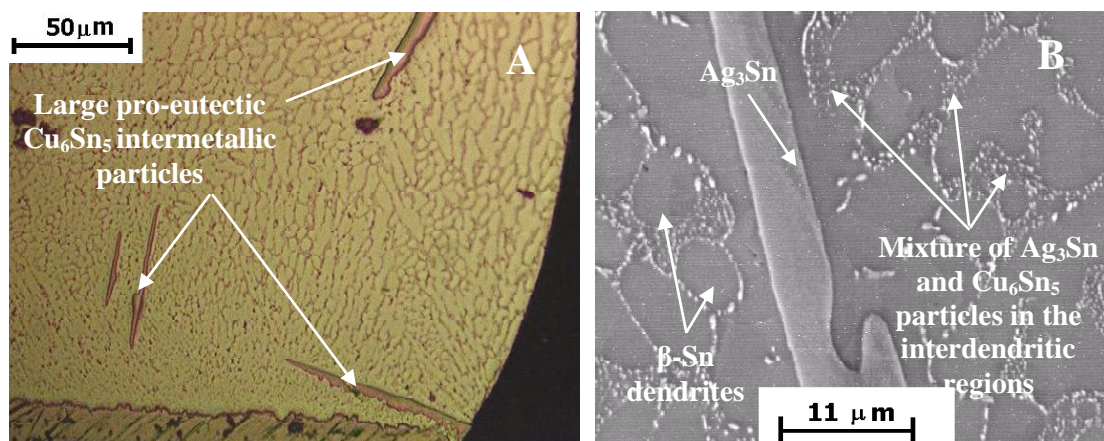


Figure 8. Optical (A) and SEM (B) micrographs of the typical solidified microstructure of Sn-3.8Ag-0.7Cu alloy [25].

Large IMC growth can be reduced whether thermodynamically (by reducing Cu and Ag content) or kinetically (by increasing solder joint cooling rates) [26].

The microstructure of near-eutectic Sn-Ag-Cu alloys is highly influenced by solder joint cooling rates. Therefore their physical and mechanical properties are also determined by cooling rates.

2.2.2. Near-eutectic Sn-Ag-Cu alloy microstructure: dependence on cooling rate

Most solder-joints assembled in a SMT production line have small volume and they are provided with a very good path for the latent heat dissipation during solidification. As a result, they have a rapidly solidified microstructure [9]. The resulting microstructure of the solder joint is highly influenced by soldering process conditions, such as peak temperatures, time above liquidus, cooling rates, solder volume, metallization area of components and PCBs and others. The growth morphology of the phases developing in the alloy during crystallization affects the resulting microstructure.

Examples of the microstructures of the near-eutectic Sn-Ag-Cu alloy obtained under different cooling rates are shown in the Figure 9 [27].

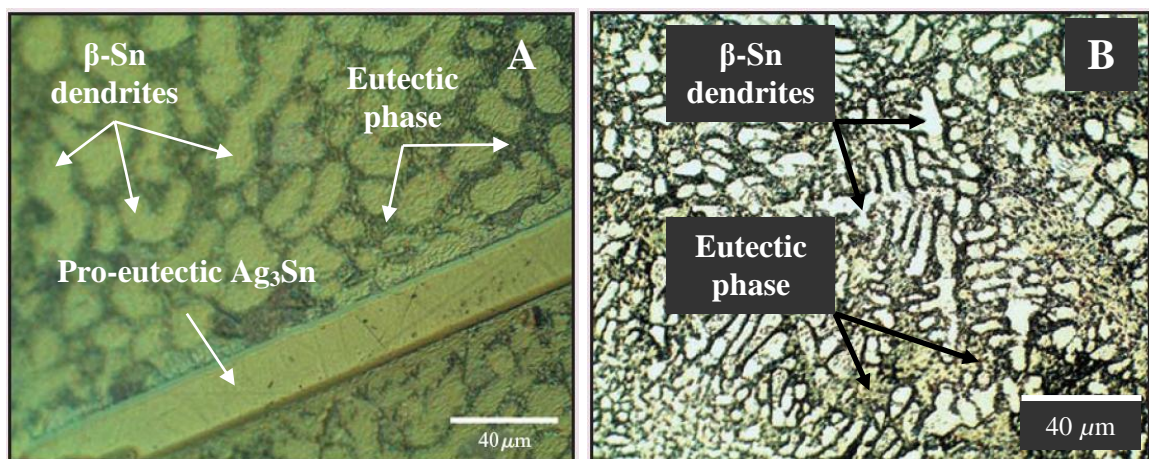


Figure 9. Microstructure of near-eutectic Sn-Ag-Cu solder solidified at (a) very slow cooling rate (0.02 °C/s); (b) very fast cooling rate (100 °C/s) [27].

Thus, Figure 9(A) shows the microstructure of a solder, solidified under a very slow cooling rate 0.02 °C/sec. The presence of a large pro-eutectic intermetallic phase is clearly evident. Slow cooling rates result in a coarsened structure with dendrites which are quite close to spheroidal. At the same time, fast cooling rates (100 °C/sec) result in microstructures typically as shown in Figure 9(B). In this case no pro-eutectic phases can be noted. The β -Sn dendrite structure is finer and more developed with extended dendrites and dendrite arm visible.

Ternary eutectic composition liquid is solidified in the interdendritic region during the latest stages of solidification [27]. Fast heat removal during solidification results in the increase of the thermal gradient at the dendrite growth front, which leads to further more fine branching of dendrites. As long as the eutectic structure is represented by IMC dispersion in β -Sn matrix and the Cu_6Sn_5 and Ag_3Sn intermetallic particulates are the main hardening agents of the near-eutectic Sn-Ag-Cu system, a high strength as well as high resistance to creep deformation is expected to be obtained with the rapidly cooled samples. From the fact that large pro-eutectic Cu_6Sn_5 and Ag_3Sn intermetallics are usually observed in the slowly cooled microstructures a conclusion can be derived that these precipitates nucleate and grow in the early stages of solidification, decreasing the amount of Ag and Cu that could be entrapped in the inter-dendritic regions at final solidification stages, that is reducing the amount of hardening agents in the inter-dendritic zones [9].

The growth of large pro-eutectic Ag_3Sn plates can be kinetically inhibited by fast cooling rates such as 1.5 °C/s or higher during solder joint crystallization [16]. However, there are pros and cons of rapid cooling rates in real production: the components to be mounted and the printed circuit boards can be damaged because of thermal stress and that would be a very undesirable effect. It has been reported that reducing the Ag content in Sn-Ag-Cu system is quite effective in terms of control of Ag_3Sn plate growth [9].

2.2.3. Near-eutectic Sn-Ag-Cu alloy microstructure: dependence on alloying elements

The microstructure and properties of the Sn-Ag-Cu alloy system is strongly dependent on alloying elements and impurities, such as Cu, Ag, Sb, Zn, Bi, In, Co, Fe and others.

Several authors [22, 26] have reported the effect on solder joint microstructure of the Ag content changing from 3.8% to 2.0%. For this range of Ag content in the alloy, the melting temperature of the Sn-Ag-Cu system essentially remains the same, close to the eutectic one. If the Ag content is higher than 3%, the pro-eutectic IMC Ag_3Sn can easily develop into large needles, under slow or moderate cooling rates ($1\text{ }^\circ\text{C/s}$). For Ag content less than 3%, the formation of the pro-eutectic IMC Ag_3Sn is inhibited even under quite low cooling rates ($0,02\text{ }^\circ\text{C/s}$). Higher Ag contents result in finer β -Sn dendrites and ternary eutectic structure, which could be explained by the effect of growth induced gradients of composition on dendrite growth fronts and the following branching of dendrites. Finer structure provides higher microhardness, compared with coarse one [22]. But on the other hand, higher hardness means less ductility and consequently shorter thermal fatigue life. According to the investigations, the near-eutectic Sn-Ag-Cu alloys with Ag content less than 3 wt.% are more suitable for the electronics industry in terms of their microstructure and mechanical properties [22, 26].

In similar studies [28], it was found that the tensile strength of the alloys is strongly dependent on the dispersion morphology of fine IMC Ag_3Sn in the interdendritic regions and area fraction of the ternary eutectic phase. A ternary alloy with the composition Sn-3.0Ag-0.5Cu, i.e. with lower Ag and Cu content, was recommended for the electronics industry [28].

The influence of Cu content on near-eutectic Sn-Ag-Cu alloy microstructure has been investigated [29, 30]. The authors observed that the pro-eutectic phase which segregates in

Sn–3.6Ag–1.0Cu alloy is Cu_6Sn_5 , which was in good correspondence with the phase equilibrium diagram for the system.

The dependence of mechanical properties of Sn–Ag–Cu alloys on Cu content has been also studied [31]. The range of the copper content variation was from 0.2 to 0.7 wt.%. Authors discovered that increase in Cu content stimulates the dendritic growth of β -Sn. It has also been reported [26] that the increase in the amount of Cu promotes pro-eutectic Ag_3Sn IMC formation. The same authors reported that Cu content influences the liquidus-solidus temperature range of a given composition of an alloy – i.e. so called “pasty range”. For soldering, it is strongly recommended to have as small a “pasty range” as possible in order to prevent solder joint defects. Thus, for Cu content 0,7% and Ag content variation from 2,1 to 2,7%, the “pasty range” changes from 2 to 4 °C respectively. At the same time for Cu content 0,9% and equal variation of Ag content, the “pasty range” changes from 15 to 17 °C [26]. Consequently, the “pasty range” of near-eutectic Sn-Ag-Cu solders is quite sensitive to Cu content (but not to Ag content) above its eutectic composition.

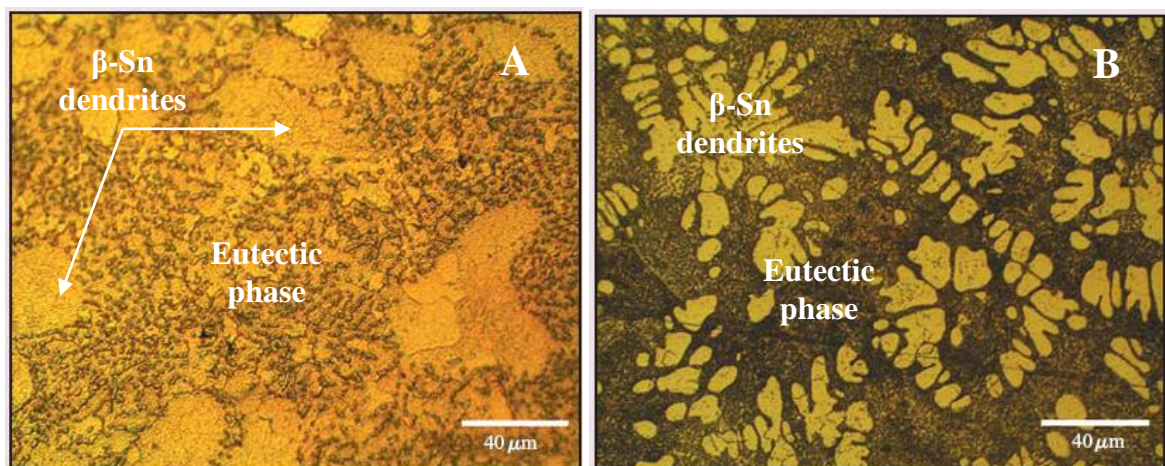


Figure 10. Microstructure of Sn–3.8Ag–0.7Cu–0.7Zn solder solidified at (a) 0,02 °C/s; (b) 100 °C/s [9].

The effect of Zn addition to the Sn-Ag-Cu system was investigated [27, 32] in order to control IMC formation. Zn additions can modify both the ternary eutectic and β -Sn dendrites. Figure 10 shows microstructures of Sn-3.8Ag-0.7Cu-0.7Zn solder solidified at two cooling rates (a) 0,02 °C/s and (b) 100 °C/s [11]. No large Ag₃Sn intermetallics were observed. Moreover, the ternary eutectic and β -Sn dendrites were significantly modified compared to the Sn-3.8Ag-0.7Cu alloy (figure 9). This can be explained by the reduction in the amount of undercooling before crystallization, as was mentioned above in Table 3 [27].

Addition of such elements as Fe and Co to the Sn-Ag-Cu system [29] has been reported to modify the matrix structure, producing more eutectic. These additions inhibit solder joint interfacial reactions [9].

2.3. Mechanical properties of lead-free solders

Several researchers [33] have investigated the microstructure-property relations of the lead-free alloys. As was mentioned above, the microstructure of the Sn-rich Sn-Ag-Cu system is significantly influenced by the presence of Cu, Ag and other alloying elements. The β -Sn dendrite structure is commonly observed in this system. The strain hardening of these solders is a function of the amounts of the alloying elements and the degree of plastic deformation. Higher plastic deformation and higher amount of alloying elements lead to solder joint hardening [9]. At the same time, in deformed and annealed SAC solders processes of recrystallization and grain growth take place, depending on the magnitude of plastic deformation and conditions of annealing. These two processes occur in pure Sn even at room temperature, while Sn-0.7Cu recrystallizes after annealing at 150 °C for 48 hr, requiring a small deformation of around 20% [9]. For the Sn-3.5Ag-0.7Cu system and

Sn–3.5Ag the magnitude of deformation should be more than 30% in order to recrystallize during annealing at 150 °C for 48 hr [9].

It has been reported [9] that Sn–3.5Ag–0.7Cu system has the highest microstructural stability during deformation and annealing comparing to the other lead-free solder candidate alloys.

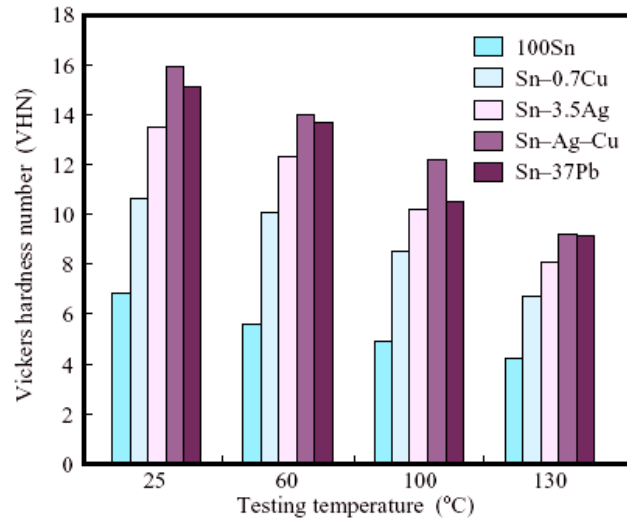


Figure 11. Microhardness of lead-free and Sn–Pb alloys as a function of testing temperature (sample cooling rate 4.0 °C/s, testing load 50 g, VHN is an average value of ten measurements) [9].

Figure 11 shows the comparison of microhardness of different lead-free alloys and traditional Sn-Pb eutectic solder. Vickers hardness number is plotted as a function of testing temperatures between 25 and 130 °C. As can be seen from Figure 11, the Sn-Ag-Cu alloy has the highest hardness within the range of tested solder compositions and this feature remains as the temperature increases. Pure Sn exhibits the lowest performance at all the temperatures. Sn–37Pb eutectic composition is close to Sn–3.5Ag–0.7Cu in hardness, including at elevated temperatures. There is a trend of gradual hardness reduction with

increase in temperature for every composition. Sn–37Pb and Sn–3.5Ag–0.7Cu have almost the same hardness at 130 °C [33].

In [34], properties of lead-free solder joints, based on Sn–3.5Ag–4.8Bi, Sn–3.5Ag–0.7Cu and Sn–3.5Ag alloys and with Cu and Au/Ni(P) coatings on the substrate, were investigated in terms of duration of the soldering process and intermetallic compound morphology and size. The shear strength of the lead-free solder joints assembled using Cu substrates was not drastically affected by IMC size or reflow time [34]. Nevertheless, when intermetallics occupy two thirds of a joint gap (in area), the shear strength can drop significantly. The shear strength of the solder joints assembled using Au/Ni(P) surface finish is lower than that of Cu, and decreases more rapidly with increase of intermetallic layer thickness or reflow time. The electrical characteristics (resistance) of lead-free alloys increases and then decreases with increase of the aging time or reflow duration for both Cu and Au/Ni(P) surface finishes. This could be explained by the IMC growth in the solder joint [34]. For instance, extended reflow time can result in interfaces bridged by large Ag₃Sn intermetallics, which have lower resistance than the bulk solder.

Solder alloy (wt. %)	Test method			
	Ring and plug shear strength (MPa)	Four-point bend shear strength (MPa)	Flip-chip shear strength (MPa)	Lap-joint shear strength (MPa)
63Sn–37Pb	32,7	29	9,2	50
Sn–3.65Ag	37,2	28	11,4	38
Sn–0.7Cu	27,0	-	9,2	-
Sn–3.8Ag–0.7Cu	35,1	47	12,5	39
Sn–3.5Ag–3Bi	-	-	-	49,6
Parameters				
Strain rate (mm/min)	0.10	0.10	15	0.25
Solder-joint gap (mm)	175	76	10	20
Reference	C. Foley et al. [35]	B. A. Cook et al. [36]	D. R. Frear et al. [37]	S. K. Kang et al. [34]

Table 4. Shear strength of lead-free solder joints (to Cu substrate) [9]

The mechanical properties of solder joints are more difficult to determine than those of bulk solders. Many variables should be taken into consideration, such as: solder volume, solder joint geometry and soldering process parameters, all of which can affect solder joint mechanical properties. Table 4 [9] compares the shear strength test results of different lead-free solders. The information provided clearly demonstrates, that shear strength can vary over quite a wide range, depending on test method, solder joint gap and strain rate.

2.4. Thermal-fatigue properties of lead-free solders

One of the most important reliability issues connected with solder joints is their micro-structural stability in thermal-cycling conditions. During service life, solder joints are subjected to thermal loads and very often the working temperature can vary in a quite considerable range. For instance, electronic control units and sensors placed in a vehicle engine's compartment can be subjected to extreme cycling conditions: from up to +150 °C (when the engine is running) down to -25 °C (in the winter time when a vehicle is left standing). Since all materials (and phases within materials) expand and contract at different rates, this change can lead to damage of printed circuit board interconnections and mounted components. Resulting stresses can lead to material cracking or can be accommodated within materials if they are ductile enough.

Several authors [38] have described the thermal-fatigue behavior of Sn-3.5Ag-3.0Bi and Sn-3.8Ag-0.7Cu in comparison with traditional Sn-Pb compositions. They have reported that the thermal-fatigue behavior of lead-free samples is more highly influenced by the thermal-cycling parameters (peak temperatures and cycle duration) than Sn-Pb solders. Figure 12 [38] shows the thermal-fatigue properties of lead-free solders and traditional eutectic Sn-Pb composition. For this experiment thermocycles were used with the following parameters: temperature range - from 0 °C to 100 °C, cycle duration - 30

minutes. As can be seen from the Figure 12 (a), the thermal-fatigue behaviour of lead-free solder-joints is better than for lead-containing samples.

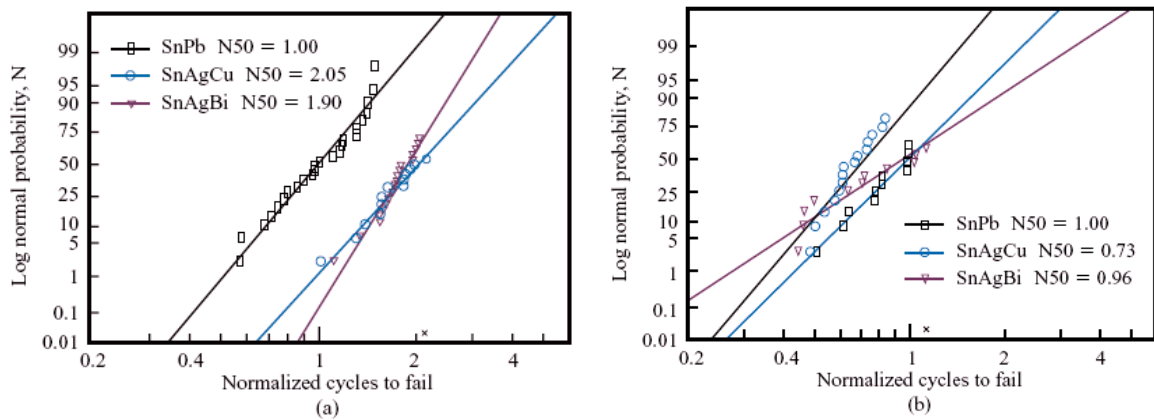


Figure 12. Thermal fatigue properties of lead-free solder joints and eutectic Sn–Pb tested under following conditions: (a) 0 °C to 100 °C, 30-min cycle time; (b) - 40 °C to 125 °C, 240-min cycle time [38]

At the same time, both lead-free and eutectic Sn-Pb solders exhibit almost the same thermal-fatigue behavior if the cycling conditions are more extreme: temperature range – from -40 °C to 125 °C, cycle duration – 240 minutes, which is shown in Figure 12(b). It has been reported that cycling temperatures higher than 125 °C drastically reduce solder joint thermal-fatigue resistance [38].

The thermal-fatigue properties of lead-free alloys were also studied in terms of content of intermetallic precipitates such as Ag_3Sn [39, 40]. The Ag content in lead-free solders was within the range of 2,1 – 3,8%. Different solder joint cooling rates were used: 0.5 °C/s and 1.7 °C/s. For thermal-cycling parameters, two modes were chosen: 0 – 100 °C and - 40 – 125 °C with cycle durations of 30 and 120 minutes. The best thermal-fatigue properties were demonstrated by the solder joints assembled with Sn–2.1Ag–0.9Cu alloy with a cooling rate of 0.5 °C/s and thermal-cycle duration of 120 minutes. They were found to be less dependent on cooling rates than those with Ag content of 3,8%. For thermal-cycle

duration of 30 minutes, and cooling rate of 0.5 °C/s, the best thermal-fatigue properties were demonstrated by the solder joints based on high-Ag-content solder Sn–3.8Ag–0.7Cu. Authors have noted that a slow cooling rate gives advantages in terms of thermal-fatigue resistance despite the Ag content or thermal-cycling test conditions [39]. It has been observed that in low-Ag content solder joints the crack propagation occurs inside the bulk solder, whereas in high-Ag content solder joints the fatigue crack propagation was noted to develop on the solder-metallization pad interface. This suggests higher ductility of low-Ag solder joints compared with high-Ag ones. Authors [39, 40] have pointed out that the influence of intermetallic Ag₃Sn precipitates on solder joint thermal-fatigue properties is a complex issue if the precipitates are located along crack propagation path. The presence of large Ag-based intermetallics is not desirable and, in terms of improving a solder joint reliability, it would be recommended to suppress excessive Ag₃Sn intermetallic formation [39, 40].

It was found that the fatigue crack propagation mechanism is different for the lead-free solder joint samples and lead containing ones [40]. Thus, as is shown in the Figure 13, in lead containing samples microstructural coarsening occurs near the failing interface, which can be caused by accumulated strains at the solder-metallization pad interface and repeated thermo-cycling load. This consequently promotes local softening and fatigue crack propagation. This effect is well known for traditional eutectic Sn-Pb solder joints [42]. In the case of lead-free solder compositions, it was observed that β-Sn phase recrystallizes in regions of high plastic deformation, in particular near the solder joint – metallization pad interface, Figure 14. The recrystallized regions are subject to creep deformation and provide relatively easy paths for crack propagation, which reduces the thermal-fatigue life [25].

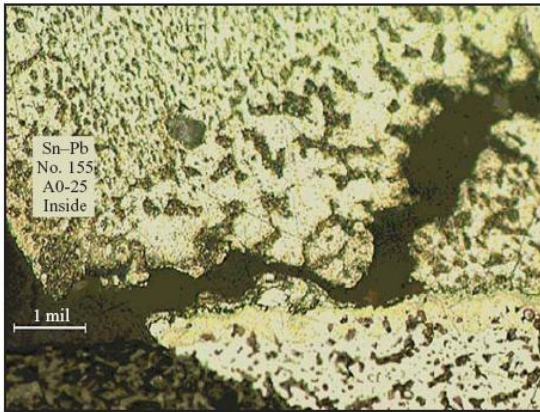


Figure 13. Thermal-fatigue crack propagation in eutectic Sn–Pb solder joint (thermal-cycling: 0 –100 °C, 30-min cycle), [40]

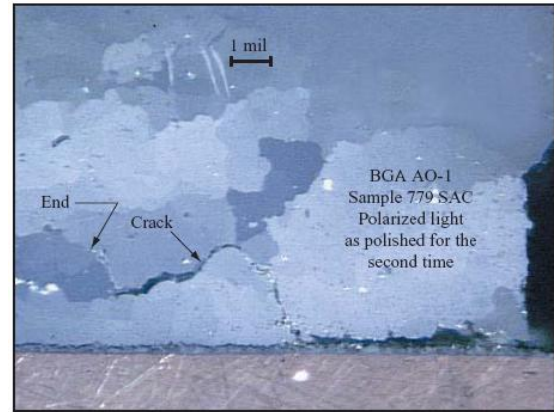


Figure 14. Thermal-fatigue crack propagation in Sn–3.8Ag–0.7Cu solder joint (thermal-cycling: - 40 –125 °C, 42-min cycle), [25]

Solder joint thermal-fatigue behavior in terms of different material combinations of solders and finish metallization is a complex issue. Some isothermal mechanical testing of lead-free solders under a strain-controlled condition has been reported [37]. The best mechanical-fatigue life among a large variety of lead-free and lead-containing solders was exhibited by Sn–0.7Cu alloy in combination with Ni or Cu pad metallization [37, 42]. In the case of Sn–0.7Cu composition, the thermal-fatigue failure mechanism does not involve solder-IMC interfaces and failure occurs as a result of massive solder deformation, what can explain the thermal-fatigue test results among the solders investigated [42]. It has been reported that the thermal-fatigue life of solder joints based on Sn–0.7Cu composition is 5,322 cycles with Cu pad metallization and 6,588 cycles with Ni. The temperature range used while testing was: - 40 – 125 °C [43].

2.5. Interfacial reactions in lead-free solder joints

2.5.1. During soldering

Despite the fact that interfacial reactions between pad metallization and molten solder are essential in terms of providing proper interconnection, they should not exceed certain

limits, otherwise they can result in a decrease in solder joint strength and deterioration in solder joint reliability. According to the results of several studies devoted to interfacial reaction investigation while soldering, the interfacial reactions can be divided into three stages: dissolution of a pad metallization surface into liquid solder [44–46], intermetallic boundary layer formation [46–48] and intermetallic precipitate separation [49–50]. If interfacial reactions are excessive and affect solder joint strength properties, a barrier on the coating layer is introduced over the pad metallization to prevent IMC growth during reflow. Interfacial reactions never stop and continue in the solid state while a device is in service, though the solid state reaction kinetics are many orders of magnitude slower than those in the liquid state.

It has been reported [44, 45] that the interfacial reactions in lead-free solder joints are faster and more numerous than in lead-containing ones. This can be explained by increased Sn content and temperatures of lead-free technologies. Authors [44, 45] noted that Cu and Ni metallization dissolution kinetics and consequent intermetallic precipitate growth are more intensive for lead-free solders. A variety of investigations have been carried out recently in order to understand the nature of interfacial reactions while using lead-free solder compositions. The main factors affecting the path of interfacial reactions are reported to be: solder composition [44, 45], presence and material of barrier layer [48, 49], soldering conditions [46], alloying elements [29, 30], solder volume [47].

The intensity of interfacial reactions will be a function of soldering peak temperatures, time above liquidus and Sn content. It has been reported that molten Sn is the most active metal to react with pad metallization, dissolving it and forming intermetallic compounds. But even small additions of alloying elements such as: Bi, Ni, Co, Fe and others can significantly inhibit or change growth characteristics of intermetallic precipitates [29, 30].

It has been proved that intermetallic growth kinetics are strongly affected by the relationship between solder pad area and solder volume [47, 48].

The nature of a barrier layer over solder pad metallization (electroless, electroplated etc.) affects the interfacial reactions as well. For instance, it has been noted [45] that electroless Ni over a Cu substrate dissolves into molten Sn-rich solders more quickly than an electroplated layer. Nowadays electroless Ni(P) barrier layers are being studied due to their benefits in terms of technological process and cost. But on the other hand, the presence of P causes more complex interfacial reactions while soldering and during device service life [49–50]. It has been also noted that the method of solder deposition influences intermetallic precipitates formation. Thus, while using soldering paste, the IMCs tend to spall more dramatically than IMCs segregated while reflowing an electroplated solder [49].

2.5.2. During annealing

There is a serious reliability concern connected with lead-free solder joints subjected to annealing at elevated temperatures (150 °C). This phenomena is caused by the formation of a second intermetallic layer over the first one followed with void formation between pad metallization and interfacial intermetallic layer [33, 51]. The void formation can be explained by the Kirkendall effect [52], consisting of imbalance of atomic (Cu and Sn) fluxes across the diffusing interface. It is assumed that Sn atoms diffuse through the interfacial intermetallic layer into the Cu substrate more slowly than Cu atoms diffuse out of the substrate into the bulk solder. Void formation was observed in solder joints on Cu substrates subjected to annealing at 150 °C; the voids were located between the interface intermetallic layer and the Cu substrate. The longer the annealing time the bigger the voids. After a certain annealing duration, the voids coalesce into a layer, which significantly reduces solder joint tensile strength [51]. As a result of numerous investigations in this field, it was proposed to implement diffusion barrier layers over substrates, or to introduce

alloying elements into lead-free alloys in order to retard interfacial intermetallic layer growth [30, 53].

2.6. Alloy composition optimization

Lower amounts of Cu and Ag in the Sn–Ag–Cu system inhibit the intermetallic formation thermodynamically. This phenomenon was fully described by several investigators [39, 40]. The presence of intermetallic precipitates becomes of high importance as solder volume decreases: growing intermetallic phases (Ag_3Sn) can physically connect pad metallization, affecting the solder joint electrical properties [54]. A large amount of intermetallic precipitates in the crystallized solder microstructure can affect the solder joint's mechanical properties and consequently its reliability. Therefore, lower amounts of Ag_3Sn intermetallics are preferable. It was noted that Cu content over its eutectic composition in the Sn–Ag–Cu system promotes Cu_6Sn_5 intermetallic phase formation in considerable amounts. This effect can be intensified while using Cu pad metallization. In addition, high Cu content increases the “pasty range” – the gap between the liquidus and solidus temperatures [26], which is not beneficial in terms of solder joint reliability. The recommended Cu content in Sn–Ag–Cu soldering alloy should not exceed 0.7–0.9 wt.% [26].

2.6.1. Minor alloying element additions

Small additions of some alloying elements to the Sn–Ag–Cu near-eutectic system were reported to reduce IMC formation. For instance, small Zn additions suppress Ag_3Sn intermetallic formation [32], which can be explained by the reduction in the amount of undercooling before β -Sn dendrite solidification (the possibility of large Ag_3Sn IMC segregation will be reduced kinetically upon solder joint cooling, as solidification time will

decrease). Sn–Ag–Cu alloys modified with Zn addition are less sensitive to cooling rates than those without Zn. This could be beneficial in terms of flexibility in soldering conditions during production. Moreover, SAC alloys modified with Zn additions display different interfacial reaction characteristics while reflowed on Cu substrates [27, 55]. It has been reported [55] that small Zn additions to the Sn–Ag–Cu near-eutectic system suppress the excessive intermetallic interfacial layer formation while a Cu substrate is being used. In order to improve the lead-free solder joint reliability, it was proposed to use some other minor alloying elements as an addition to the Sn–Ag–Cu system, such as In, Co, Ni, Fe [29, 30, 53]. Minor elements cause some drawbacks as well: it will be more difficult to control the alloy composition, it can cause alloy hardening and it will affect the technologies of solder alloy production, increasing their final cost.

2.6.2. Tin pest

There is one more serious reliability issue connected with Sn as a main component of the soldering alloys. Tin has an allotropic transformation occurring below 13 °C, so called “Tin pest” when white tin (i.e. β -Sn with the tetragonal structure) transforms into grey tin (i.e. α -Sn the with cubic structure). This causes a large volume change and consequent surface cracking. This type of transformation was observed in the system Sn–0.7wt.%Cu [26, 56]. However, solder joint samples assembled using SAC alloys and subjected to temperatures lower than – 40 °C for two years have not show any structural transformations [26]. The allotropic transformation causes very serious reliability issues and it is strongly desirable to modify the solder alloy composition in order to suppress this transformation. It has been reported, that a small amount of Bi retards the transformation [57] but at the same time it brings another reliability concern – they reduce solder joint thermal-fatigue life, caused by the hardening effect of Bi on SAC alloys [39, 40].

2.7. Ultrasound modification of crystallizing alloy microstructure

Ultrasound microstructure modification of crystallizing alloys has a long history. Different investigators reported the advantages of ultrasonic implementation upon alloy crystallization. Y. Sokolov [58] first investigated the impact of ultrasound vibration on processes of different metals crystallization in 1935. Other researchers [59, 60] continued work in this area, investigating the mechanisms of nucleation and crystal growth in the ultrasound field. Works of the authors V.I. Danilov et al.[61, 62] discovered the nature of the processes of nucleation and crystal growth of undercooled organic substances under applied ultrasound field. A.P. Kapustin [63] carried out a wide range of experiments and described more precisely the phenomenon of ultrasound influence on solidifying metals. The investigations in this area are still of great importance nowadays, since phenomena involved are not well understood yet.

Process analysis of ultrasound field influence on crystallizing metal is considered to be a very complicated issue. In order to understand the entire range of physical phenomena taking place in solidifying metal within ultrasound, one should possess a well developed understanding of system crystallization stages and effects occurring while the system is under influence of ultrasonic vibrations.

The resulting microstructural characteristics are highly dependent on the following parameters of the solidification process: mixing intensity and impurity diffusivity coefficients; rate of crystal growth, temperature gradient and amount of undercooling near the solid-melt interface. Modifying these parameters one could obtain a desirable resulting microstructure. Ultrasound vibration introduction during crystallization can affect the degree of undercooling and the shape of the solidification front, which consequently changes the structure, suppressing dendritic crystal growth morphology [64].

Ultrasound vibration of a threshold intensity introduced into a solidifying metal, produces special conditions for solidification. The main phenomena taking place in a solidifying alloy during ultrasound vibration are: cavitation effect, acoustic flows, radiation pressure and viscous friction [64].

In liquid alloys, as in other liquid media, cavitation can occur if the vibration pressure of ultrasonic waves exceeds a threshold level which is individual for every system. Since liquid alloys have a large amount of gases dissolved, cavitation bubble formation is promoted even at moderate ultrasound intensities. Difference of gas solubility in liquid and solid phases results in excessive gas concentration in the liquid phase, which consequently creates an additional source of cavitation bubbles and lowers the cavitation threshold value [64].

Cavitation affects solidifying microstructure in two ways: due to shock waves radiated while cavitation bubbles collapse near the solid-liquid interface (the growing crystals are being continuously broken) and by the alloy's local homogeneity and thermodynamic equilibrium deviation (as a result of a bubble collapse) which changes the conditions for the nucleation site formation and liquid-solid phase transition parameters [64].

Acoustic flow generation in a liquid alloy is caused by energy losses in the system. Acoustic flows result in mixing in the liquid part of the system and have an impact on the temperature field distribution and intensify processes of convective diffusion. The particle velocity and acoustic flows result in viscous friction, which can be explained by differences of vibration velocities of liquid and solid phases. Apart from the mechanical influence on growing crystals, the viscous friction can affect the liquid-solid interface, consequently changing the conditions of new crystals nucleation and growth [64].

Cavitation effects merit close attention. Analyzing different mechanisms of influence of cavitation on the formation rate of nucleation sites, two assumptions can be derived.

The first: while cavitation is taking place, the pulsing bubbles appear in the liquid alloy. The volume of the bubble increases drastically during the half-period of rarefaction of travelling acoustic wave, which results in surrounding liquid phase evaporation inside the bubble. Evaporation and bubble expansion result in a temperature drop inside the cavity and, in case this temperature is lower than its equilibrium value, the liquid phase near the interface bubble wall – the liquid will be undercooled. Consequently the bubble walls can be the site of nucleation. At the next half-period of compression of the acoustic wave, the bubble collapses. Small crystals, having just nucleated, leave its walls travelling into the liquid phase. This detachment occurs due to a difference in the motion speeds of liquid and solid phases. After the full collapse of the cavitation bubble, it radiates a shock wave which carries nucleation sites and small crystals further into the liquid phase [64].

The second assumption: the cavitation effect is based on shock wave generation while bubbles are collapsing. Having collapsed, a bubble radiates not only shock waves, but also transfers its energy into heat and the temperature rises locally. At the same time shock waves produce high pressure regions, which locally change the alloy melting temperature and shift it towards higher values. The pressure increase inside the melt is equal to the system's undercooling increase and results in promotion of nucleation site formation [65]. It should be noted that part of the energy released when a bubble collapses transfers into heat, raising the temperature of surrounding regions and suppressing nucleation.

As it concerns the viscous friction, this effect causes spalling of smaller crystals from the main ones and changes the surface tension values at the solid (crystal) – liquid interface [64]. Due to the molten alloy viscosity every movement of solid particles within the melt is connected with friction.

2.8. Voiding

As mentioned in section 2.2.2, one of the major aspects influencing a solder-joint's long-term reliability is its microstructural integrity. Formation of a non-equilibrium microstructure during solidification of lead-free solders results in a microstructural homogeneity decrease compared to the lead-containing ones [9]. It has been reported by several authors [66, 67] that lead-free solder-joints are more exposed to voiding than traditional lead-containing ones. Voids become troublesome when they form in large quantities, reducing a solder-joint cross-sectional area [66]. According to the IPC-610-D [68] standard for electronic assemblies, the maximum voids' area should not exceed 25% of solder-joint cross-section. Research carried out by Wickham et al. showed that void level in lead-free PBGA solder-joints does not exceed 15% regardless of soldering conditions [69].

Raiyo Aspandiar [70] proposed a classification of voids commonly detected in solder-joints as follows: macro voids, planar micro voids, shrinkage voids, micro via voids, pin hole voids and Kirkendall voids (table 5). Some of those (shrinkage voids) are unique for the SAC solders, caused by its solidification sequence [70]. Voiding in solder-joints was also investigated by Jang et al. [71] who described an additional type of void unique for lead-free assemblies, and occurring during solid state ageing. Jang et al. have reported that these voids are always found to be attached to the intermetallic particles in the solder matrix, especially to those formed during interfacial processes on a substrate's surface.

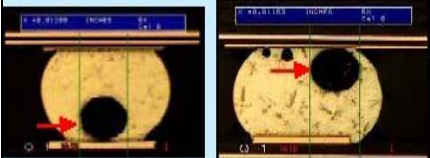
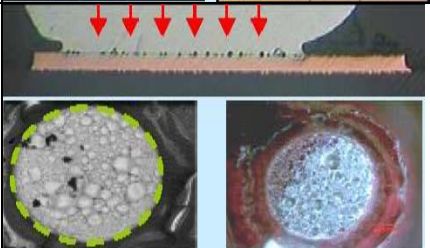
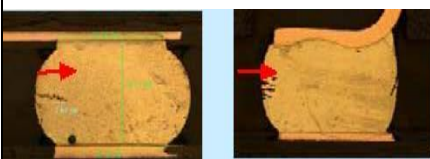
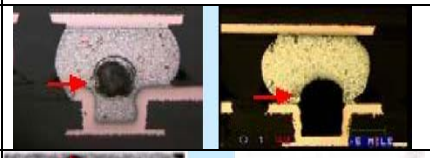
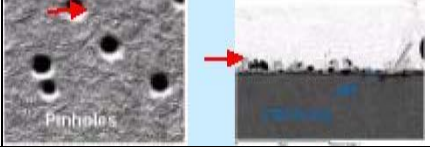
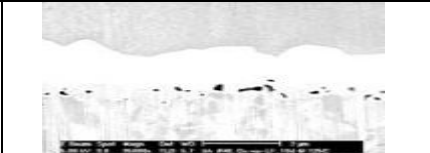
Type of Voids	Description	Photos
Macro Voids	Typically 100 - 300 μm in diameter, caused by the evolution of unstable ingredients of the fluxes and found to randomly spread in the solder-joint	
Planar Micro Voids	Usually smaller than 25 μm in diameter, presumably caused by anomalies in the surface finish (contaminations or oxidization) and usually found to spread at solder-substrate interface in one plane	
Shrinkage Voids	Form in a shape of linear cracks with `dendritic` edges, usually developing from the surface of the solder, but also found in the bulk. Caused by the solidification sequence of lead-free solders	
Micro-Via Voids	Typically from 100 μm in diameter caused by microvias in soldering pads	
Pinhole Voids	Typically from 1 μm in diameter, caused by deviations in the copper plating process and found to be located in copper metallization pads of PCBs	
Kirkendall Voids	Typically of sub-micron size, found between the intermetallic layer and the Cu substrate, caused by difference in interdiffusion rate between Cu and Sn.	

Table 5. Types of voids in solder-joints (PCB – Printed Circuit Board) [70]

Brief summary of the literature survey section

Despite the large choice of soldering alloys available nowadays, electronics manufacturers prefer using the Sn-Ag-Cu or Sn-Cu-Ni based solders, since they exhibit better technological flexibility and reliability.

New environmentally-friendly alloy compositions comprise of more than 95% of Tin and their mechanical and physical properties are influenced by the Tin to a much greater extent compared to the traditional lead-containing solders. Moreover, lead-free alloys proposed

for the replacement have more complicated composition (additions of alloying elements: Cu, Ag, Ni etc.), which results in intermetallic phase formation during solidification and, consequently, in deterioration of a solder-joints microstructural integrity.

There is a continuous search for the optimal soldering alloy composition and for ways of improving the existing ones (in terms of their microstructural stability and long-term reliability). Near-eutectic solders are considered to be the most preferable choice due to their contracted melting range, resulting in reduction of soldering defects. The microstructure of a solder can be influenced thermodynamically (levels of alloying elements), kinetically (cooling rates) and energetically (electromagnetic field, ultrasound etc.). These approaches can be only partially implemented by the electronics industry, since there are a vast number of variables involved in the soldering process and, for instance, an attempt to improve one of them can lead to deterioration of another essential parameter. In order to achieve enhanced solder-joint reliability, all the factors affecting its microstructure are being investigated separately with subsequent integration.

The most common techniques for evaluation of a solder-joints long-term stability and reliability are: thermal-cycling testing, ageing under elevated temperature and current load testing which can rapidly reveal microstructural changes occurring in a solder-joint during service life.

The data obtained to date on lead-free solders is not sufficient to make long-term predictions of their reliability in different conditions (space applications etc.) and extended research is required to achieve enhanced performance of new environmentally-friendly solders.

3. MICROSCOPY TECHNIQUES

3.1. Reflected light microscopy

Reflected Light Microscopy is designed for the study of opaque specimens which are not able to transmit light. For the study of opaque objects (usually in metallurgy applications), light must be directed vertically through the microscope objective lens onto the surface of the specimen and, being reflected, returned to the microscope objective and hence to an eyepiece, view screen or camera [72].

3.2. Cross-polarized light microscopy

Cross-polarized light microscopy is designed to observe optically anisotropic samples. A reflecting light microscope with a cross-polarized option includes two main parts: a polarizer (which is placed in the light path before the sample) and an analyzer (located in the light path between the rear aperture and eyepieces). The interaction between plane-polarized light and the surface of a doubly-refracting sample (such as a Sn-rich alloy) will produce two separate wave components polarized in mutually perpendicular planes. This phenomenon is used in cross-polarized light microscopy for obtaining image contrast. Thus, the speed of these two components is different and their correlation will vary in different areas of the sample's surface. After reflecting from the specimen, the components of the light become out of phase and the analyzer serves for their recombination to obtain image contrast [73].

In the present study, the Olympus Vanox BH-2 microscope was used, equipped with video camera Olympus DP70 connected to a computer.

3.3. Scanning electron microscopy

The scanning electron microscope (SEM) is nowadays a widely used instrument in various fields of science. It allows observation on a nanometre to micrometre scale in a wide range

of materials [74]. SEM acquires images of a specimen surface by scanning it with beam of electrons of high energy. The electrons from the beam interact with atoms of the specimen's surface producing signals containing information about composition and other properties of the specimen (such as surface topography, electrical conductivity). It also permits acquisition of three dimensional-like images. The interaction of the electron beam with the surface being investigated produces different type of signals, such as: secondary electrons, backscattered electrons, characteristic X-Rays and other photons of different energy. In the present study, the scanning electron microscope served to supplement the light microscope, providing large depth of field images of higher resolution and supplying with information about phases existing within samples.

The typical SEM consists of the components depicted in figure 15. The system works under a vacuum of about 10^{-4} Pa. The electron gun with a filament (usually made of tungsten [75]) is placed on top of the electron column. Being heated, the filament emits a beam of electrons which are driven away by an accelerating voltage of 1 – 30 keV applied between the filament and the anode in the electron gun. Further on their way down, electrons meet a series of condenser lenses and apertures. Magnetic lenses control the diameter of the beam as well as focus the beam on the specimen. Apertures (micron-scale holes in metal film which the beam passes through) change geometric parameters of the beam. Thus, the electron beam, collimated by the electromagnetic condenser lenses, passes through the aperture and is focused by the objective lens. It is scanned over a sample surface in a rectangular set of lines, named a raster, by scanning coils. The diameter of the electron beam before it reaches the sample surface is about 1-10 nm. Electron interaction with the sample surface results in the production of secondary electrons (SE), backscattered electrons (BSE), characteristic X-rays, light (cathodoluminescence), specimen current and transmitted electrons. These types of signal all require specialized detectors that are not

usually all present on a single machine. Figure 15 also depicts the electron beam interaction with a sample surface. Released secondary electrons from the sample are collected by a secondary electron detector, converted into a voltage and amplified.

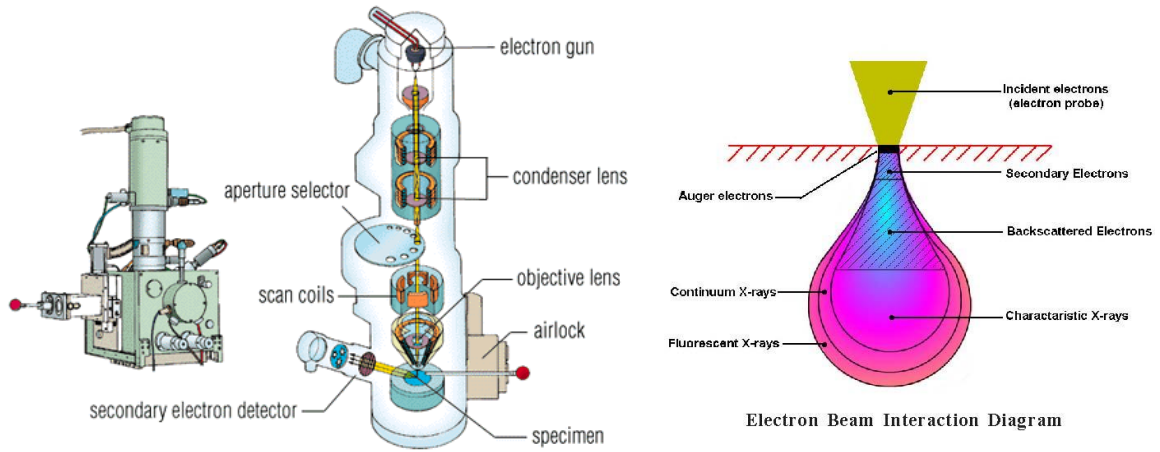


Figure 15. Typical structure of a scanning electron microscope and an electron beam interaction diagram [76]

Secondary Electrons are emitted from the sample with energy less than 30 keV, and are primarily produced by the inelastic interactions between beam electrons and weakly bonded electrons in the sample. An Everhart-Thornley (E-T) detector is used to convert the secondary electrons into an electrical signal in order to create an image representing the topology of the scanned sample's surface (figure 16).

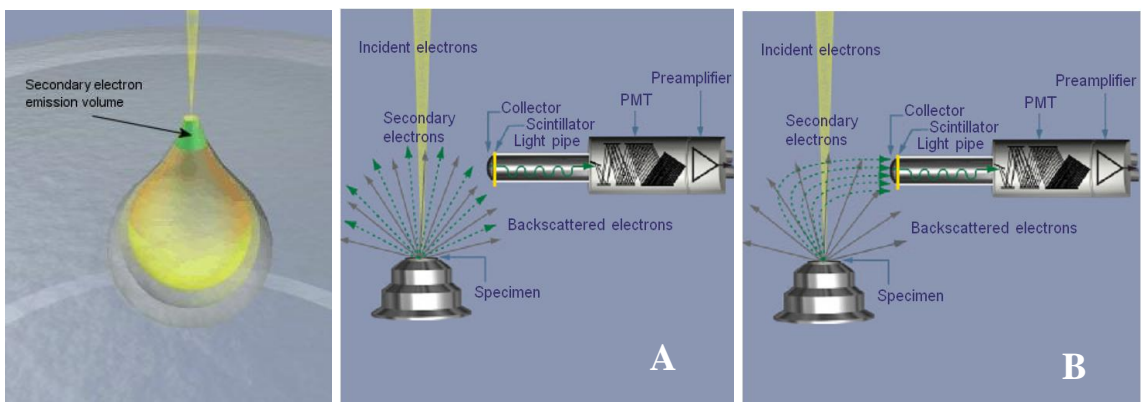


Figure 16. Secondary electrons emission volume and their detection (A: bias off; B: bias on) [76]

Backscattered Electrons are produced as a result of elastic interactions between the electron beam and the nuclei of atoms. These electrons keep their velocity (travel in straight lines) and they come back out of the sample. The number of BSE increases with the increase of the atomic weight. Thus, the BSE detector, which is located on the BSE path, can be used to obtain an image showing different elements [74].

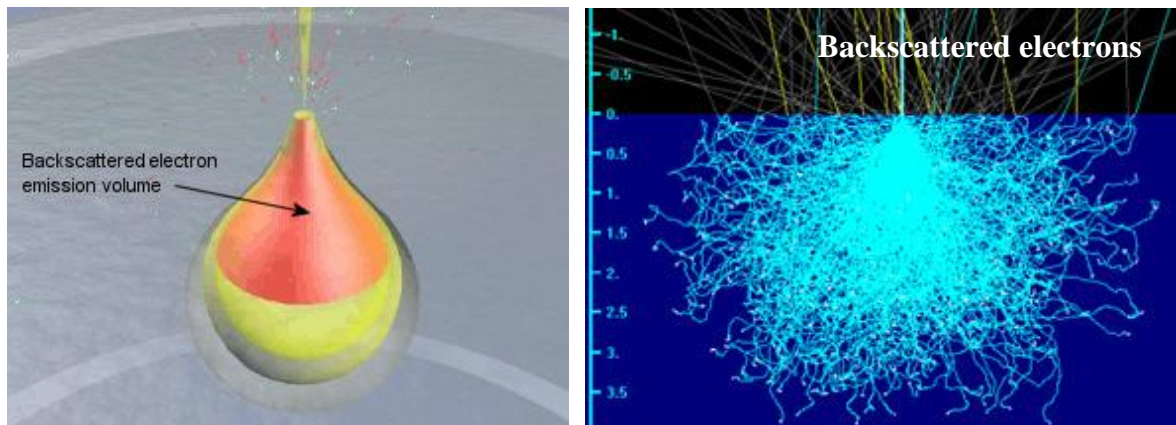


Figure 17. Backscattered electrons emission volume and their traces [76]

In this project a Field Emission Gun Scanning Electron Microscope (FEGSEM) – FEI Sirion 200, was used. In addition to ultra-high resolution imaging, it is equipped with an Energy Dispersive X-ray (EDX) detector and Electron Backscattered Diffraction (EBSD) facilities.

3.4. Electron Backscattered Diffraction

Electron Backscattered Diffraction (EBSD) is a technique for obtaining information about a specimen's crystallographic data. EBSD is coupled with scanning electron microscopy and can be supplied in an SEM as an option. In EBSD the investigated sample is tilted at 70° from the horizontal. The incident electron beam strikes the sample surface producing diffracted electrons which are detected by means of a fluorescent screen. The pattern formed by the diffracted electrons on the fluorescent screen is unique for every crystalline material and it is a characteristic of the crystal structure and orientation of the sample

region from which it was generated. Different types of crystallographic information can be obtained from the diffraction pattern: type of the crystal lattice and crystal orientation, grain boundary misorientations and information about crystalline imperfections. EBSD mapping is quite a common technique for obtaining crystallographic data which describes the polycrystalline sample's surface. In this case, the electron beam scans the sample surface measuring at each point, with set resolution, the crystal orientation. The resulting map will show the grain morphology, orientations, and boundaries. This data can also be used to reveal the crystalline texture in the material. Thus, EBSD analysis can provide quantitative information concerning sample microstructure, which would be an important addition to the SEM analysis results. An example of a diffraction pattern with Kikuchi bands (pair of lines formed on the fluorescent screen of the EBSD detector as a result of backscattered electron diffraction) is depicted in figure 18 [77].

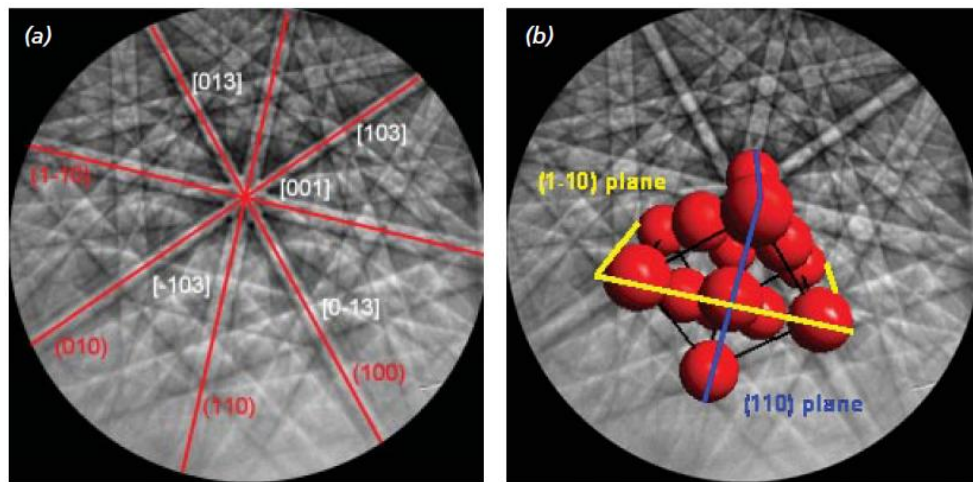


Figure 18. The diffraction pattern with the Kikuchi band unit cell orientation [77]

Figure 18(a) shows an example of diffraction pattern, where the Kikuchi bands are labeled with the Miller indices of the crystal planes that formed them. Figure 18(b) depicts a unit cell orientation which generates this pattern with the corresponding crystal planes shown.

In the following figure, the principal EBSD system components are depicted. The sample placed in the vacuum chamber is tilted at 70° from the horizontal. Electronic hardware and

software controls the beam position scanning the points of interest on a tilted crystalline sample. A phosphor screen which is fluoresced by electrons from the sample generates the diffraction pattern which is viewed by a sensitive charge coupled device (CCD) video camera. A computer controls the EBSD experiment analyzing the diffraction patterns and processing and displaying the results.

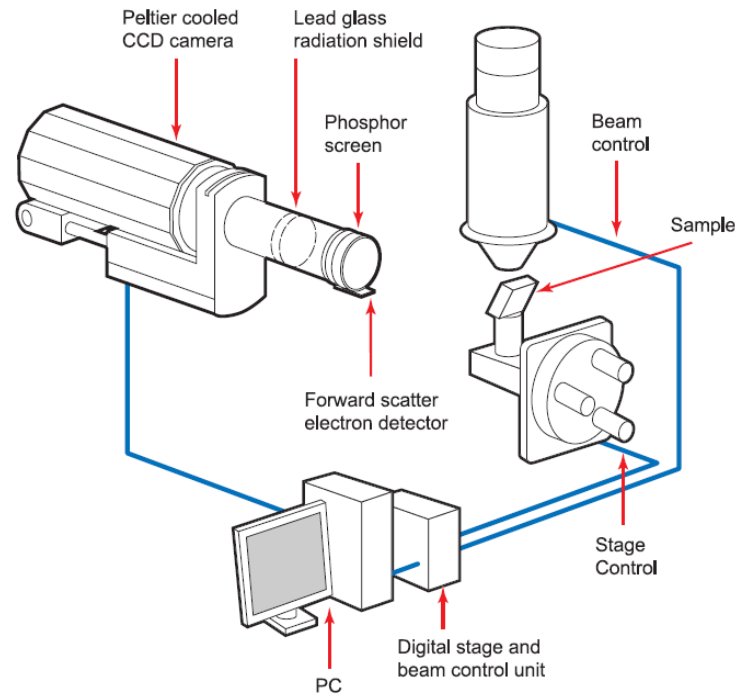


Figure 19. EBSD system components [77]

3.5. Energy Dispersive X-Ray Analysis

Quite often SEM is equipped with an Energy Dispersive (EDX) detector which enables both quantitative and qualitative elemental analysis of a sample.

An EDX system consists of a sensitive X-ray detector, a liquid nitrogen vessel for cooling and software to collect and process the data obtained (energy spectra) [74]. The detector is placed in the sample chamber as close to the specimen as practicable in order to collect the maximum possible energy of incoming X-rays by ionization. The X-ray entering the detector is converted into an electrical signal of proportional size; the resulting electrical impulses are amplified, registered and can be presented as energy spectra. Every element is

represented by characteristic X-rays. The detector is made of semiconductor silicon or germanium crystals which operate at low voltages to improve sensitivity. EDS system software analyses the energy spectrum in order to determine the abundance of specific elements, and can create an element composition map showing the spatial distribution of elements in a sample.

In this work, a Princeton Gamma Technology Avalon EDX system was used.

4. MATERIALS AND EXPERIMENTAL METHODS

The aim of this project is to optimize the microstructural homogeneity of lead-free solders by varying different affecting factors (cooling kinetics, compositional variations, ultrasound vibration influence on crystallizing alloy), to improve the reliability of lead-free solder joints. This chapter introduces the materials being used during the experiments and gives details about the techniques used in specimen preparation.

4.1. Materials

Since the SAC alloy family is considered to be the most popular choice in the electronics industry nowadays (due to its superior chemical resistance, wetting properties, lower cost and lower melting point compared to other lead-free solder alternatives), SAC305, SAC405, CASTIN (with addition of antimony) and SN100C alloys were chosen for investigation. The table below shows their composition.

Solder Alloy	SAC305 Sn96.5 – Ag3.0 – Cu0.5	SAC405 Sn95.5 – Ag4.0 – Cu0.5	CASTIN Sn96.2 – Ag2.5 – Cu0.8 – Sb0.5	SN100C Sn – Cu0.7 – Ni0.05 + Ge
Manufacturer	KOKI ltd.	Heraeus GmbH	AIM ltd.	AIM ltd.
Melting range	217 - 220 °C	217 - 225 °C	217 – 225 °C	227 °C
Composition	wt %	wt %	wt %	wt %
Sn	balance	balance	balance	balance
Cu	0.5 ± 0.25	0.5 ± 0.2	0.75 ± 0.25	0.7 ± 0.25
Ag	3.5 ± 0.25	4.5 ± 0.2	2.5 ± 0.25	< 0.05
Sb	-	< 0.02	0.5 ± 0.25	< 0.05
Al	< 0.003	< 0.001	< 0.001	< 0.001
As	< 0.01	< 0.02	< 0.05	< 0.03
Au	< 0.05	< 0.001	< 0.05	-
Bi	< 0.01	< 0.03	< 0.03	< 0.03
Cd	< 0.001	< 0.002	< 0.01	< 0.002
Fe	< 0.01	< 0.02	< 0.08	< 0.02
In	< 0.1	< 0.01	< 0.01	-

Table 6. Alloy compositions with level of impurities, guaranteed by manufacturer (data were taken from manufacturers' datasheet forms). Flux content in the soldering pastes comprises from 10 to 11%. Main alloy components are highlighted in bold.

Solder Alloy	SAC305 Sn96.5 – Ag3.0 – Cu0.5	SAC405 Sn95.5 – Ag4.0 – Cu0.5	CASTIN Sn96.2 – Ag2.5 – Cu0.8 – Sb0.5	SN100C Sn – Cu0.7 – Ni0.05 + Ge
Manufacturer	KOKI ltd.	Heraeus GmbH	AIM ltd.	AIM ltd.
Melting range	217 - 220 °C	217 - 225 °C	217 – 225 °C	227 °C
Composition	wt %	wt %	wt %	wt %
Ni	< 0.003	< 0.005	< 0.005	0.05
Zn	< 0.001	< 0.002	< 0.005	< 0.002
Ge	-	-	-	0.01
Pb	< 0.05	< 0.03	< 0.05	< 0.05

Continuation of Table 6

4.2. Metallographic specimen preparation

Doing solder sample preparation for investigation by means of light microscopy or SEM, considerable care must be taken in order to obtain a cross-section reflecting all the micro structural features of the material without damaging it. Since the solder alloy compositions investigated contain more than 95% Sn, they are quite plastic and a substantial attention should be paid while grinding and polishing in order to prevent the surface from smearing. For solder joint sample preparation, the low speed diamond saw “Accutom-2 Struers” cutting machine was used.

4.2.1. Mounting

The proper choice of mounting method is essential for obtaining adequate results, since the polymerization temperature can affect the microstructure of samples being investigated causing solid state transformations. Moreover, mounting can cause chemical reactions and mechanical stress within samples. Taking into consideration these facts, universal acrylic cold mounting resin “Struers VeroCit Powder” was used with a polymerization temperature of about 40 °C. The solder and solder joint samples were mounted using “SeriForm” cylindrical mounting cups according to instructions provided by supplier. Figure 20 shows a mounted sample.

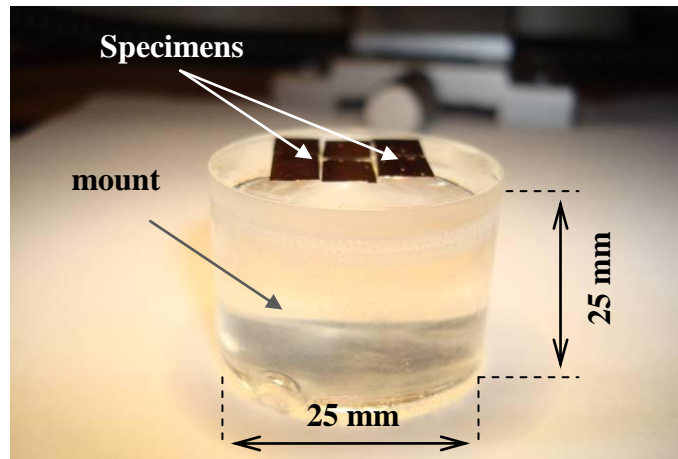


Figure 20. Mounted specimen

4.2.2. Grinding

The first step of the procedure for mechanical preparation aims to remove damaged or deformed material while cutting through and reaching the point of interest within the sample. The grinding process can be divided into stages depending on the steps of changing of abrasive material (usually silicon carbide paper). Each successive step of the grinding process should be done with a finer abrasive material than the step before (i.e. 220 grit → 500 grit → 1000 grit → 2400 grit, where grit is the number of grains of the silicon carbide per square inch of the abrasive paper). Each step is meant to remove the scratches (damaged surface) from the previous stage of preparation. It is of high importance to wash the sample surface and holding disk of a grinding machine every time the abrasive paper is changed. This prevents the sample surface from being scratched by residue of removed material and fallen out particles of the abrasive paper from the previous step. After a sample was treated with the finest abrasive paper it needs to be washed and dried before the following step of polishing.

In the present study, grinding and polishing was carried out by means of the “Struers TegraPol-21” machine (figure 21) and proceeded in 4 steps described in table 7. The direction of the sample holder rotation was contrary to the direction of the grinding disc rotation.



Figure 21. Struers TegraPol-21

Stage	Silicon carbide paper grade, grit	Duration, min	Force, N	Disk speed, rpm	Coolant
1	220	1	10	150	water
2	500	0,5	10	150	water
3	1000	0,5	10	150	water
4	2400	1	10	150	water

Table 7. Typical grinding procedure

4.2.3. Polishing

Like grinding, polishing is meant to remove the damage introduced by previous operations. This is achieved with steps of successively finer abrasive particles. Polishing is carried out on special polishing cloths. The choice of cloth and lubricant depends on the features of material to be polished. As mentioned above, solder alloy compositions are quite soft and ductile and the right choice of polishing agent is essential. In the present study, colloidal silica with a grain size of approximately $0.04 \mu\text{m}$ and a pH of about 9.8 was used for polishing and showed remarkable results. The combination of chemical activity and fine abrasion produces scratch-free and deformation-free sample surfaces. It is noteworthy that, due to colloidal silica's chemical activity, it causes a slight etching effect on the samples.

Figure 22 shows the SAC405 alloy microstructure after polishing with colloidal silica and after final etching with 5% HCl solution in methanol.

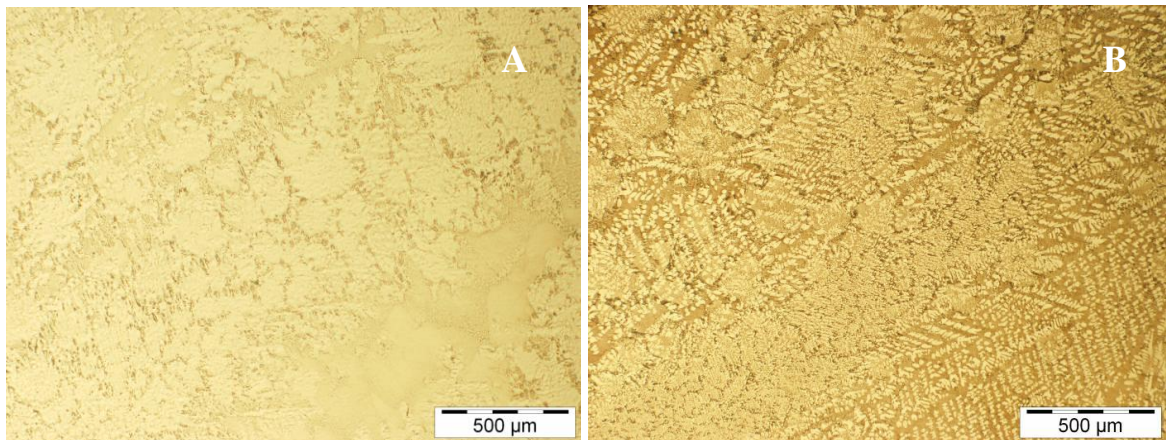


Figure 22. Cross-section of a SAC405 solder sample after final polishing: (A) before etching; (B) after etching in 5% HCl solution in methanol for 20 seconds.

The polishing procedure used in the present study is described in the following table:

Stage	Polishing cloth	Duration, min	Force, N	Disk speed, rpm	Polishing agent
1	Porous neoprene	5	10	300	Colloidal silica

Table 8. Typical polishing procedure

4.2.4. Metallographic etching

Metallographic etching is used to observe the micro structural details of an alloy due to the difference in the reaction rate between the etchant and the different phases in the alloy. As result of such chemical reactions, a surface topography or difference in phase reflectivity can be created which provides an increased contrast during sample examination by means of light microscopy. The reagent can be chosen according to the investigated alloy micro-structural features: either to remove more soluble phases or to etch high energy sites, such as grain boundaries. Etching time is quite important in terms of obtaining a qualitative picture of a sample surface with no artifacts on it.

In the present study 5% HCl solution in methanol was used as etchant. The average etching time was 20 – 30 seconds.

Deep etching. For the three-dimensional investigation of the phase morphologies present within the solder bulk, a technique of deep etching was used. The deep-etching solution was prepared consisting of: 5% of sodium hydroxide, 3.5% of orthonitrophenol and 91.5% of distilled water. The solder specimens were immersed in the etchant at 80 °C for approximately 30 minutes. The etchant removes β -Sn matrix and leaves the intermetallic precipitates (Cu_3Sn and Cu_6Sn_5) unreacted.

4.3. Bulk solder specimen preparation for microstructural investigation

For investigation of microstructural features of the bulk lead-free soldering alloys mentioned in section 4.1, the following technique of sample preparation was used. Soldering paste was divided into portions of 0.25 gram using precision digital scales (Sartorius R300S). It was then reflowed by means of Gallenkamp Magnetic Stirrer Hotplate 400 being placed in a stainless steel pot (10 cm in diameter and 2 cm deep). The temperature of the hot plate was kept at 250 °C and every sample was held in the molten state for 30 seconds. After this, samples were cooled in air. Mounting, grinding and polishing were then carried out in order to prepare samples for the light and scanning electron microscopy investigation.

4.4. Cooling experiment

In order to perform the analysis of the lead-free alloy microstructure dependence on cooling rates, the samples preparation was carried out as follows: 0.25 gram portions of soldering paste were placed into a glass tube (figure 26B) and reflowed by means of Hot-Air Gun RYOBI 2002LCD with the air flow temperature of 260 °C. Every specimen was held in the molten state for 30 seconds and cooled down using different mediums and

equipment. The cooling rates were measured by means of a K-type thermocouple ($\varnothing 0.15\text{mm}$ bare wire) immersed into the sample and National Instruments software installed on a personal computer. The thermocouple signal reading rate was 4 measurements per second (figure 23). To achieve the cooling rate of $2700\text{ }^{\circ}\text{C}/\text{sec}$ water was used as a quenchant. In the case where the samples were left to solidify in air, the measured cooling rates were about $1\text{ }^{\circ}\text{C}/\text{sec}$. The hot air gun was used in cold air flow mode to increase the specimen cooling rate. Depending on the air flow speed, the measured cooling rates were 10 and $24\text{ }^{\circ}\text{C}/\text{sec}$.

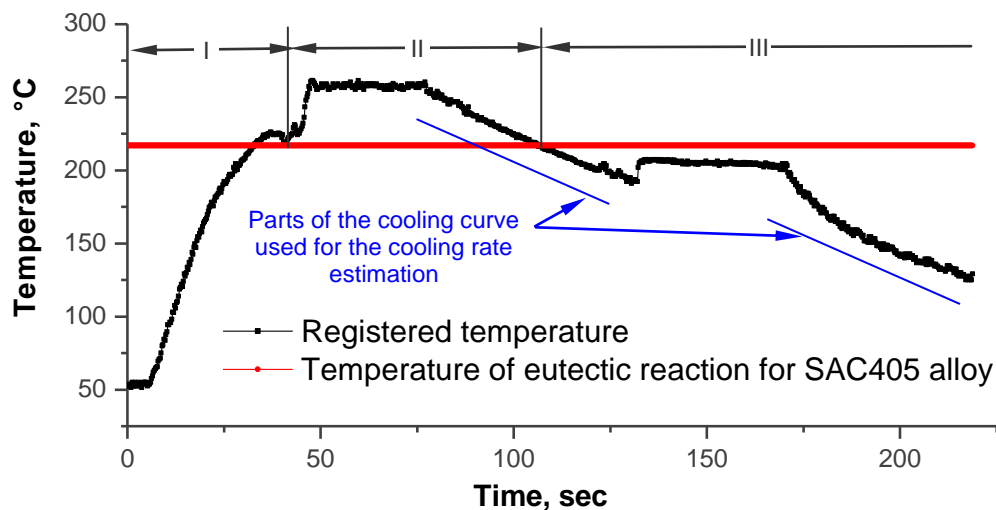


Figure 23. Example of a registered thermal-profile for SAC405 specimen.

Where I – heating, II – reflow and III – solidification stage

4.5. Image analysis

After metallographic specimen preparation and scanning electron microscopy investigation the images obtained were analyzed by means of “IQ Materials” software (figure 24). In greyscale images, each pixel has a value between 0 and 255 that determines how dark or light a shade of grey it is. Phases in images encompass a limited range of values along this continuum. Adjusting the detection level, the software separates the phases existing in the

image, since they have different shades of grey. This allows estimation of the area fraction of phases or structures, and hence grain size and particle size analysis.

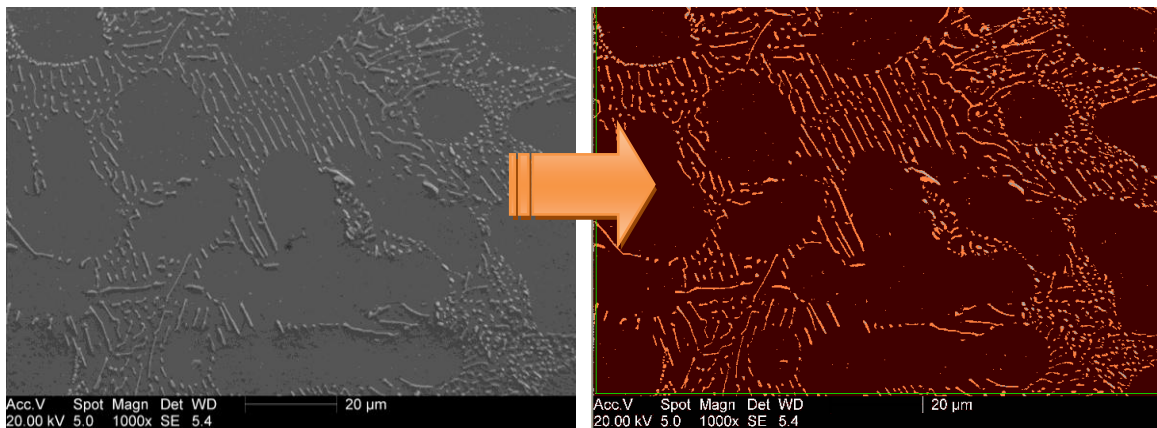


Figure 24. Image processing by “IQ Materials” for performing particle size analysis.

Intermetallic particles dispersed in the interdendritic region are highlighted in orange

4.6. Ultrasonic experimental methods

4.6.1. Application of an ultrasonic field into bulk solders

In the present work, for the application of ultrasonic vibration during solder crystallization, the experimental assembly was built as shown in figure 25.

The solder samples of different alloy compositions were placed in the hollow part of the glass tube (see figure 26B). The temperature monitoring and thermal-profile plotting was carried out by means of a K-type thermocouple and National Instruments software, with the rate of 4 readings per second. The tip of the thermocouple ($\varnothing 0.15\text{mm}$ bare wire) was adjusted in the centre of the hollow part of the glass tube (figure 26B) and the solder specimens, prepared as described in section 4.3, were placed on top. The reflow of specimens was performed by means of the Hot-Air Gun RYOBI 2002LCD with the air flow temperature of $260\text{ }^{\circ}\text{C}$. After 30 seconds in the molten state, the hot air flow was switched off and the ultrasound field was generated during specimen crystallization. Samples were then mounted, ground and polished according as described in section 4.2.

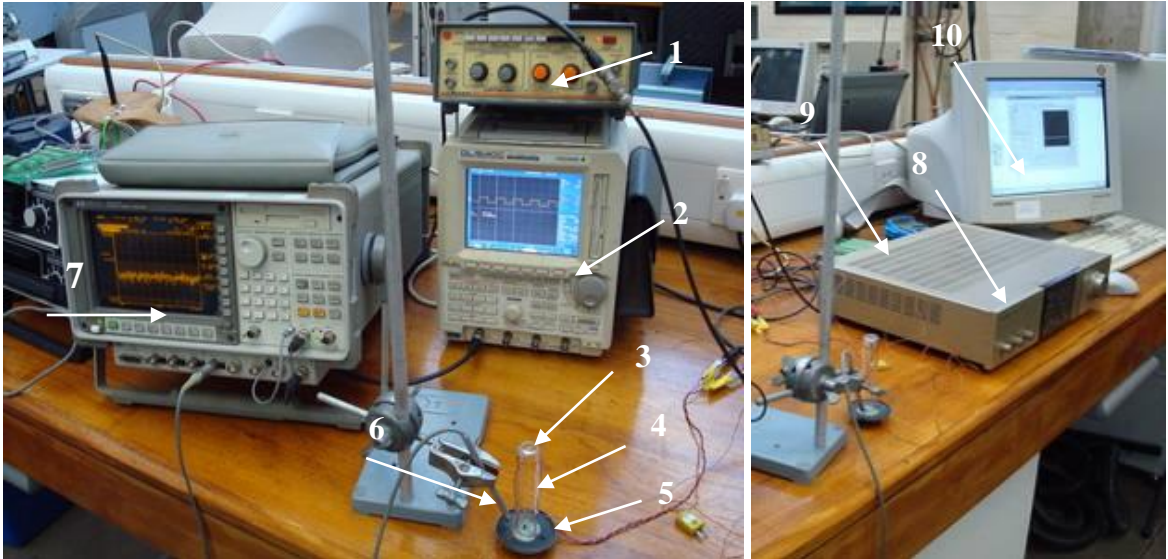


Figure 25. Experimental assembly for solder crystallization within an ultrasound field.

Where: 1 – impulse generator for ultrasonic vibration generation; 2 – oscilloscope; 3 – hollow part of the glass tube with solder sample and the K-type thermocouple; 4 – glass tube; 5 – speaker, driven by means of the impulse generator; 6 – microphone for the speaker’s amplitude-frequency response measuring; 7 – dynamic signal analyzer; 8 – audio amplifier; 9 – interface PCB for reading signals from thermocouples by means of computer; 10 – PC with installed Lab View software for reading signals from thermocouples

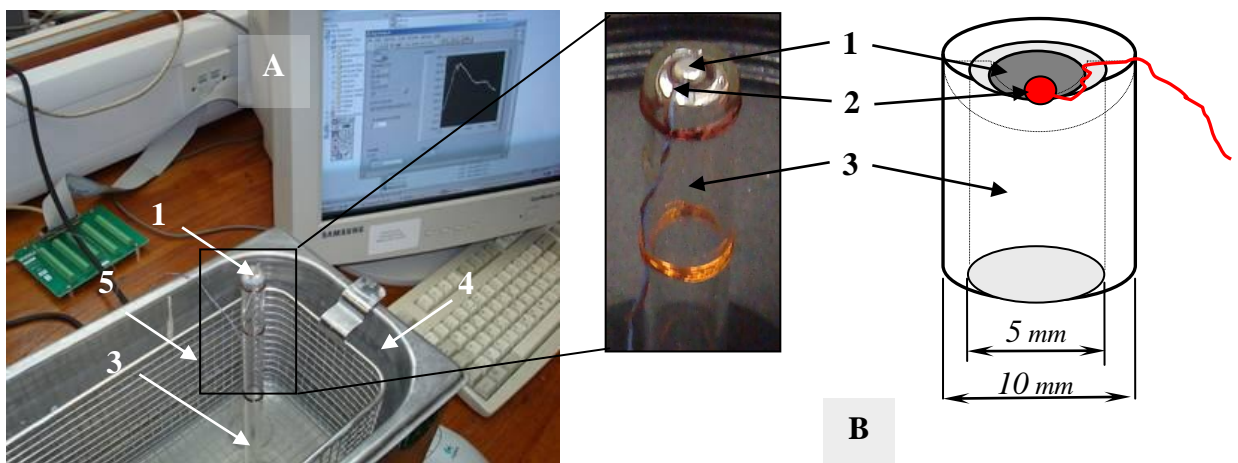


Figure 26. Ultrasound bath implementation as a source of ultrasonic field

where: 1 – solder sample, 2 – K-type thermocouple, 3 – glass tube, 4 – tank of the ultrasound bath and 5 – supporting basket

In order to introduce an ultrasound field of higher intensity into the molten solder, an ultrasonic bath Ultrawave U500 was used (figure 26A). The ultrasonic tank of the bath was driven by a 280-watt generator and its bottom measured 14 centimeters by 24 centimetres. The glass tube with a diameter of the flat base of 6 cm, was placed on the supporting basket (figure 26A). Preparation of samples with the ultrasound bath was again carried out as described earlier.

To compare the ultrasound intensity introduced into the molten solder for both cases (ultrasound bath and loudspeaker), the following technique was implemented: a scale was attached to the glass tube and the width of the tube deflections during ultrasound initiation was estimated by means of optical microscope (figure 27). The deflection value is proportional to the ultrasound amplitude.

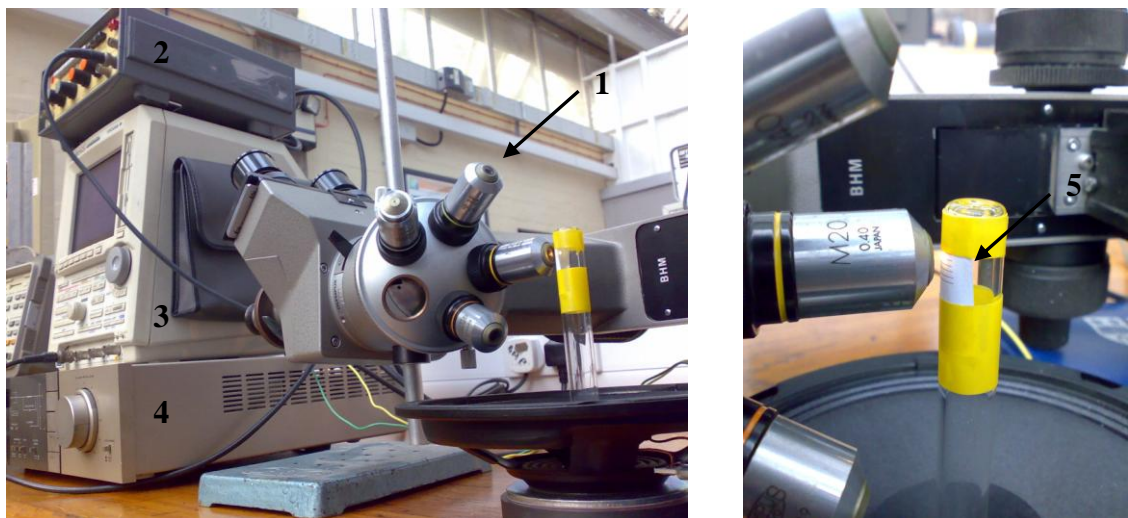


Figure 27. Experimental assembly for the ultrasound wave amplitude estimation.

where: 1 – optical microscope Olympus BH; 2 – impulse generator, 3 – oscilloscope, 4 – audio amplifier, 5 – scale bar

The scale attached to the tube was prepared by means of a laser-jet printer with the scribed line width of 0.1 mm. The average particle size of the toner powder from the printer was approximately 10 μm . The figure 28 shows the scribed line enlarged.

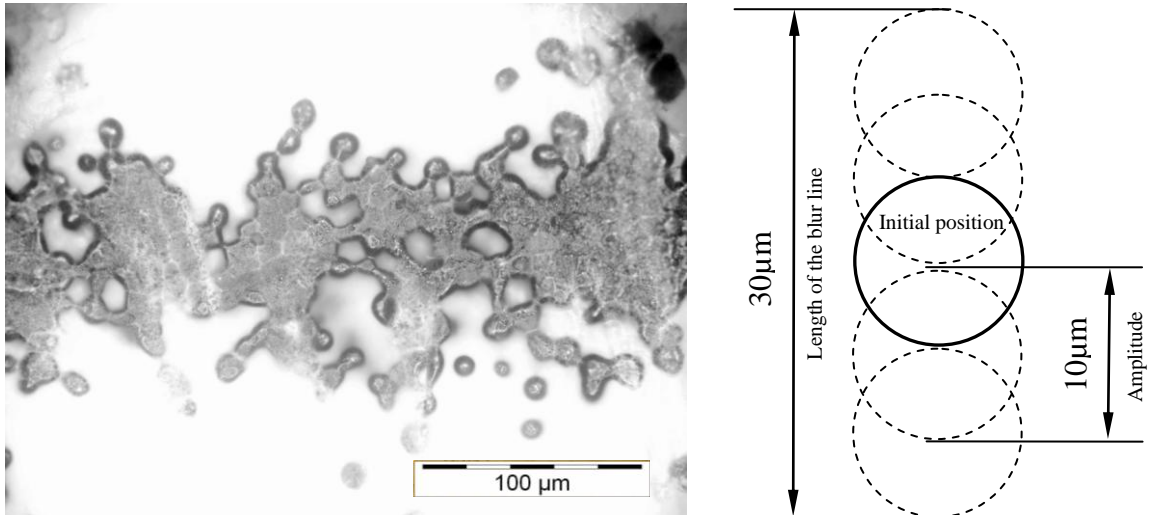


Figure 28. Enlarged scribed line of the scale attached to the tube and oscillation scheme of the stand alone dots

During the ultrasound initiation the edges of the scribed line became blurred. For instance, in the case of ultrasound of 18 kHz generated by the loudspeaker, the length of the blur line produced by stand alone dots was about 30 μm. This means that their oscillation amplitude was 10 μm (since the dot diameter is 10 μm approximately).

Given that a very rough approximation for the oscillation amplitude of the glass tube is equal to the oscillation amplitude of the particles in the liquid media (molten solder), the ultrasound intensity ' I ' and sound pressure ' P ' can be estimated as follows [78]:

$$\begin{aligned}
 P &= A\omega\rho c \\
 I &= \frac{1}{2}\rho c A^2 \omega^2 \quad (1)
 \end{aligned}$$

where A is the amplitude of the sound wave; ω is radian frequency of the wave; ρ is density of the media and c is speed of the sound in the media.

Thus, assuming that the solder density is 7 310 kg/m³; the wave velocity in the melt is 2230 m/s, the amplitude of the sound wave during implementation with the loudspeaker is 10 μm and during implementation with the ultrasonic bath 50 μm, the sound pressure in the melt will be a value of 8th order magnitude (in Pascals) for the ultrasonic bath and 7th

order for the loudspeaker. This does not seem to be feasible, since this level of the sound pressure cannot be achieved in the melt under conventional conditions. A more sophisticated experimental setup should be implemented such as in [64]. The typical value of the pressure of a sound wave travelling through a melt, causing the cavitation effect, is a magnitude of 6th order [79]. The assumption chosen (that the oscillation amplitude of the glass tube is equal to the oscillation amplitude of the particles in the liquid media) does not consider sound wave reflection and attenuation processes at the interface and in the solder bulk. Consideration of these parameters is essential for more accurate measurements. However, this approach is very complicated since the wave processes depend on many variables and it requires further experimentation. Such investigations were not the primary motivations in this study.

At this stage it was more important to estimate the difference in sound pressure/ultrasound intensity for both experimental assemblies. The ratio of the ultrasound intensity introduced into melt by means of ultrasound bath (operating on frequency of 30 kHz) and the loudspeaker (operating on frequency of 18 kHz) is expressed as:

$$\frac{I_{UB}}{I_{loudspeak}} = \frac{0.5 \times 7.31 \cdot 10^3 \times 2230 \times (2\pi \cdot 18 \cdot 10^3)^2 \times (50 \cdot 10^{-6})^2}{0.5 \times 7.31 \cdot 10^3 \times 2230 \times (2\pi \cdot 30 \cdot 10^3)^2 \times (10 \cdot 10^{-6})^2} = 69.4, \quad (2)$$

Thus, it can be seen that the ultrasound bath was more effective source of the ultrasonic vibrations and the microstructural changes of a solder were expected to be more prominent in this conditions.

4.6.2. Ultrasonic introduction into solder-joints

For investigation of influence of ultrasound field on crystallizing solder between Cu substrates, the samples were prepared as follows: firstly, two pieces of polished and cleaned Cu plates (20 × 30 × 1mm) were fixed in the holder connected with glass wave

conductor (glass tube with a diameter of the flat base of 6 cm) by means of Henkel styrene monomer (figure 29(A)). The glass tube was placed on the supporting basket. The opposite ends of the Cu plates were set parallel to each other with a 0.2 - 0.5 mm space between them. The solder paste was then filled into the gap. The specimen was put into an ultrasonic bath and reflowed by means of the Hot-Air Gun RYOBI 2002LCD with the air flow temperature of 260 °C and the dwell time duration of 30 seconds. At the end of 30 second reflow, the hot air gun was switched off and the ultrasonic field of 30 kHz was activated during the solder-joint crystallization. Then the soldered specimens were polished to uniform dimensions and cut into small pieces with rectangular cross section 1 × 5 mm using the low speed diamond saw “Accutom-2 Struers”. Parallel clumps of the diamond saw held obtained solder-joints as shown in figure 29B, which allowed the strips to be cut without deformation.

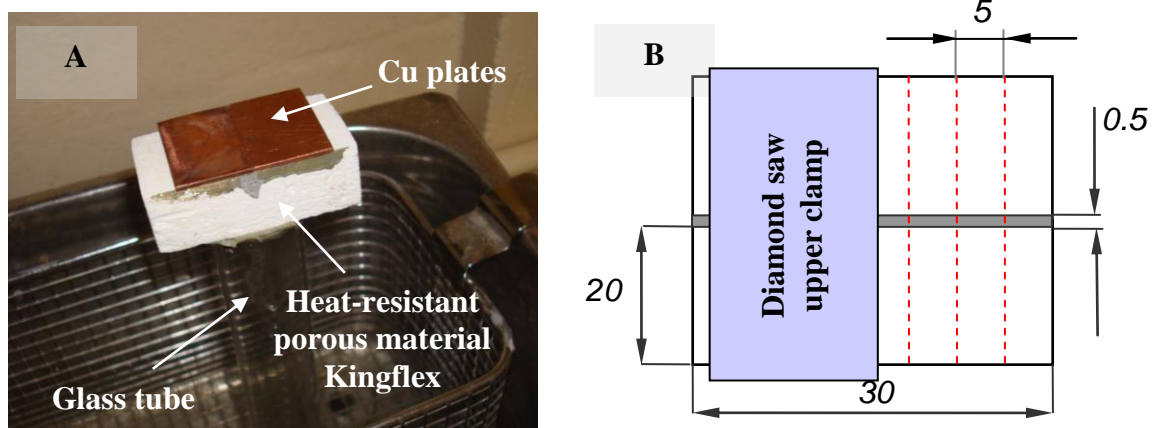


Figure 29. (A) ultrasound introduction into a solder-joint (B): sectioning of prepared samples (dimensions are in millimeters)

4.7. Tensile strength experimental setup

For tensile testing, solder-joint samples with geometrical dimensions described in previous paragraph (figure 29(B)) were placed in the clamps of the MTS 810 materials test system

(figure 30). Tensile testing was carried out at room temperature with a constant cross-head speed of 0.1 mm/s.

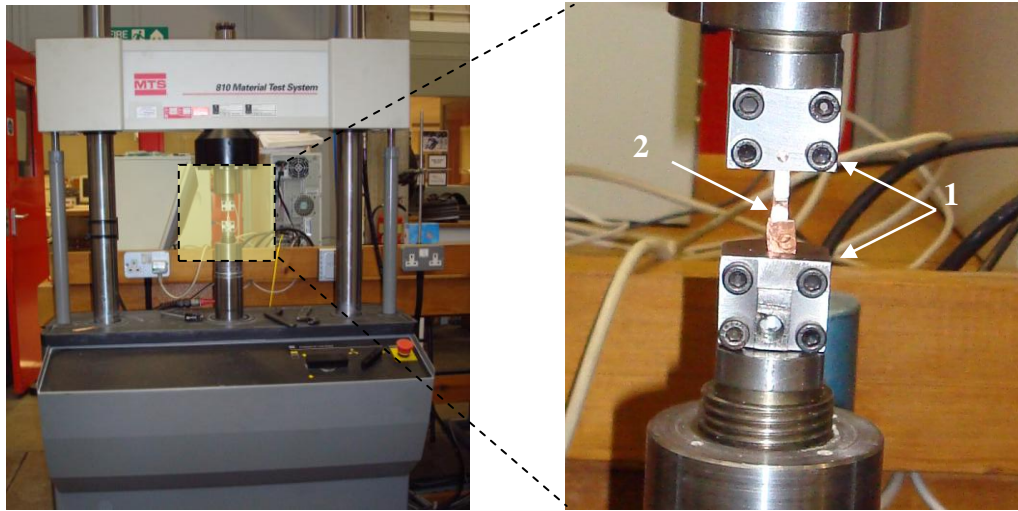


Figure 30. MTS 810 Materials Test System. 1 – clamps, 2 – solder-joint sample

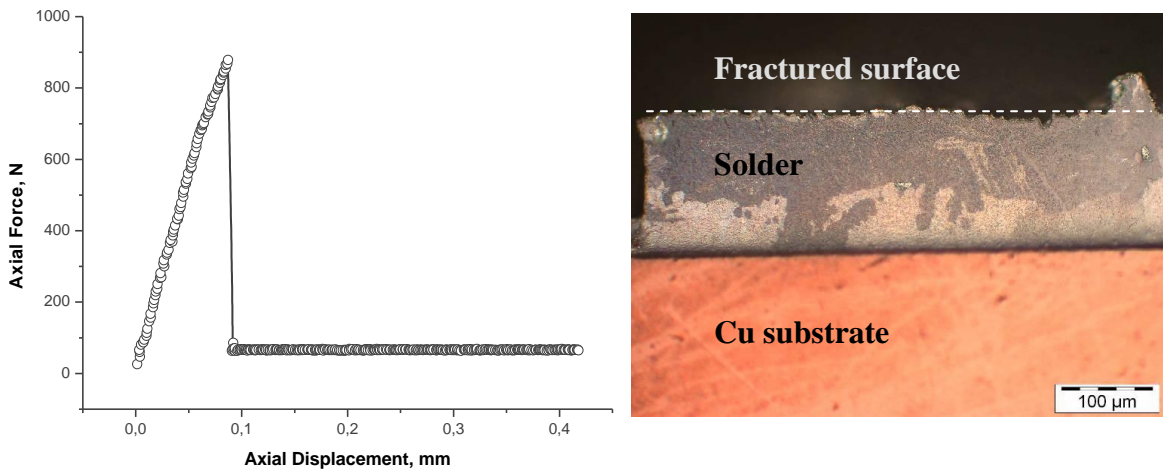


Figure 31. Load to failure graph and corresponding fractured sample of the solder joint assembled with SAC305 soldering alloy

Since all the tested samples exhibited brittle fracture and there were no changes in the transverse cross-sectional area of the joint during testing (figure 31), later in this work it is assumed that the solder joint tensile strength is directly proportional to the load to failure applied and the term “tensile strength” was used in the subsequent sections.

4.8. Solder-joint sample preparation for the IMC layer investigation

In order to investigate the dependence of the solder-joint tensile strength on IMC layer width, the samples were obtained under the following conditions: two pieces of polished and cleaned Cu plates (20×30 mm) were laid on the fireproof brick; they were set parallel to each other with a 0.2 - 0.5 mm space between the plates. The solder paste was filled into the gap and reflowed with peak temperature of 250 °C (which corresponded to the temperature of the air flow of 260 °C generated by the hot-air gun) and time above liquidus of 5, 30, 60, 300, 600 and 1200 seconds. The soldered samples were polished to uniform dimensions and cut into small pieces with rectangular cross section (1×5 mm) using a diamond cut-off saw as described earlier.

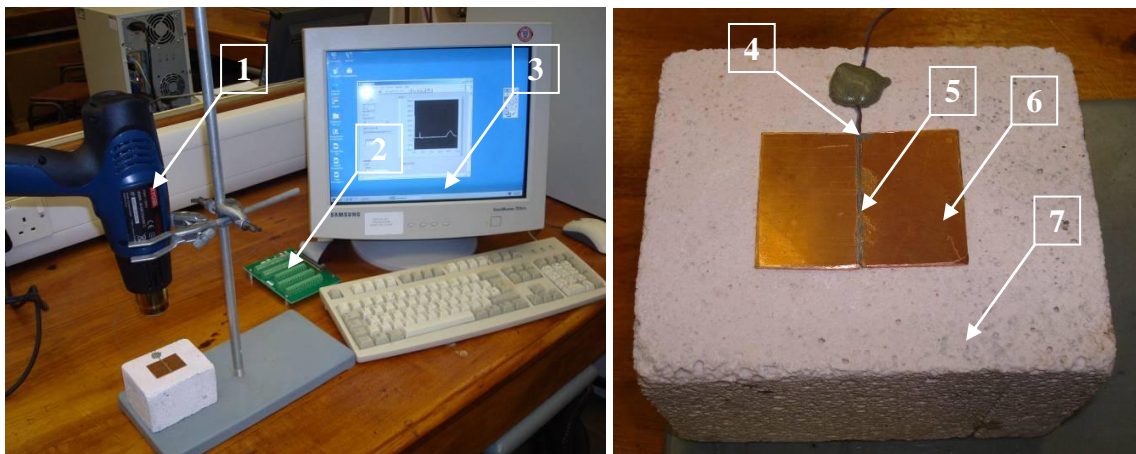


Figure 32. Experimental assembly for samples preparation: 1 – hot air gun; 2 – interface PCB for reading signals from the thermocouple by means of computer; 3 – PC with installed Lab View software for reading signals from the thermocouple; 4 – thermocouple immersed into solder on 1 mm distance from the edge of the substrates; 5 – soldering paste; 6 – copper plates; 7 – fireproof brick

Tensile strength testing was performed then with subsequent metallographic investigation.

4.9. Thermal-cycling experimental method

The procedure for the sample preparation for thermal-cycling experiments was the same as described in section 4.8. The samples were mounted, ground, polished and then extracted

from the mount in order to carry out microstructural investigation in their initial state. This meant that the transverse section through the joint was polished and hence subsequent changes during thermal-cycling could be maintained. Thermal-cycling was performed manually and, since the set of investigated samples was subjected to the equal conditions, the results obtained can reveal the difference in microstructural evolution of different solder compositions during thermal-cycling loads. The solder-joints were reinvestigated after every 100 cycles without repeated polishing of their surface. This made it possible to observe microstructural changes on the grain boundaries and at the near-interface region with Cu substrate by means of light and scanning electron microscopy. Although only 400 thermal-cycles were performed, the results indicate main trends.

The thermal-cycling conditions were relatively extreme in terms of rate of temperature change: samples were held for 300 seconds in the hot air flow (150 °C) produced by the hot-air gun and then they were put into liquid nitrogen for 20 seconds (this amount of time was enough to lower the solder-joint temperature to - 40 °C). A set of solder-joint samples (5 pieces) was tightened together with a copper wire (0.5 mm in diameter) and the tip of a K-type thermocouple was inserted in the middle of the assembly. In this experiment standard insulated K-type thermocouple was used with bead diameter 0.55mm and wire diameter of 0.25mm. The temperature was monitored by the APPA 100 Series Multimeter with the rate of 1 reading per second. The measured cooling rate of the solder-joint was approximately 10 °C/sec and the heating rate 5 °C/sec. For the temperature homogenization within the solder-joints, they were held for an additional 260 seconds in the air flow of 150 °C. The thermal-cycling diagram is depicted in the figure 33.

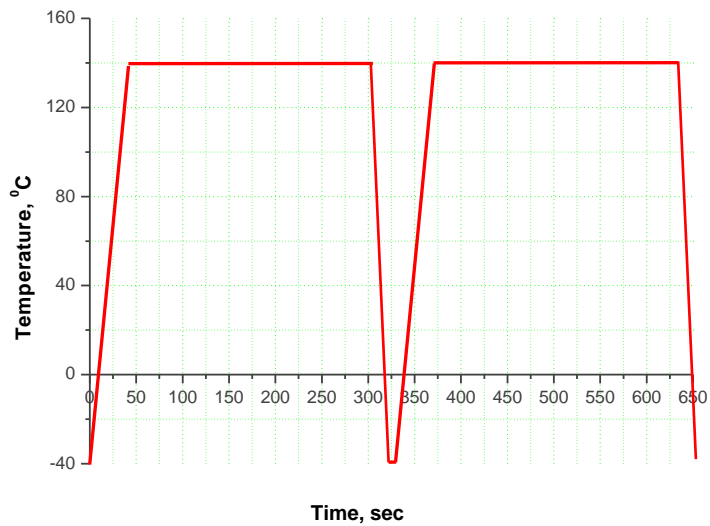


Figure 33. Thermal-cycling diagram

4.10. Ageing experiments

In order to simulate the situation of a solder-joint operation under elevated temperatures, various specimens (bulk solders and solder-joints) were placed in the Gallenkamp furnace for solid state ageing at 160 °C. After a certain ageing duration, samples were taken out from the furnace, repetitively polished (since Cu and its compounds appeared to oxidize quite rapidly which complicated the analysis (figure 34)) and investigated.

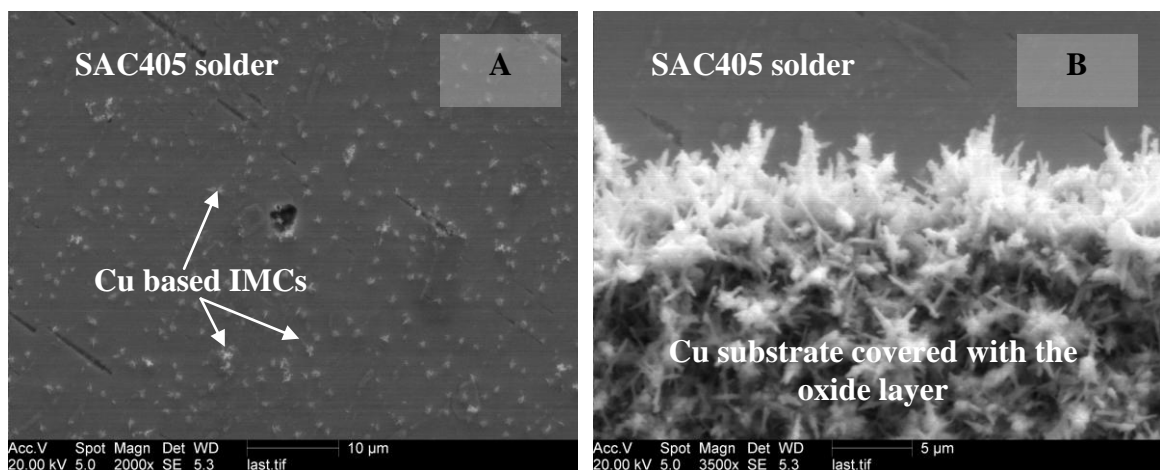


Figure 34. Oxidation of Cu substrate (B) and IMCs with Cu content (A) after 1800 hours of ageing in air atmosphere at 160 °C

4.11. Sample preparation for investigation of crystallographically-faceted voids

Some crystallographically-faceted voids were found in solder-joints. In the study devoted to these crystallographically-faceted voids, two types of Cu substrates were used: (i) FR4 single layer PCB with copper pads manufactured by Dipmicro Electronics and (ii) copper plates 99.98% cut into pieces of $20 \times 30 \times 1$ mm. The lead-free alloys SAC405 (Sn95.5 – Ag4.0 – Cu0.5), CASTIN (Sn96.2 – Ag2.5 – Cu0.8 – Sb0.5) and SN100C (Sn – Cu0.7 – Ni0.05 + Ge), pure Sn (99,99) and lead-containing alloy Sn60Pb40 were used as soldering material to join the substrates. The procedure for the solder-joint preparation was as follows:

- (i) FR4 PCB was cut into strips of 5×20 mm; 38% HCl solution was used to remove oxidized layer from the Cu metallization surface. The time duration of the cleaning process was 1 minute. Soldering paste was then spread on the PCB strip surface with a total weight of 0.05 gram (measured by digital scales Sartorius R300S). In order to make a ‘sandwich’ structure the second strip was placed on top (figure 35).

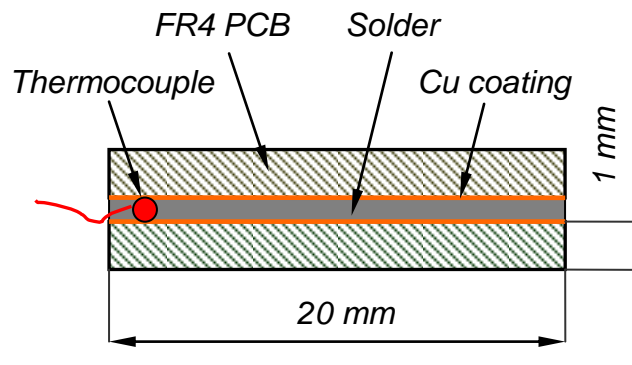


Figure 35. Schematic diagram of a solder-joint assembled with use of FR4 single layer printed circuit board (sandwich structure). The third dimension is 5mm

These assemblies were reflowed by means of the Hot-Air Gun RYOBI 2002LCD with the air flow temperature of 260 °C. Every specimen was held in the molten state for 30 seconds and cooled in air. The cooling rates were measured by means of a thermocouple attached to the sample and National Instruments software with the signal reading rate of 4 measurements per second. The average cooling rate was about 1.4 °C/sec.

- (ii) The second type of solder-joint was prepared as follows: two pieces of polished and cleaned Cu plates (20 × 30 × 1mm) were laid on the fireproof brick and set parallel to each other with a 0.2 – 0.5 mm space between them. The soldering paste was filled into the gap and reflowed by means of the Hot-Air Gun with the air flow temperature of 260 °C and time above liquidus of 30 seconds. The measured cooling rate in the air was about 0.8 °C/sec. The soldered samples were polished to uniform dimensions and cut into small pieces with rectangular cross section in dimension of 1 × 5 mm using a diamond cut-off saw (as shown in section 4.6.2).

All the samples were then mounted into epoxy resin and, after its polymerization, the cross sectioning was carried out with the following steps: 220 Grit SiC abrasive → 500 Grit → 1000 Grit → 2400 Grit → final polishing using colloidal silica. The prepared cross-sections were not etched. After cross-section preparation, the specimens were examined with a Field Emission Gun Scanning Electron Microscope (FEI Sirion 200). Following this, solder-joint ageing at the temperature of 160 °C was performed in a Gallenkamp furnace.

5. EXPERIMENTAL RESULTS

5.1. Microstructural investigation of lead-free solders

5.1.1. Alloy composition influence on microstructural features

As mentioned above, the soldering alloys used during the present study are SAC405 (Sn95.5 – Ag4.0 – Cu0.5), SAC305 (Sn96.5 – Ag3.0 – Cu0.5), CASTIN (Sn96.2 – Ag2.5 – Cu0.8 – Sb0.5) and SN100C (Sn – Cu0.7 – Ni0.05 + Ge). The first three of these are depicted in the figure 36 which shows the Sn-rich corner of the Sn-Ag-Cu phase equilibrium diagram enlarged.

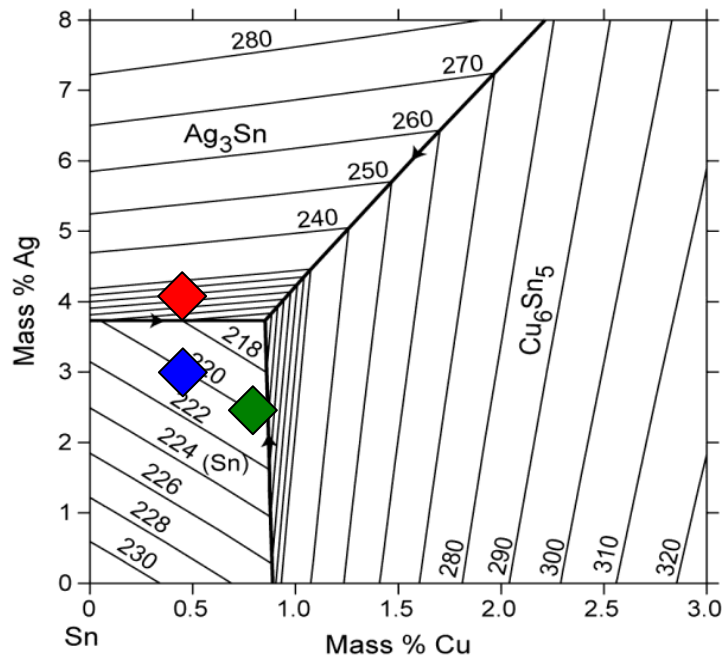


Figure 36. Sn-rich corner of Sn-Ag-Cu phase equilibrium diagram,

where \blacklozenge – SAC405, \blacklozenge – SAC305, \blacklozenge – CASTIN [11]

In the Sn96.2 – Ag2.5 – Cu0.8 – Sb0.5 system, small additions of Sb were found to be dissolved in the β -Sn matrix. Sb additions in combination with decreased Ag content lower the amount of undercooling before crystallization. For SN100C alloy, minor additions of Ni result in solder shrinkage reduction and ductility increase, which is important for stress

accommodation. Even though Ni could form a series of intermetallic particles with Sn, its concentration is too low to produce them in considerable quantities.

In order to investigate microstructural features of the lead-free soldering alloys mentioned above, the technique of sample preparation described in section 4.3 was used. The pictures obtained during light microscopy investigation are depicted in the table below (table 9).

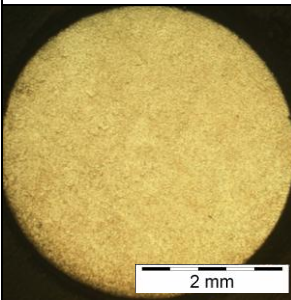
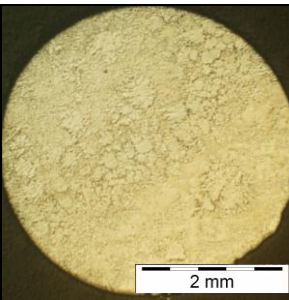
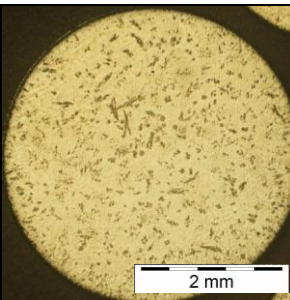
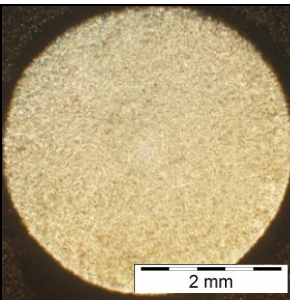
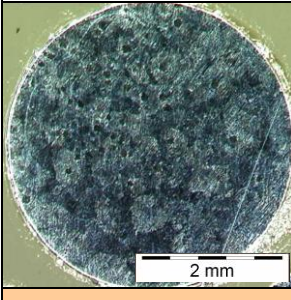
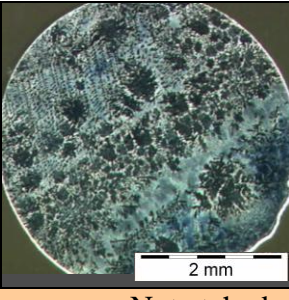
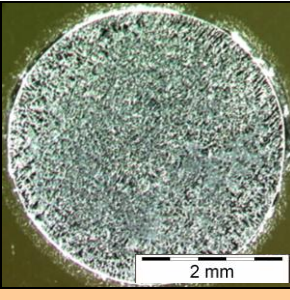
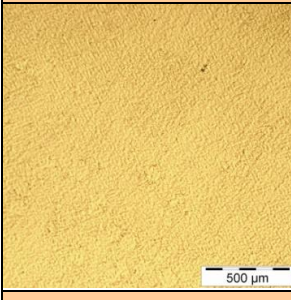
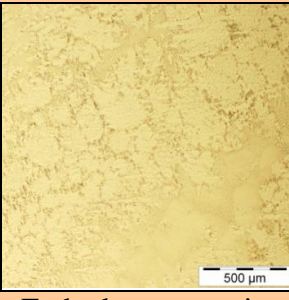
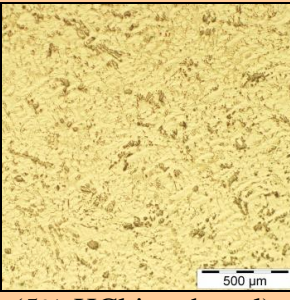
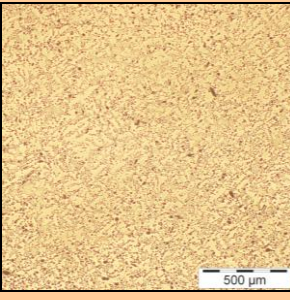
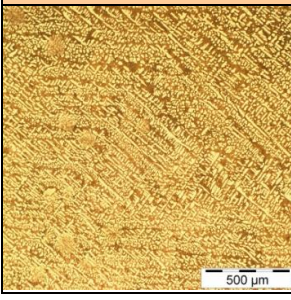
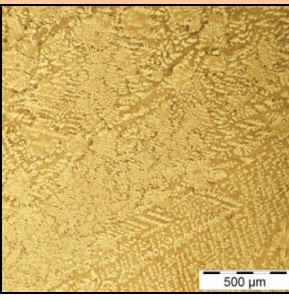
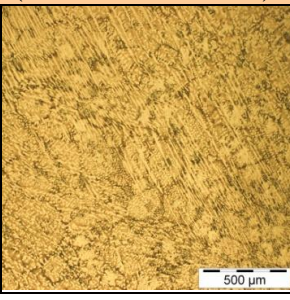
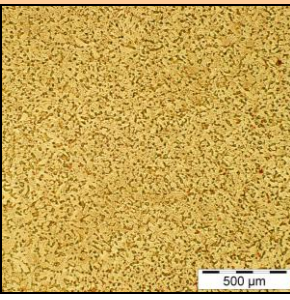
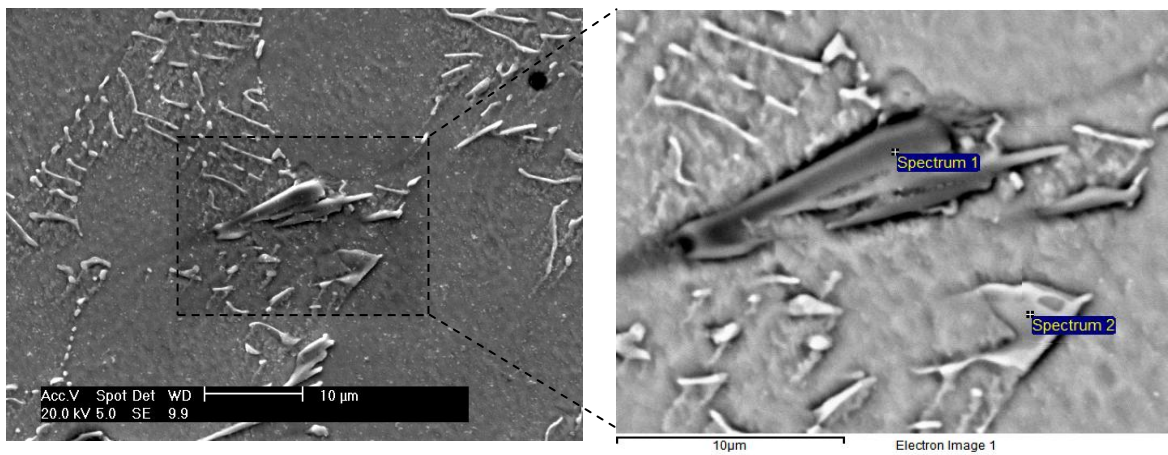
SAC305:	SAC405:	CASTIN	SN100C
			
			
Not etched cross-sections			
			
Etched cross-sections (5% HCl in ethanol)			
			

Table 9. Lead-Free alloys microstructure comparison

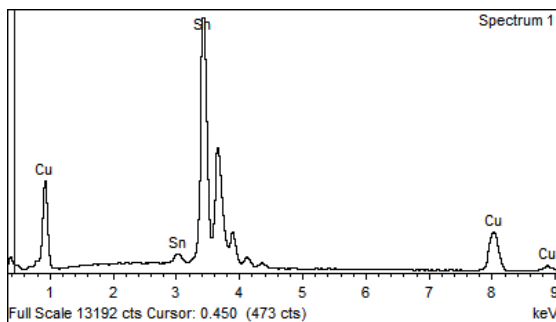
(250 °C for 30 seconds followed by air cooling: cooling rate 0.7 C°/s)

The upper row of the images shows the not-etched cross-sections of 0.25 gram solder samples of different alloy composition. The row of the images below shows the same area of the same samples but taken by means of different microscope with larger focal distance which reveals more contrast between phases. Images in the rows below show enlarged areas of the same samples before and after etching. Conditions for all the sample preparation is as described in paragraph 4.3.

In order to justify the compositions of the IMC precipitates mentioned in the paragraph 2.2.1, the EDX quantitative analysis was carried out (figure 37).

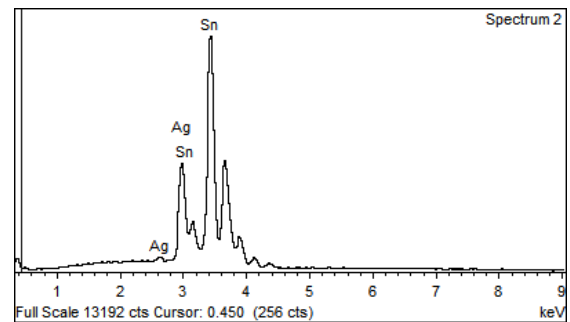


Spectrum 1:



Element	Atomic%	Chemical composition
CuL	54.36	Cu₆Sn₅
Sn L	45.64	
Totals	100.00	

Spectrum 2:



Element	Atomic%	Chemical composition
Ag L	74.85	Ag₃Sn
Sn L	25.15	
Totals	100.00	

Figure 37. EDX analysis of the IMC precipitates in the bulk of SAC305 solder

Comparing the cross sections of the SAC alloy samples shown in table 9, it was noted that the distribution of Cu_6Sn_5 intermetallics through the solder bulk is not uniform (in contrast with the Ag based intermetallics). Whilst Ag_3Sn intermetallics are uniformly spread in interdendritic regions (eutectic phase), the Cu_6Sn_5 intermetallics tend to be present in interdendritic regions non-uniformly, clustering in a “grain-like” structure (figure 38). No IMCs in β -Sn dendrites were noted.

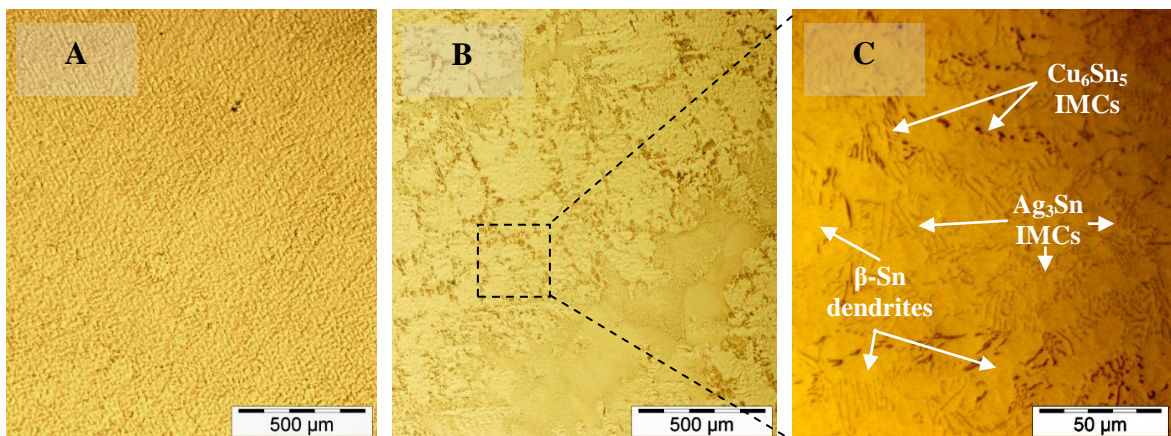


Figure 38. A: SAC305 alloy – the non-uniform Cu_6Sn_5 distribution in interdendritic regions starts to appear; B: SAC405 alloy: non-uniform Cu_6Sn_5 distribution in interdendritic regions is more evident; C: enlarged area of the micrograph B (250 °C for 30 seconds followed by air cooling)

At higher Ag composition (SAC405: Sn95.5 – Ag4.0 – Cu0.5), the IMC precipitates Cu_6Sn_5 tend to cluster to a larger extent (compared to the SAC305: Sn96.5 – Ag3.0 – Cu0.5 composition). At the same time, no clustering effect was noted for the CASTIN (2,5% Ag) and SN100C (0% Ag) alloys. The IMCs Cu_6Sn_5 were found to be spread uniformly through the interdendritic regions. However, for the CASTIN alloy the Cu-based precipitates were observed to form on a larger scale, compared with SAC and SN100C.

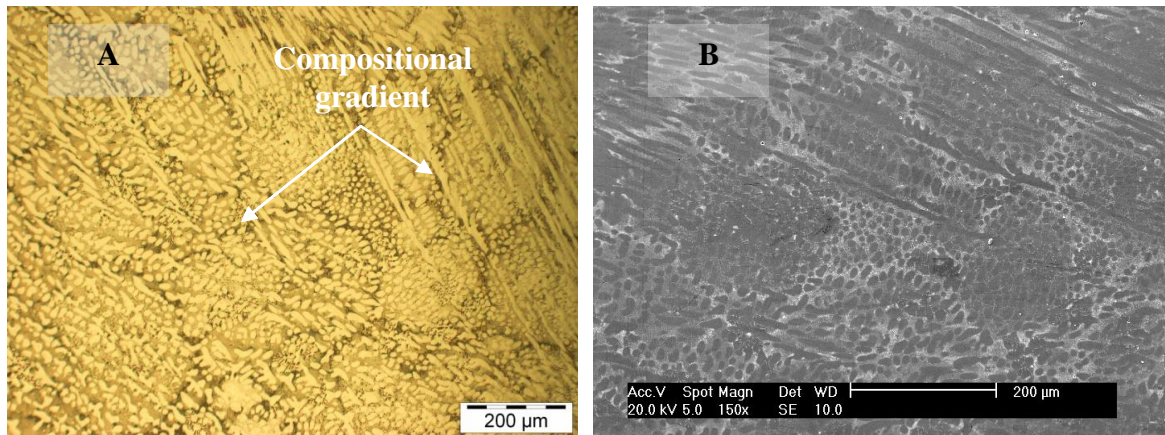


Figure 39. Microstructure of CASTIN alloy: (A) reflected light image (B) SE image
 Solder sample was prepared as described in section 4.3, the cross-section was etched after polishing

The CASTIN differs from the SAC family by the presence of the antimony in the alloy composition. The antimony forms a series of intermetallic precipitates with the other chemical elements of the alloy: Sn and Cu, but none of those were found during the investigation. Presumably, their quantity is too low due to low amount of Sb in the system (0.5%). The only IMC particles distinguished during the investigation were Cu_6Sn_5 and Ag_3Sn .

At the same time it was observed that the Antimony dissolves in the eutectic regions between β -Sn dendrites (figure 39). Etching and SE analysis revealed non-uniform distribution of Sb through the solder sample volume. Compositional gradients can be seen in the figure 39.

For the further investigation of the phase morphologies present within the solder bulk, the technique of deep-etching was implemented as described in section 4.2.4. This technique helped to reveal the three-dimensional morphologies of the intermetallic precipitates which exist in different alloy compositions (SAC, CASTIN) and provided better understanding of their structure (figures 40-43).

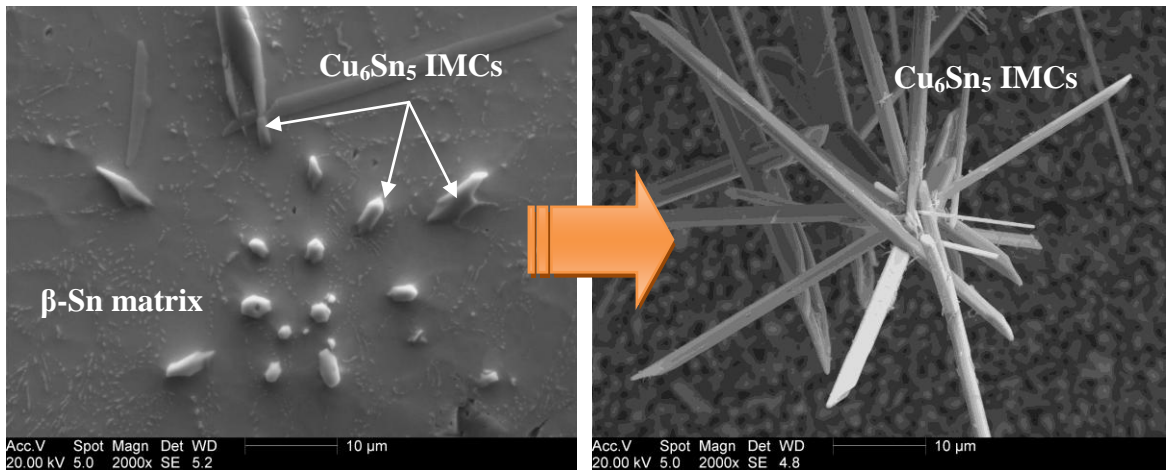


Figure 40. β -Sn matrix dissolution by means of deep-etching solution (SAC405 solder)
Solder reflow conditions: peak temperature 250 °C, duration in molten state 60 seconds

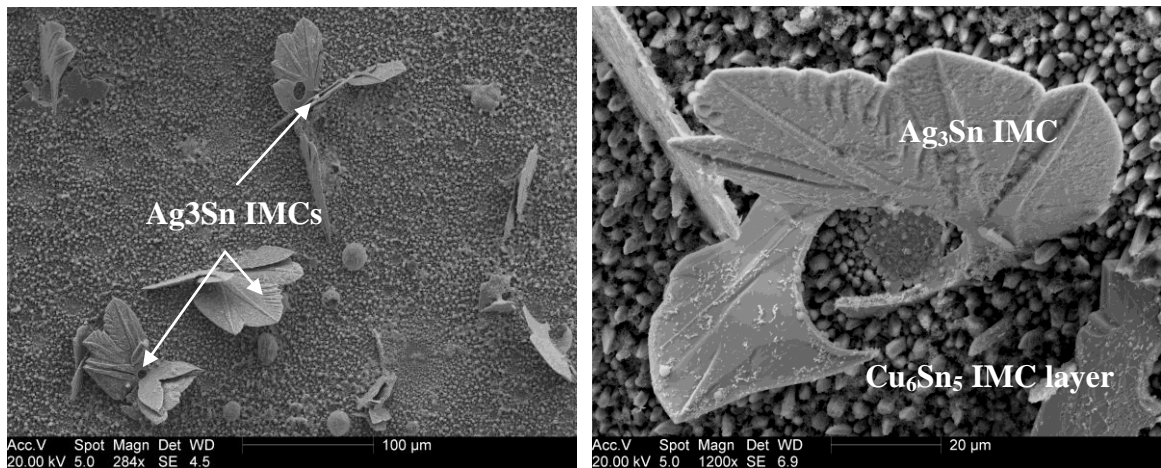


Figure 41. Ag_3Sn leaf-like plates growing on top of the intermetallic layer in a solder-joint assembled with use of Cu substrate and SAC405 soldering paste. (peak reflow temperature 250°C, duration in molten state 60 seconds)

A quantitative analysis of the intermetallic precipitates composition was carried out before deep-etching (figure 39, left side), since EDX quantitative analysis cannot provide precise results when dealing with three-dimensional objects (figure 40, right side).

As can be seen from the micrographs above, the Ag_3Sn pro-eutectic IMC particles form in the shape of plates (often in a flower-leaf shape). The round holes inside the Ag_3Sn

'leaves' presumably result from void formation during solder solidification. The flux content in the soldering pastes being used comprised of 10-11 weight %. In some cases the reflow time can be insufficient for the flux residues or dissolved gases to escape from the volume of molten solder and they can be trapped within.

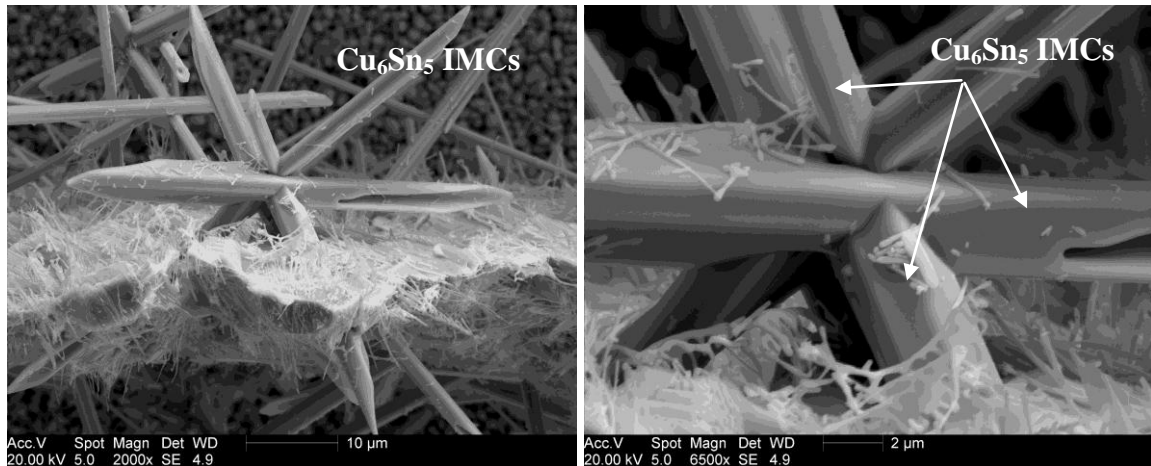


Figure 42. Cu₆Sn₅ pro-eutectic needles held in place by the residual β-Sn matrix in a solder-joint assembled with Cu substrate and SAC405 soldering paste. (Peak reflow temperature 250°C, duration in molten state 60 seconds)

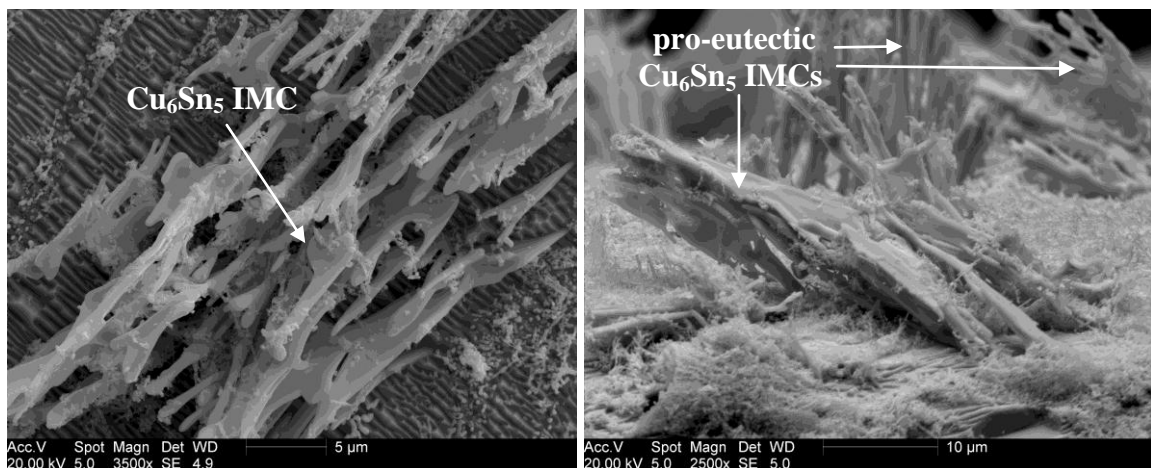


Figure 43. Cu₆Sn₅ pro-eutectic IMCs held in place by the residual β-Sn matrix in a solder-joint assembled with use of Cu substrate and CASTIN soldering paste. (Peak reflow temperature 250°C, duration in molten state 60 seconds)

Nevertheless, despite all the beauty of the intermetallic precipitates shown in the pictures, they represent quite undesirable formations in terms of long-term solder stability, since their physical and mechanical properties significantly differ from those of the β -Sn matrix (table 10).

	SAC305	CASTIN	SN100C	Sn	Ag ₃ Sn	Cu ₆ Sn ₅	Cu ₃ Sn	Ni ₃ Sn ₄
Young's Modulus, GPa	54	51.16	-	50	-	85.56	108.3	133.3
Vickers Hardness, Kg/mm ²	13.3	-	16.1	-	-	378 ± 55	343 ± 47	365 ± 7
Density (kg/m ³) × 10 ³	7.4	7.38	7.4	7.31	9.93	8.28	8.9	8.65
Electrical Resistivity (Ω·m) × 10 ⁻⁸	15	12.1	13	11,5	-	17.5	8.93	28.5
Thermal Conductivity (W/(m·K))	58.7	57.26	64	66.8	-	34.1	70.4	19.6
Thermal Expansion (10 ⁻⁶ /K)	-	-	13.3	22*	19	16.3	19.0	13.7

* Crystallographically anisotropic

Table 10. Physical properties of Lead-Free solders and intermetallic phases (data taken from sources [80] and [81] and solder paste technical datasheets provided by manufacturers). Data on the matrix (Sn) is highlighted in yellow

Consequently, there is a need for solder joint microstructure optimization which should aim not only for microstructural refining but also inhibition of intermetallic phase formation.

Many authors have reported on the negative effect of intermetallic compounds on mechanical properties of lead-free solder-joints [9, 22, 26, 39, 40, 82] which degrade their mechanical integrity. For instance, large Ag₃Sn platelets induce brittle fracture at an

interface and provide crack initiation sites. They decrease elongation at lower temperatures by providing the origin of tensile failure [82]. The excessive formation of Cu_6Sn_5 intermetallics in the bulk and on the substrate interface decreases solder-joint strength, which will be shown further. While performing tensile strength experiments in the present study, it was also observed that large Cu_6Sn_5 intermetallic precipitates can promote fracture development (figure 44).

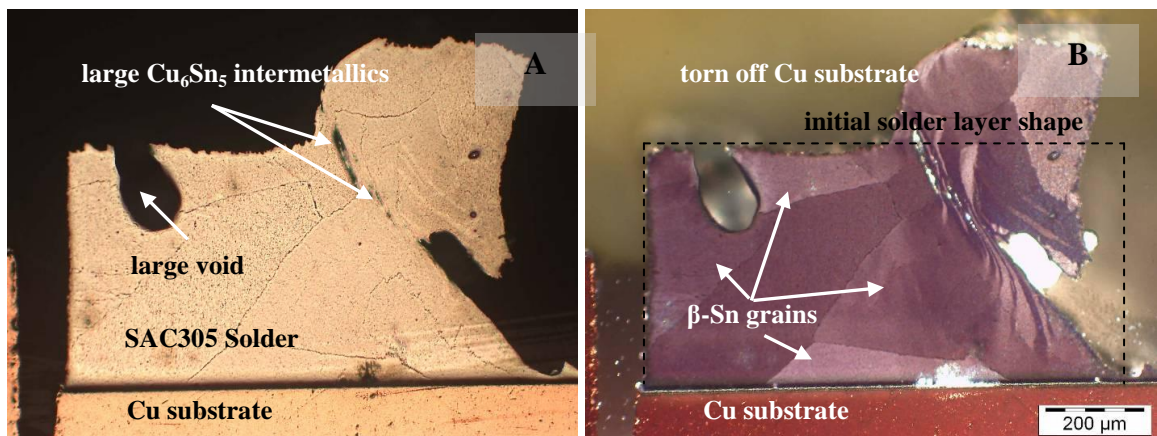


Figure 44. Fracture promoting by large Cu_6Sn_5 IMCs. (A) reflected-light image; (B) image in cross-polarized light; (250 °C for 30 seconds followed by air cooling)

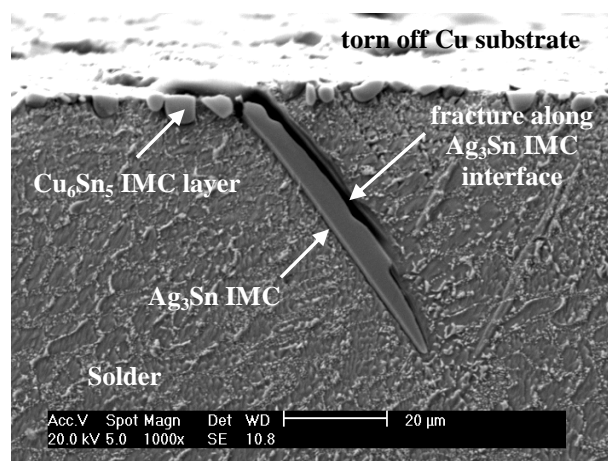


Figure 45. Fracture development along the Ag_3Sn IMC interface during tensile strength testing (SAC305 solder); 250 °C for 30 seconds followed by air cooling

The possible ways of influencing the solder microstructure in order to improve its mechanical integrity are: (i) thermodynamic (composition variation) described above; (ii) kinetic (cooling dynamics) and (iii) energetic (electromagnetic, ultrasound field influence on solidifying alloy). In the present study, cooling rates and ultrasound vibration influence on solder microstructure are considered.

5.1.2. Cooling rate influence on solder microstructure

Cooling kinetics is one of the most important criteria of the solidification process which defines the resulting microstructure. Fast cooling rates can suppress formation of large intermetallic precipitates.

In order to perform the analysis of the lead-free alloys' microstructure dependence on cooling rates, the procedure of samples preparation as described in section 4.4 was implemented. Subsequent microstructural investigations of the samples obtained showed that the solidification kinetics strongly affect the resulting solder microstructure. High cooling rates result in remarkable reduction of the average dendrite size and promote equiaxed growth (figure 46, 47). High cooling rates also lead to reduction in the average IMCs size, restrict the IMCs kinetically from segregation on a large scale (figure 48). The IMCs tend to spread uniformly within the interdendritic regions as the cooling rate increases (figure 46).

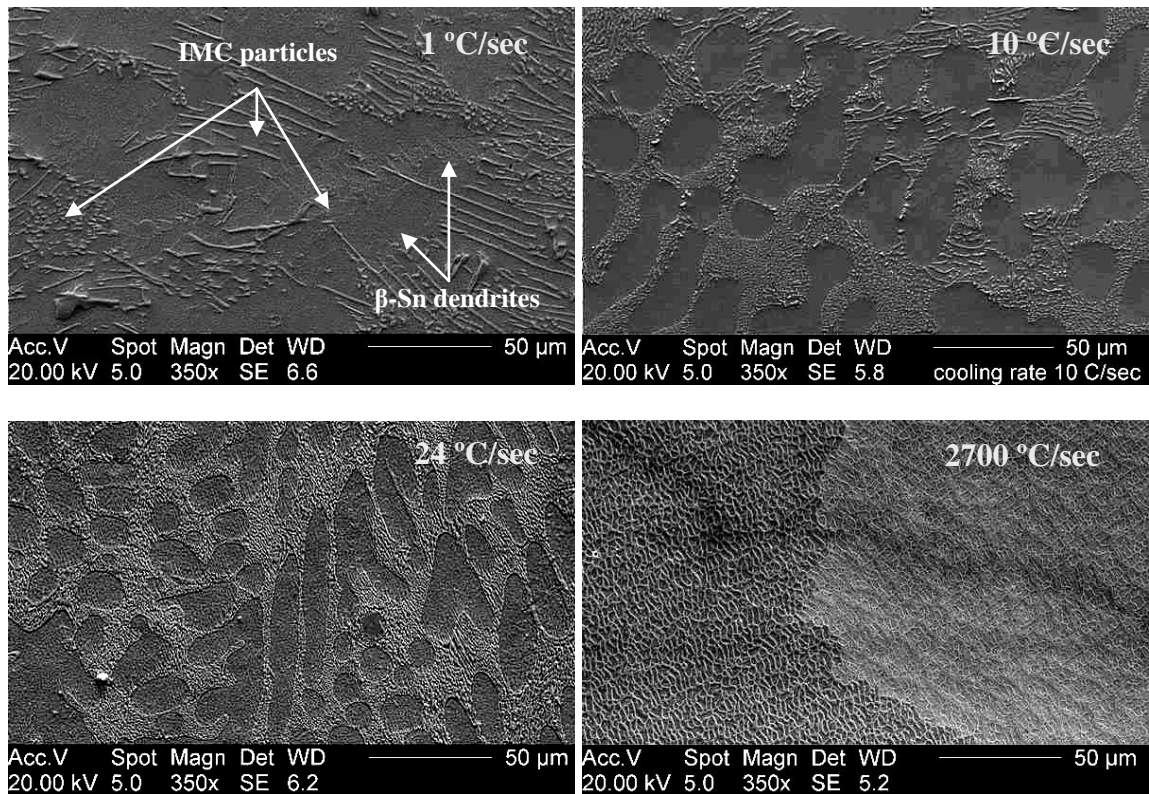


Figure 46. SEM images of SAC405 solder alloy microstructure: fast cooling rates result in decrease of the average dendrite and intermetallic particle size

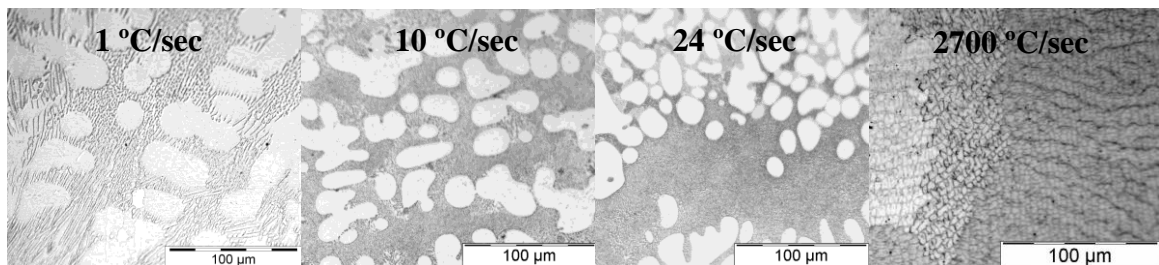


Figure 47. SAC405 alloy microstructure dependence on cooling rates. Bright areas – β -Sn dendrites; dark areas – eutectic phase (Cu_6Sn_5 and Ag_3Sn precipitates in the β -Sn matrix)

The average β -Sn dendrite size and maximum length of IMC needles in the interdendritic region was estimated by means of the “IQ Materials” software. The procedure is described in the section 4.5.

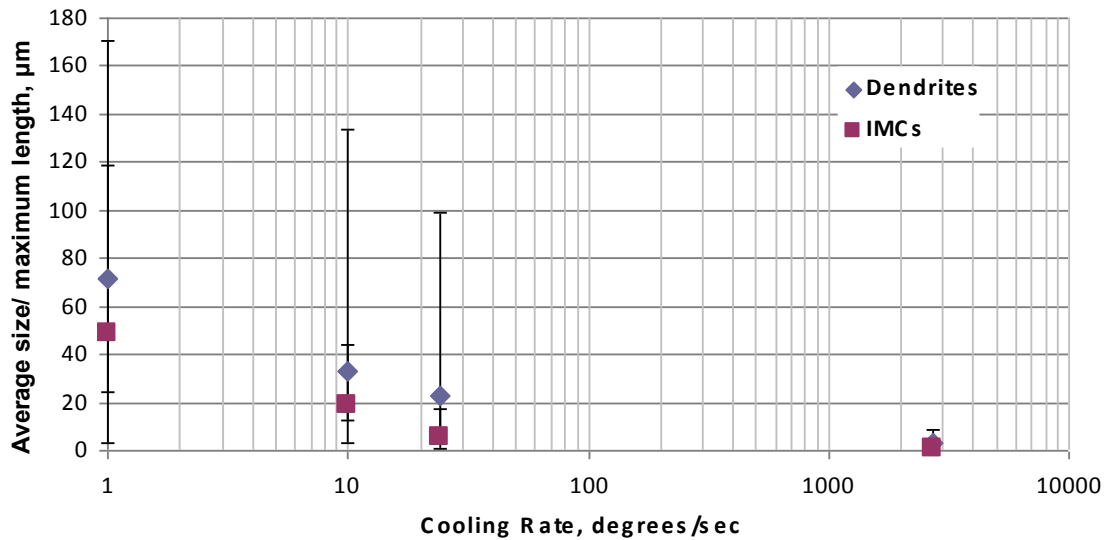


Figure 48. Average dendrite size and maximum length of IMC needles dependence on cooling rate for SAC405 solder paste

It was observed that cooling dynamics strongly affect the crystallization time. For instance, it took approximately 30 seconds for a sample to crystallize under conventional conditions (cooling rate is 1 °C/sec) and, in contrast, the crystallization duration for a cooling rate of 2700 °C/sec is 0.3 second (figure 49). The amount of undercooling before crystallization tends to increase with the increasing cooling rate (figure 49).

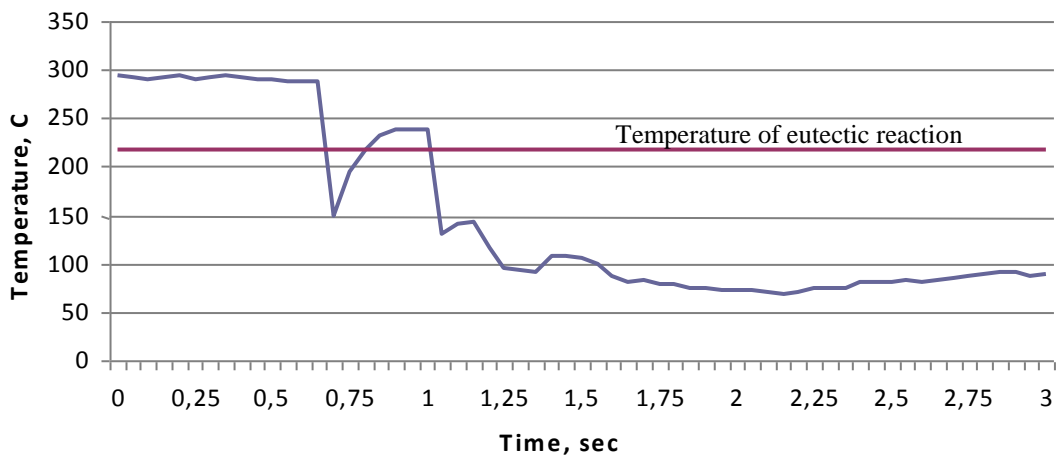


Figure 49. Enlarged area of the cooling part of the thermal-profile. Cooling rate is about 2700 °C/sec, the amount of undercooling achieved is 73 °C. In this experiment SAC305 solder was used

Comparing the microstructures obtained at the cooling rate of 24 °C/sec with those obtained at lower cooling rates (1 and 10 °C/sec), one can suggest that cooling rate of 24 °C/sec significantly reduces the average IMCs size. Such a cooling rate could be implemented on a production line by means of forced air convection in the cooling zone of conveyor reflow ovens. Thus, the IMC formation during solder joint solidification would be kinetically restricted. However fast cooling rates could damage printed circuit boards and components to be soldered, introducing stress during fast heat removal.

5.1.3. Ultrasound modification of solder microstructure

5.1.3.1. Crystallization of bulk solders

5.1.3.1.1. Dependence of amount of undercooling on ultrasonic field

The ultrasonic vibration introduction during solder crystallization was implemented by means of the experimental assembly described in section 4.6.1.

Before carrying out experiments, reference thermal-profiles for different alloy compositions were obtained. The solder samples were placed in the hollow part of the glass tube and the tip of the K-type thermocouple was attached to the samples. The thermocouple signals during heating by a hot-air gun were recorded using National Instruments software, installed on the computer. The thermocouple signal measurement rate was 4 times per second. An examples of a reference thermal-profile is shown in the figure 50(a) .

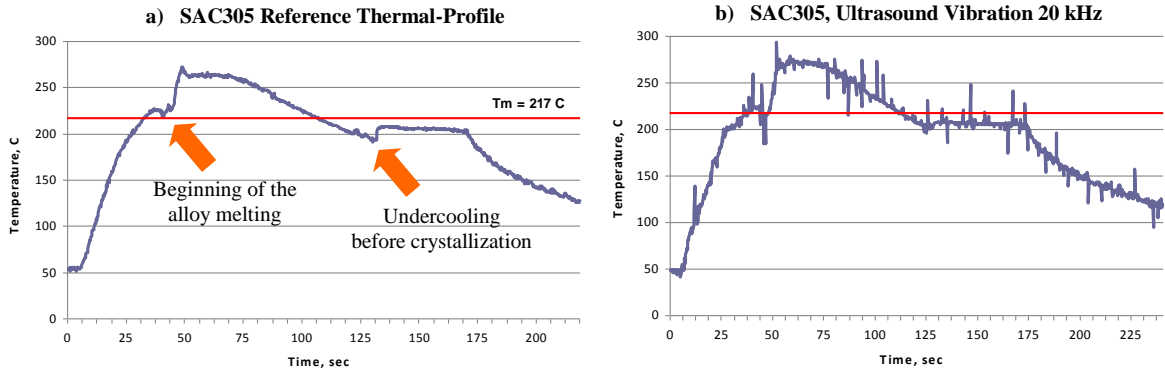


Figure 50. The reference thermal-profile and the thermal-profile obtained under influence of a 20 kHz ultrasound field on SAC305 solder

Referring to the thermal-profile, the following parameters of the process can be defined: heating up rate, cooling rate, maximum temperature, time above liquidus, amount of undercooling before crystallization. From the reference thermal-profile in figure 50 it can be seen that the solder sample cooling rate was 1 °C per second (for more details see section 4.4), the amount of undercooling 26 °C and the time above the liquidus in the molten state 55 seconds.

During the experiments with the ultrasound the following samples were prepared: eight reference samples and samples subjected to ultrasonic vibration during crystallization with frequencies 10, 12, 14, 16, 18 and 20 kHz (3 pieces for each frequency). Three alloy compositions were used: SAC 305, SAC 405 and CASTIN. Having analyzed the thermal-profiles recorded, the following graph of the amount of undercooling required before crystallization was plotted:

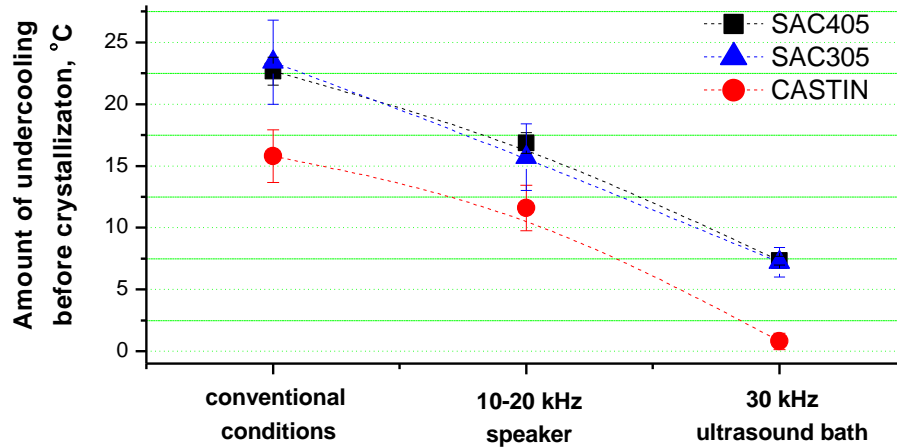


Figure 51. Amount of undercooling before crystallization

The ultrasonic vibration reduces the amount of undercooling required for the beginning of the alloy solidification. This effect is also a function of alloy composition (figure 51). Thus, solder composition optimization in combination with ultrasound can lower the amount of undercooling drastically. This is a desirable effect since smaller amounts of undercooling prevent the large-scaled intermetallic particles from segregating.

The degree of undercooling depends on ultrasound intensity. In the experiments with the ultrasonic bath working with a frequency of 30 kHz and higher ultrasound intensity (roughly estimated as 69.4 times more than intensity of the loudspeaker), the average undercooling level for SAC305 alloy was 7 °C compared to the one of 17 °C within a range of frequencies of 10-20 kHz whilst using the speaker (figure 51).

5.1.3.1.2. Dependence of the solder microstructure on the ultrasonic field

For alloy solidified within an ultrasonic field of 30 kHz (as described in section 4.6.1), the grain size tends to be finer, equiaxed and more randomly oriented (figure 52).

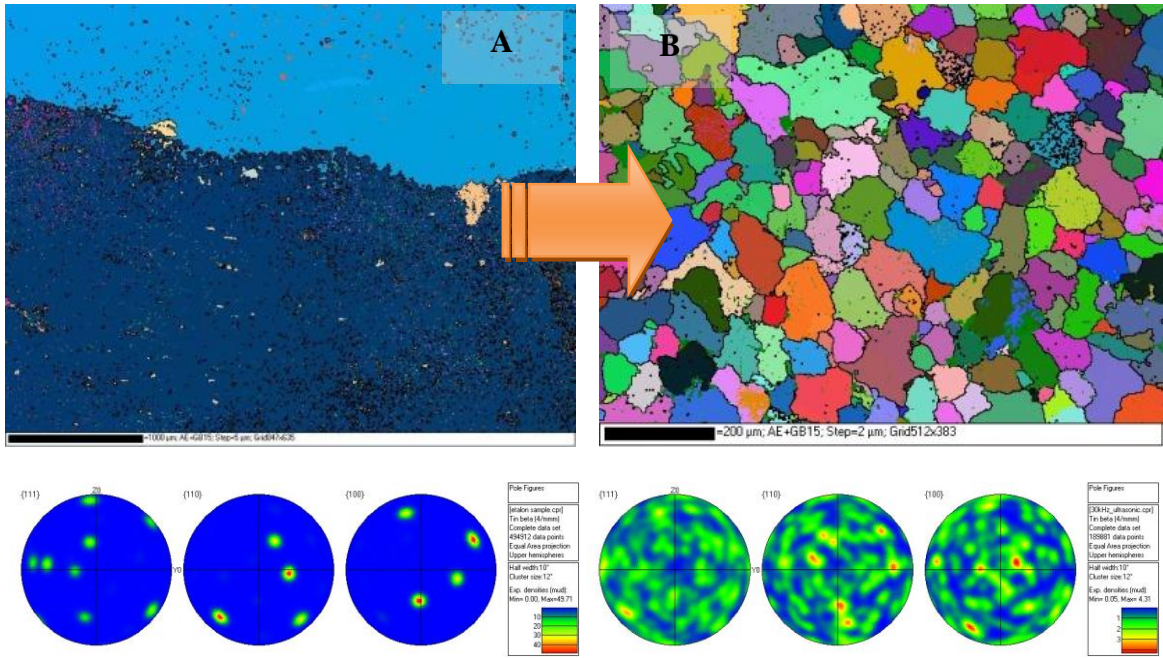


Figure 52. EBSD map and pole figures of a SAC305 solder sample: (A) obtained under conventional conditions; (B) solidified within an ultrasound field of 30 kHz

For the experiments with ultrasonic vibration frequencies of 12, 14, 16, 18, 20 and 22 kHz the sound pressure produced by the speaker of the experimental assembly was measured every time (as shown in the figure 53(A)) whilst the samples were solidifying. The sound pressure versus frequency was plotted based on measurements:

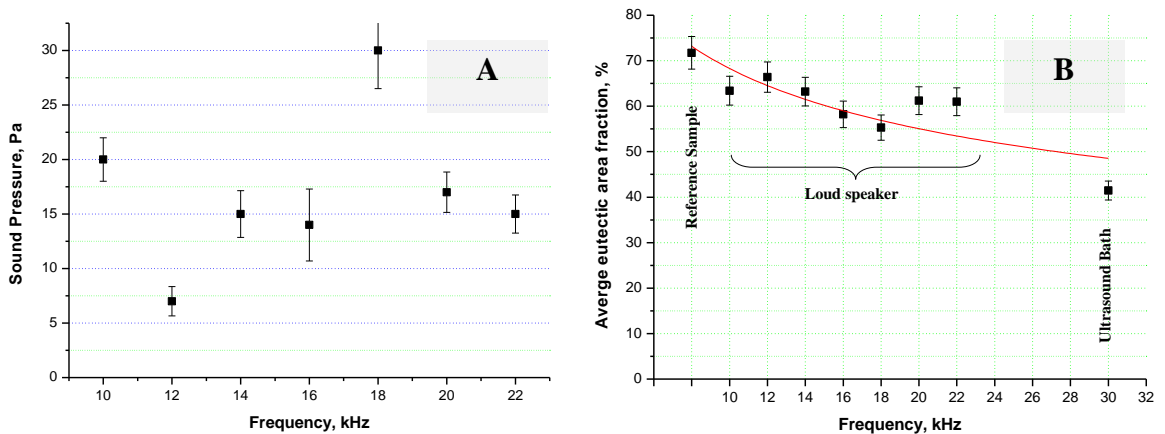


Figure 53. A: Speaker sound pressure vs. frequency curve; B: Eutectic phase proportion vs. frequency for soldering alloy SAC405

Ultrasound vibration during solder solidification results in a decrease in amount of eutectic phase formation (figure 53(B)) and promotes more uniform distribution of intermetallic particles (figure 54). The quantitative analysis of the cross-sections was performed by means of “IQ Materials” metallographic software (for more details see section 4.5).

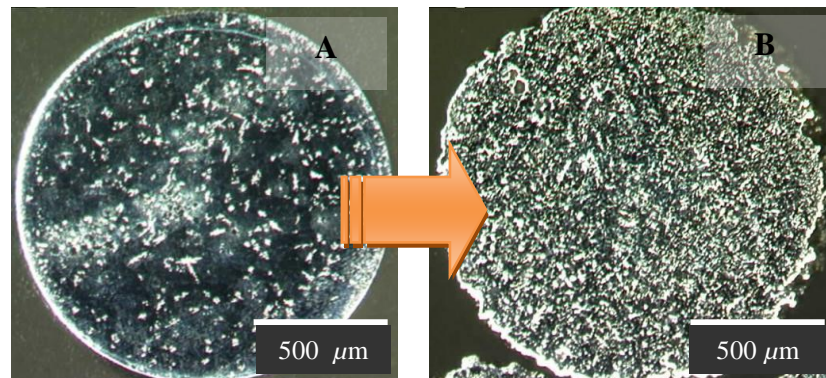


Figure 54. Microstructural refining of CASTIN alloy solidified within ultrasound field: (A) solidification under convectional conditions: large conglomerates of Cu_6Sn_5 intermetallics are present; (B) solidification under ultrasound vibration at 30 kHz: the intermetallics are spread more uniformly across the sample

5.1.3.2. Crystallization of a solder-joint system within an ultrasonic field

While performing the same series of experiments with solder-joints, it has been noted that ultrasound intensifies diffusion processes at the liquid alloy – substrate interface, causing more intensive substrate material (Cu) dissolution and, consequently, resulting in more copious intermetallic phase formation (figure 55). The tensile strength test results showed weakening of the solder-joints subjected to the ultrasound vibration during solidification (figure 56).

The procedure of the solder-joint samples preparation is explained in section 4.6.2.

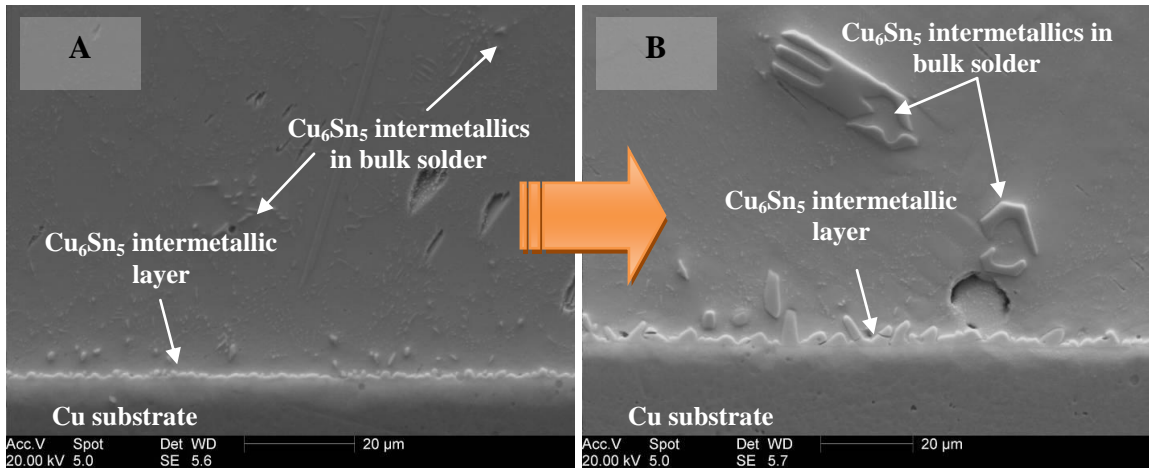


Figure 55. Solder-joint based on SAC405 alloy. (A): solidified under conventional conditions; (B) solidified within an ultrasonic field of 30 kHz

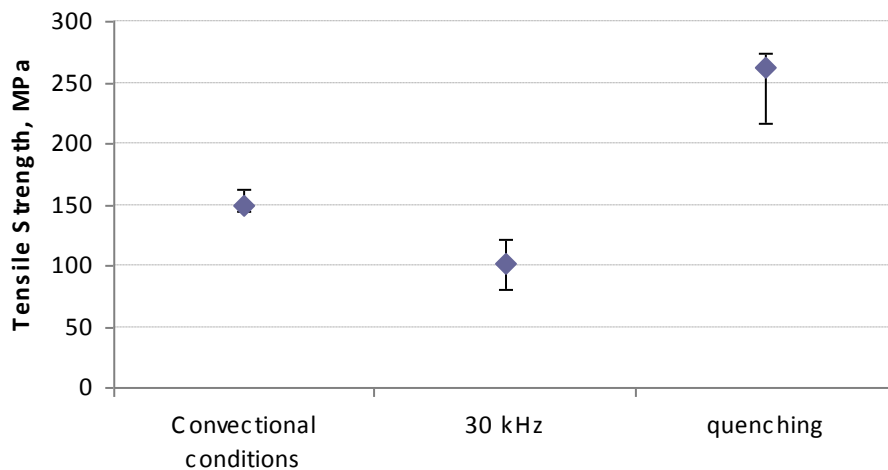


Figure 56. Tensile strength testing results (SAC405 alloy)

The tensile strength testing was conducted according to the technique described in the section 4.7. The graph given in the figure 56 also depicts tensile strength data for quenched solder-joints based on SAC405 alloy. The quenching was carried out in water medium with cooling rate of 1710 °C/sec for comparison purposes. Quenched solder-joints showed the best tensile strength results in the group.

5.2. Dependence of solder-joint tensile strength on IMC layer width

In order to investigate the dependence of solder-joint tensile strength on IMC layer width, the samples were prepared under the conditions described in the section 4.8.

Before performing tensile strength testing, solder-joints obtained after cutting of each soldered sample into strips were prepared for metallographic investigation, which revealed interfacial IMC layer morphology (figure 57, 58).

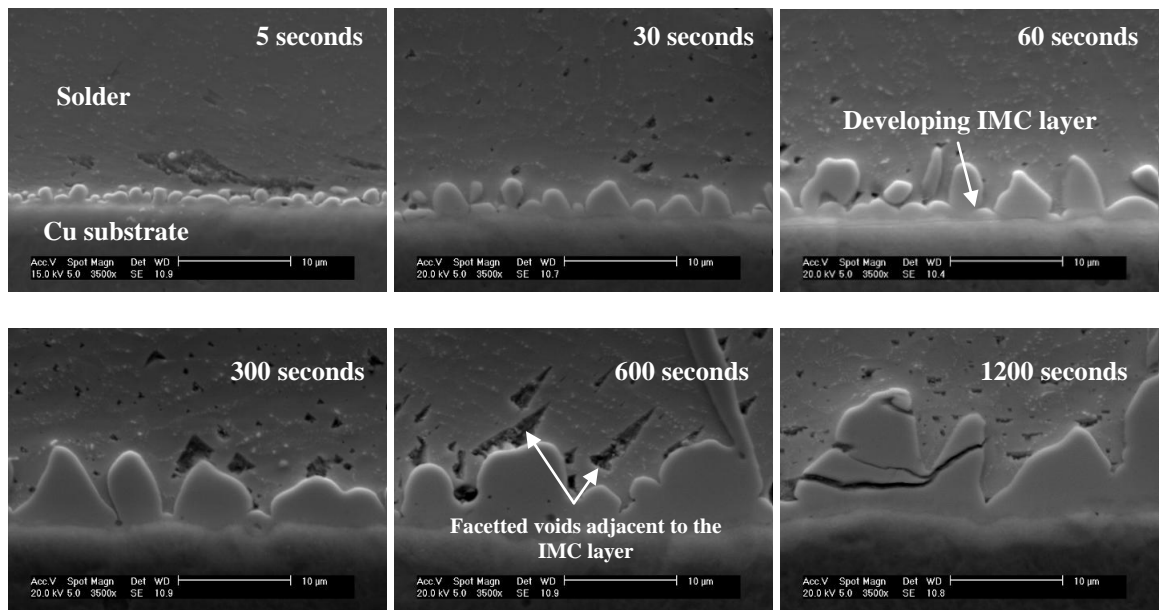


Figure 57. Interfacial intermetallic layer development on Cu substrate as dwell time increases. Soldering alloy – SAC405.

Dwelling time increase results in IMC layer growth and separation into two layers with different chemical composition: Cu_6Sn_5 and Cu_3Sn (figure 58). The IMC interfacial layer also tends to crack as it develops into solder. The IMC layer separation into two stratum with different compositions was justified by means of the EDX analysis (figure 59).

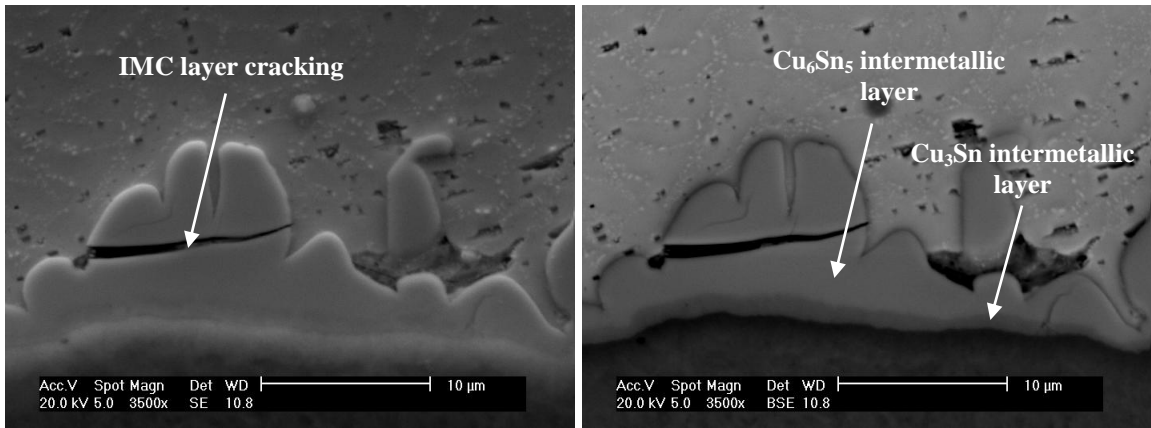


Figure 58. Crack propagation in the developing intermetallic layer and intermetallic layer separation into two layers, Cu_6Sn_5 and Cu_3Sn , as the reflow time increases. SAC405 alloy, dwell time 1200 seconds, peak temperature 250 °C

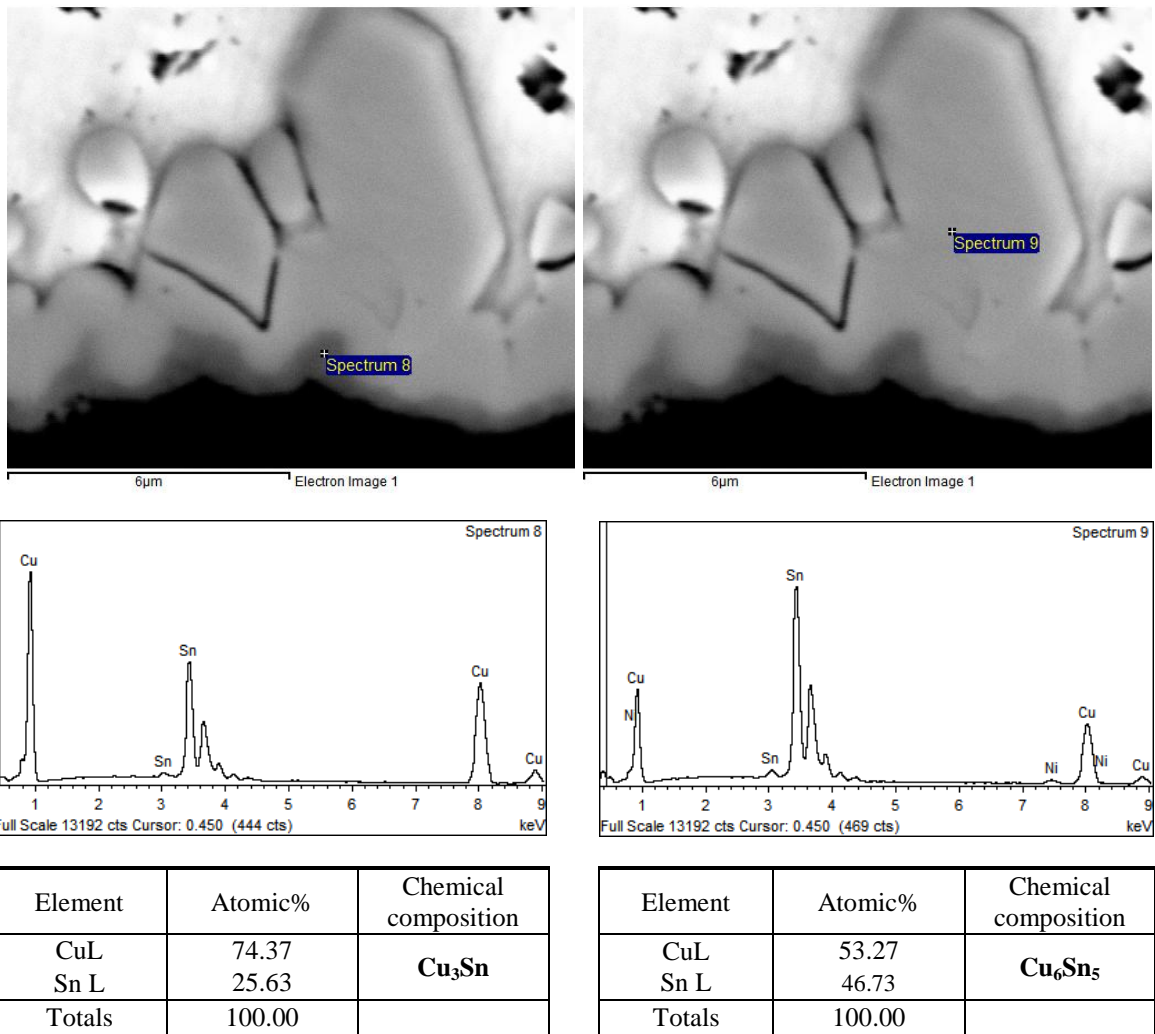


Figure 59. IMC layer EDX analysis results (SAC405)

While performing the experiment, the following correlations were obtained: IMC layers grow as scalloped layers during reflow as $\sqrt[3]{t}$, where t is reflow time (figure 60(A)). Solder-joints held for 30-60 seconds above the liquidus temperature achieved maximum tensile strength (see figure 60(B)). It was noted that Cu_6Sn_5 intermetallic precipitates have quite brittle nature and, having developed to considerable size (8-10 μm), they tend to crack weakening the solder-joint in the near-interface region (figure 58, 61). The IMC layer width was calculated as the average height of the Cu_6Sn_5 scallops in a micrograph.

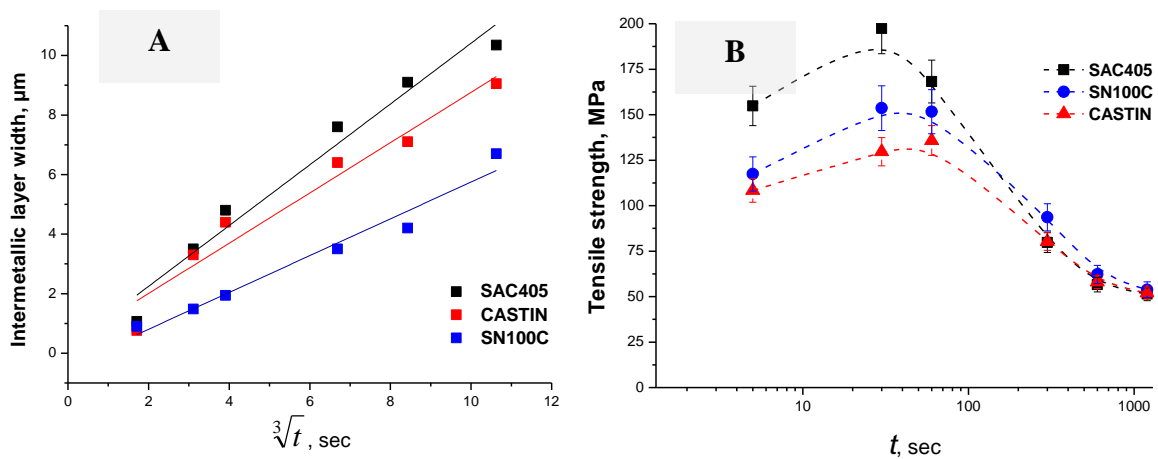


Figure 60. Intermetallic layer width (A) and tensile strength (B) dependence on time in molten state (t)

Since it was found that the interfacial intermetallic layer on Cu substrate for all investigated solder alloys tends to crack as it develops towards the solder part of a solder-joint, an attempt was undertaken to estimate the cracks development dependence on the intermetallic layer thickness. A coefficient 'A' was introduced. The coefficient A is the ratio between the summed lengths of cracks within the intermetallic layer and the intermetallic layer length in a micrograph (figure 61).

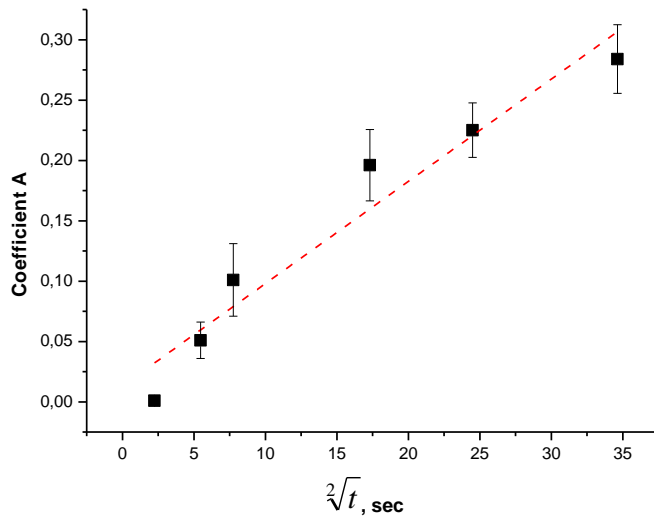
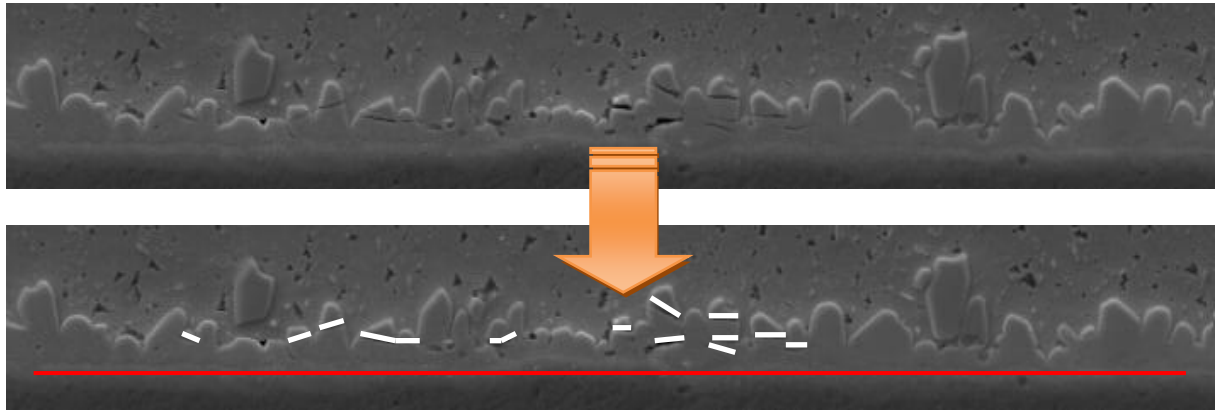


Figure 61. Method of calculation of the coefficient A: total length of cracks divided by the length of the intermetallic layer; t - time in molten state

After investigation of fractured samples it was noted that, in the solder-joints with considerable IMC layer width, fracture always occurs through the intermetallic layer (figure 62).

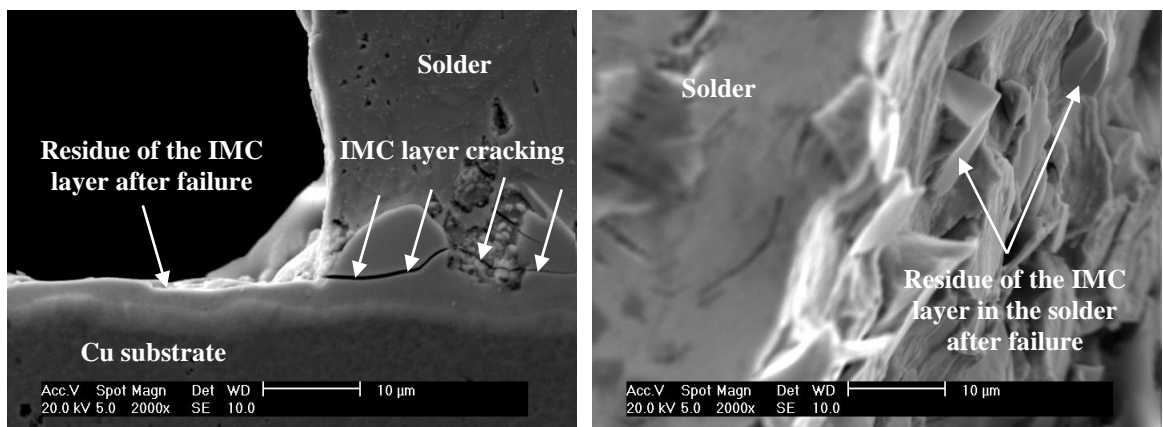


Figure 62. Typical mechanism of the solder-joint failure subjected to 1200 seconds reflow time: fracture occurs through the IMC layer. (SAC405 solder)

In contrast, in solder-joints with an intermetallic layer width of less than 6.5 μm fracture occurs along the solder – intermetallic layer or on the intermetallic layer – substrate interface (figure 63).

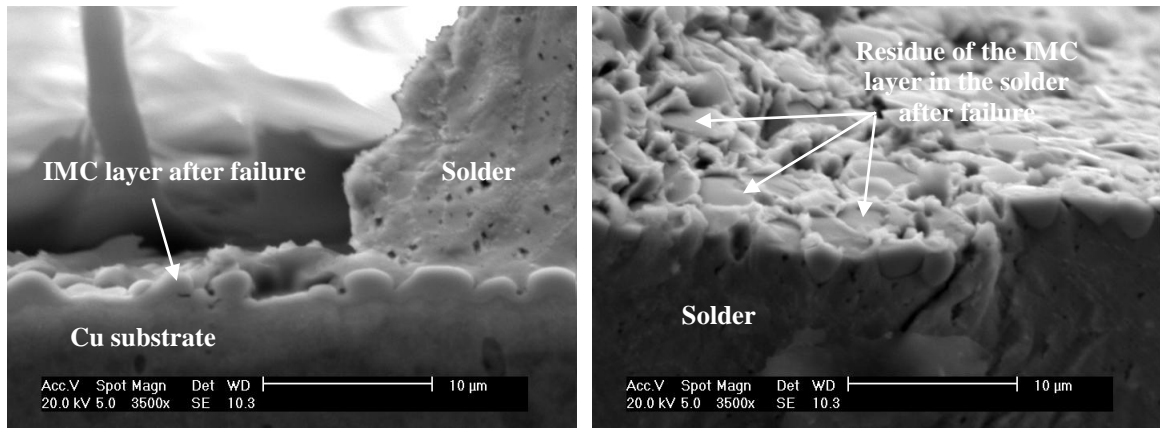


Figure 63. Typical mechanism of solder-joint failure subjected to 30 seconds reflow time: failure occurs on the IMC layer – substrate or IMC layer – solder interface.

(SAC405 solder)

5.3. Microstructural transformations within solder joints

Solder joints are being constantly subjected to different types of loads (thermal, mechanical, electrical) during the service life of an electronic device. It is of high importance to develop an understanding of the processes occurring in solder material under load conditions in order to preserve microstructural stability and make the joint last longer. During this project, attempts were made to investigate microstructural transformations in lead-free solder joints due to thermal-cycling and annealing at elevated temperatures.

5.3.1. Microstructural transformations due to thermal-cycling

Thermal-cycling experiments were carried out in order to compare the stability of microstructure of lead-free and lead-containing solders and to investigate the microstructural changes occurring in a solder bulk while thermal-cycling.

The procedure for the sample preparation for thermal-cycling experiments is explained in section 4.9.

Thermal-cycling load causes solder-joint failure on the grain boundaries and in the bulk solder near the intermetallic layer interface (figure 64, 65). Due to the thermal expansion anisotropy of β -Sn [83], the grains with a considerable misorientation expand by different amounts in different directions during heating. The resulting stresses produce microstructural changes on the grain boundary and, consequently, leading to crack initiation and growth (figure 64). The microstructural evolution of the solder joints as the number of the thermal-cycles increases is depicted in appendix 1.

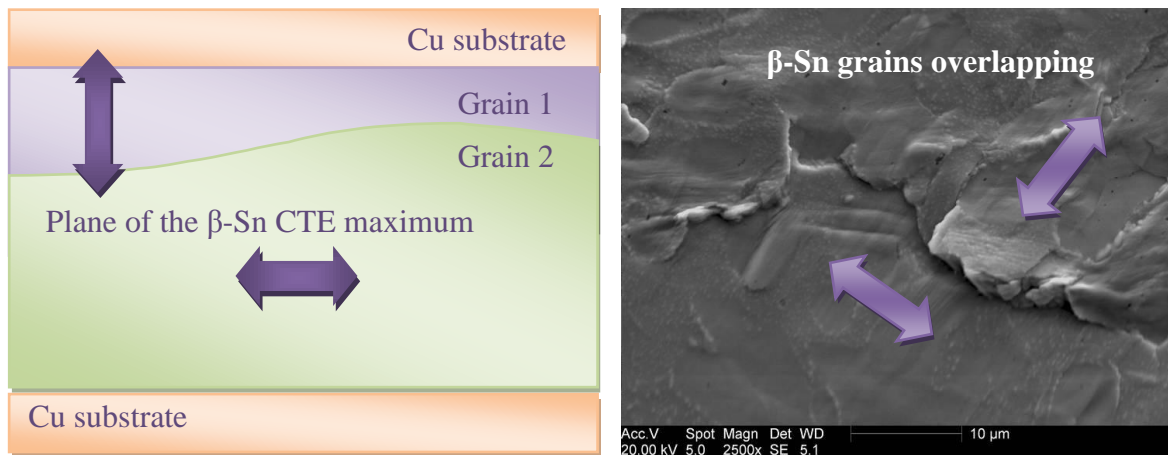


Figure 64. Microstructural changes on grain boundaries during thermal-cycling. Right picture shows overlapping of grains in SAC405 solder subjected to 200 thermal-cycles.

At the substrate-solder interface the solder microstructure is also highly stressed due to the CTE mismatch of the materials involved. The processes of plastic deformation and recrystallization produce finer β -Sn grains in this region [84]. The phenomenon of recrystallization on the grain boundaries and substrate-solder interface was proved by means of EBSD analysis (figure 66).

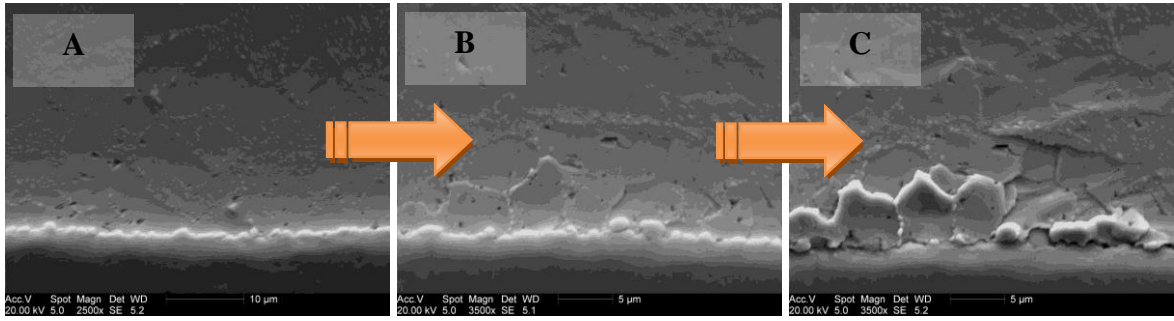


Figure 65. SAC405 solder-joint microstructure evolution during thermal-cycling: (A) solder-joint as received; (B) 200 thermal-cycles; (C) 400 thermal-cycles

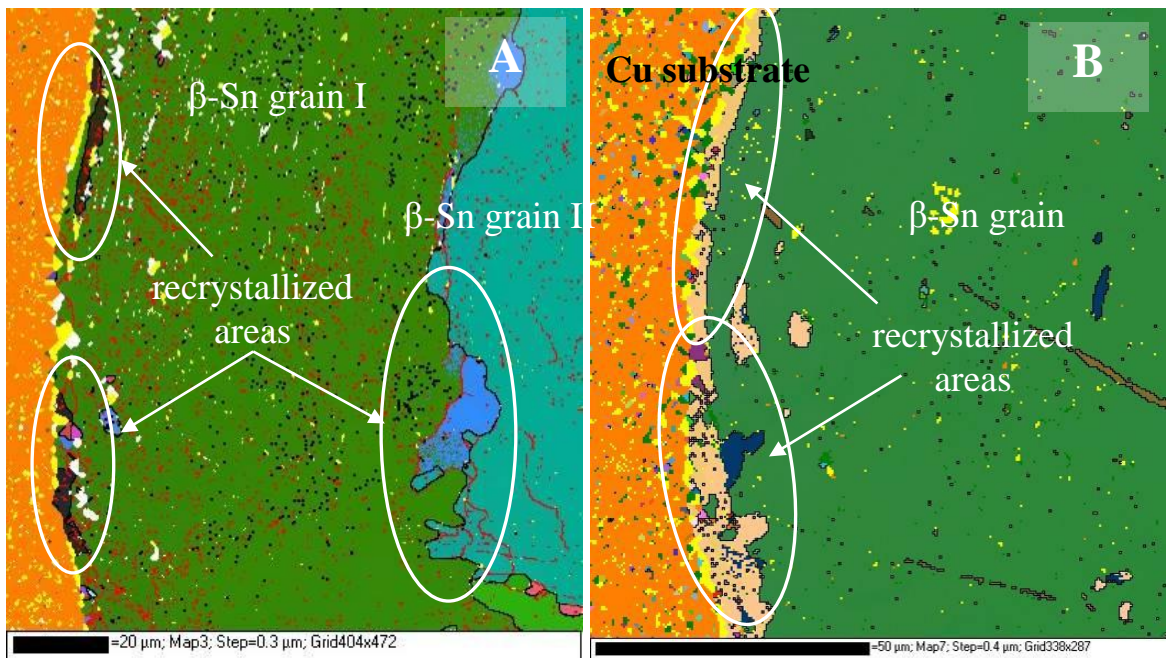


Figure 66. EBSD maps of SAC405 sample (A) after 200 thermal-cycles: β -Sn macro grain starts to recrystallize on the substrate-solder interface and grain boundary; (B) after 300 thermal-cycles: recrystallization process in the near-interface region develops further

Due to β -Sn anisotropy, the mechanical stability of lead-free solder-joints depends on the number of β -Sn grains existing within the solder volume and their mutual orientation. The relative crystallographic orientation of the grains plays a very important role. In figure 67 optical images of different areas of one solder-joint subjected to 200 thermal-cycles are

depicted. It can be seen that in the area 'A' thermal-cycling resulted in crack initiation at the grain boundary, whereas no changes can be noted at the grain boundary in the area 'B'. Since these two areas were subjected to the same cycling conditions, the mutual orientation of the β -Sn grains in area 'B' is less susceptible to thermal-cycling loads.

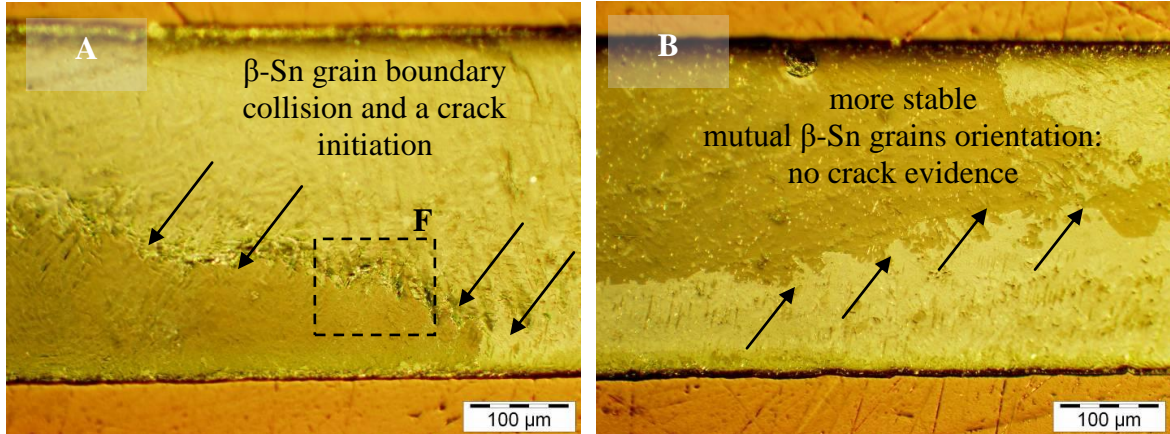


Figure 67. SAC405 solder joint subjected to 200 thermal-cycles. Light microscopy images in cross-polarized light

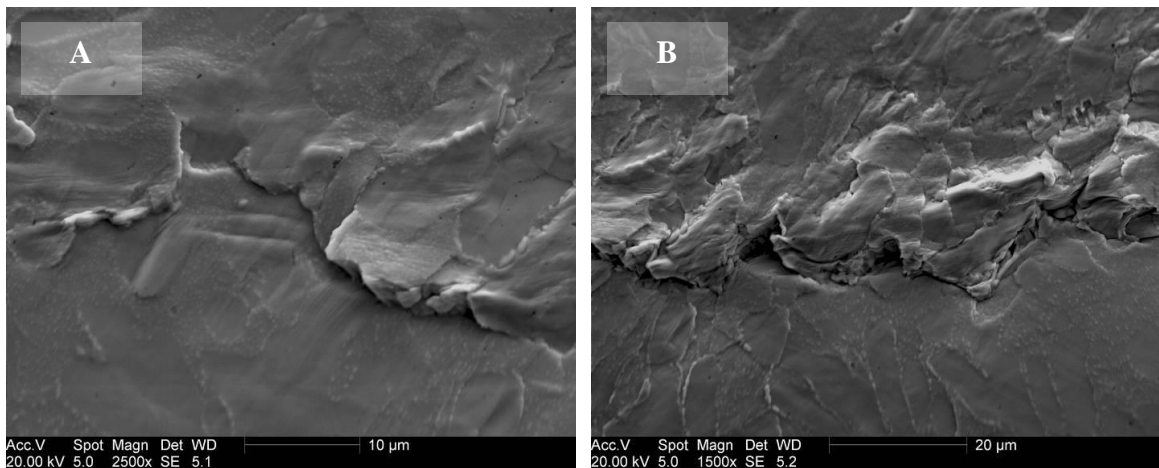


Figure 68. Enlarged area F from the figure 67. (A): grains collision after 200 thermal-cycles; (B): grains collision after 400 thermal-cycles;

Further investigation was carried out in order to compare thermal-cycling resistance and the difference in microstructural evolution of lead-free solders and lead containing ones

(table 11). The following results were obtained: after the first 50 thermal-cycles a slight microstructural change was noted in the lead-containing solder joints: the grain boundaries became more distinguishable. No microstructural changes were noted in lead-free solder-joints. After 150 thermal-cycles grain boundaries became clearly evident in lead-free samples and crack initiation was observed in lead-containing ones. 250 thermal-cycles led to significant grain boundary sliding and crack propagation in Sn60Pb40 samples. Nevertheless, SAC405 samples showed quite strong microstructural resistance to cycling conditions compared to the lead-containing solder-joints. Grain boundary sliding and solder smearing in the near-interface region were noted in these samples with no crack initiation. Lead-containing solders tend to produce finer structure with a large amount of crystallographically disoriented grains upon solidification; these solder joints appeared to be the weakest ones in terms of microstructural resistance to cycling conditions (table 11).

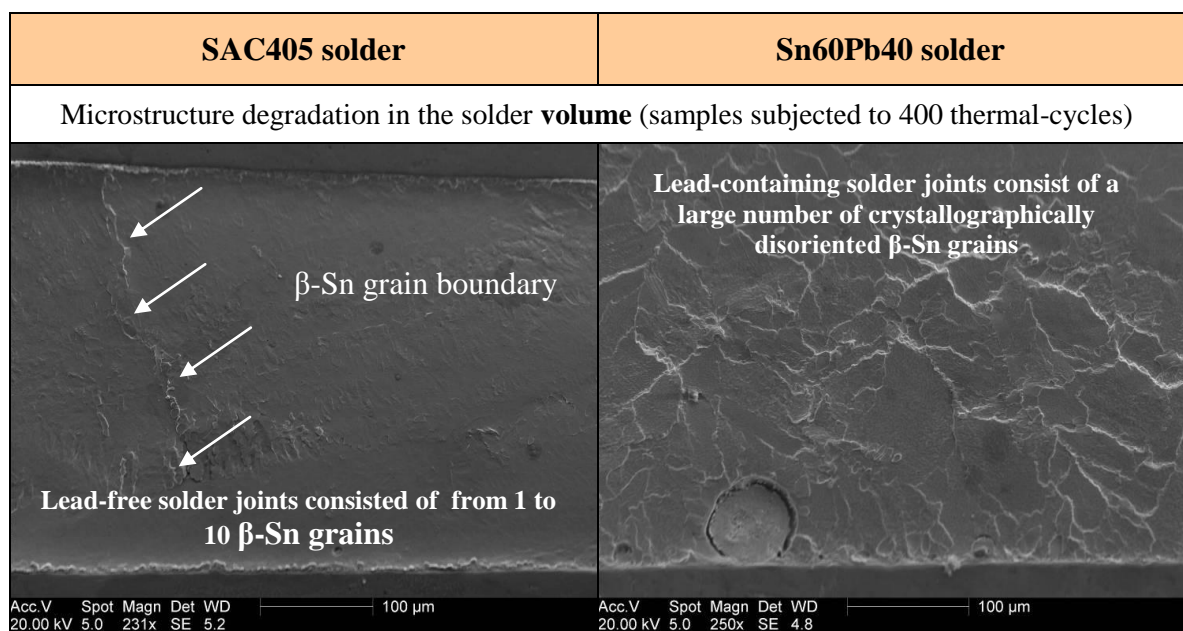


Table 11. Comparative analysis of SAC405 and Sn60Pb40 alloys microstructure degradation under thermal-cycling load conditions

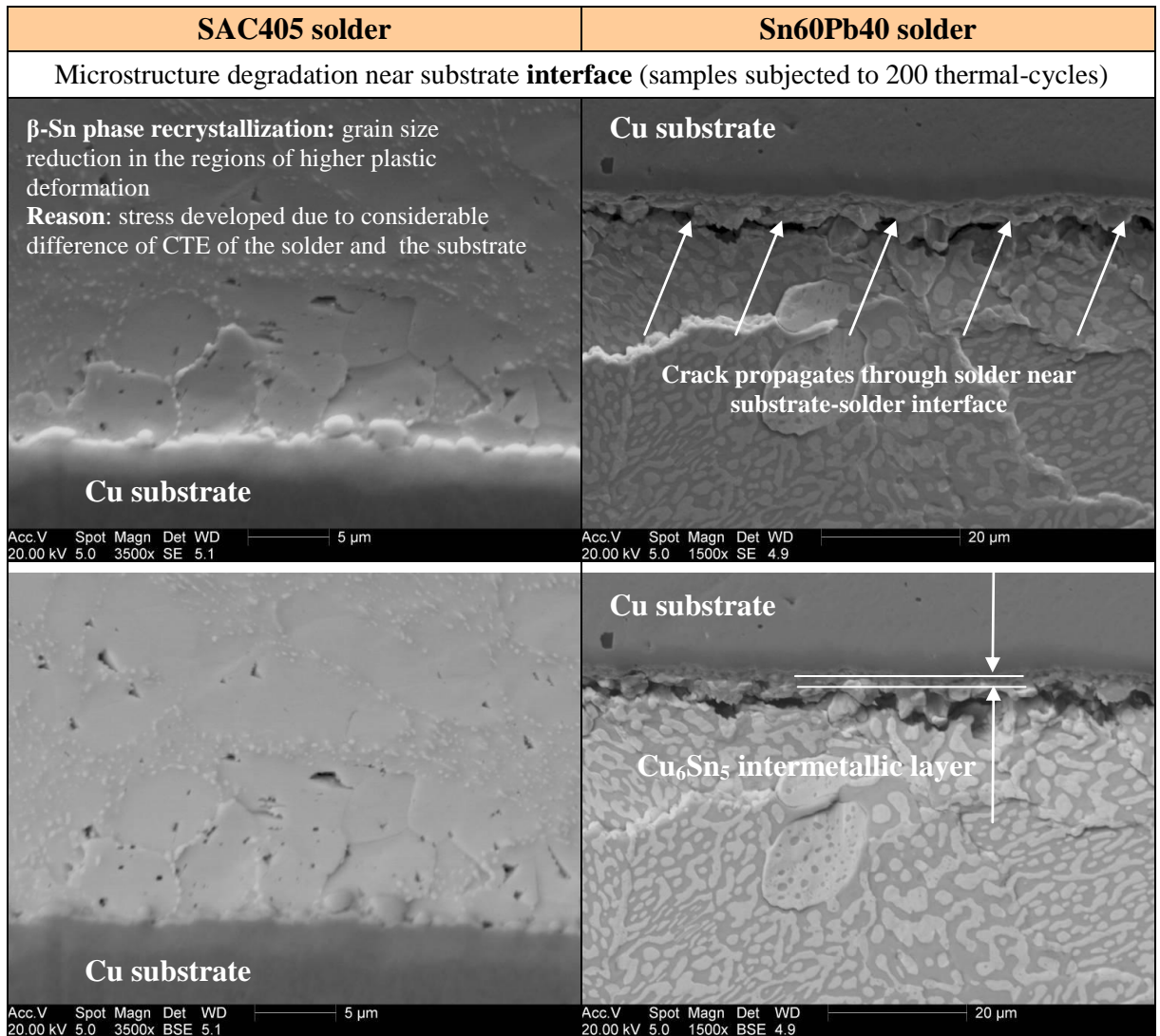


Table 11 (continued). Comparative analysis of SAC405 and Sn60Pb40 alloys
microstructure degradation under thermal-cycling load conditions

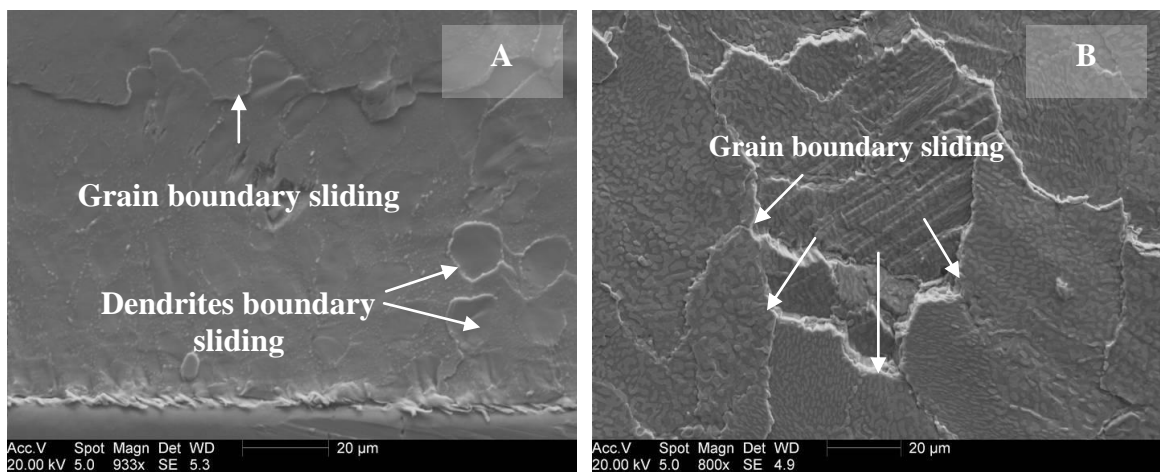


Figure 69. SEM images of (A) SAC405; (B) Sn60Pb40 solder-joint subjected to 250
thermal-cycles

Appendix 1 shows microstructural evolution of solder-joints obtained under different conditions (ultrasound, quenching) and different alloy compositions.

It was observed that, in parallel to the structural changes on the grain boundaries while thermal-cycling, another process is taking place: intermetallic precipitate growth. This can be seen in the microstructures of the rapidly cooled samples (figure 70), but this phenomenon also occurs within the samples obtained under moderate cooling rates.

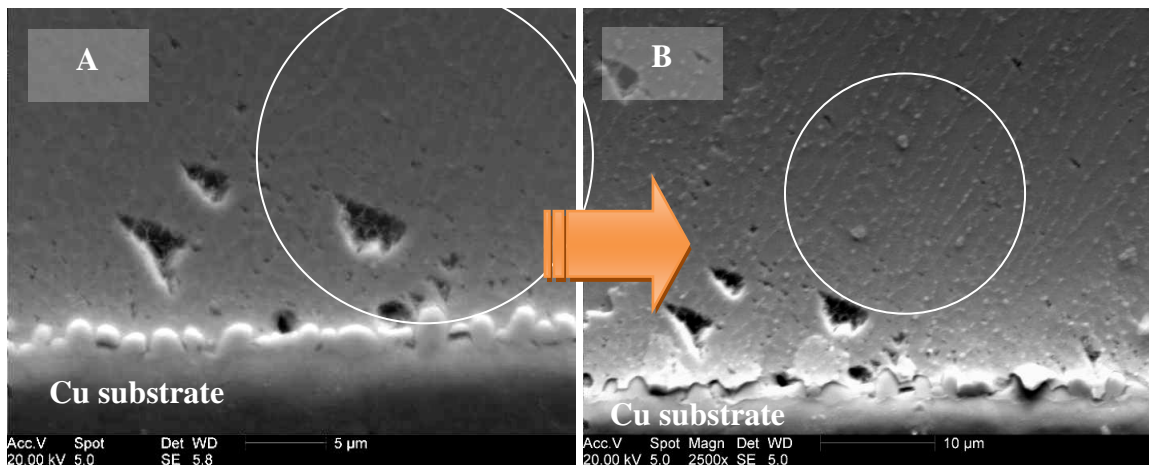


Figure 70. SEM images of (A) SAC405 in as received condition (rapidly cooled sample); (B) after 250 thermal-cycles: IMCs are now more evident in the bulk; changes along the interface with substrate are also evident

5.3.2. Tensile strength testing of cycled samples

The set of the samples subjected to thermal-cycling load conditions was further investigated in terms of tensile strength.

Apart from one sample, the samples subjected to 100 thermal-cycles give lower strength than those which have not been cycled. The weakest tensile strength values were demonstrated by lead-contained solder-joints and solder-joints treated with ultrasound. The dwell time (time above liquidus) also influences the tensile strength results. Higher strength with increase in dwell time above the liquidus and with increase in cooling rate was observed (figure 71).

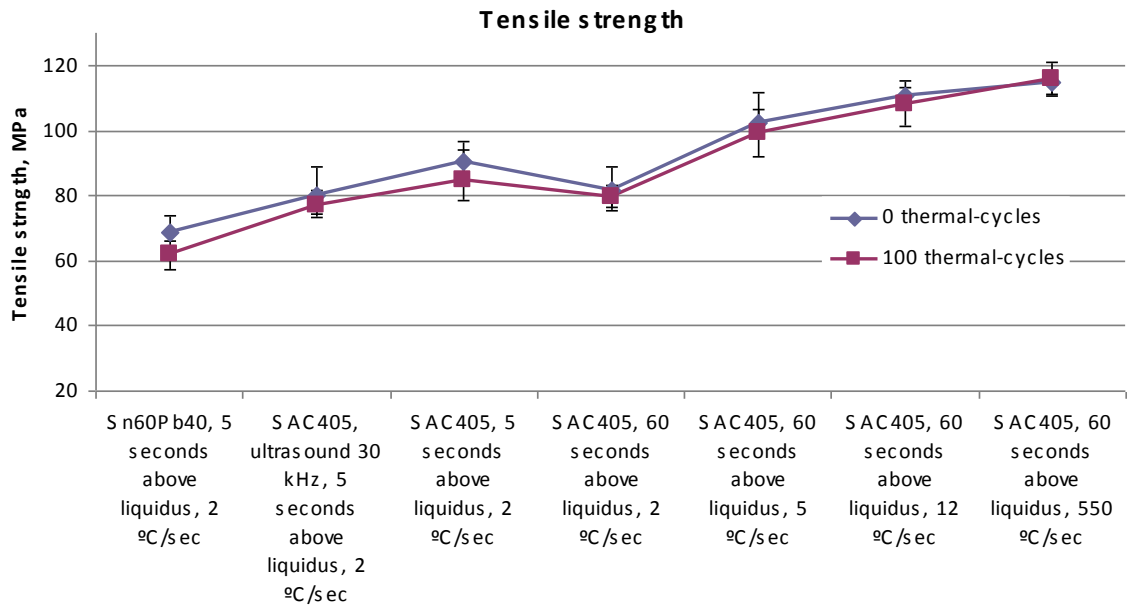


Figure 71. Solder joint tensile strength dependence on different soldering conditions

In the reference samples fracture occurred on the substrate-solder interface. In contrast, the thermally-cycled samples fractured both on the substrate-solder interface and in the solder bulk along grain boundaries (figure 72).

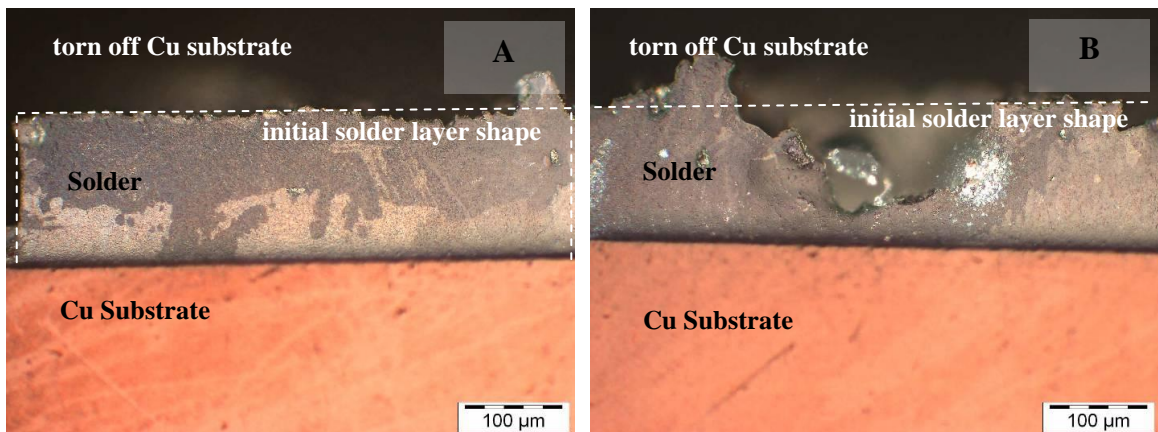


Figure 72. Cross-polarized light images of fractured SAC405 solder joints. (A): reference sample (5 seconds above liquidus, 2 C°/sec): fracture occurred along the substrate-solder interface; (B) thermal-cycled sample (100 cycles): fracture occurred both on the substrate-solder interface and in the solder bulk along grain boundaries

5.3.3. Microstructural transformations during solid state annealing

5.3.3.1. In solder bulk

In order to simulate the situation of solder-joint operation under elevated temperatures, various specimens (bulk solders and solder-joints) were placed in a furnace for solid state ageing at 160 °C (for more details see section 4.10).

SAC405, CASTIN, SN100C and Sn60Pb40 bulk solders were subjected to solid state ageing with subsequent metallographic investigation:

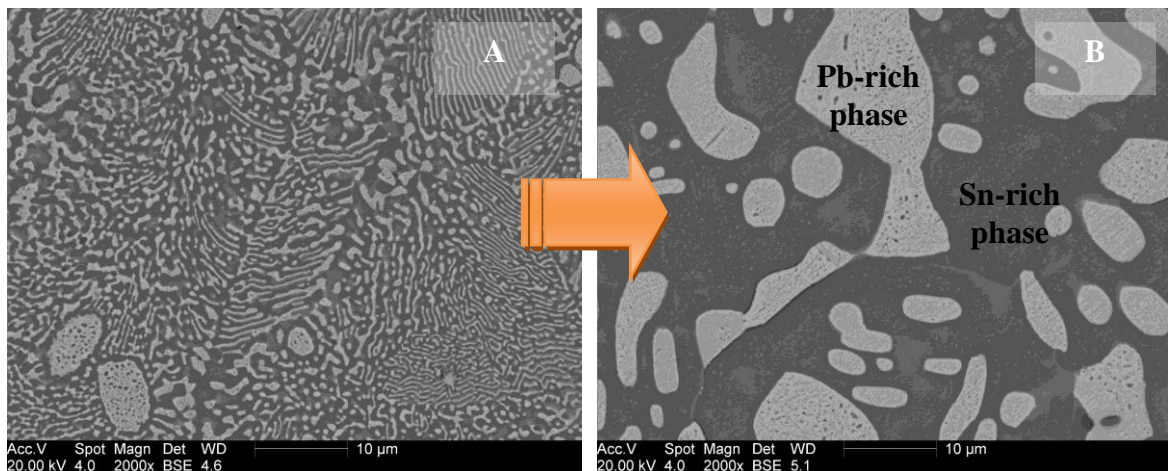


Figure 73. Micro-structural changes in Sn60Pb40 solder: (A) before and (B) after 1800 hours at 160 °C

The Sn60 Pb40 solder specimens showed rapid coarsening of the microstructure during the solid-state annealing (figure 73). In their initial state the microstructure consisted of a fine mixture of Pb- and Sn-rich phases. After 1800 hours of ageing at 160 °C coarse grains of lead and tin were present.

In the lead-free solder samples (SAC405, CASTIN, SN100C) the intermetallic precipitates modified drastically (figure 74). Thus, the Ag_3Sn precipitates enlarged in the former interdendritic regions where they were formed in the latest stages of the solidification

process during eutectic reaction, whereas Cu_6Sn_5 intermetallic particles showed more rapid growth and were found to be distributed along the grain boundaries of the coarsened microstructure (figure 74, 75).

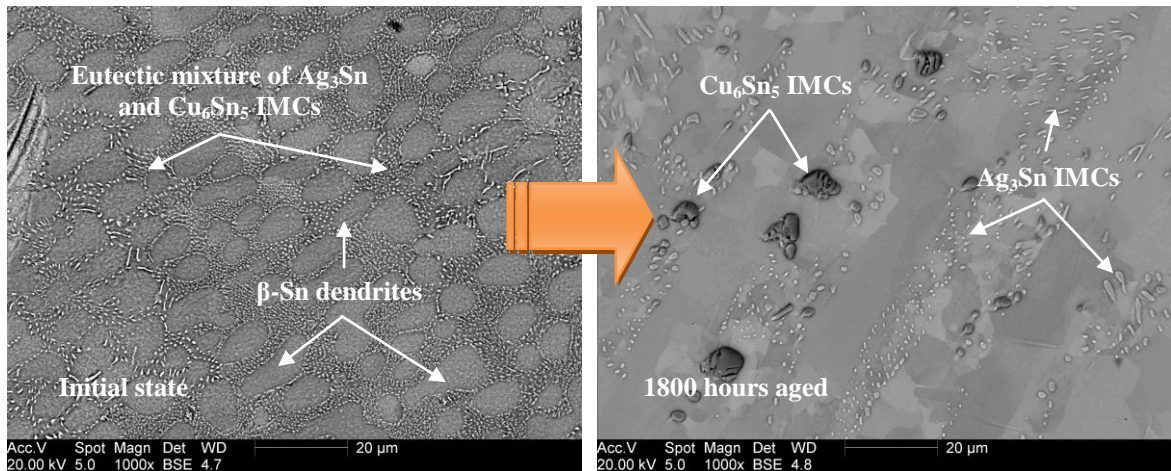


Figure 74. Micro-structural changes in SAC405 solder after 1800 hours at 160 °C (similar images we obtained for other lead-free compositions)

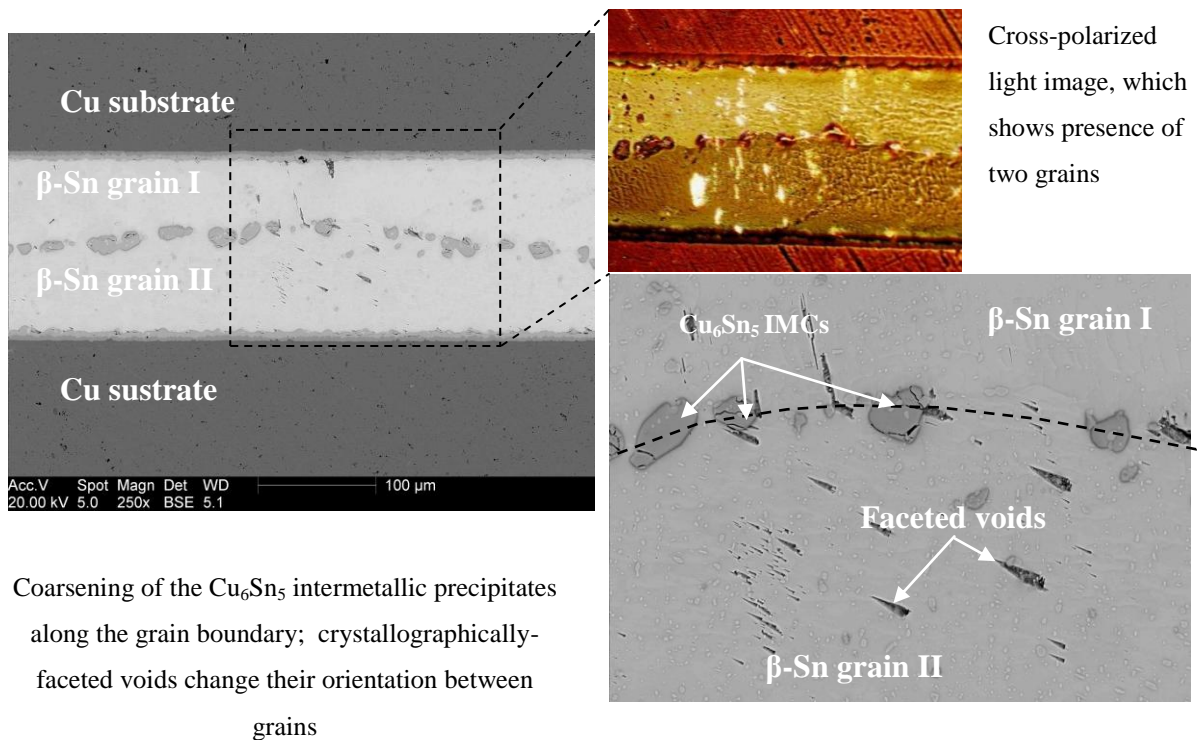


Figure 75. SAC405 solder-joint annealed for 1800 hours at 160 °C

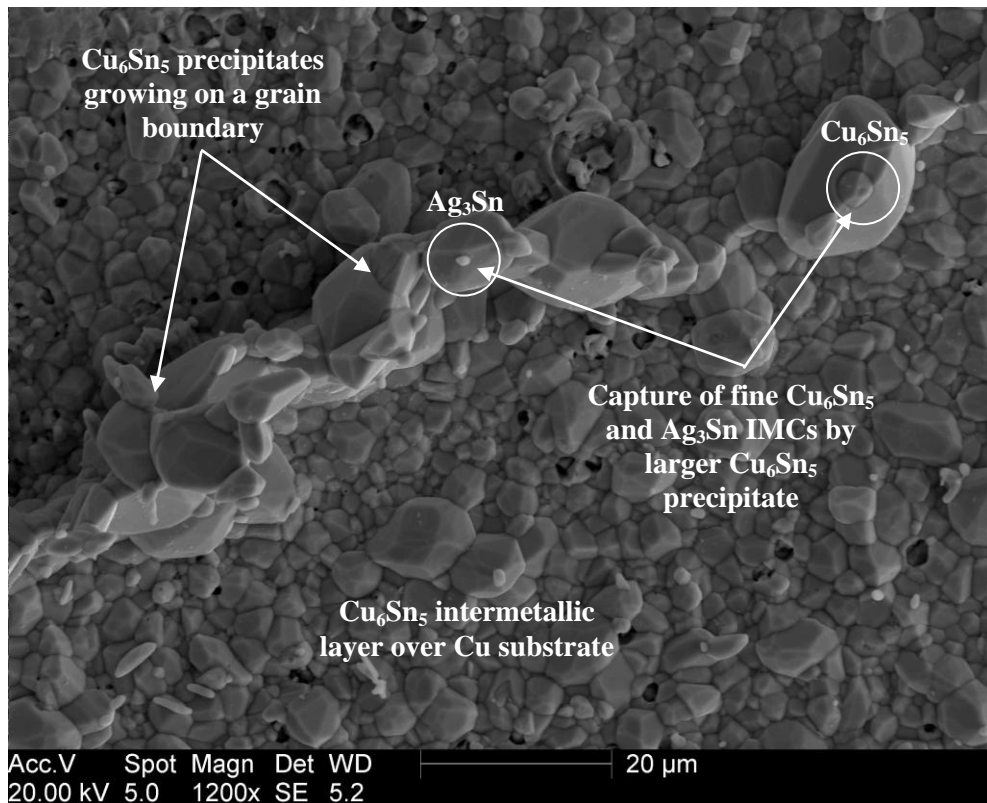


Figure 76. SAC405 solder joint annealed for 1800 hours at 160 °C and deep-etched

After removal of the β -Sn matrix by means of deep-etching solution (see section 4.2.4 for more details) in the annealed solder-joint samples, the three dimensional images of Cu_6Sn_5 intermetallic particles coarsened along the grain boundaries were obtained. It can be seen how during precipitate growth they can entrap smaller Cu_6Sn_5 and Ag_3Sn precipitates (figure 76).

5.3.3.2. On the substrate-solder interface

In order to investigate the kinetics of the processes at the solder – Cu substrate interface in the solid state, solder-joint samples were subjected to annealing for different durations at 160 °C with subsequent cross-section preparation for SEM/BSEM analysis and deep-etching for intermetallic layer morphology investigation (figure 77-78).

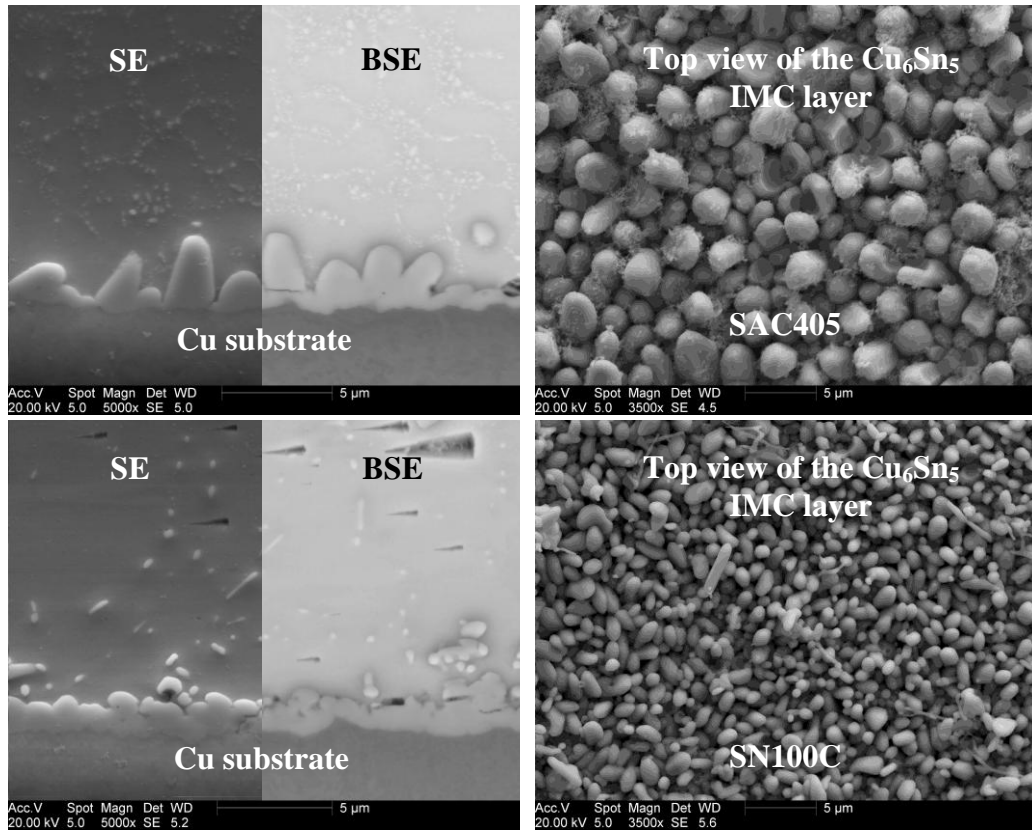


Figure 77. Intermetallic layers in SAC405 and Sn100C solder joints in initial state

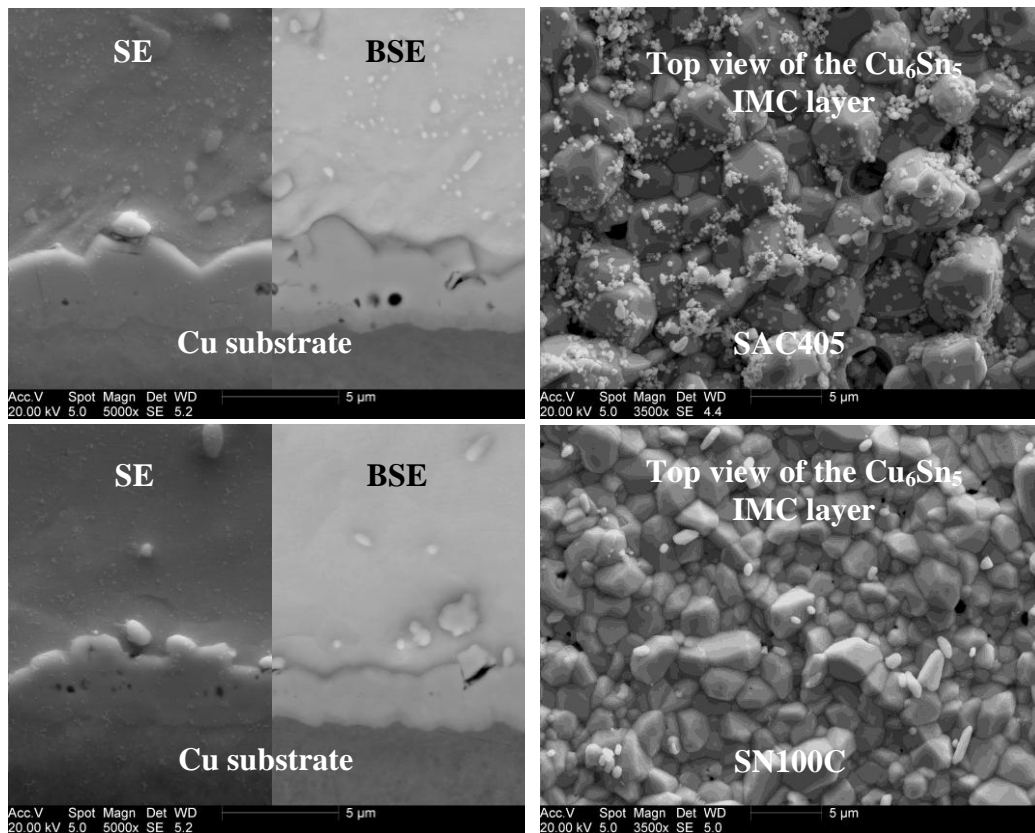


Figure 78. Intermetallic layers in SAC405 and Sn100C after 230 hours at 160 °C

The average thickness of the intermetallic layers was calculated as the average height of the Cu_6Sn_5 and Cu_3Sn scallops in a micrograph. The chemical composition of the IMC layers was justified by the EDX quantitative analysis, as shown in section 5.2.

The results are shown in the figure 79. Thus, it can be seen that the Cu_6Sn_5 intermetallic layer develops considerably faster than Cu_3Sn , especially in solder-joints based on SAC405 alloy. The Cu_3Sn intermetallic layer was not found in solder-joints assembled with Sn100C soldering paste in initial state; although it starts do develop while annealing at elevated temperature (160 °C).

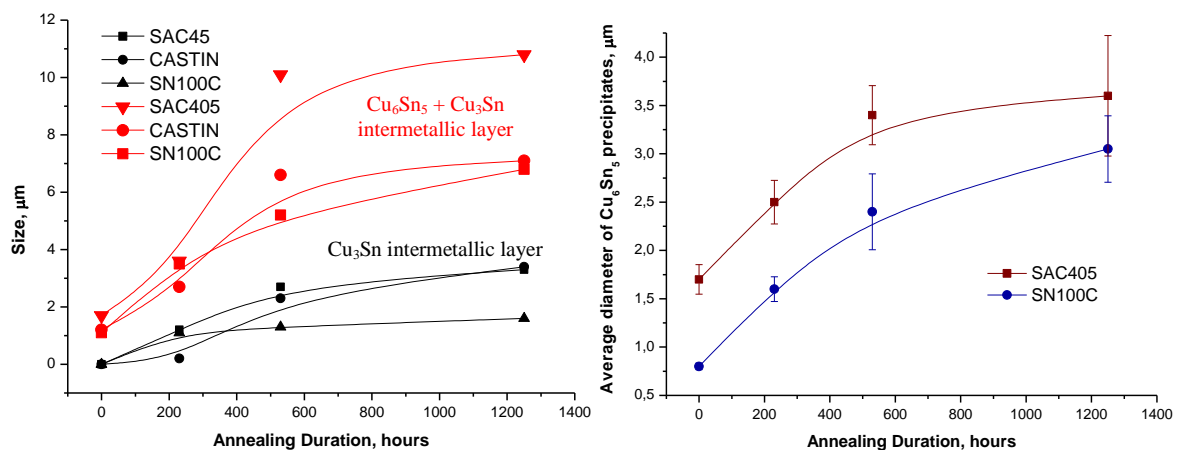


Figure 79. Intermetallic layer evolution during solid-state annealing

5.4. Voiding and phenomenon of crystallographically-faceted voids formation

While carrying out the experiments and investigating lead-free solders microstructure, various types of voids were observed. The classification of the voids in solder joints given by Raiyo Aspandiar, Intel Corporation [70] is given in section 2.2.8. In the present study other types of voids not mentioned in this classification were observed. Such as: micro-voids in the bulk filled with solder in the final stages of solidification and crystallographically-faceted voids (figure 80, 81). Concerning the micro-voids partially-filled with solder, one can surmise that at a certain stage of development, the void wall

was broken and liquid solder filled the cavity. Depending on the time and temperature, the void was filled fully or partially. The crystallographically-faceted voids are of particular interest, as they have not been previously described. The more detailed findings about this phenomenon are presented in the following section. Full overview of the voids observed in this study is presented in appendix 2.

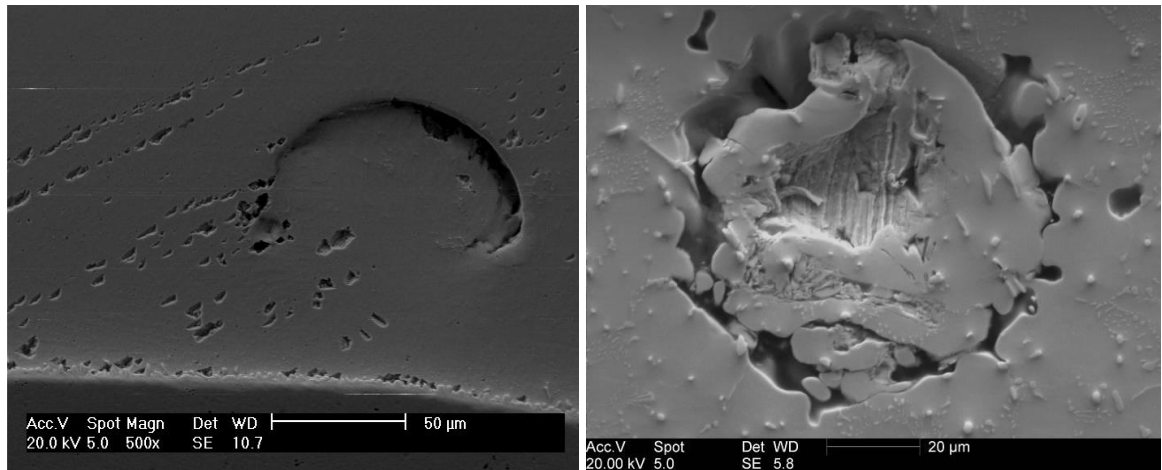


Figure 80. Example of micro-voids partially filled with solder (SN100C)

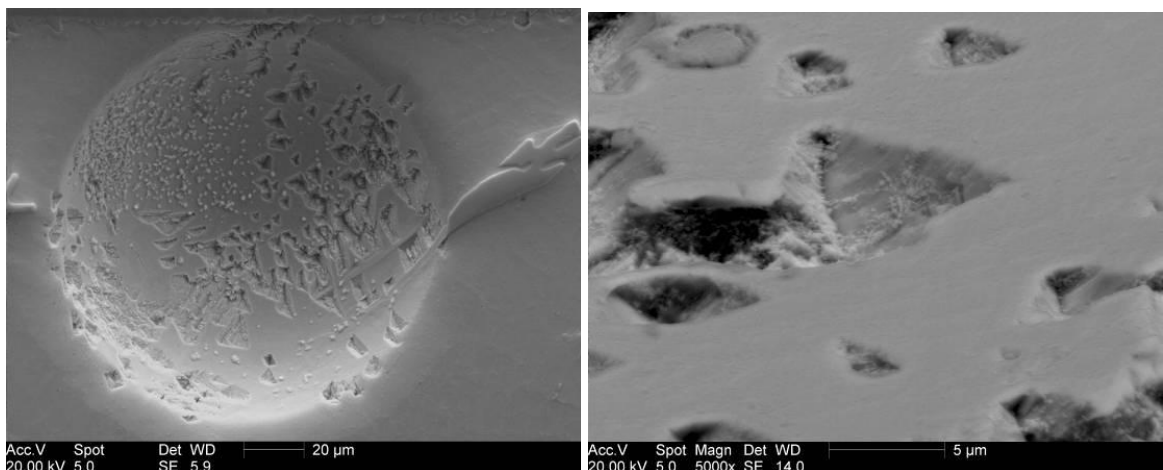


Figure 81. Example of crystallographically-faceted voids (SAC405)

5.4.1. Crystallographically faceted voids in ‘as soldered’ state

5.4.1.1. Solder joints with ‘massive’ copper substrate (substrate thickness > 10 000 μm)

In the framework of the experiments carried out, the crystallographically-faceted voids (CFV) were constantly observed. Later an attempt was made to investigate this phenomenon separately from the experiments described in previous sections. The technique for specimen preparation is given in section 4.11.

It was proved by means of EBSD analysis that the CFV are always correlated with β -Sn grain crystallographic orientation and form in a tetragonal shape (figure 82). Depending on the cross-section plane, they can be observed as triangles, rectangles, squares or triangles with cut ends (figure 83).

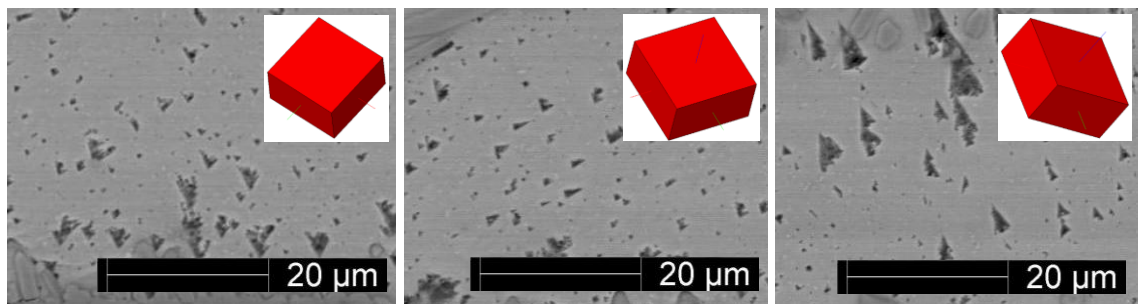


Figure 82. Correlation between void shape and β -Sn grain crystallographic orientation, revealed by EBSD analysis (SN100C alloy, not etched cross sections)

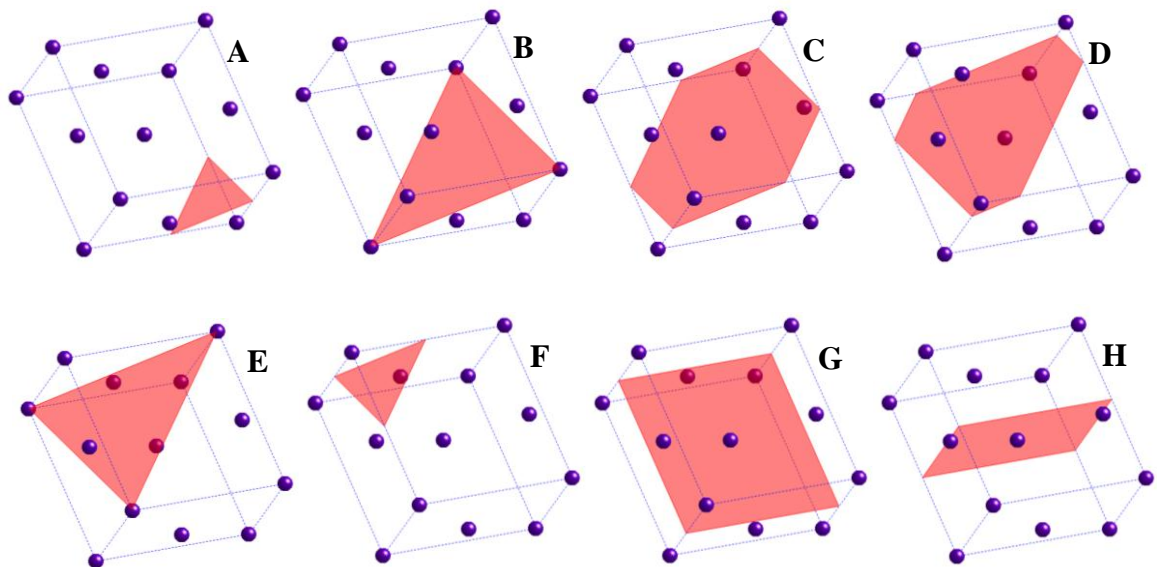


Figure 83. β -Sn crystallographic unit cell sectioned in different planes: A-F: Plane with Miller indices (111); G: Plane with Miller indices (001); H: Plane with Miller indices (010)

The CFV were found to occur all the way through the solder-joint volume, which was proved by continuously polishing and checking the void distribution. At the same time, it was observed that the CFV tend to be located near the substrate-solder interface (i.e. near the Cu_6Sn_5 intermetallic layer) and near bulk intermetallic precipitates (figure 84).

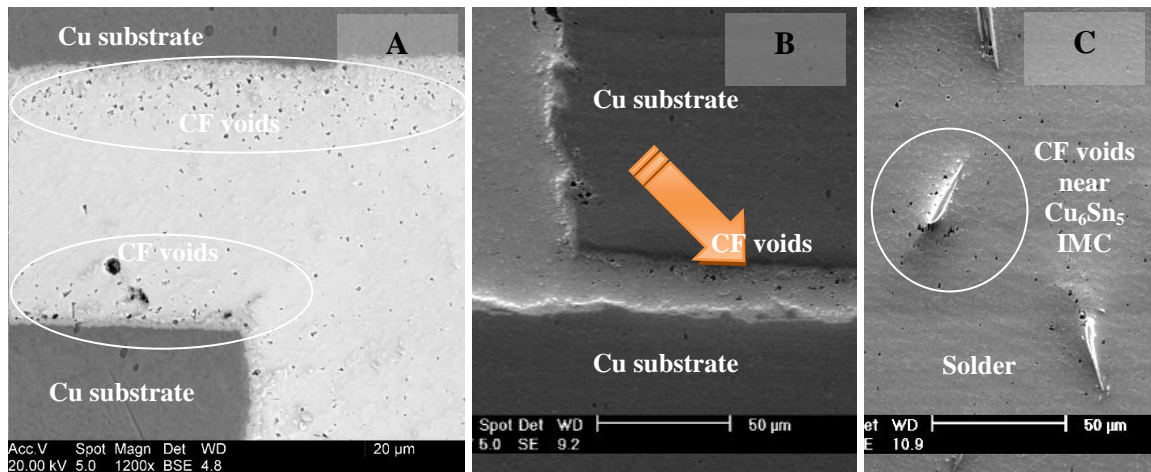


Figure 84. (A), (B): BSE and SE images of different solder-joints based on Sn100C alloy (not etched). The CFVs in this case have higher density of distribution close to the substrate-solder interface; (C): SE image of a solder joint based on SAC305 alloy (not etched). The CFV have higher density of distribution close to the Cu_6Sn_5 IMCs

Performing further experiments, it was noted that there is a correlation between the volume fraction of crystallographically faceted voids within the solder joint and the distance between copper substrates: the thinner the gap between two substrates, the more copiously CF voiding is developed (figure 85).

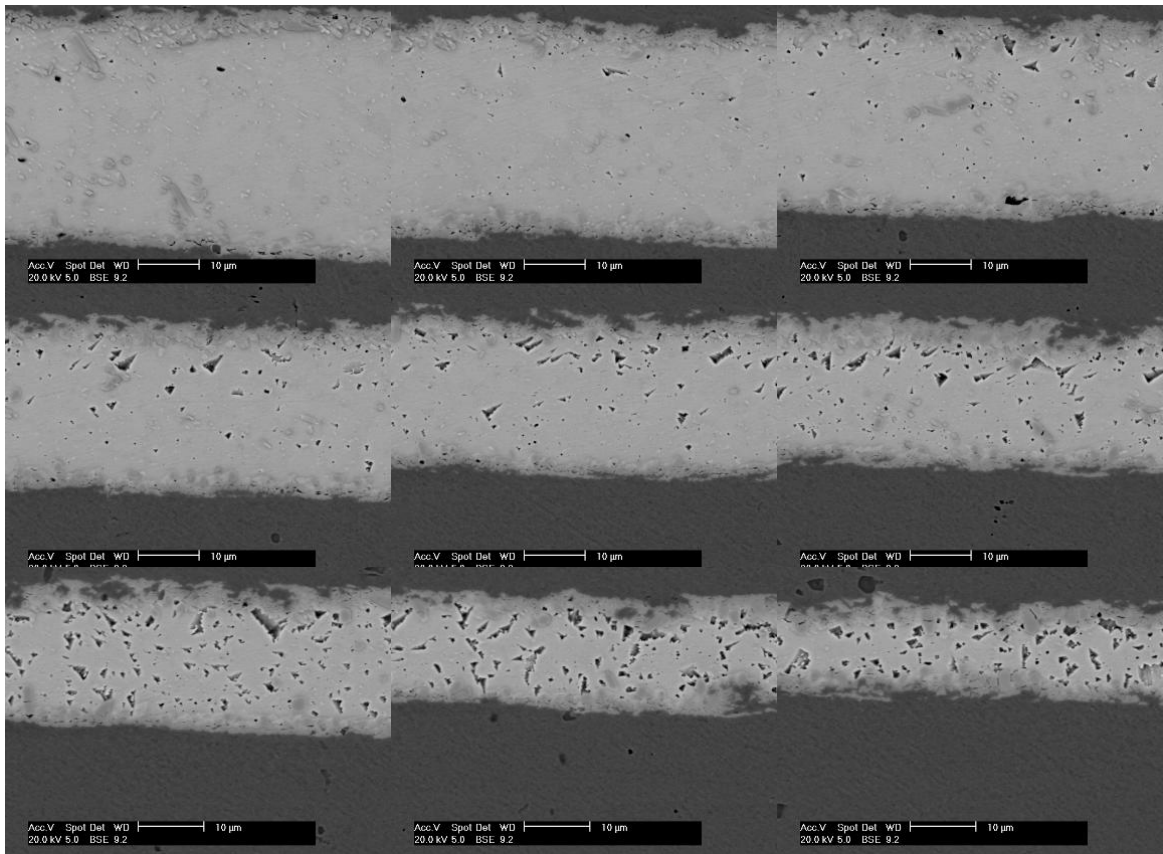


Figure 85. Series of BSE images of a solder joint based on Sn100C alloy (not etched) reflecting dependence of density of CFV on the distance between Cu substrates

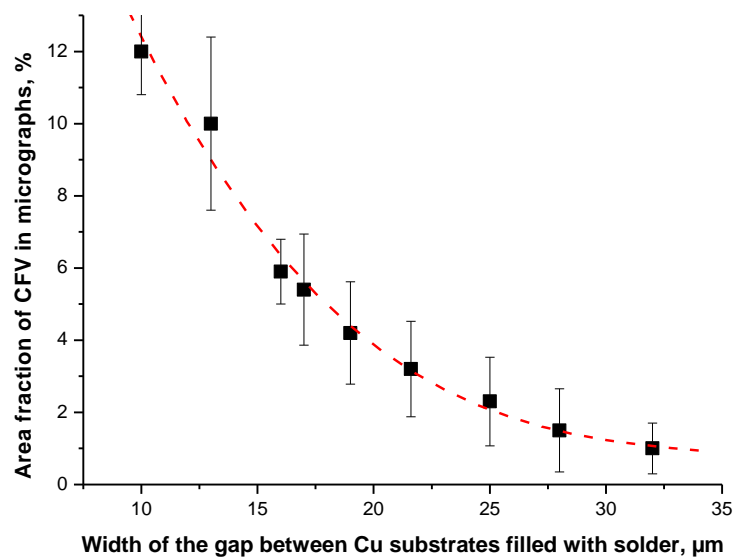


Figure 86. Dependence of CFV formation on distance between substrates in solder-joint

The area fraction of the CFV in the solder-joints was calculated by means of the “IQ Materials” software as described in section 4.5.

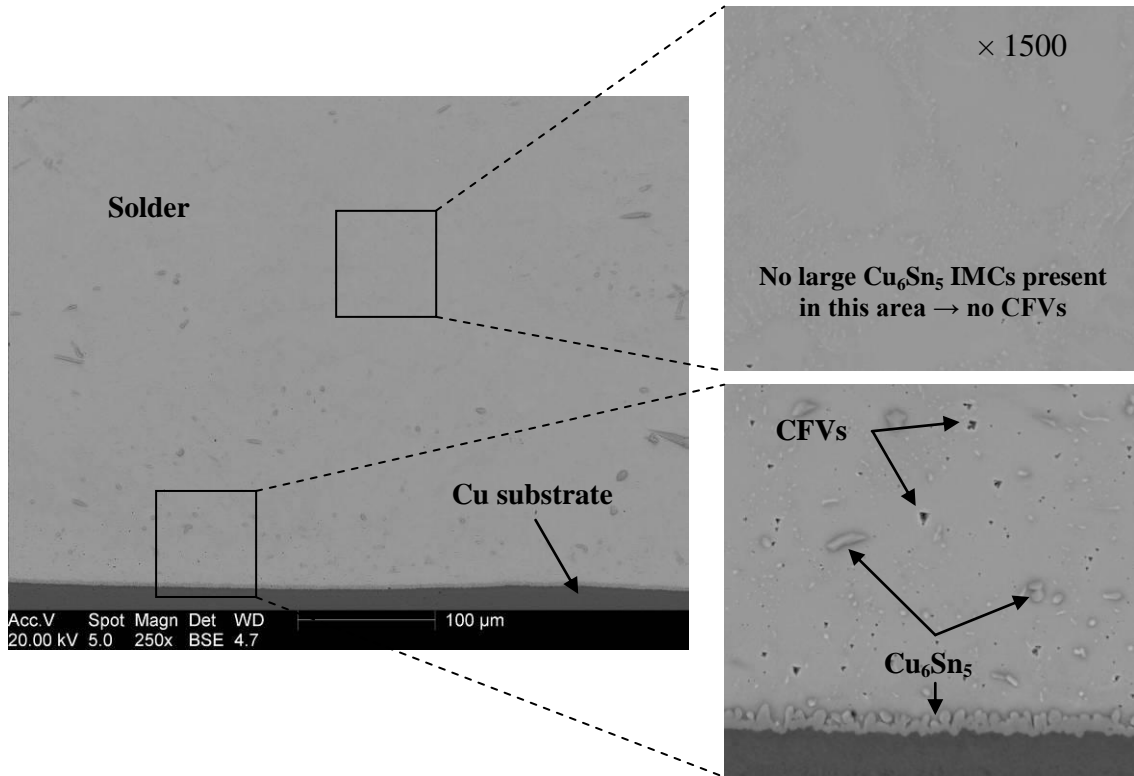


Figure 87. BSE image of a solder joint based on Sn100C alloy (not etched): preferred CFV formation in the volume close to the Cu₆Sn₅ intermetallic phase (Cu₆Sn₅ intermetallic layer and Cu₆Sn₅ bulk precipitates)

The crystallographically-faceted voids tend to form in the areas near the Cu₆Sn₅ interfacial intermetallic layer or close to the bulk Cu₆Sn₅ intermetallic precipitates (figure 84, 87, 88). With Ag₃Sn particles, no such intensive CFV formation was observed. An assumption can be derived that Ag₃Sn phase does not promote the CFV formation, or promotes this phenomenon, but with considerably slower rates compared to the Cu₆Sn₅ phase.

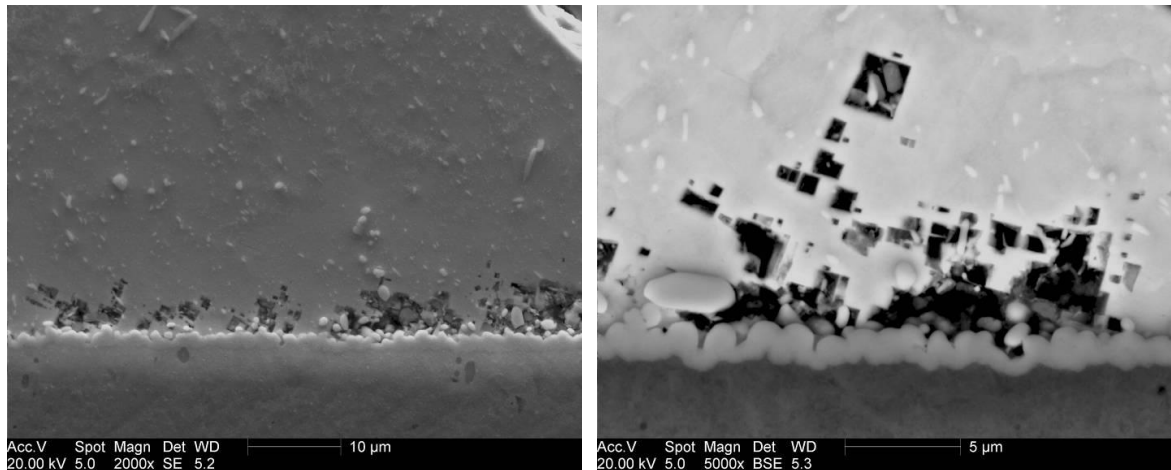


Figure 88. CF void formation on the Cu_6Sn_5 IMC layer – solder interface. Sn100C solder on Cu substrate; not etched; soldering conditions as described in section 4.11.

In order to investigate whether the CF voiding phenomenon is unique for lead-free solders, lead-containing solder-joints were prepared with use of Sn60Pb40 solder and copper plates according to the technique described in section 4.11. The microstructure obtained (figure 89) presents a fine mixture of Sn-rich (dark areas) and Pb-rich (light areas) phases. Due to substrate dissolution and diffusion in molten state, Cu_6Sn_5 intermetallics were found in the solder-joint bulk (figure 89(A)). It was observed that close to the volume of Cu_6Sn_5 IMCs formation, the homogeneity of this mixture decreases and large fractions of Pb-rich phase appear, as part of Sn was used for the Cu_6Sn_5 IMC formation.

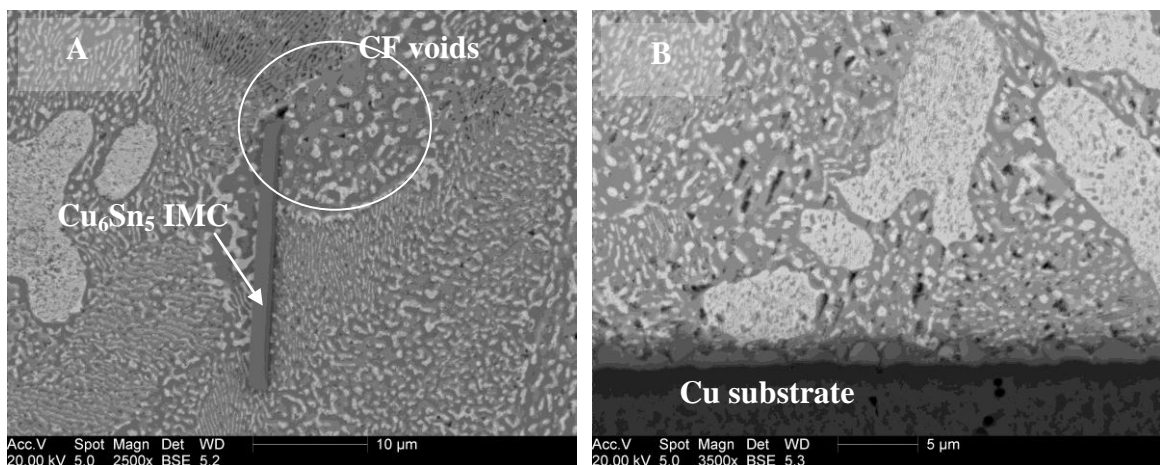


Figure 89. CF voids in a lead-containing solder-joint

The CF voids were observed in these samples locating close to the IMC layer – solder interface and near bulk Cu_6Sn_5 IMCs. The only difference from the lead-free solder-joints is that the CF voids are geometrically limited by the size of Sn-rich phase in the mixture and one may assume that Pb-rich phase will prevent clustering and growth of such voids.

Experiments with pure Sn (99.99) used as solder for joining copper plates exhibited the same results (the samples preparation was carried out as described in section 4.11, Sn (99.99) powder was used instead of soldering paste). The CF voids formation in these solder-joints in ‘as soldered’ state is depicted in figure 90. Again, the area fraction of CF voids was strongly dependent on the distance between Cu substrates, increasing with the distance decrease.

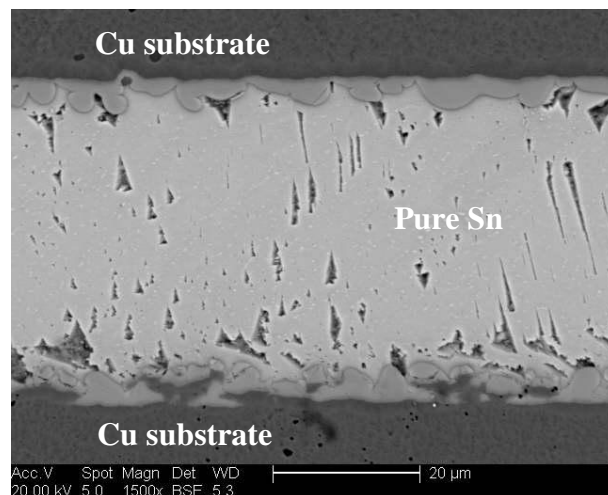


Figure 90. CF voids in a pure Sn based solder-joint

5.4.1.2. Solder joints with ‘thin’ copper substrate (substrate thickness < 50 μm)

While using copper substrates 35 - 50 micrometers thick (printed circuit boards FR4, FR2), the formation of CFV was observed to be retarded and only occasional cases of voids were noted within such type of solder-joints (figure 91). Moreover, in the solder-joints assembled with printed circuit boards, the crystallographically faceted void formation under elevated temperatures (160 °C) occurs much slower compared to the samples

prepared with a ‘massive’ copper substrate. The Cu substrate thickness thus plays an important role in the phenomenon of CFV formation.

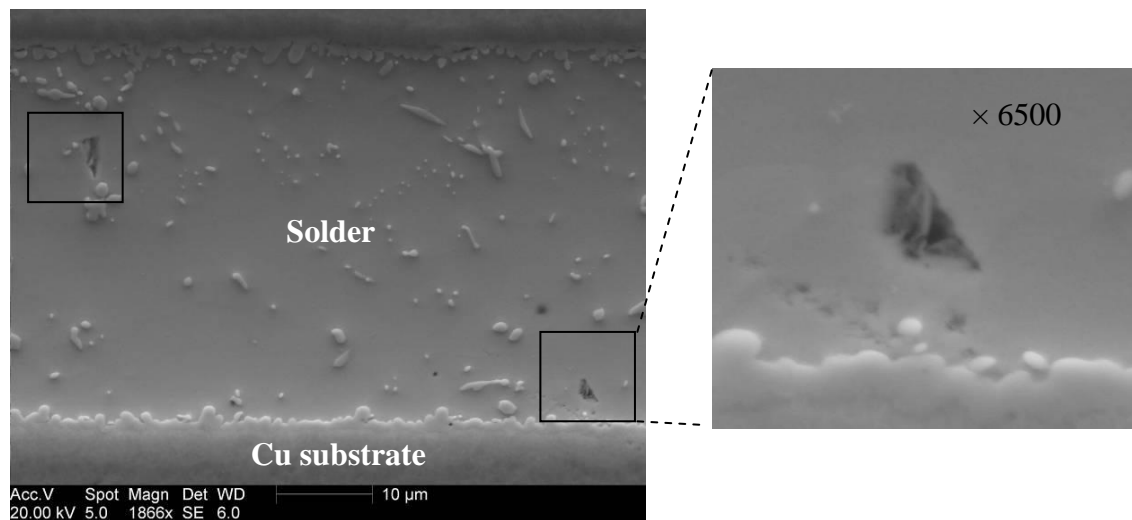


Figure 91. SE image of a solder joint based on SN100C alloy assembled with use of FR4 PCB: occasional CFV are observed

5.4.1.3. Pure bulk Tin (Sn) without substrate

While investigating the microstructure of pure Tin samples obtained by reflowing Tin powder with 99.99 purity under conditions described in section 4.3, the crystallographically-faceted voids were still observed but appeared to be quite rare and no groups of CFV were found (figure 92). They could be found stand-alone through the material bulk and in drastically lower amounts compared to the previous cases.

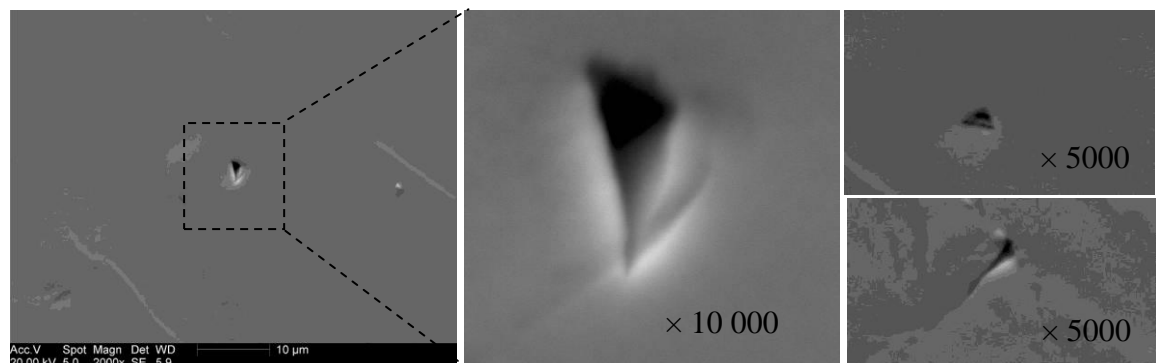


Figure 92. CFV formation in pure Sn (99,99 purity)

5.4.1.4. Bulk SAC, CASTIN and Sn100C solders without substrate

While investigating the microstructure of SAC, CASTIN and SN100C bulk solder samples obtained under conditions described in section 4.3, singular crystallographically-faceted voids were observed with rare cases of grouping. Comparing these alloys, no difference was noted in terms of the quantity and morphology of CFV. The voids were found both in interdendritic regions (in β -Sn matrix) and in β -Sn dendrites (figure 93).

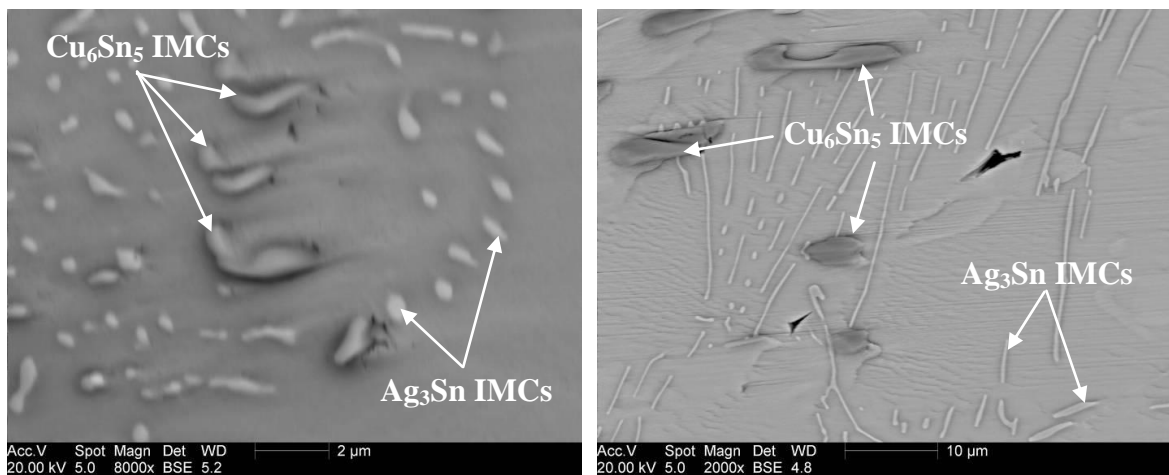


Figure 93. CFV formation in SAC alloy family

5.4.2. Faceted void evolution during solid-state annealing

5.4.2.1. Solder-joints with 'massive' copper substrate (substrate thickness > 10 000 μm)

Subsequent ageing of the samples under conditions described in section 4.10, resulted in more copious CF voids formation, their clustering and growth. It noteworthy that CV voids were always found to develop more intensively near the Cu₆Sn₅ intermetallics in the solder bulk or near the interfacial IMC layer on Cu substrates (figures 94, 96, 97, 98).

Figure 94(B) shows that the CF voids preferably developed near the biggest scallop of the intermetallic layer. Further ageing resulted in clustering of the voids into a large macro-void propagating along the interface with the intermetallic layer (figure 94(C)).

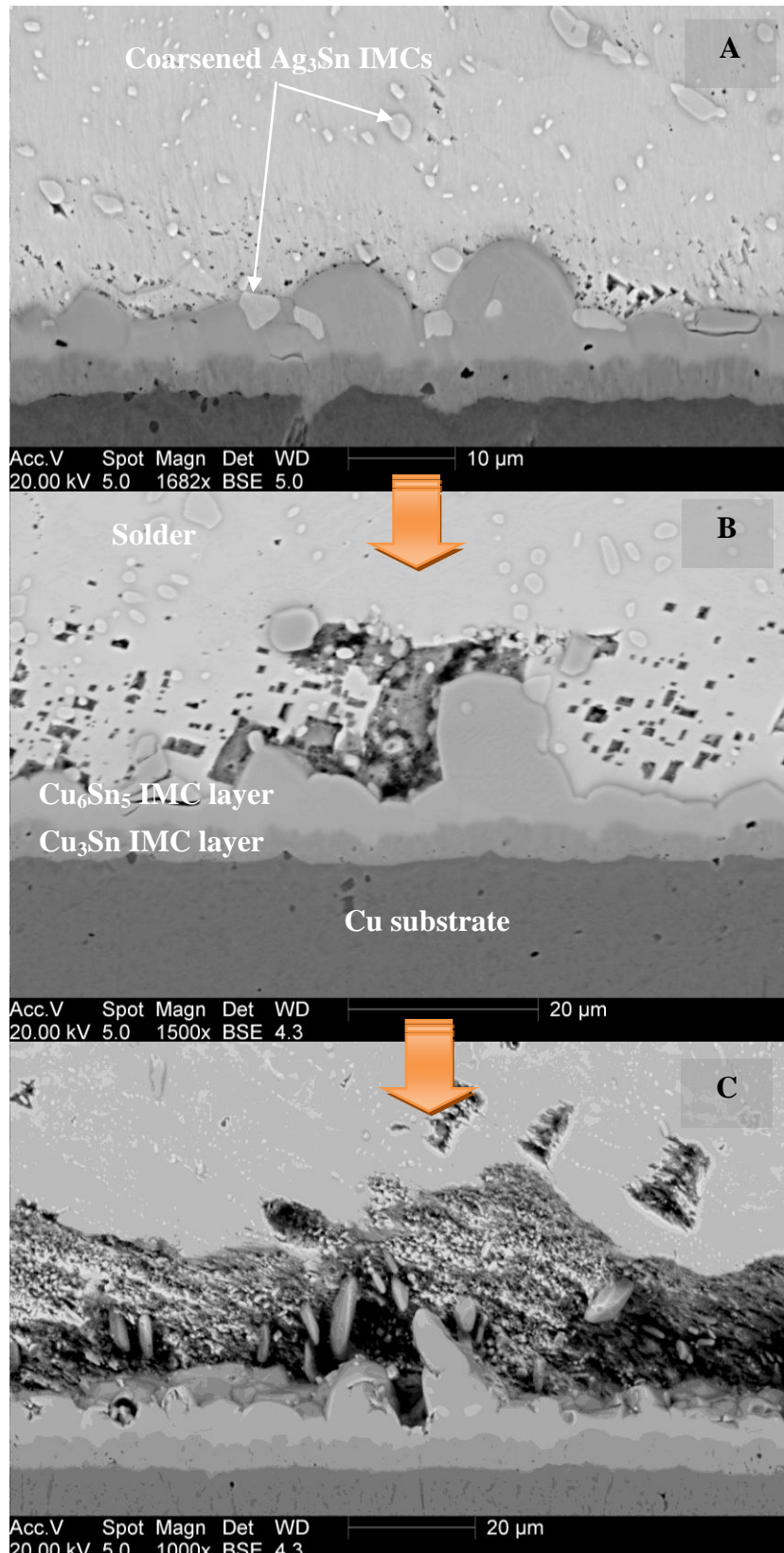


Figure 94. CF voids development at the near-interface region: (A) – 1800 hours of ageing; (B) – 2700 hours of ageing; (C) – 4200 hours of ageing (solder – SAC405)

Solid-state ageing resulted in growth of the intermetallic precipitates Cu_6Sn_5 and Ag_3Sn in the bulk of the β -Sn matrix. The interfacial intermetallic layer also showed development (figure 95), separating it into two sub layers: Cu_6Sn_5 and Cu_3Sn . The chemical composition of those was proved by the Energy Dispersive X-Ray analysis. The Cu_6Sn_5 part of the IMC layer developed faster compared to the Cu_3Sn one (figure 95(A)) during the beginning of ageing. The IMC layers width was calculated as the average height of the Cu_6Sn_5 and Cu_3Sn scallops in a micrograph. The IMC layer growth rate decreases with the increase of the annealing duration. Simultaneously with the IMC layer development, the adjacent CF voids exhibit clustering and growth. The area fraction of the CF voids in the near-interface region as the ageing time increases is depicted in figure 95(B).

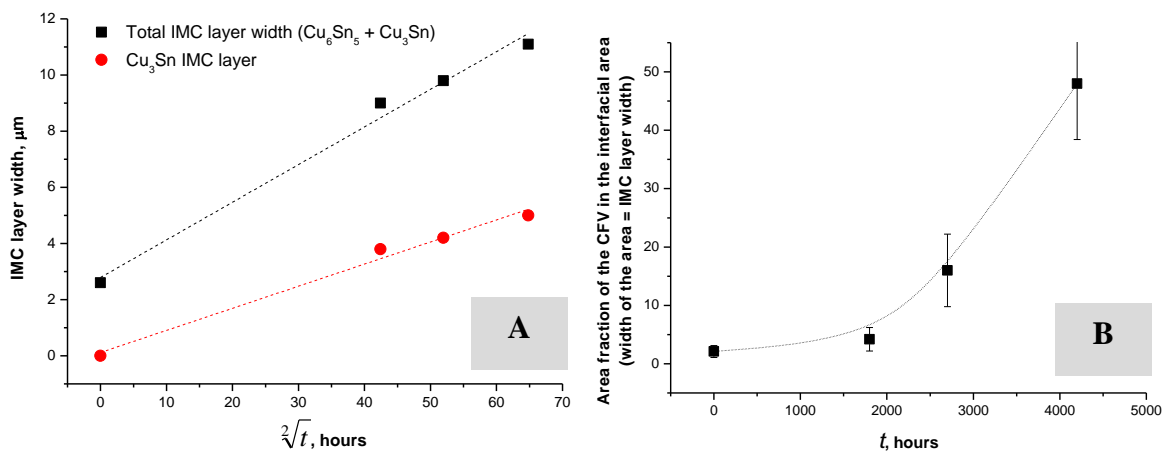


Figure 95. (A): kinetics of the IMC layers growth and (B): area fraction of the CF voids in the near-interface region as the ageing time increases; t is annealing duration in hours

However, the clustered macro-voids did not propagate along the interface with the Cu_6Sn_5 IMC layer uniformly. Further cross-sectioning into the bulk showed that there were regions with no clustered macro-voids (figure 96).

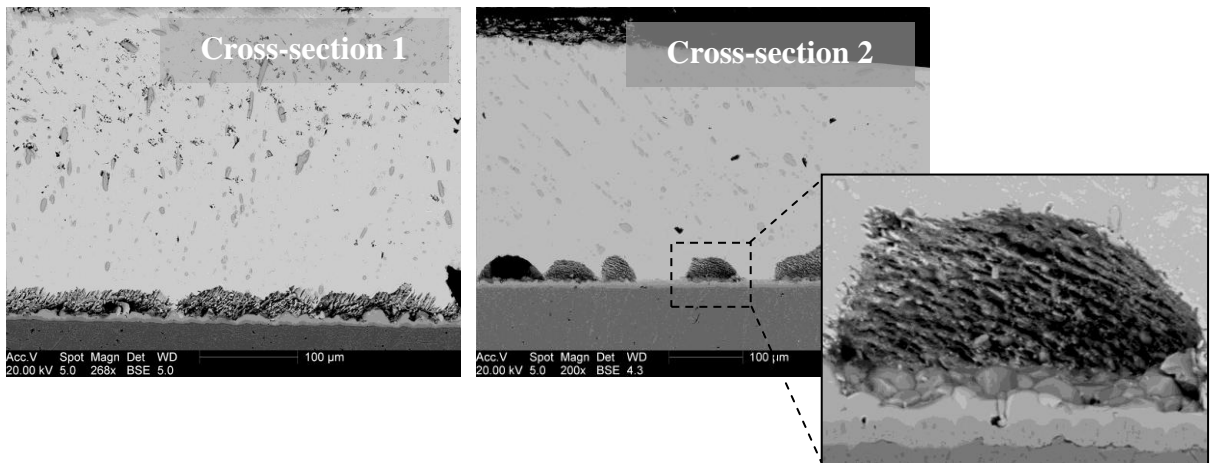


Figure 96. CF voids development at the near interface region after 4200 hours of ageing
(solder – SAC405)

Investigations of the bulk of the β -Sn matrix showed preferable CF void development in the areas adjacent to the IMC precipitates (figure 97) and their development as the ageing time increased (figure 98).

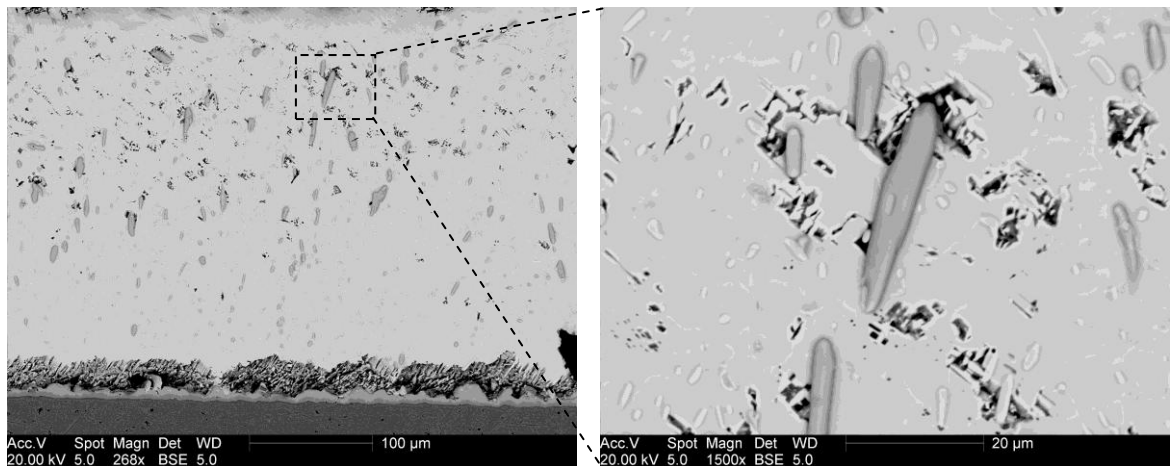


Figure 97. CF voids development in the SAC405 solder bulk after 4200 hours of ageing

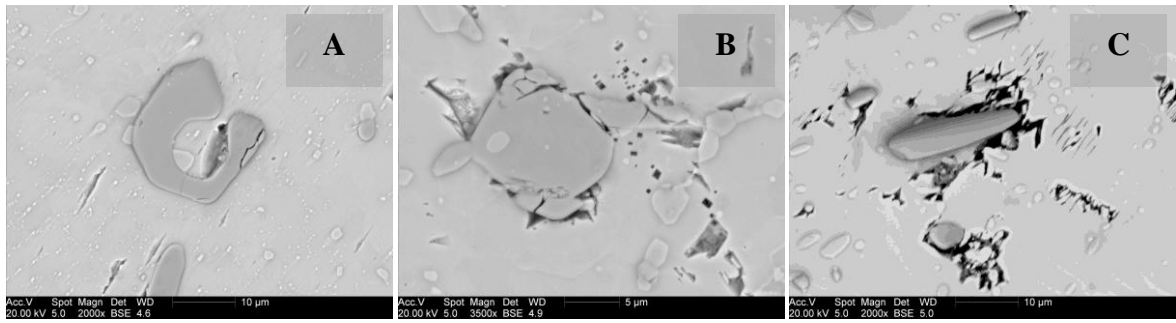


Figure 98. CF voids development in the SAC405 solder bulk after: (A) 1320 hours of ageing; (B) 1800 hours of ageing; (C) 4200 hours of ageing

As mentioned above, depending on the plane of the solder-joints cross-sectioning, different shapes of the voids were observed. They were always found to form in correlation with the β -Sn matrix crystallographic structure: as β -Sn has a body-centered tetragonal crystal lattice, the CF voids were always observed to form in a shape of tetragon (figure 99(A)) or in a shape of clustered tetragons (figure 99(B)). For more images of CF voids formed in the bulk, see appendix 2.

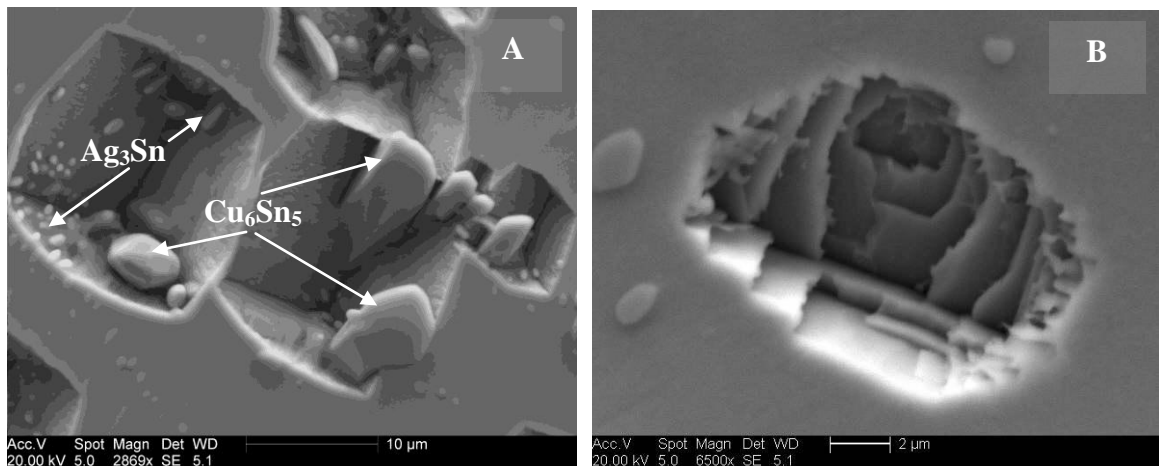


Figure 99. SE images of solder-joints assembled with SAC405 soldering paste, subjected to annealing at 160 °C for 3720 hours. Cross-sections were not etched before the analysis

5.4.2.2. Solder joints with 'thin' copper substrate ($< 50 \mu\text{m}$)

The most repeatable pattern of microstructural evolution with the CFV formation was shown with the solder-joints assembled with use of printed circuit boards FR4 with copper metallization of $50 \mu\text{m}$. In 'as soldered' state only just a few cases of CF voiding were noted (figure 91), whereas during solid-state ageing at $160 \text{ }^\circ\text{C}$ they were observed to form intensively as annealing was progressing (figure 100). Simultaneously with void development, the Cu_6Sn_5 and Cu_3Sn intermetallics in the bulk and in the IMC layer drastically increased their volume fraction (figure 101).

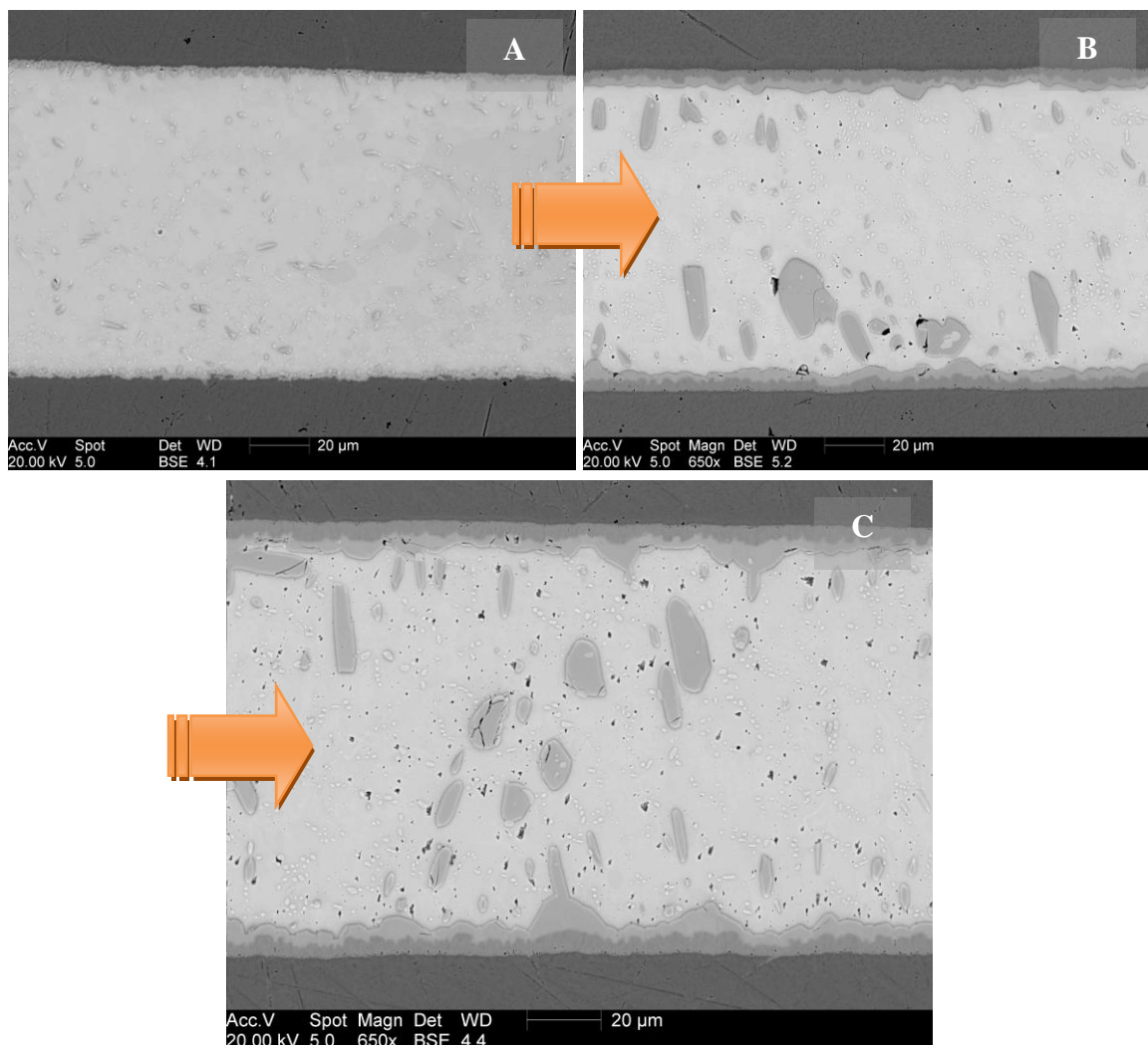


Figure 99. Cross-sections of a solder-joint: (A) – as soldered state; (B) – 1800 hours of ageing (C) – 4200 hours of ageing (SAC405 soldering paste)

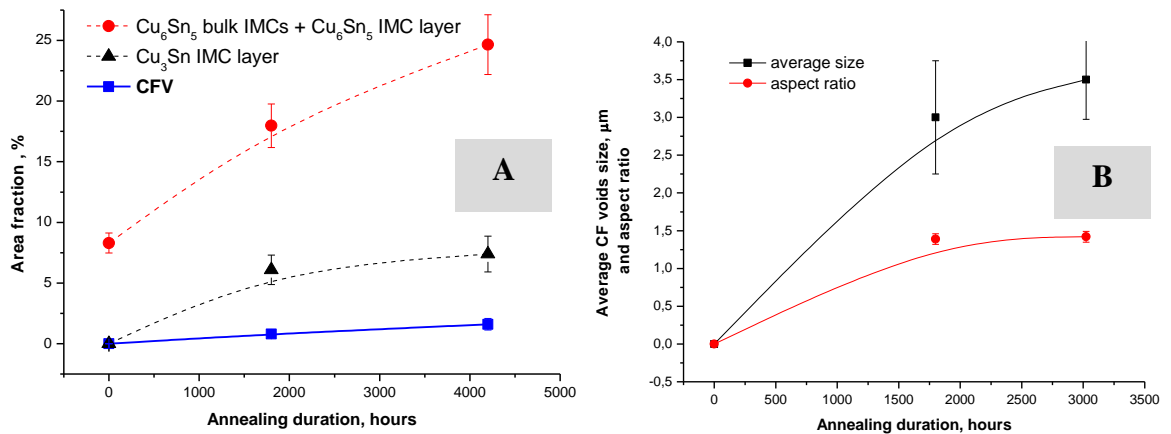


Figure 101. (A): area fraction of IMCs and CFVs and (B): increase of the average CFV size as annealing progresses (SAC405)

The aspect ratio of CFV depends on the mutual orientation of the cross-section plane and β -Sn grain orientation.

5.4.2.3. Bulk solders without substrate

It was observed during investigation of the annealed lead-free bulk solders that CF voids form quite rarely compared to their development in solder-joints, but they are still present. They spread through the bulk randomly, but are always found to locate near the Cu_6Sn_5 intermetallics (figure 102).

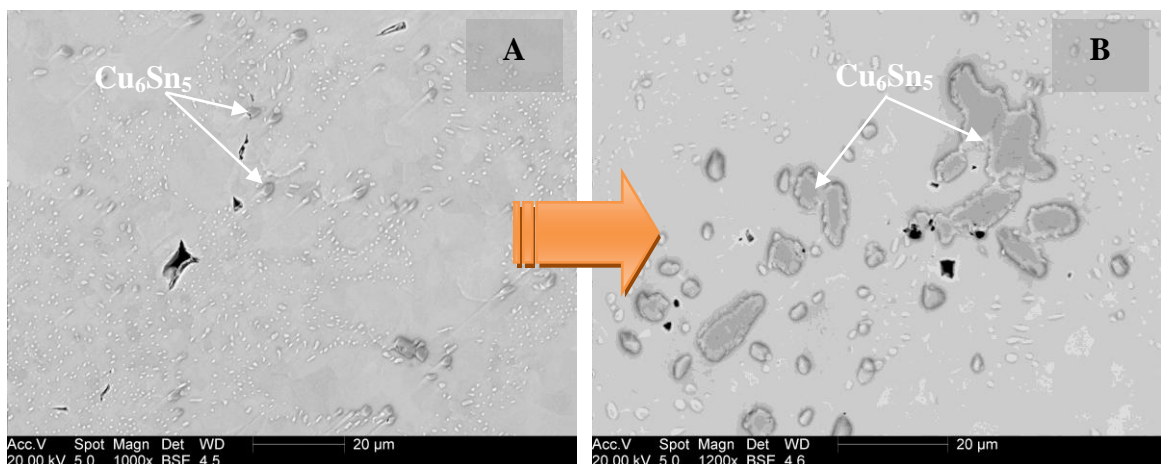


Figure 102. Cross-sections of bulk solders SAC405: (A) – 1800 hours of ageing; (B) – 4200 hours of ageing

Considering the maximum quantity of the CF voids found in bulk materials near the intermetallics as the annealing duration increases, the graph depicted in figure 103(A) was plotted. It noteworthy, that the maximum number of CF voids found near IMCs in the solder bulk increases simultaneously with the average IMC's size increase (figure 103(B)).

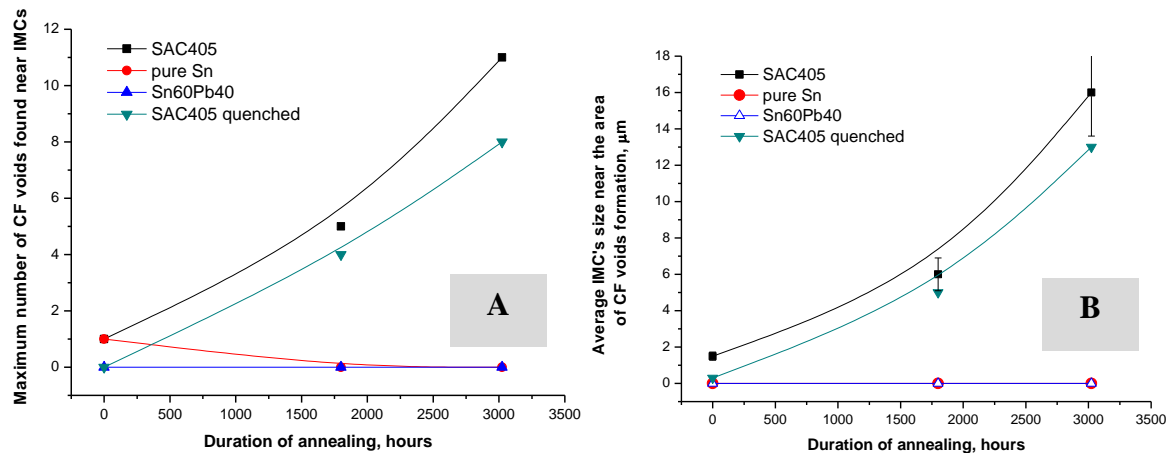


Figure 103. (A): maximum number of CF voids found near IMCs and (B): average IMC's size near the area of CF voids formation, mm

As can be seen from the data collected, bulk Sn and bulk Sn60Pb40 samples were not affected with CF voids formation, whereas, SAC405 alloy have these voids even in initial state. In quenched SAC405 solders (in water medium with cooling rate of $1710\text{ C}^\circ/\text{sec}$) no CF voids were observed in “as soldered” state (figure 104(A)). The average Cu_6Sn_5 and Ag_3Sn intermetallic size in those in their initial state did not exceed $0,3\ \mu\text{m}$. However, subjected to the following annealing, quenched samples showed rapid IMC precipitate growth (figure 104(B)) and subsequent CF voids formation, with their quantity increasing as the ageing progressed (figure 103(A)).

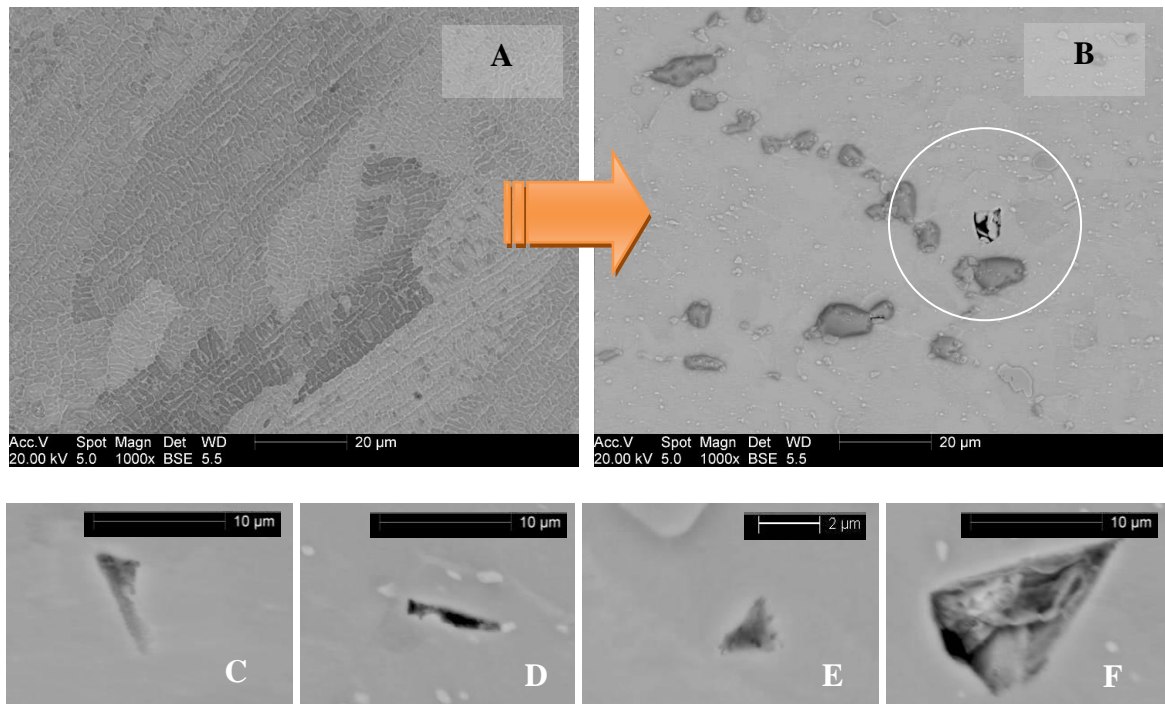


Figure 104. (A): BSE image of quenched SAC405 alloy before annealing (B): BSE image of the sample after aging for 1800 hours at 160 °C; (C-F): CFVs in annealed samples.

Brief summary of the experimental results

Investigations coupled with advanced characterisation techniques (Field Emission Gun Scanning Electron Microscopy and Electron Backscattered Diffraction) revealed a strong dependence of the lead-free alloys' microstructure on their composition and solidification conditions. Lower amounts of alloying elements (such as Ag content less than 2.5% in CASTIN and SN100C alloys) result in increase of solder microstructural integrity.

Solidification conditions (cooling rates, ultrasound) modify the geometry and distribution of intermetallic precipitates (IMCs) and β -Sn dendrites. For instance, a cooling rate of 24 °C/sec (SAC405 alloy) lowered the maximum IMC needles length to 2 μ m compared to 44 μ m at 1 °C/sec. Ultrasound at 30 kHz increases the microstructural homogeneity of bulk

solders and lowers the amount of undercooling (from 24 °C to 7 °C for SAC 405 alloy).

However, some of these conditions cannot be implemented in real production.

It was shown that ultrasound deteriorates the strength characteristics of a solder-joint due to the intensification of the interfacial diffusional process. This results in more intensive growth of the interfacial IMC layer. The solder-joint tensile strength is highly dependent on the interfacial IMC layer which has an optimal width of approximately 2µm.

Thermal-cycling revealed a difference in the microstructural evolution and fracture mechanism of both lead-free and lead-containing solder-joints. Tensile strength experiments showed that in the lead-free cycled samples fractures move from the substrate interface into the solder bulk, propagating intergranularly. An average 7% strength reduction was obtained for lead-free samples subjected to 100 thermal cycles. Lead-free solders appeared to be more resistant to thermal-cycling loads due to lower amount of grains within a solder-joint: lead-free solder-joints were observed to consist from 1 to 10 β-Sn grains, whereas lead-containing ones comprised of up to 96 grains. 150 thermal-cycles resulted in crack initiation in lead-containing solder-joints, whereas lead-free ones exhibited only slight changes on the grain boundaries.

Ageing resulted in rapid coarsening of a solder-joint microstructure and preferable IMCs growth along the β-Sn grain boundaries. The interfacial IMC layer separates into two strata: Cu₃Sn and Cu₆Sn₅ as it develops into the solder.

It was shown that IMC layers grow as scalloped layers during reflow as $\sqrt[3]{t}$ (where t is reflow time) and as a layer during annealing as $\sqrt[2]{t}$ (where t is annealing time).

The growth rate of the IMC layer is highly dependent on alloy composition. The solder-joints based on SN100C solder (0.05% Ni) exhibited almost twice lower interfacial IMC layer growth rate compared to SAC alloys (no Ni additions).

Crystallographically-faceted voiding (CFV) was observed in solder-joints in the 'as soldered' state and during subsequent ageing. The voids were found to be strongly dependent on the width of Cu substrate. It was observed that the volume fraction of the CFV is also highly dependent on the distance between Cu substrates. Greater distances between Cu substrates result in a decrease in CFV volume fraction.

It was shown that the CFV volume fractions with the thin substrates are associated with IMC particles and IMC layers, which can be explained by the shrinkage model. The large CFV fractions observed in the massive substrates are too large to be solely explained by this model.

6. DISCUSSION

Microstructure investigations of lead-free solders

Alloy composition influence on solder microstructural features

Light microscopy studies coupled with FEGSEM investigation revealed microstructural features of lead-free alloys (alloy compositions are shown in section 4.1).

It was shown that the microstructure of Sn-rich alloys is represented by β -Sn dendrites decorated with the eutectic phase. The eutectic phase is a mixture of Ag_3Sn and Cu_6Sn_5 precipitates entrapped into the β -Sn matrix. The composition of the intermetallic precipitates was justified by EDX analysis and was consistent with the results of previous investigations [9].

Comparing microstructures of the SAC alloys, clustering of Cu_6Sn_5 intermetallics was noted, while the Ag_3Sn intermetallics were spread uniformly in the interdendritic regions. The clustering effect depends on the Ag weight fraction in SAC alloys. At higher Ag content of 4% (SAC405), the IMC precipitates Cu_6Sn_5 tend to cluster to a larger extent compared to the alloy composition comprising 3% of Ag (SAC305). In addition to clustering, Cu_6Sn_5 IMCs increase in size in the SAC405 system (figure 38). Knowing the solidification sequence for Sn-rich alloys described in paragraph 2.2.1, it can be surmised that these are the pro-eutectic Cu_6Sn_5 IMCs which tend to cluster upon solidification.

The probable explanation of this phenomenon could be that the higher the Ag content in the alloy the further away the composition moves from the system's eutectic point and hence, the melting temperature rises. This results in 'pasty range' growth (the difference between solidus and liquidus temperature for a fixed alloy composition). The larger the 'pasty range' (8 °C for SAC405 compared to 3 °C for SAC305), the higher the possibility of segregation of pro-eutectic intermetallic phases of considerable size in the early

solidification stages. Presumably the pro-eutectic Cu_6Sn_5 IMCs tend to cluster upon solidification.

It is noteworthy that no clustering was observed for the CASTIN (2,5% Ag) and SN100C (0% Ag) alloys. The IMCs Cu_6Sn_5 were found to be spread uniformly across interdendritic regions for these compositions. However, for the CASTIN alloy the Cu-based precipitates were observed to form on a larger scale, compared with SAC and SN100C ones. The CASTIN differs from the SAC family by the presence of the Antimony in the alloy composition. The Antimony forms a series of intermetallic precipitates with the other chemical elements of the alloy: Sn and Cu, but none of those were found during the investigation. Presumably, their quantity is too low due to low amount of Sb in the system (0.5%). The only IMC particles found during investigation were Cu_6Sn_5 and Ag_3Sn .

Subsequent etching with light microscopy and BSE analysis of CASTIN samples revealed a non-uniform distribution of Sb through the solder sample volume (figure 39).

During investigation of the three-dimensional morphology of IMC particles formed within lead-free solder-joints, it was found that the development of large (pro-eutectic) Ag_3Sn IMCs is highly dependent on solder composition. Thus, they were found in solder joints based on SAC405 and SAC305 soldering pastes (with Ag content 4% and 3% respectively) on the Cu substrate interface, whereas, CASTIN solder with a Ag content of 2,5% did not show any evidence of pro-eutectic Ag_3Sn IMC formation. For Cu_6Sn_5 pro-eutectic IMCs, segregation was found to be promoted by Copper substrate dissolution during its reaction with molten solder, which served as a supplementary source of Cu in addition to Cu content in solder composition (0.5% for SAC305 and SAC405; 0.7% for SN100C and 0.8% for CASTIN alloys). Nevertheless, large Cu_6Sn_5 pro-eutectic IMC compounds were also found in bulk solders without Cu substrates if the cooling rates were less than 1 °C/sec.

The three-dimensional morphology of Ag_3Sn IMCs can be described as leaf-like platelets. It was found that the large Ag_3Sn platelets grow at the developing front of the interfacial intermetallic layer on a substrate and the voids (see appendix 3). It is worthwhile to note that large Ag_3Sn platelets usually have voids in the middle. These voids were presumably formed by dissolved gases and flux residues in the molten solder and could provide nucleation sites for Ag_3Sn IMCs [82]. Figure 3.1(D) of the appendix 3 shows preferable growth of the large pro-eutectic Ag_3Sn IMCs on the walls of a macro-void, which supports the assumption about void efficiency as nucleation site for Ag_3Sn IMCs .

The three-dimensional morphology of large pro-eutectic Cu_6Sn_5 IMCs in SAC alloys was found to be of two kinds: needle type whiskers and hollow-type hexagonal faceted whiskers (see appendix 3, figure 3.2). Frear et al. [85] argued that the large pro-eutectic Cu_6Sn_5 precipitates can grow by a screw dislocation mechanism from the Cu substrate, and that the hollow part of the whiskers could be a result of the core dissolution caused of its high energy, which later fills with molten solder, as the whisker grows into the β -Sn matrix. Large pro-eutectic Cu_6Sn_5 IMCs were also found in solder bulk. They should have a different formation process, presumably caused by supersaturation in the high-Cu content solder.

At the same time, in the CASTIN alloy Cu_6Sn_5 pro-eutectic IMC particles were found to segregate in an irregular shape which differs from ‘whiskers’ of SAC alloy family (see appendix 3, figure 3.3). Presumably small additions of Sb and the lower amount of Ag (2.5%) in the composition affects the process of the IMC nucleation and growth. Additionally, the amount of undercooling for the CASTIN alloy is considerably lower compared to that for SAC alloys (as it was shown in section 5.1.3. of the present work), which could provide a different path of development for the pro-eutectic Cu_6Sn_5 IMCs,

since the reduced undercooling brings a kinetic limitation upon pro-eutectic IMC segregation.

It is noteworthy that, despite the fact that CASTIN alloy has 2.5% of Ag in its composition, the pro-eutectic Ag-based intermetallics were not found. Apparently all of Ag_3Sn intermetallic particles form in the latest stages of solidification during the eutectic reaction, since they were found to be uniformly spread in the interdendritic regions and had the same size (appendix 3, figure 3.4). The probable explanation for this fact again could be the reduced amount of undercooling before crystallization compared to the SAC alloy family. Thus, the reduced amount of undercooling would kinetically reduce the possibility of large pro-eutectic Ag_3Sn intermetallic precipitate segregation.

The large intermetallic precipitates affect microstructural integrity of solder-joints and, consequently, their mechanical stability in stress conditions (figures 44 and 45). Therefore, it is necessary to limit the possibility of their formation by lowering the Cu and Ag content in solder alloys and decreasing the amount of the undercooling, which can be achieved by the addition of minor alloying elements such as Sb, Zn etc. [9]. Fast cooling rates can also suppress large pro-eutectic IMC formation.

Cooling rate influence on solder microstructure

Cooling rates in real production can vary from 2 to 0.25 °C/sec, depending on the thermal-profile recommended by the solder manufacturer and the thermal mass of the components being soldered. Faster cooling rates can result in stress accumulation in the solder-joints, printed circuit boards and component packaging (due to CTE mismatch), which will increase the probability of failure during the electronic device service life.

As was shown in the present work, the solder-joint microstructure (in particular IMC phase formation) is strongly affected by the cooling rates. Fast cooling rates limit kinetically the

time duration for the IMCs to segregate within and result in finer branching of the β -Sn dendrites and more uniform distribution of the intermetallic particles in the interdendritic regions. For instance, in the solder-joints solidified with a cooling rate of 24 °C/sec, the fine β -Sn dendrite structure was well developed and no pro-eutectic phases were noted. On the other hand, Cu_6Sn_5 and Ag_3Sn IMCs are the major hardening agents dispersed in the eutectic phase and a rapidly cooled microstructure is expected to have higher strength and, consequently, higher resistance to creep deformation, shortening a solder-joint thermal-fatigue life [9]. In contrast, moderate cooling rates (less than 1 °C/sec) promote large pro-eutectic IMCs formation in the early stages of solidification, diminishing the quantity of Cu and Ag that can form intermetallic precipitates in the later solidification stages and that can be incorporated in the interdendritic regions. Hence, moderate cooling rates lower the dispersion-hardening effect of the interdendritic zones.

In view of the above, one may conclude that cooling rate optimization is a complicated issue since a vast number of variables is involved. Lowering the amount of alloying elements (Ag and Cu) could be an effective approach in terms of suppressing the intermetallic phase formation and improving solder-joint microstructural homogeneity, rather than cooling rate increase. However, reducing the amount of the alloying elements will result in an increase in the melting temperature of the system, which is undesirable from a technological point of view.

Ultrasound modification of solder microstructure

In the present study an attempt was undertaken to modify the microstructure of lead-free solder by the introduction of an ultrasound field during its solidification. The supposition for this challenge was the lack of information concerning the influence of ultrasound on the solidification processes in solders, but a vast amount of information about ultrasound

microstructure optimization is available for the casting industry, particularly concerning Al-based alloys. It has been reported by various investigators [63, 64, 79], that ultrasound implementation during crystallization promotes microstructural refining, which could be positive in terms of the homogeneity of solder-joints. The challenge was therefore to investigate the influence of an ultrasound field on IMCs formation.

The introduction of ultrasonic energy causes many nonlinear effects in a molten system, such as acoustic cavitation, acoustic streaming and radiation pressure, which could influence the solidification process drastically [79].

The first phenomenon observed, while carrying out experiments of bulk solders crystallization within an ultrasound field, was a decrease in the amount of undercooling required for solidification. This brings kinetic restrictions on the development of large pro-eutectic IMC (section 5.1.3.1). The typical amount of undercooling for SAC solders in conventional conditions was found to be about 24 °C (figure 51), whereas ultrasound of 30 kHz decreases this to 7 °C. CASTIN solder showed considerably smaller amounts of undercooling: 16 °C in case of solidification without ultrasonic influence and about 1 °C for ultrasound of 30 kHz. Thus, ultrasound promotes the crystal nucleation within the melt and prevents its further undercooling. Presumably, this phenomenon can be explained by the cavitation effect (section 2.7): small bubbles filled with gas, vapor or their mixture form within the liquid in consequence of local pressure drops caused by travelling acoustic waves of high intensity. The bubbles form during the wave's half-period of rarefaction. These bubbles represent unstable formations and can collapse during the wave's half-period of compression, producing a shock wave and consequently producing high pressure regions [79]. According to the Clausius-Claperon equation (3), the melting temperature of an alloy is proportional to the pressure applied:

$$T_m = T_n + \frac{T_n \Delta V}{\Delta H_m} (P - P_0) \quad (3)$$

where T_n is the melting point at the atmospheric pressure, P_0 . ΔV and ΔH_m are the volume change and enthalpy change during liquid-solid transformation, respectively. Consequently, in the high pressure regions the local melting temperature elevates, which increases the probability of undercooling and nucleation [79].

Hence, the ultrasound vibration implementation in combination with optimization of solder alloy composition can lower the amount of undercooling drastically, shifting it down to negligible values. This is a desirable effect in terms of inhibition of pro-eutectic IMC phase formation.

For solder compositions SAC405, SAC305 and CASTIN ultrasound promotes finer and more isotropic structure formation, causing the formation of a large number of equiaxed randomly-oriented grains (figure 52). It also promotes more uniform distribution of IMC particles (figure 54) in the solder bulk and lowers the amount of eutectic phase (figure 53). As mentioned above, the excessive formation of the eutectic phase shortens a solder-joint thermal-fatigue life due to hardening effect. Consequently, the decrease in its formation would be a desirable result.

Nevertheless, despite all the positive effects that ultrasound brings during bulk crystallization, refining the resulting microstructure, ultrasound deteriorates strength characteristics of solder-joints, causing more intensive diffusional processes at the substrate interface and promoting the dissolution of the substrate into the molten solder, which results in excessive intermetallic layer formation (figure 55). It is the interfacial intermetallic layer that largely defines the solder-joint strength characteristics (see below).

Dependence of solder-joint tensile strength on IMC layer width

In the present study intermetallic layers with different widths (0.7 – 10 μm) were grown on Cu substrates (as described in section 4.8) in order to estimate the resulting strength characteristics of a solder-joint. Soldering pastes SAC305, SAC405 and SN100C were used for this purpose. Reflow time duration was used as an instrument of controlling the IMC layer thickness.

A typical microstructure in investigated samples was observed to be a layer of Cu_6Sn_5 IMCs over Cu substrate (figure 57). The Cu content in the molten solder along the substrate interface is relatively high and may be close to the limits of solubility. During solidification process, the concentration of Cu in the interface region meets the limit and Cu begins to precipitate locally forming the Cu_6Sn_5 IMC layer. Since the heterogeneous nucleation needs lower activation energy [86], precipitation starts on the substrate surface and the layer develops into the solder volume. Having formed over the Cu substrate, the intermetallic layer tends to separate into two sub-layers with formation of fine Cu_3Sn stratum as the reflow time increases. However, the growth rate of the Cu_3Sn layer is slower than that of Cu_6Sn_5 . For the SN100C alloy it was obtained that the IMC layer development of both compositions Cu_6Sn_5 and Cu_3Sn is considerably retarded compared to that for SAC alloys (figure 60(A)). This is consistent with previous investigations [87, 88].

It was shown that IMC layers grow as scalloped layers during reflow as $\sqrt[3]{t}$, where t is reflow time (figure 60(A)).

The IMC layer development is considered to be a good indicator of metallurgical bonding, since the solder-joint would be hold in place only due to Van der Waals forces and surface tension in absence of the intermetallic layer [89].

Nevertheless, it was observed that Cu_6Sn_5 intermetallics are quite brittle and having developed to a considerable size (approx. 10 μm), tend to crack during solidification

(presumably due to the large difference of CTE with the β -Sn matrix) as shown in figure 58, 61. This consequently will bring the weakening of solder-joint, which was proved experimentally (figure 60(B)).

The tensile strength testing showed deterioration of solder-joint performance with the IMC layer width increase. Insufficient intermetallic layer development also decreases solder-joint tensile strength. There is an optimal width of the interfacial intermetallic layer of about 2 μm , which corresponds to the maximum tensile strength and can be obtained by narrowing the reflow time down to the 30 - 60 seconds range depending on alloy composition and peak reflow temperature (figure 60).

Reflow time in the real production line can be 45 - 90 seconds depending on the features of the soldering paste being used and thermal mass dispersion of the components being soldered. Based on the experimental data obtained, one may suppose that reduction of dwelling time would be quite desirable in order to improve solder-joint mechanical performance. However, this is a very delicate issue when it concerns the real production as far as many factors affecting the process are involved (condition of the surfaces to be soldered, considerable thermal mass of some components etc.).

Microstructural transformations within solder joints

Microstructural transformations during thermal-cycling

Microstructure development within lead-free solder joints during thermal-cycling load conditions and its impact on solder strength characteristics were investigated. This evaluation is of high interest, since in service, solder-joints are being constantly subjected to the thermal-cycling conditions corresponding to the environmental temperature variations or 'power on-of' cycling. In this study solder-joint specimens were subjected to

the extreme cycling conditions with the temperature range of $-40 - +150$ °C as described in section 4.9.

First of all, it is worthwhile to note that the β -Sn phase, which comprises more than 95% in solder alloys being investigated, has highly anisotropic properties. The most important of those in the thermal-cycling environment is anisotropy in the coefficient of thermal expansion (CTE). Thus, at 30 °C, the thermal expansion coefficients in the principal directions are $\alpha_{[1\ 0\ 0]} = \alpha_{[0\ 1\ 0]} = 16.5 \times 10^{-6} \text{ K}^{-1}$ and $\alpha_{[0\ 0\ 1]} = 32.4 \times 10^{-6} \text{ K}^{-1}$ [83]. This means that the thermally-stressed β -Sn grain boundaries will serve as sources of crack initiation due to largest stress localization caused by the β -Sn thermal anisotropy. The CTE of Cu substrate is $16.5 \times 10^{-6} \text{ K}^{-1}$ [83], which perfectly fits with β -Sn CTE in two principal directions and differ drastically (about 50%) in the third one (table 12).

<i>Elements/Solders</i>	$\alpha/(10^{-6} \text{ K}^{-1})$						
	100 K	200 K	293 K	500 K	800 K	1100 K	1500 K
Copper ^[90]	10.3	15.2	16.5	18.3	20.3	23.7	–
Lead ^[90]	25.6	27.5	28.9	33.3	–	–	–
Silver ^[90]	14.2	17.8	18.9	20.6	23.7	27.1	–
Tin* ^[90] Crystallographically anisotropic	16.5	19.6	22.0	27.2	–	–	–
Solders		-70 °C	20 °C	140 °C			
Sn-37Pb (eutectic) ^[91]		24.0	24.0	24.0			
Pb-10Sn ^[91]		27.8	28.9	30.5			
Sn-Ag-Cu (eutectic) ^[93]			21.6	23.8			
IMC precipitates			20 °C				
Ag ₃ Sn ^[92]			19				
Cu ₆ Sn ₅ ^[92]			16.3				

Table 12. Thermal expansion coefficients. Highlighted in green – at soldering temperatures; highlighted in yellow – at room temperature

Thus, in the case of mutual disorientation of the planes of equal CTE between β -Sn grains and Cu substrate, the solder volume near the interfacial IMC layer and in the intergranular regions represents a highly stressed area, which would fail during thermal-cycling. The experimental results have proved this assumption. Microstructural development as the number of thermal-cycles increases is shown in appendix 1. Thus, due to the thermal expansion anisotropy of β -Sn, the grains with a considerable misorientation expand by different amounts in different directions during heating. The resulting stresses produce micro-structural changes on the grain boundary and, consequently, leading to crack initiation and growth (figure 64). Microstructural transformations on the grain boundaries and substrate interface were observed by means of EBSD analysis. Recrystallization takes place in these regions, which is consistent with previous investigations [84].

In view of the above, a conclusion can be derived that the mechanical stability of Sn-based solder-joints depends on the number of β -Sn grains existing within the solder volume and their mutual orientation. Tensile strength experiments showed that in the cycled samples fracture moves from the substrate interface into solder bulk, propagating intergranularly. An average 7% strength reduction was obtained in solder-joints subjected to 100 thermal-cycles compared to those in initial state (figure 71). Presumably, a 'monocrystal' solder-joint with matching mutual plane orientation of equal CTE of β -tin and Cu substrate, would be even more favorable in terms of its stability under thermal loads. In the framework of the experiments carried out, the solder part of the lead-free solder joints consisted of between 1 and 10 β -tin grains.

As was previously shown, the ultrasound vibration implementation during solder solidification resulted in finer microstructure formation with a high amount of randomly oriented grains. This would consequently result in a deterioration of the solder-joints mechanical properties in terms of thermal-cycling loads.

Comparing microstructural resistance to thermal-cycling environment between lead-free solder-joints and lead-containing ones showed that lead-containing solder joints tend to produce higher amounts of β -Sn grains upon solidification than lead-free ones and fail earlier due to crack initiation and propagation along the grain boundaries. This disparity of the number of grains developed within the solder bulk of lead-free and lead-containing solder-joints can be explained by the difference of undercooling required before solidification. It has been reported that the amount of undercooling for Sn-Pb eutectic is 1.9 degrees, whereas for SAC solders it can exceed 30 degrees [9]. During the present work it has been shown, that the average amount of undercooling for the SAC405 solder is 24 degrees.

The coarsening behavior of the lead-free solder-joints microstructure during thermal-cycling was also noted. This can be explained by solid state diffusion acceleration while specimens were held under peak temperatures of the thermal-cycles. Coarse grains have lower energy content than fine ones, which serves as a driving force for this solid state transformation [94]. This phenomenon was more clearly observed during annealing experiments.

Microstructural transformations during solid state annealing

Solid state annealing was performed in order to evaluate solder-joint microstructure development in a quite rigorous environment which can be faced by electronic devices in some applications (for instance sensors and control units of a vehicle engine). The annealing temperature was 160 °C

High-temperature annealing causes intermetallic precipitates to grow preferentially along the grain boundaries, since diffusion occurs faster along these than through the bulk. In contrast to the large pro-eutectic Cu_6Sn_5 IMC whiskers which form during solidification,

the Cu_6Sn_5 IMC which develop during solid-state annealing have completely different morphology (i.e. rounded shapes with faceted edges).

The lead-free solder samples showed quite considerable microstructural changes after 1800 hours of ageing at 160 °C. In addition to coarsening of the matrix microstructure, the intermetallic precipitates modified drastically. Thus, the Ag_3Sn precipitates enlarged in the interdendritic regions where they were formed on the latest stages of solidification process during eutectic reaction, whereas Cu_6Sn_5 intermetallic particles showed more rapid growth and were found to be distributed along the grain boundaries of the coarsened microstructure.

Interfacial IMC layer on Copper substrate modifies during ageing. It separates into two growing stratum Cu_6Sn_5 and Cu_3Sn . The growing rate of the stratum is different for different lead-free alloys and retards as the ageing is progressing (figure 79).

It was shown that IMC layers grow as a layer during annealing as $\sqrt[3]{t}$, where t is annealing time (figure 95 (A)).

Phenomenon of crystallographically-faceted voids formation

In the framework of the experiments carried out during this project, the crystallographically-faceted voids (CFV) were constantly observed. The attempt undertaken to investigate this phenomenon separately from the experiments described in previous sections provided the following results:

- (i) regardless of the composition, the phenomenon of CF voids formation was observed in Sn-rich alloys (SAC405, SAC305, CASTIN, SN100C, Sn60Pb40 and pure Sn);
- (ii) the CF voids are strongly dependent on the substrate features: always found in solder-joints assembled with the use of a “massive substrate” ($> 10\,000\ \mu\text{m}$) in the

“as soldered” state, whereas in solder-joints assembled with use of PCBs (metallization < 50 μm) they start to appear generally only during ageing;

- (iii) the volume fraction of the CFV is highly dependent on the distance between Cu substrates. Greater distances between Cu substrates result in a decrease in CFV volume fraction.
- (iv) the CF voids are always found close to the bulk Cu_6Sn_5 and Ag_3Sn IMCs or interfacial IMC layer with Cu substrate;
- (v) ageing under elevated temperatures promotes CF void growth and clustering into large conglomerates.

One of the hypotheses which could be proposed for description of this phenomenon is that the driving force for CF void formation could be fields of stress which occur in the Sn-Ag-Cu system upon its solidification. This system is not uniform and yields three phases upon solidification. It was shown that pure bulk Sn and Sn-Pb alloys are free from the CF formation and development during annealing (figure 103(A)). Moreover, the features of the substrate (its thickness) can drastically affect the CF void formation and evolution.

The fact that the CF voids are faceted suggest that they must form in the solid state (not the liquid state) presumably by the condensation of vacancies in the matrix.

During annealing when the specimens were subjected to exposure at 160 $^{\circ}\text{C}$, diffusion in Sn plays an important role in microstructural changes, since Sn is at 85% of its absolute melting point (in Kelvin scale) where the vacancy concentration is very high and substitutional diffusion is very rapid. At these temperatures, it seems feasible that vacancies could cluster and grow to form voids in response to a denser phase growing within the less dense Sn.

The coefficients of crystal lattice packing and consequently density of intermetallic particles Ag_3Sn and Cu_6Sn_5 forming in the solder bulk are higher than that of β -Sn matrix

(table 13). During intermetallic precipitate formation from the pure components, the resulting volume of the new phase will be less than the volume of the pure components involved in the reaction. For instance, in the case of Cu_6Sn_5 precipitating, the resulting volume according to the rule of mixtures would be about 5,5% less than that of the two pure components (and about 6% less for Ag_3Sn). This contraction upon IMC precipitation will induce a very significant tensile stress in the surrounding matrix nearby and a global shrinkage in the solder as a whole. The nucleation of voids will reduce the stress near IMCs. Figure 101 (A) demonstrates a correlation between IMC volume fraction and CFV fraction for thin Cu substrates.

Crystal lattice modeling by means of “CrystalMaker” software provides the following results:

Phase	Structure	Density	Unit cell volume	Filled space per unit cell	Void space per unit cell
β -Sn	Body-Centered Tetragonal	7.31 g/cc	108.085 Å ³	65.712 Å ³ (60.80%)	42.373 Å ³ (39.20%)
Cu	Face-Centered Cubic	8.97 g/cc	47.046 Å ³	35.136 Å ³ (74.68%)	11.910 Å ³ (25.32%)
Ag_3Sn	Orthorhombic	9.93 g/cc	147.899 Å ³	108.237 Å ³ (73.18%)	39.662 Å ³ (26.82%)
Cu_6Sn_5	Monoclinic	8.31 g/cc	779.367 Å ³	535.725 Å ³ (68.74%)	243.643 Å ³ (31.26%)

Table 13. Data on phases (crystal lattice parameters were taken from [83])

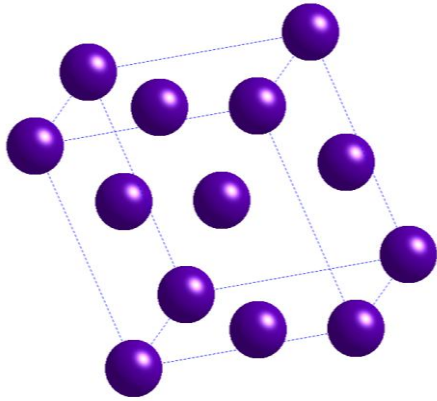


Figure 105. **β -Sn phase**: body-centered tetragonal structure:
 $a = b = 5.83 \text{ \AA}$, $c = 3.18 \text{ \AA}$

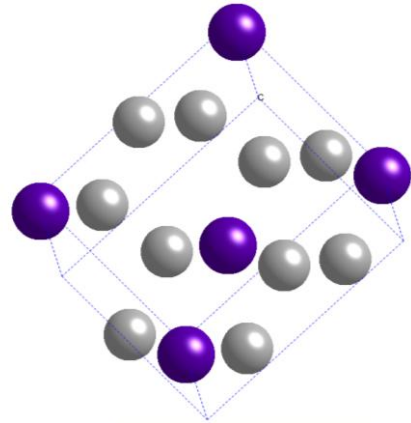


Figure 106. **Ag_3Sn phase**: Orthorhombic;
 $a = 5.969 \text{ \AA}$, $b = 4.78 \text{ \AA}$, $c = 5.1843 \text{ \AA}$;
 $\alpha = \beta = \gamma = 90^\circ$

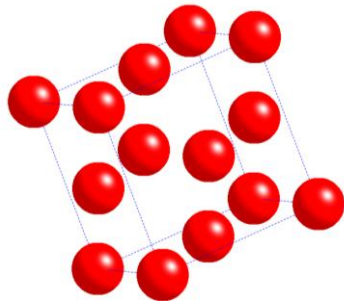


Figure 107. **Cu phase**: face-centered cubic lattice:
 $a = b = c = 3.61 \text{ \AA}$

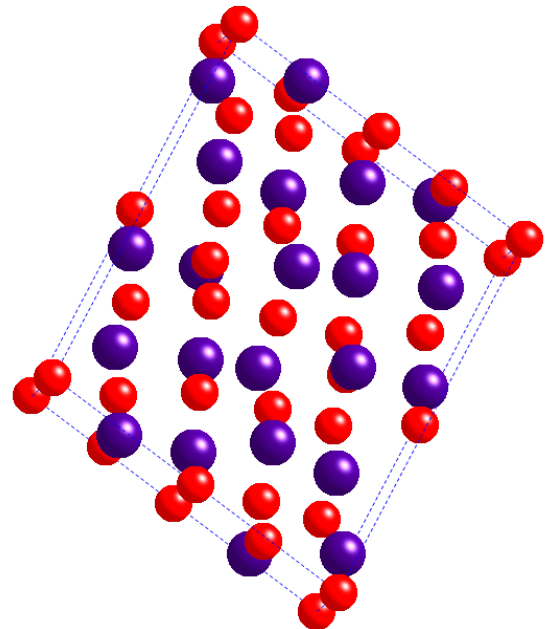
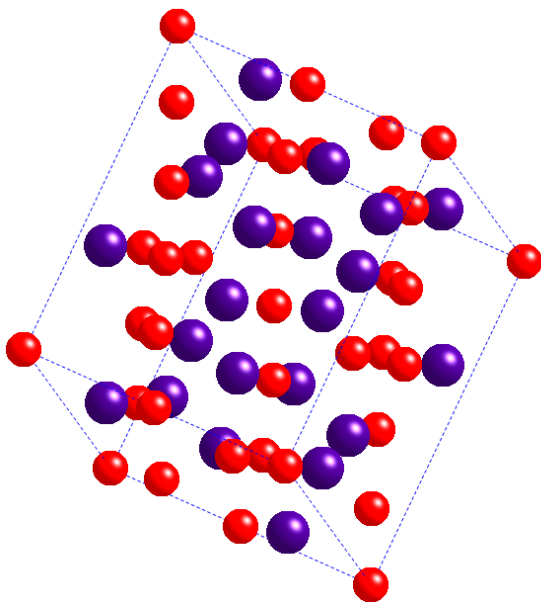


Figure 108. **Cu_6Sn_5 phase**: Monoclinic (low temperature modification $< 460 \text{ K}$);
 $a = 11.02 \text{ \AA}$, $b = 7.28 \text{ \AA}$, $c = 9.83 \text{ \AA}$; $\alpha = \gamma = 90^\circ$, $\beta = 98.8^\circ$

As can be seen from figure 101(A), the volume fraction of Cu_6Sn_5 IMCs in the solder-joint of 25% corresponds to the volume fraction of the CF voids of approximately 2%. As mentioned above, the Cu_6Sn_5 phase is 5.5% smaller than the β -Sn matrix. If the volume fraction of Cu_6Sn_5 IMC is denoted as “f” and the misfit is completely relieved by void formation then the maximum void fraction would be $(0,055 \times f)$ %. Given that the highest value of f is about 25% then this could account for a void fraction of about 1.4%. Considering the Ag_3Sn IMCs which have a volume fraction in SAC 405 alloy about 5% and contract upon their precipitation up to 6%, it can be seen that this precipitation can account for the additional voiding in the β -Sn matrix, increasing the CFV fraction up to 2% and over.

Typically SAC solders contain 0.5% Cu. In the absence of a Cu source, this would obviously place an upper bound on the Cu_6Sn_5 volume fraction at 1%. The initial Cu_6Sn_5 fraction in solder-joints appears to be far above 1% (figure 101(A)) which suggests that interaction with the substrate is occurring very quickly. The Cu_6Sn_5 IMCs formation in the bulk of solder-joints assembled with use of Sn60Pb40 (figure 89(A)) and pure Sn (figure 90) solders also proves the fast kinetics of the interfacial reaction.

It noteworthy, that the IMC Cu_6Sn_5 has an allotropic transformation at 187.5 °C (η - $\text{Cu}_6\text{Sn}_5 \rightarrow \acute{\eta}$ - Cu_6Sn_5) and this transformation involves structural reorganization: hexagonal crystal lattice of η - Cu_6Sn_5 (high temperature modification) transforms into monoclinic crystal lattice of $\acute{\eta}$ - Cu_6Sn_5 (low temperature modification) [88]. This process is associated with volume change of the phase. It occurs in the solid state right after solidification (since a solder-joint could be super-cooled down to these temperatures) and is expected to introduce additional internal stress due to the subsequent expansion of $\acute{\eta}$ - Cu_6Sn_5 phase by up to 2.15% [88]. This transformation continues in the solid state during solder-joint ageing, since the time available for the transformation during soldering is not sufficient

[88] and Cu atoms continue to diffuse from the substrates producing more IMCs within the β -Sn matrix.

The fact of the non-uniform distribution of the clusters of CF voids along the IMC layer (figure 96) could be explained by the relief of differential thermal expansion which is likely to play an additional role in voiding. The thermal expansion coefficient of β -Sn is very anisotropic (as shown in this section earlier). The CTE of Cu is highly compatible with the CTE of β -Sn in one direction but not the other. Thus, due to mutual difference in grain orientation of β -Sn and Cu substrate, the worst combination can introduce an additional mismatch strain and promote voiding. A thicker substrate obviously increases the level of mechanical constraint and it will also increase the source of Cu.

It worth of note that the volume fraction of the CFV is highly dependent on the distance between Cu substrates (figure 86). Greater distances between Cu substrates result in a decrease in CFV volume fraction.

It was shown that the CFV volume fractions with the thin substrates are associated with IMC particles and IMC layers, which can be explained by the shrinkage model. The large CFV fractions observed in the case of massive substrates are too large to be solely explained by this model.

It is clear that the initial microstructure of lead-free solders is a long way from equilibrium. In order to fully understand the phenomenon of CF voids formation in Sn-rich solders, additional experiments are currently being performed.

7. CONCLUSION

In the present work different aspects of lead-free solders microstructure modification were considered and investigated. Studies of solder-joint microstructure, particularly during its ageing, discovered quite an interesting phenomenon of crystallographically-faceted voids formation. This phenomenon is of great interest as it has not been described yet. Thus, future work will be devoted to investigation the phenomenon of CFV formation.

The results obtained in the present work can be summarized as follows:

- Large pro-eutectic IMC phase's formation is highly dependent on solder alloy composition and cooling kinetics. They tend to segregate in systems with Ag and Cu content over 2,5 wt% and 0,5 wt% respectively if the cooling rates are moderate (less than 1 °C/sec). Pro-eutectic Ag₃Sn IMCs segregates in the shape of leaf-like platelets; Cu₆Sn₅ IMCs presented the following kinds of shapes: needle type whiskers and hollow-type hexagonal faceted whiskers for SAC alloys and irregular shaped formations for CASTIN alloy. The large intermetallic precipitates affect microstructural integrity of solder-joints and, consequently, their mechanical stability under stressed conditions.
- Fast cooling rates promote equiaxed dendrite growth and more uniform distribution of the intermetallic particles in the interdendritic regions. The average β-Sn dendrite and IMC precipitates size rapidly decreases with the cooling rate increase. For instance, a cooling rate of 24 °C/sec (SAC405 alloy) lowered the maximum IMC needles length to 2μm compared to 44 μm at 1 °C/sec. On the other hand, fast cooling rates promote hardening but shorten solder-joint thermal-fatigue life.
- Ultrasound implementation upon solder crystallization causes two types of effects affecting solder-joint mechanical properties:

Positive effects of ultrasound vibration implementation:

- (i) promotes fine and equiaxed structure formation;
- (ii) reduces the eutectic phase formation (up to 30% compared to the eutectic phase content in samples solidified under conventional conditions);
- (iii) promotes more uniform distribution of intermetallic particles within bulk solder;
- (iv) lowers the amount of undercooling (ultrasound of 30 kHz lowers the amount of undercooling from 24 °C to 7 °C for SAC 405 alloy and from 12 °C to 1 °C for CASTIN alloy).

Negative effects of ultrasound vibration implementation:

- (i) ultrasound intensifies diffusion at liquid alloy-substrate interface resulting in copious intermetallic phase formation.
- Excessive development of the interfacial intermetallic layer (over 10 μm) drastically weakens solder-joint strength. An optimal IMC layer width found to be approximately 2 μm.
 - Thermal-cycling affects the microstructural evolution and the fracture mechanism of solder-joints of both lead-free and lead-containing solders. In cycled lead-free samples, fractures move from the substrate interface into the solder bulk, propagating intergranularly. An average 7% strength reduction occurs for lead-free samples subjected to 100 thermal cycles. Lead-free solders are more resistant to thermal-cycling loads due to lower amount of grains within a solder-joint (lead-free solder-joints consisted from 1 to 10 β-Sn grains, whereas lead-containing ones comprised of up to 96 grains). 150 thermal-cycles caused crack initiation in lead-

containing solder-joints, whereas lead-free ones exhibit only slight changes on the grain boundaries.

- Recrystallization resulting in a relatively small grain size occurs in highly stressed areas (grain boundaries and substrate interface) during thermal-cycling. Failure initiation and fracture propagation was observed to have intergranular path.
- Solid state annealing promotes IMC precipitates growth and segregation along the grain boundaries. The rate of Cu_6Sn_5 IMCs coarsening is considerably faster than that of Ag_3Sn IMCs. Interfacial IMC layer on the Copper substrate separates into two growing stratum of Cu_6Sn_5 and Cu_3Sn as the ageing progresses. It was shown that IMC layers grow as scalloped layers during reflow as $\sqrt[3]{t}$ (where t is reflow time) and as a layer during annealing as $\sqrt[2]{t}$ (where t is annealing time).
- The growth rate of the IMC layer is highly dependent on alloy composition. The solder-joints based on SN100C solder (0.05% Ni) exhibit almost a factor of two times lower interfacial IMC layer growth rate compared to SAC alloys (no Ni additions).
- Crystallographically-faceted voids were constantly observed while performing various experiments concerning lead-free solder-joints microstructure investigation. It was proved by means of EBSD analysis that the CFV are always correlated with β -Sn grain crystallographic orientation and form in a tetragonal shape. Solid state annealing promotes further formation of CFVs.

It was found that:

- (i) regardless the composition, the phenomenon of CF voids formation occurs in Sn-rich alloys (SAC405, SAC305, CASTIN, SN100C, Sn60Pb40 and pure Sn);

- (ii) the CF voids are strongly dependent on the substrate features: always found in solder-joints assembled with the use of a “massive substrate” ($> 10\,000\ \mu\text{m}$) in the “as soldered” state, whereas in solder-joints assembled with use of PCBs (metallization $< 50\ \mu\text{m}$) they start to appear generally only during ageing;
 - (iii) the volume fraction of the CFV is highly dependent on the distance between Cu substrates. Greater distances between Cu substrates result in a decrease in CFV volume fraction;
 - (iv) the CF voids form close to the bulk Cu_6Sn_5 and Ag_3Sn IMCs or interfacial IMC layer with Cu substrate;
 - (v) ageing under elevated temperatures promotes CF void growth and clustering into large conglomerates.
-
- It was shown that the CFV volume fractions with the thin substrates are associated with IMC particles and IMC layers, which can be explained by the shrinkage model. The large CFV fractions observed in the massive substrates are too large to be solely explained by this model.

8. FUTURE WORK

Intermetallic phase formation and voiding are quite undesirable effects in maintaining a solder-joint long-term stability and consequently electronic device reliability. Future work will be devoted to the investigation into the principles of the faceted void formation and to study the influence of IMC precipitates on a solder-joint microstructural stability under different types of load conditions.

In order to reveal the nature of CF voiding phenomenon and its dependence on parameters affecting a solder-joint during soldering, the following particular experiments will be carried out:

1. *Cooling rate influence on CF voiding.* It was shown that quenching suppresses the CFVs formation, although they develop during subsequent ageing. This experiment needs to be carried out more precisely widening the range of cooling rates.
2. *Substrate material/IMC layer composition influence on CF voiding.* Experiments with Ni substrates and Au-coated Cu substrates are in initial stages and will be continued.
3. *Substrate thickness influence on CF voiding.* In the present study only two available substrate widths were used. Dependence of the CF voids development on the substrate geometrical parameters need to be investigated more precisely.
4. *The ratio solder/IMCs volume fraction influence on CF voiding.* As it was shown, the CFVs are correlated with volume fraction of Su_6Sn_5 IMCs. The same correlation needs to be determined for Ag_3Sn and Cu_3Sn IMCs.
5. *Solder volume/ distance between Cu substrates influence on CF voiding during ageing.*

Currently, it is difficult to explain the very large void fraction occurring in a solder-joint due to differential thermal expansion of materials involved or Cu_6Sn_5 IMC phase formation. This phenomenon eventually has a complicated mechanism where a large number of variables are involved. Every variable has to be investigated separately with consequent integration and a process model development.

In order to improve solder-joint long term reliability, experiments aimed to find an optimal combination of materials used in a solder joint (soldering paste, soldering pads metallization and coating layer) will be carried out. New systems (i.e. Sn-Cu-Ni based soldering paste on Ni-coated substrates) have microstructural features different from the investigated ternary system Sn-Ag-Cu and consequently, different behaviours in loading conditions.

In the present work, microstructural evolution under current load conditions was not considered. This issue is of high interest, as high-density current will affect solid state transformations within a solder-joint during service life. Investigations in this field will be carried out.

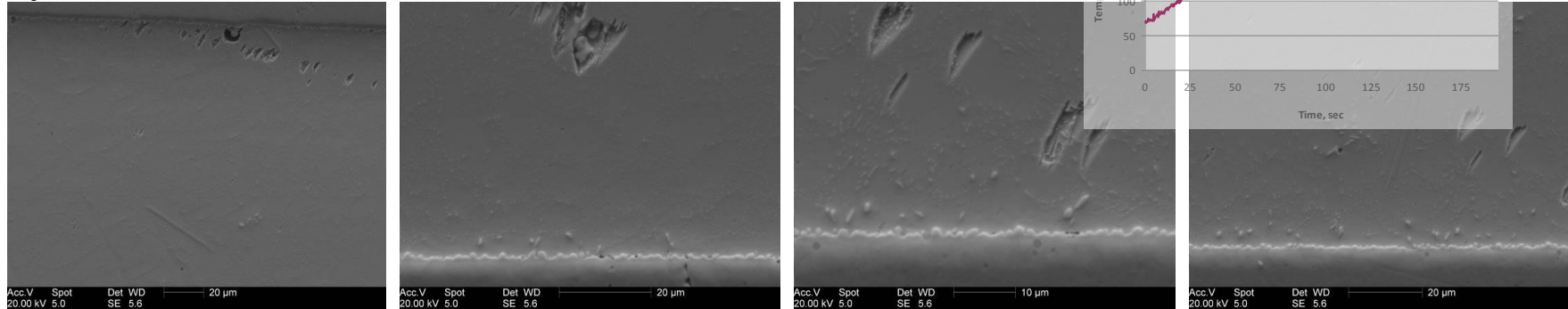
Lastly, it is of high interest to investigate influence of extreme operational conditions (extreme temperature deviations, shock and vibration, radiation impact) and their combination on solder-joint microstructural behaviour. Exemptions for the current use of Pb-containing solder alloys may be removed in the near future through legislation, further increasing the demand for suitable replacements in reliability electronics assemblies required for aerospace applications. To date, no necessary testing has been done in order to determine if current lead-free solders can meet the high-reliability and low risk requirements for military and space applications.

APPENDIX 1

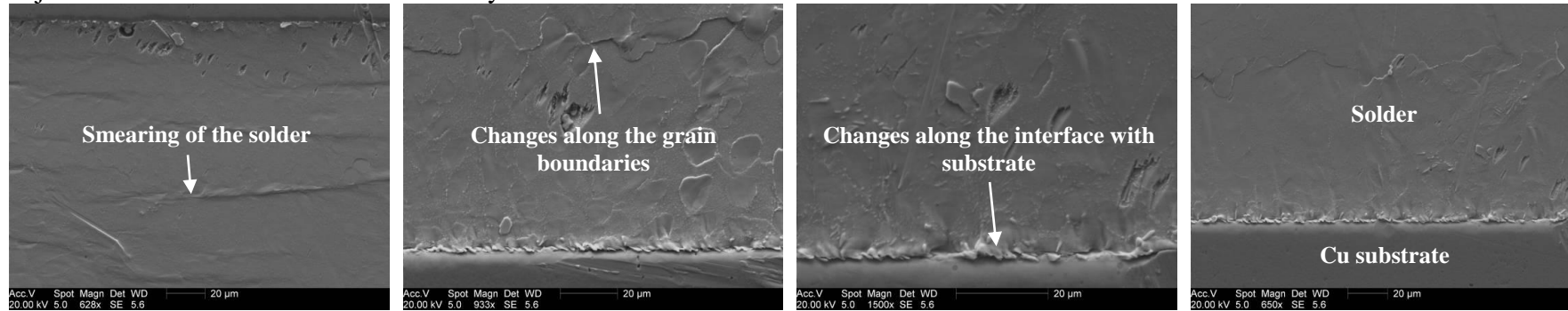
SOLDER MICROSTRUCTURAL EVOLUTION UNDER THERMAL-CYCLING CONDITIONS

Sample SAC405 (5 seconds above liquidus)

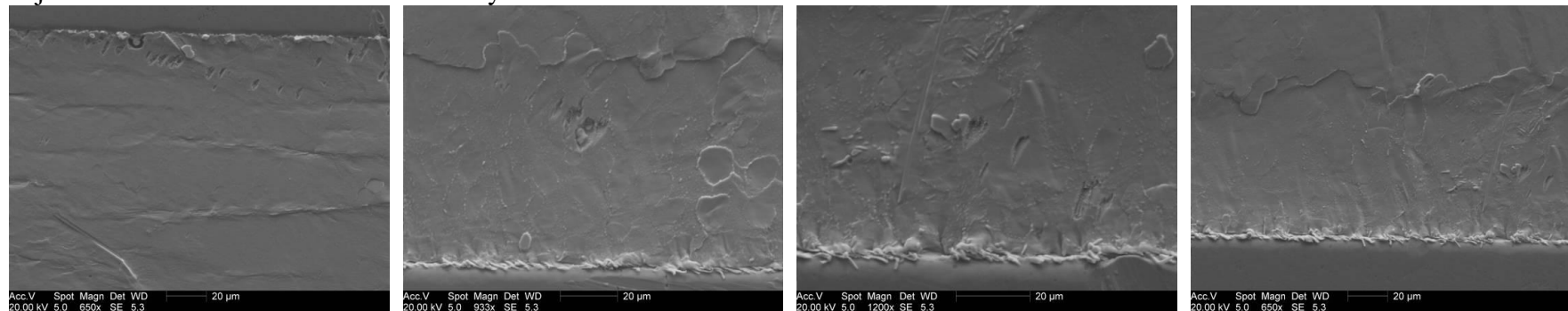
Solder-joint microstructure as received



Solder-joint microstructure after 150 thermal-cycles

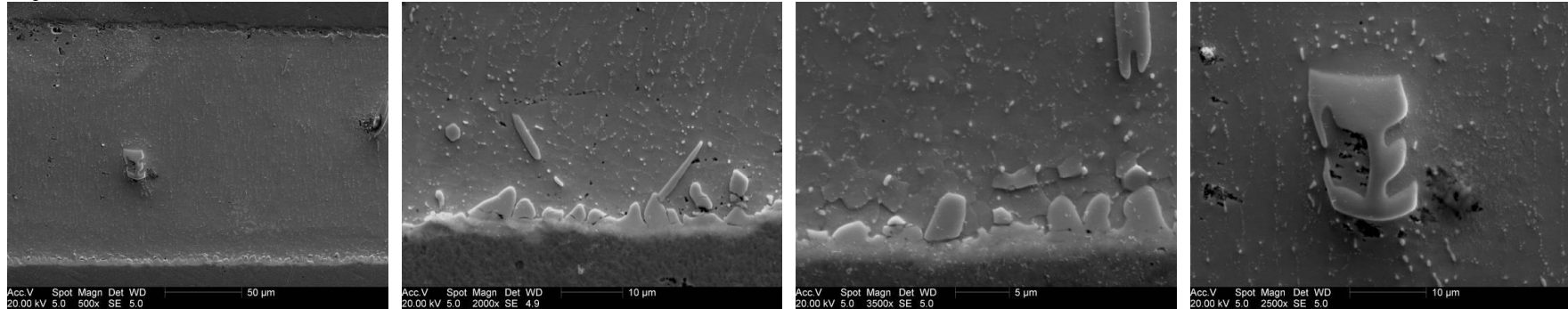


Solder-joint microstructure after 250 thermal-cycles

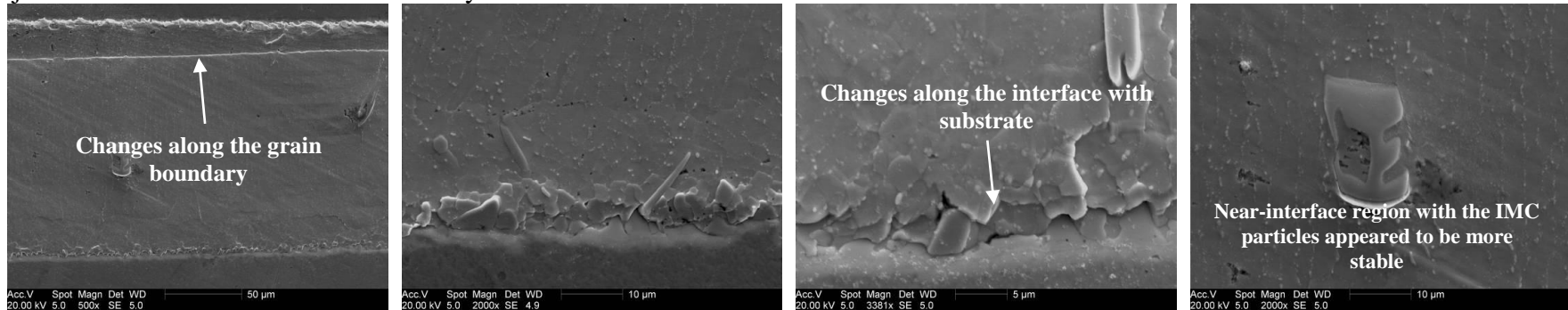


Sample CASTIN (5 seconds above liquidus)

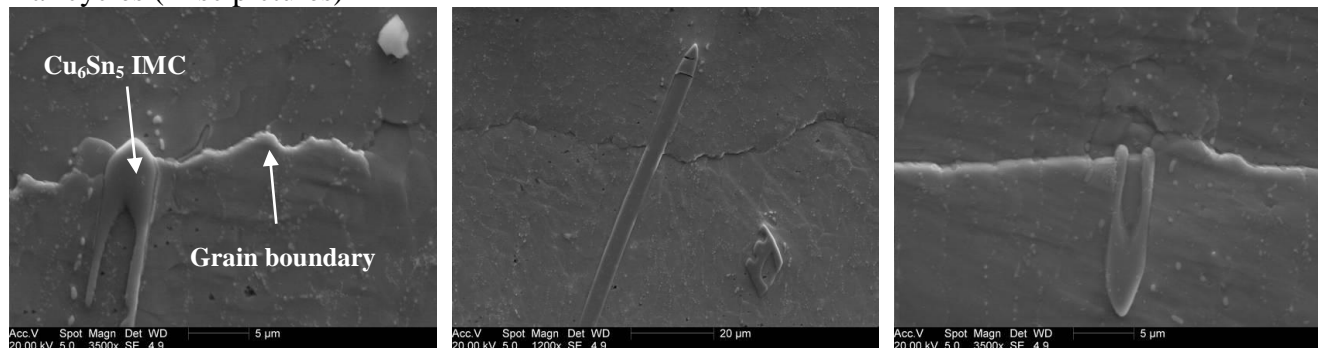
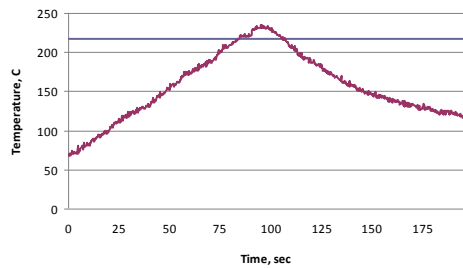
Solder-joint microstructure as received



Solder-joint microstructure after 250 thermal-cycles

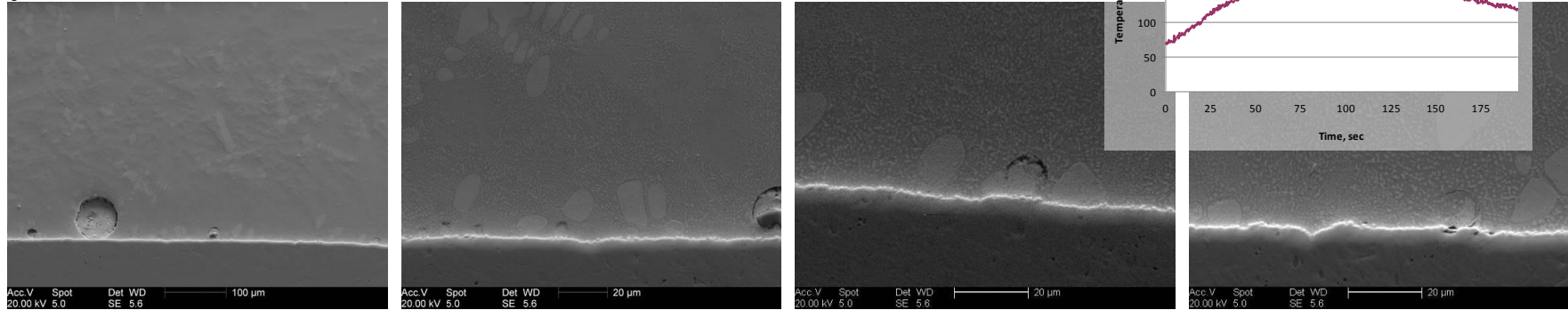


Solder-joint microstructure after 200 thermal-cycles (misc pictures)

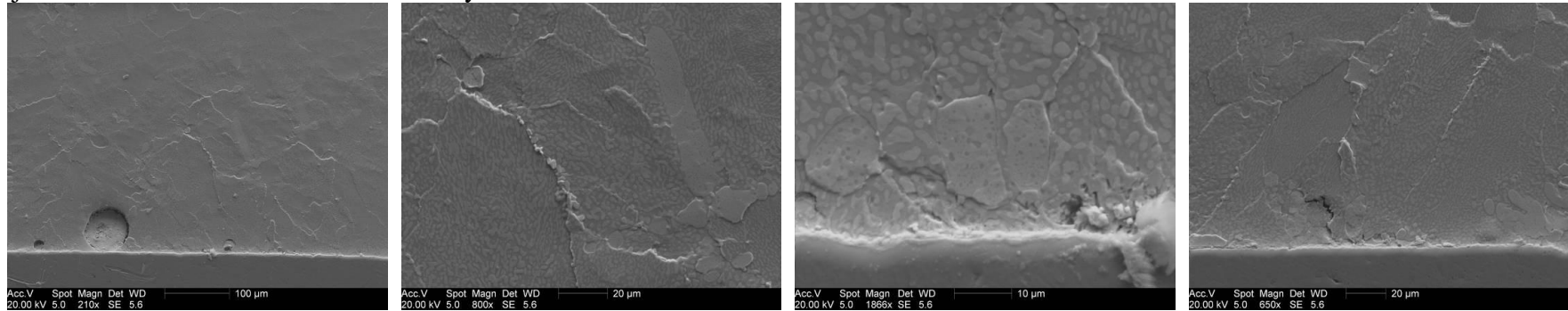


Sample Sn60Pb40 (5 seconds above liquidus)

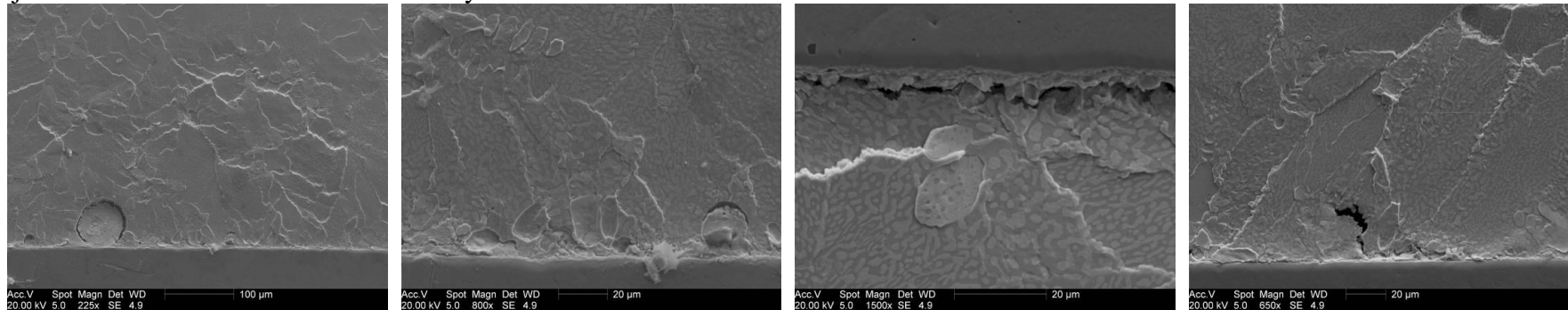
Solder-joint microstructure as received



Solder-joint microstructure after 150 thermal-cycles

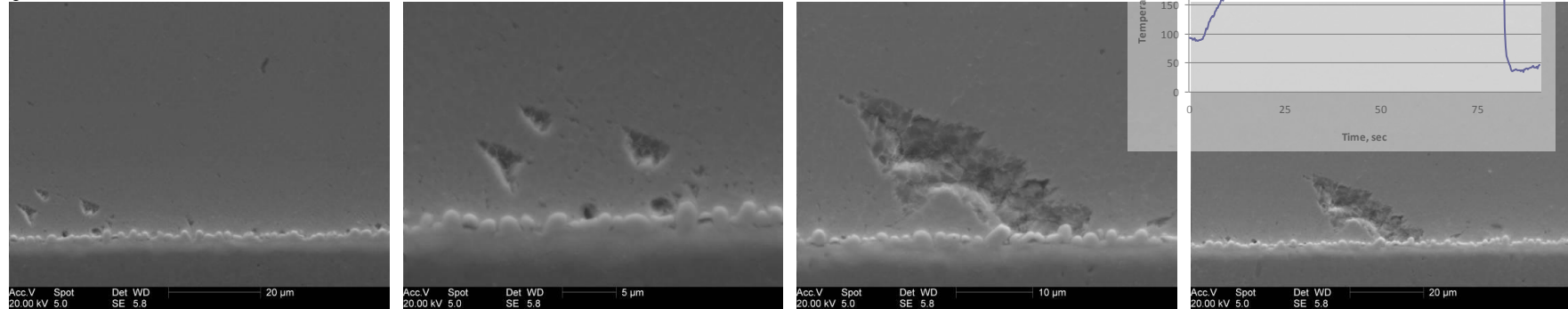


Solder-joint microstructure after 250 thermal-cycles

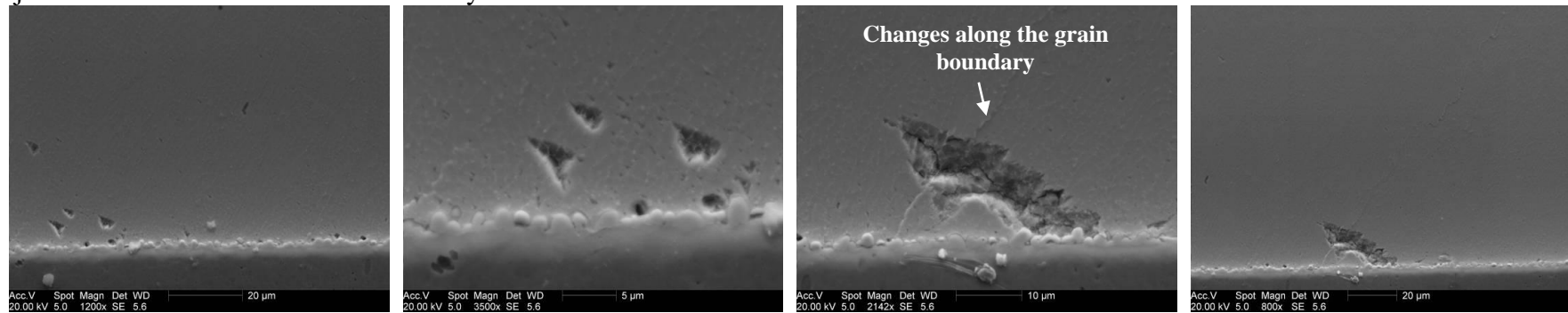


Sample SAC405, quenched (60 seconds above liquidus)

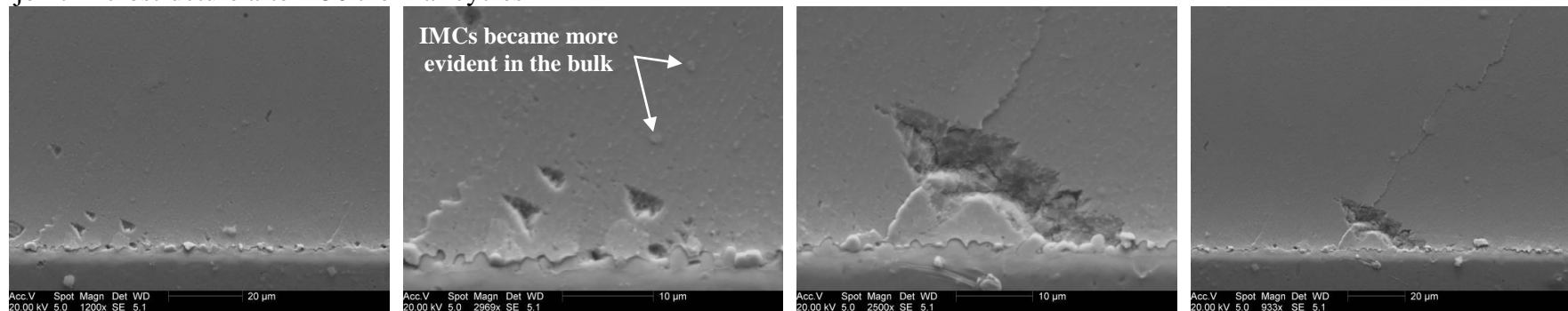
Solder-joint microstructure as received



Solder-joint microstructure after 150 thermal-cycles

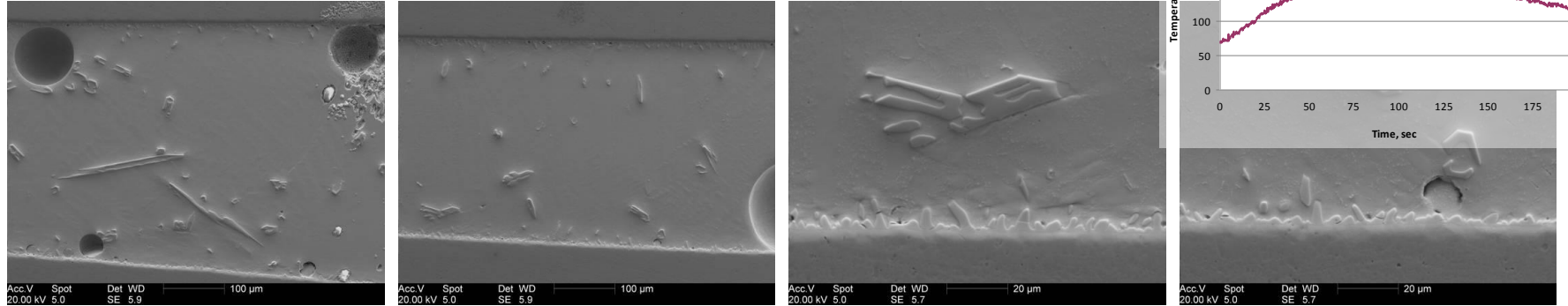


Solder-joint microstructure after 250 thermal-cycles

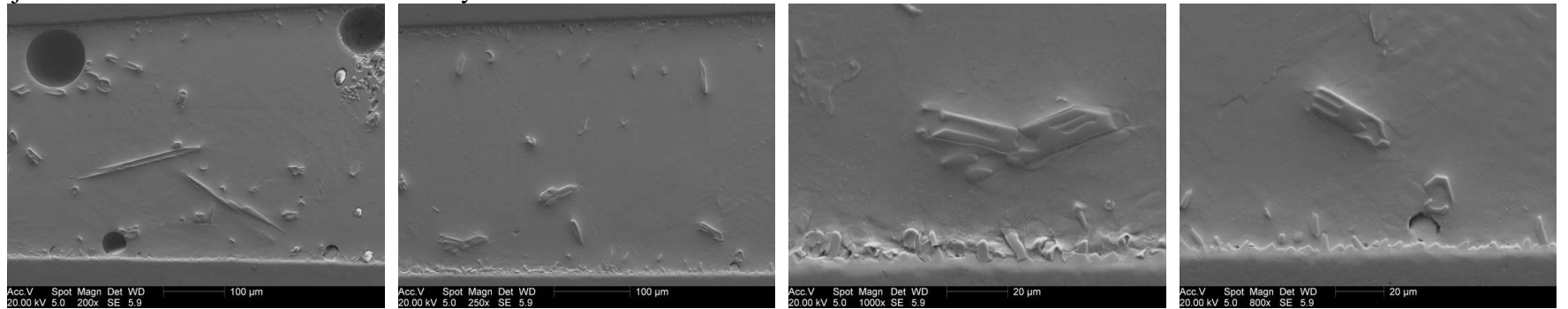


Sample SAC405, ultrasound treated (5 seconds above liquidus)

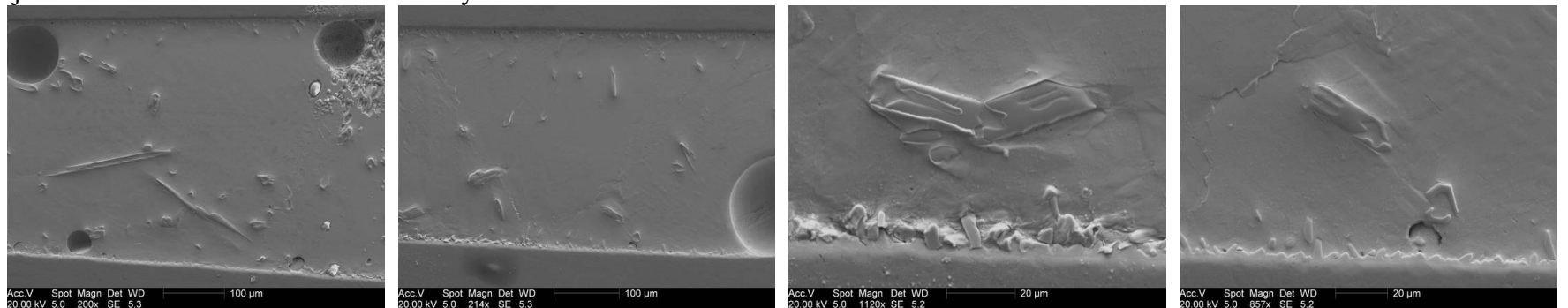
Solder-joint microstructure as received



Solder-joint microstructure after 150 thermal-cycles



Solder-joint microstructure after 250 thermal-cycles



APPENDIX 2

VOIDING IN SOLDER-JOINTS

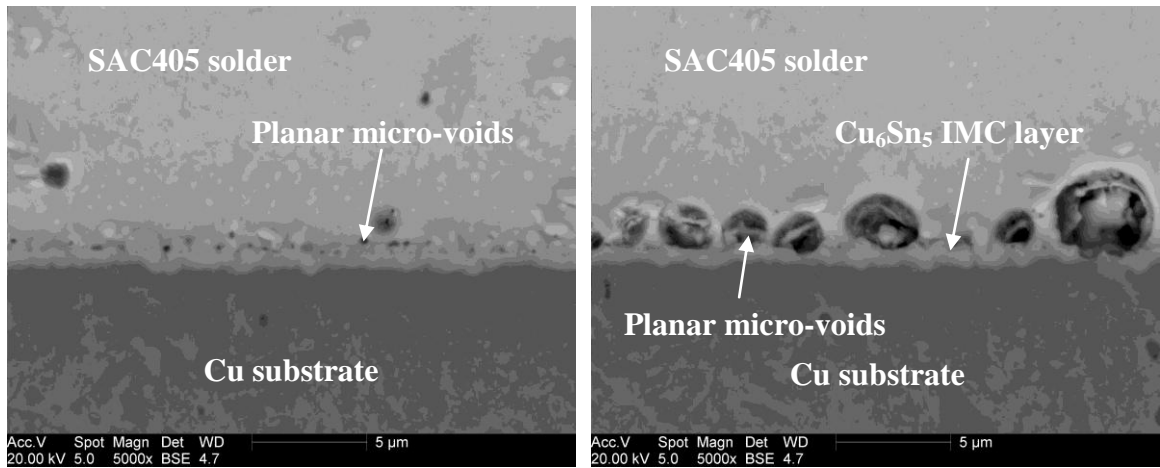


Figure 2.1. Planar micro-voids: caused by contamination on the substrate surface

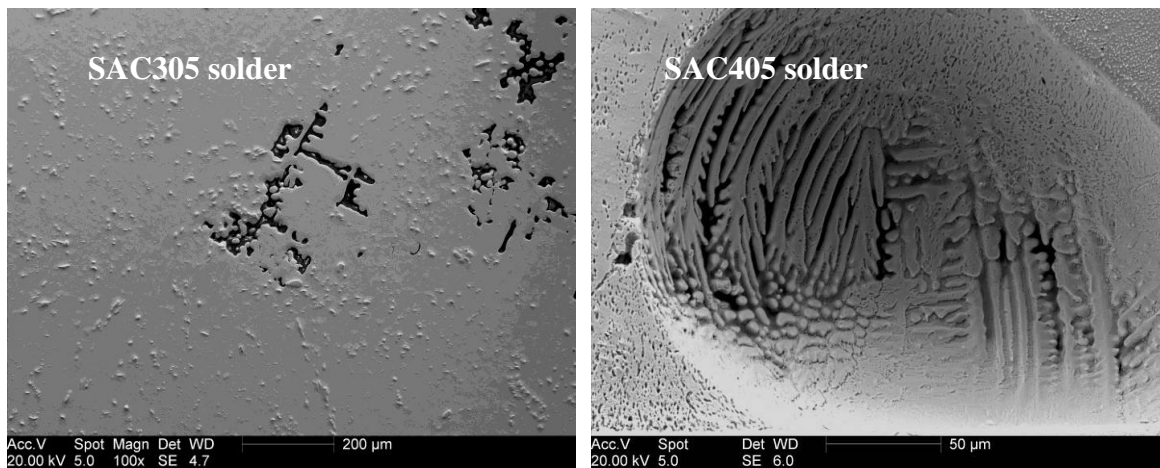


Figure 2.2. Shrinkage voids: caused by volume shrinkage in solidification of SAC solders

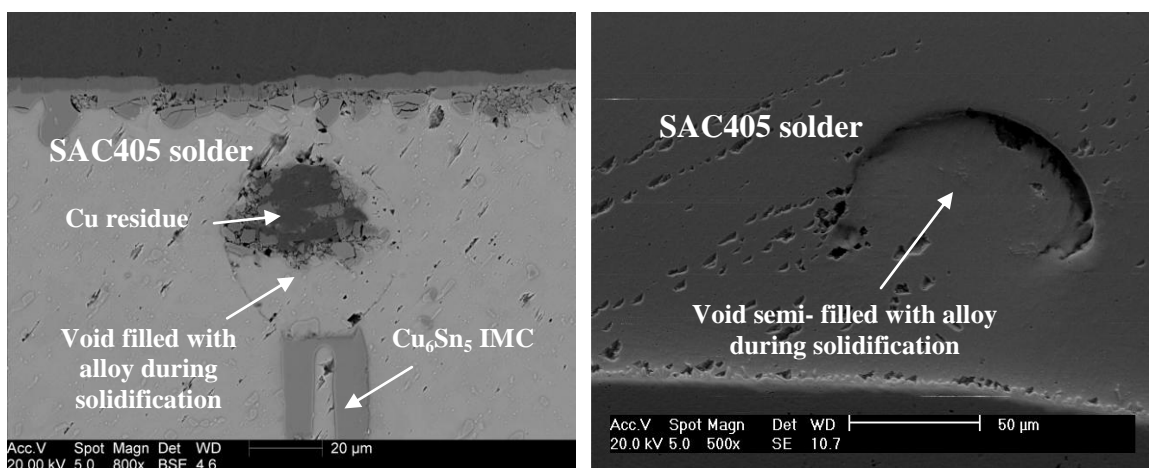


Figure 2.3. Semi-filled voids: caused by entrapped gases, flux residues or contamination

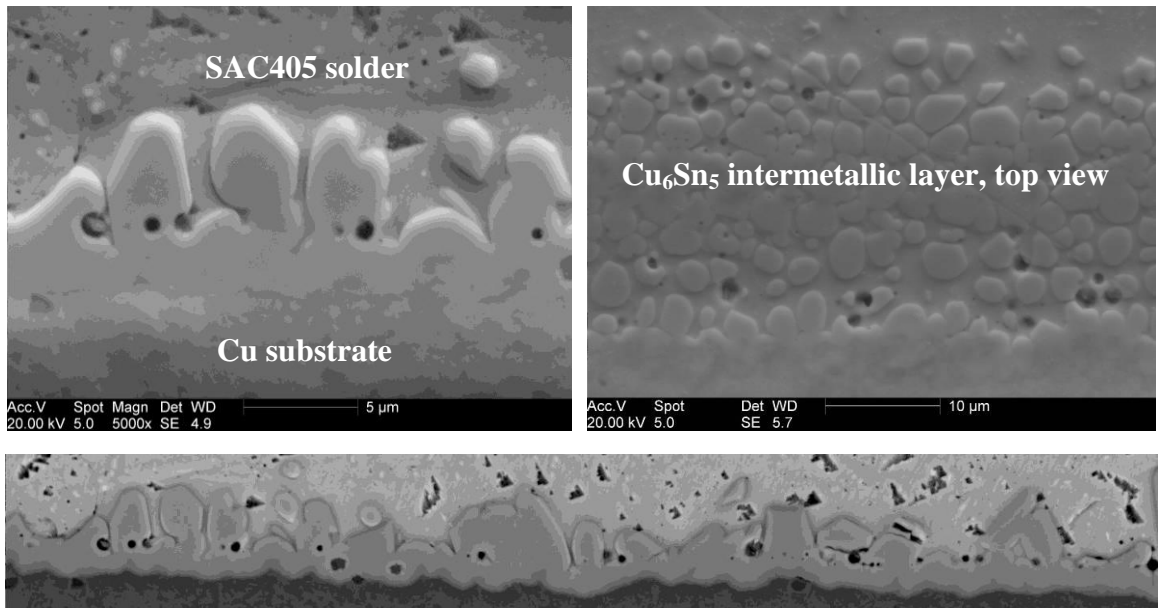


Figure 2.4. Voids through the interfacial IMC layer

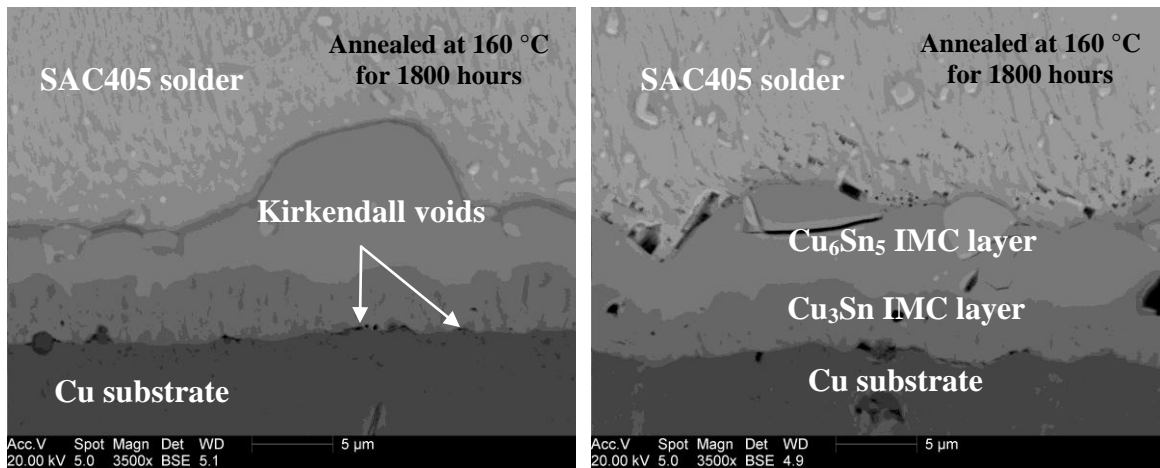


Figure 2.5. Kirkendall voids: caused by difference in interdiffusion rate between Cu and Sn

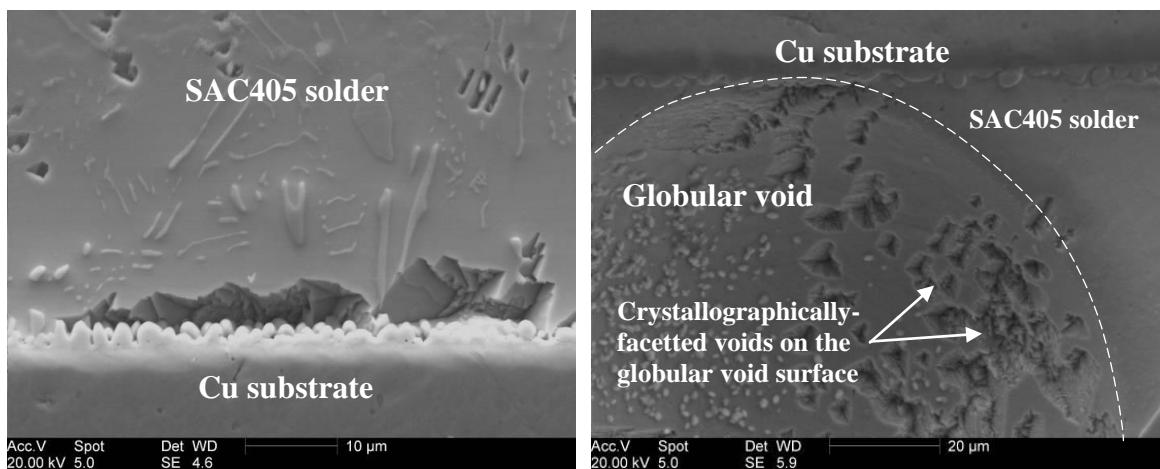


Figure 2.6. Crystallographically-faceted voids in 'as soldered' state

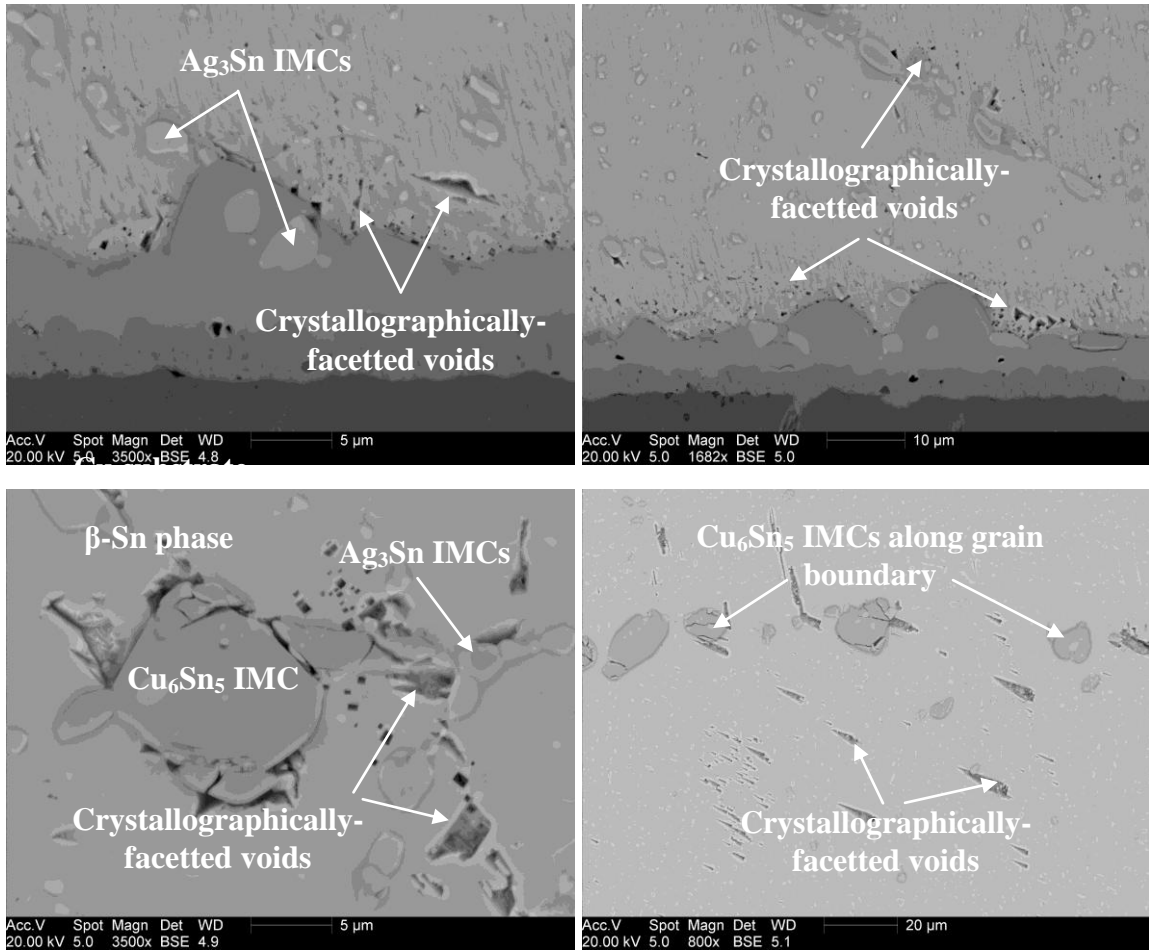


Figure 2.7. Crystallographically-faceted voids in SAC405 solder-joints after 1800 hours of annealing at 160 °C

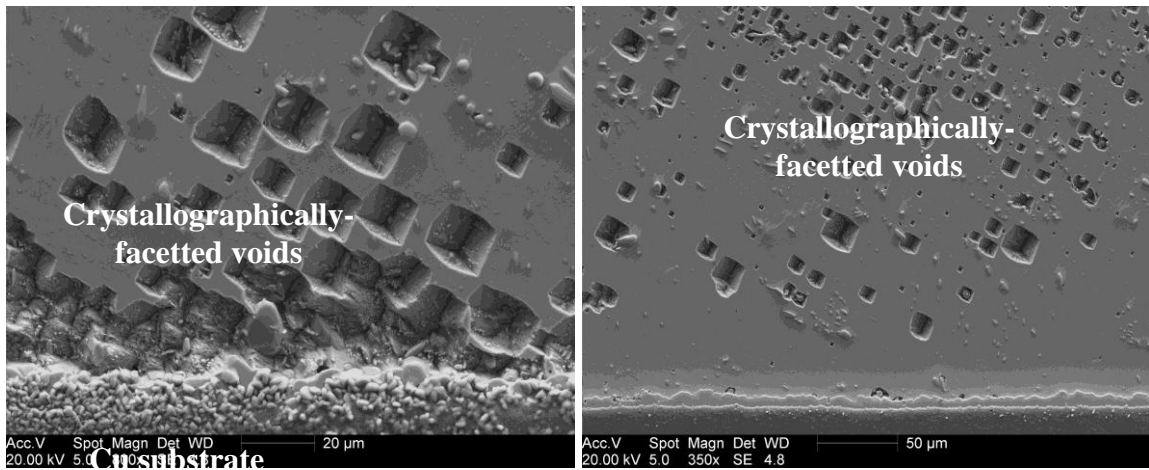


Figure 2.8. Crystallographically-faceted voids in SAC405 solder-joints after 3720 hours of annealing at 160 °C

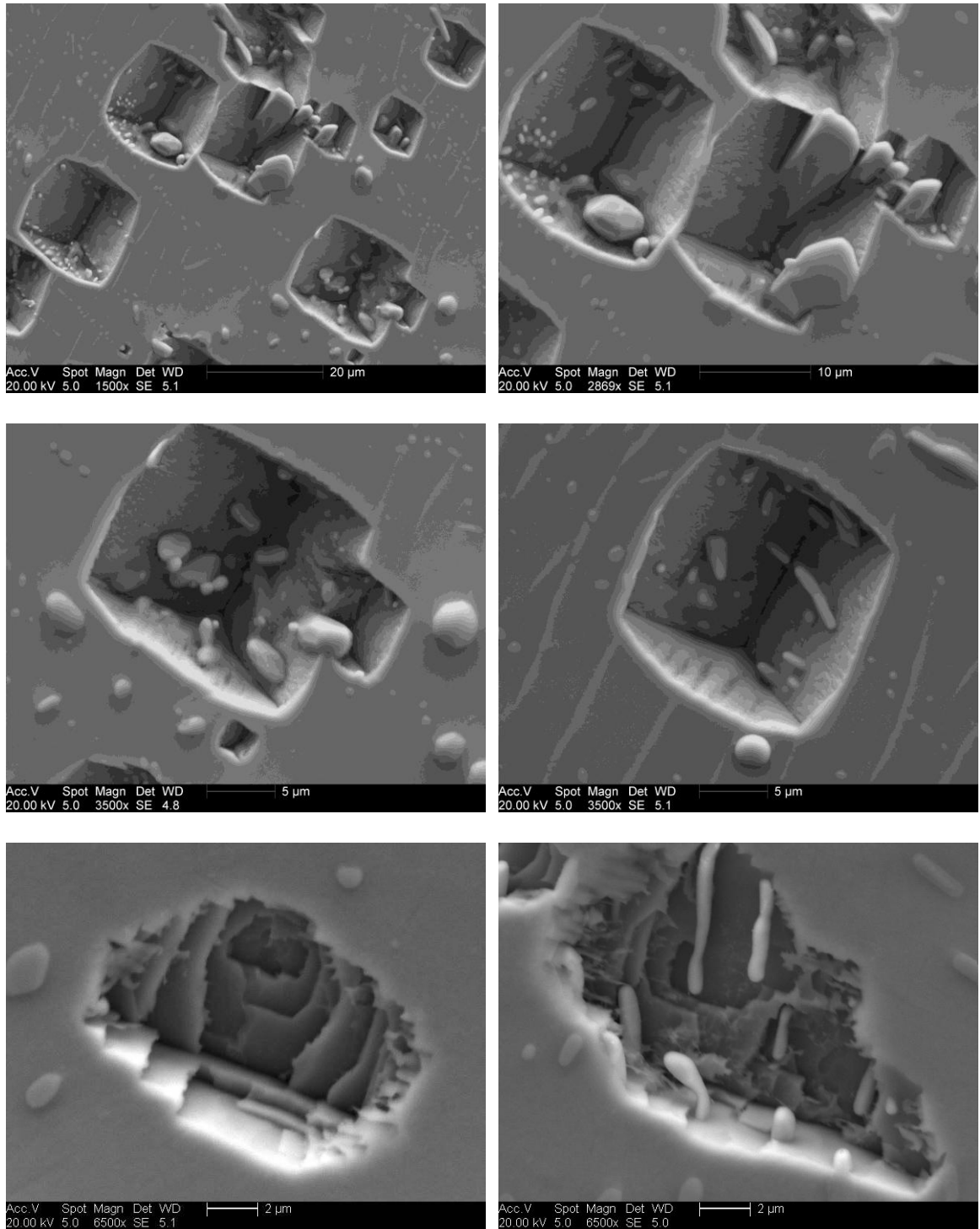


Figure 2.9. Crystallographically-faceted voids in SAC405 solder-joints after 3720 hours of annealing at 160 °C

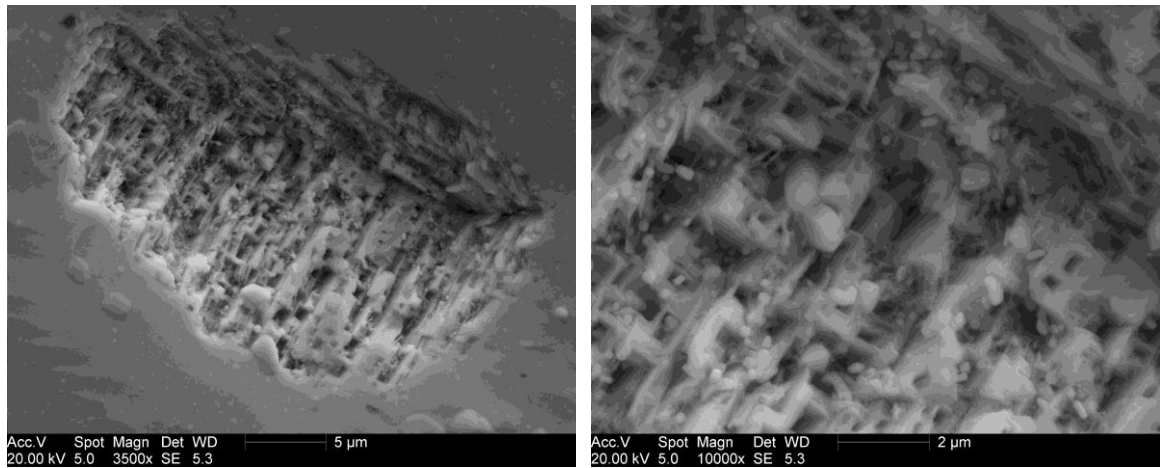


Figure 2.10. Crystallographically-faceted void in SN100C solder after 230 hours of annealing at 160 °C

APPENDIX 3

THREE-DIMENSIONAL MORPHOLOGIES OF IMCS

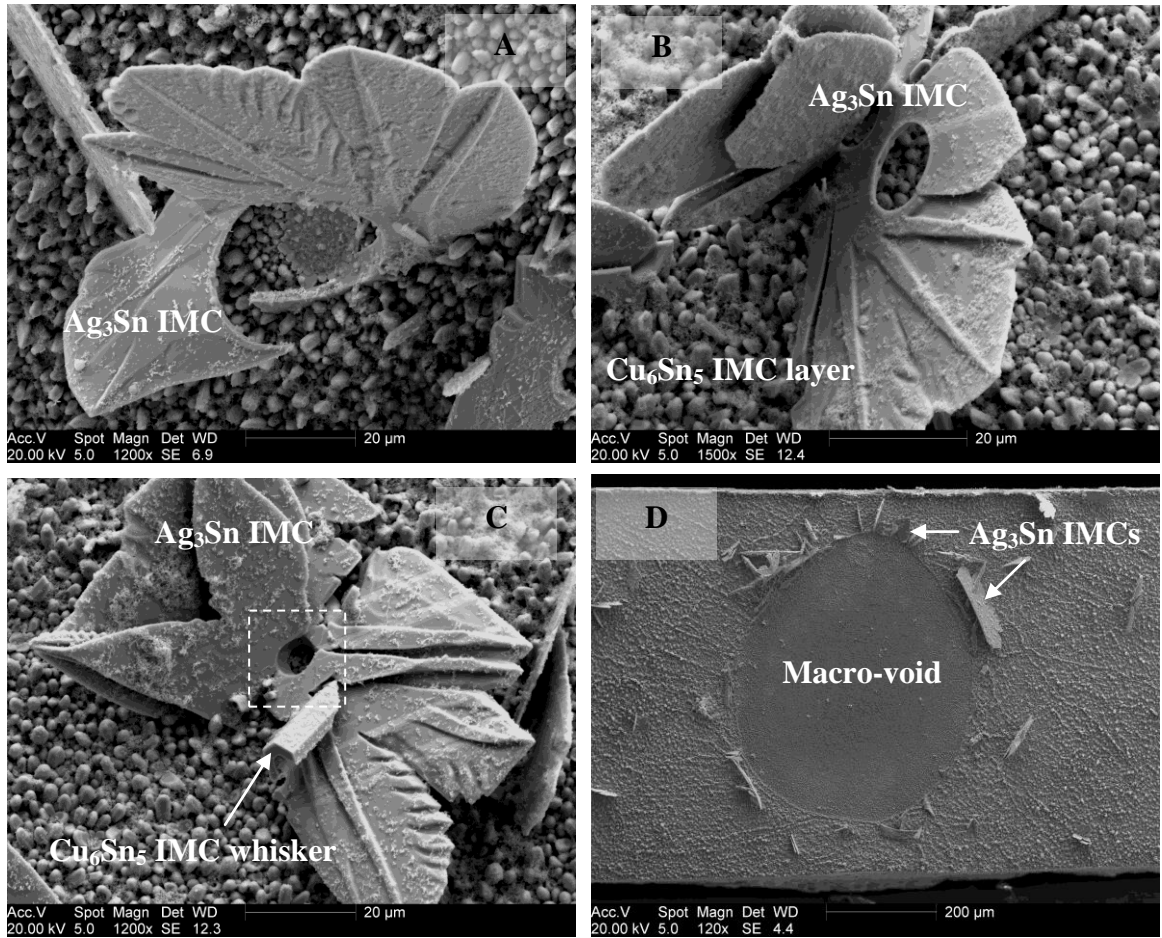


Figure 3.1. Leaf-like platelets of Ag₃Sn IMCs formed on Cu substrate in SAC405 alloy. Voids in the middle could serve as nucleation sites. The walls of macro-voids also promote pro-eutectic Ag₃Sn formation.

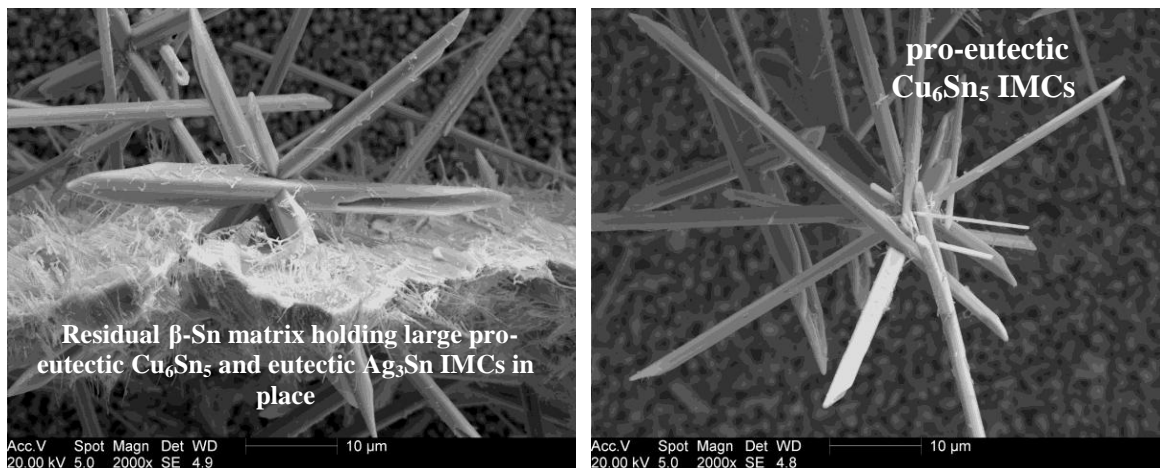


Figure 3.2. Needle type whiskers and hollow-type hexagonal faceted whiskers of Cu₆Sn₅ IMCs formed in the bulk of SAC305 alloy

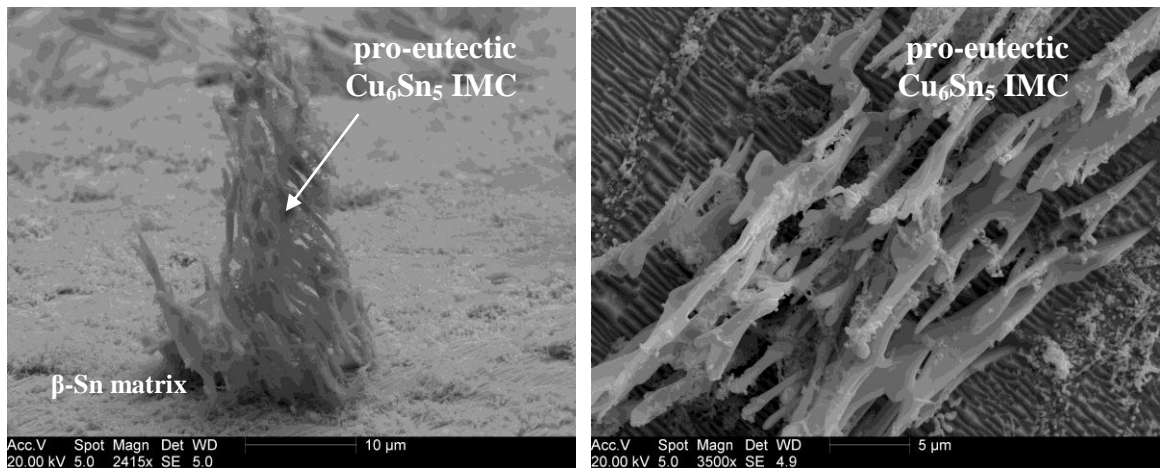


Figure 3.3. Irregularly shaped Cu_6Sn_5 IMCs formed in the bulk of SACTIN alloy

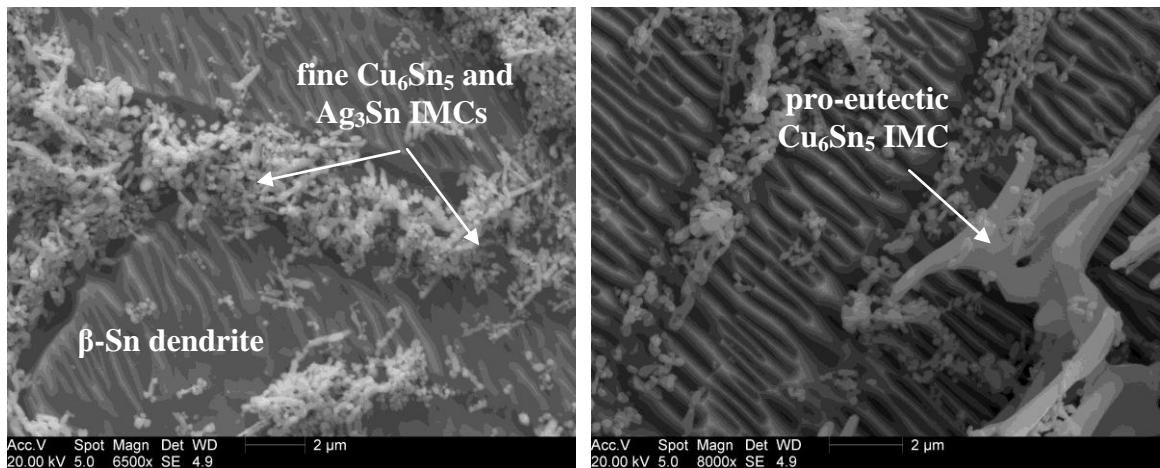


Figure 3.4. Mixture of fine Cu_6Sn_5 and Ag_3Sn IMCs in the interdendritic regions: precipitates forming on the latest stages of the solidification process during eutectic reaction.

9. REFERENCES

1. D. R. Laurence, *Clinical Pharmacology*, 3rd edn., London: Churchill, (1966), 637 p.
2. V. Grigorev, Lead-Free Technology, *J. Electronic Components*, No. 6, p.72 – 78, (2001)
3. NCM Report 0401RE96, Lead-Free Solder Project, National Center for Manufacturing Science, Ann Arbor, MI, 1997
4. <http://www.rohs.com>
5. <http://www.weee.com>
6. R. H. Esser, A. Dimoulas, N. Strifas, A. Christou, N. Papanicolau, Materials interfaces in flip chip interconnects for optical components; performance and degradation mechanisms, *J. Microelectron. Reliab.*, No. 38, p. 1307 – 1312, (1998)
7. Standard IPC/JEDEC J-STD-020C, Moisture/Reflow Sensitivity Classification for Non-hermetic Solid State Surface Mount Devices, Revision C, 2004
8. A. Rae, C. Handwerker, NEMI's Lead-Free Alloy, *J. Circuits Assembly*, Vol. 8, April issue, p. 20 – 25, (2004)
9. S. K. Kang, P. A. Lauro, D. Y. Shih, D. W. Henderson, K. J. Puttlitz, Microstructure and mechanical properties of lead-free solders and solder joints used in microelectronic applications, *IBM J. Res.& Dev.* Vol. 49, No. 4/5, p. 607 – 620, (2005)
10. J. D. Barnett, H. T. Hall, and R. B. Bennion, *J. Science* 141, X-Ray diffraction studies on tin at high pressure and high temperature, No. 3585, p. 1041 – 1042, (1963)
11. U.R. Kattner, *Phase Diagrams & Computational Thermodynamics*, NIST, (2000), 336 p.
12. C-S. Oh, J-H. Shim, B-J. Lee, and D.N. Lee, A thermodynamic study on the Ag-Sb-Sn system, *J. Alloys Compds.*, Vol. 238, No.1, p. 155 – 156, (1996)

13. *J.H.Shim, C.S.Oh, B.J.Lee, D.N.Lee*, Thermodynamic database for phase diagrams in micro-soldering alloys, *Z. Metallkde*, No 87, p 205 – 212, (1996)
14. *H.J. Fecht and J.H. Perepezko*, Metastable phase equilibria in the lead-tin alloy system, *Metall. Trans.*, Vol. 20, No. 5, p. 785 – 794, (1989)
15. *A. Sharif, Y.C. Chan, R.A. Islam*, Effect of volume in interfacial reaction between eutectic Sn–Pb solder and Cu metallization in microelectronic packaging, *Mater. Sci. Eng.*, B106, p. 120 – 125, (2004)
16. *K. W. Moon, W. J. Boettinger, U. R. Kitten, F. S. Biancaniello, and C. A. Handwerker*, Experimental and thermodynamic assessment of Sn-Ag-Cu solder alloys, *J. Electron. Mater.* No. 29, p.1122 – 1136, (2000).
17. *E. Gebhardt and G. Petzow*, Experimental and Thermodynamic Assessment of Sn-Ag-Cu Solder Alloys, *Z. Metallkde*, No. 50, p. 597, (1959)
18. *V.N. Fedorov, O.E. Osinchev and E.T. Yushkina*, referenced in *Phase Diagrams of Metallic Systems*, Vol. 26, Eds. N.V. Ageev and L.A. Petrova, VINITI, Moscow, USSR, 1982, pp.149- 150.
19. *C.M. Miller, I.E. Anderson, and J.F. Smith*, A Viable. Tin-Lead Solder Substitute: Sn-Ag-Cu, *J. Electron. Mater.*, No. 23, p. 595–601, (1994)
20. U.S. Patent No. 5 527 628, (1996)
21. *M.E. Loomans and M.E. Fine*, Tin-silver-copper eutectic temperature and composition, *Metall. Mater.Trans.* No. 31, 1155 (2000)
22. *D. W. Henderson, T. Gosselin, A. Sarkhel, S. K. Kang, W-K Choi, D-Y Shih, C. Goldsmith and K. J. Puttlitz*, Ag₃Sn plate formation in the solidification of near ternary eutectic Sn-Ag-Cu alloys, *J. of Materials Res.*, Vol. 17, No. 11, p. 2775 – 2778, (2002)
23. *A. Rosenberg and W. C. Winegard*, The growth rate of dendrites in undercooled tin, *Acta Metall.*, Vol. 2, p. 342 – 343, (1954)

24. *D. W. Henderson*, IBM, East Fishkill, NY, TMS Annual Meeting March 17, 2004
25. *D. W. Henderson, J. J. Woods, T. A. Gosselin, J. Bartelo, D. E. King, T. M. Korhonen, M. A. Korhonen, L. P. Lehman, E. J. Cotts, S. K. Kang, P. Lauro, D. Y. Shih, C. Goldsmith, and K. J. Puttlitz*, The microstructure of Sn in near-eutectic Sn–Ag–Cu alloy solder joints and its role in thermomechanical fatigue, *J. Mater. Res.*, Vol 19, No. 6, p. 1608 – 1612, (2004)
26. *S. K. Kang, W. K. Choi, D. Y. Shih, D. W. Henderson, T. Gosselin, A. Sarkhel, C. Goldsmith, and K. Puttlitz*, Proceedings of the 53rd Electronic Components and Technology Conference, New Orleans, May 2003, Piscataway, NJ: IEEE, p. 64 – 70
27. *S. K. Kang, D. Y. Shih, D. Leonard, D. W. Henderson, T. Gosselin, S. Cho, J. Yu, and W. K. Choi*, Controlling Ag₃Sn Plate Formation in Near-Ternary-Eutectic Eutectic Sn–Ag–Cu Solder by Minor Zn Alloying, *JOM*, Vol. 56, No. 6, p.34 – 38, (2004)
28. *K. S. Kim, S. H. Huh, and K. Sugauma*, Effects of cooling speed on microstructure and tensile properties of Sn–Ag–Cu alloys, *Mater. Sci. & Eng.*, Vol. A333, p. 106 – 114 (2002).
29. *I. E. Anderson, B. A. Cook, J. Harringa, and R. L. Terpstra*, Microstructural modifications and properties of Sn–Ag–Cu solder joints induced by alloying, *J. Electron. Mater.* No. 31, p. 1166 –1174, (2002)
30. *I. E. Anderson and J. L. Harringa*, Elevated temperature aging of solder joints based on Sn–Ag–Cu: Effects on joint microstructure and shear strength, *J. Electron. Mater.*, No. 33, p. 1485 – 1496, (2004)
31. *P. T. Vianco, J. A. Rejent, and J. J. Matin*, The compression stress-strain behavior of Sn–Ag–Cu solder, *JOM*, Vol. 55, No. 6, p. 50 – 55, (2003)

32. *K. L. Buckmaster, J. J. Dziejcz, M. A. Masters, B. D. Poquette, G. W. Tormoen, D. Swenson, D. W. Henderson, T. Gosselin, S. K. Kang, D. Y. Shih, and K. J. Puttlitz*, presented at the TMS 2003 Fall Meeting, Chicago, November 2003; see www.tms.org.
33. *P. Lauro, S. K. Kang, W. K. Choi, and D. Y. Shih*, Effects of mechanical deformation and annealing on the microstructure and hardness of Pb-free solders, *J. Electron. Mater.*, Vol. 32, No. 12, p. 1432 – 1440, (2003)
34. *S. K. Kang, W. K. Choi, M. J. Yim, and D. Y. Shih*, Studies of the mechanical and electrical properties of lead-free solder joints, *J. Electron. Mater.*, Vol. 31, No. 11, p. 1292 – 1303, (2002)
35. *C. Foley, A. Gickler, F. H. Lprevost, and D. Brown*, Analysis of ring and plug shear strengths for comparison of lead-free solders, *J. Electron. Mater.*, Vol. 29, No. 10, p. 1258 – 1263, (2000)
36. *B. A. Cook, I. Anderson, J. Harringa, R. Terpstra, J. Foley, O. Unal, and F. Laabs*, Shear deformation in Sn-3.5Ag and Sn-3.6Ag-1.0Cu solder joints subjected to asymmetric four-point bend tests, *J. Electron. Mater.*, Vol. 30, No. 9, p.1214 – 1221, (2001)
37. *D. R. Frear, J. W. Jang, J. K. Lin, and C. Zhang*, Pb-Free Solders for Flip-Chip Interconnects, *JOM*, Vol. 53, No. 6, p. 28 – 32, (2001)
38. *J. Bartelo, S. Cain, D. Caletka, K. Darbha, T. Gosselin, D. Henderson, D. King, K. Knadle, A. Sarkhel, G. Thiel, C. Woychik, D. Y. Shih, S. K. Kang, K. Puttlitz, and J. Woods*, Proceedings of APEX 2001, San Diego, January 14–18, 2001, LF2-2
39. *S. K. Kang, P. Lauro, D. Y. Shih, D. W. Henderson, J. Bartelo, T. Gosselin, S. R. Cain, C. Goldsmith, K. Puttlitz, T. K. Hwang, and W. K. Choi*, *Mater. Trans. (Jpn. Inst. Metals)* 45, No. 3, 695–702 (2004).

40. *S. K. Kang, P. Lauro, D. Y. Shih, D. W. Henderson, T. Gosselin, J. Bartelo, S. R. Cain, C. Goldsmith, K. J. Puttlitz, and T. K. Hwang*, Evaluation of thermal fatigue life and failure mechanisms of Sn-Ag-Cu solder joints with reduced Ag contents, Proceedings of the 54th Electronic Components and Technology Conference (IEEE Cat. No.04CH37546), Las Vegas, NV, USA, p. 661 – 667, (2004)
41. *D. Frear, D. Grivas, and J. W. Morris*, A microstructural study of the thermal fatigue failures of 60Sn-40Pb solder joints, *J. Electron. Mater.*, Vol. 17, No. 2. p. 171 – 180, (1988)
42. *J. K. Lin, A. De Silva, D. Frear, Y. Guo, S. Hayes, J. W. Jang, L. Li, D. Mitchell, B. Yeung, and C. Zhang*, Characterization of lead-free solders and under bump metallurgies for flip-chip package, *IEEE Trans. Electron. Pkg. & Manuf.*, Vol. 25, No. 4, p. 300 – 307, (2002)
43. *J. K. Lin, J. W. Jang, S. Hayes, and D. Frear*, Lead-free flip chip interconnect reliability for DCA and FC-PBGA packages, Proceedings of the 54th Electronic Components and Technology Conference (IEEE Cat. No.04CH37546), Las Vegas, NV, USA, p. 642 – 649, (2004)
44. *S. K. Kang, R. S. Rai, and S. Purushothaman*, Interfacial reactions during soldering with lead-tin eutectic and lead (Pb)-free, tin-rich solders, *J. Electron. Mater.*, Vol. 25, No. 7, p. 1113 – 1120, (1996)
45. *S. K. Kang, D. Y. Shih, K. Fogel, P. Lauro, M. J. Yim, G. Advocate, M. Griffin, C. Goldsmith, D. W. Henderson, T. Gosselin, D. King, J. Konrad, A. Sarkhel, and K. J. Puttlitz*, *IEEE Trans. Electron. Pkg. & Manuf.*, Vol. 25, No. 2, p. 1 – 7, (2002)
46. *S. K. Kang, W. K. Choi, D. Y. Shih, P. Lauro, D. W. Henderson, T. Gosselin, and D. N. Leonard*, Interfacial reactions, microstructure and mechanical properties of Pb-free solder joints in PBGA laminates, Proceedings of the 52nd Electronic Components and

- Technology Conference (IEEE Cat. No.02CH37345), Las Vegas, NV, USA, p. 147 – 153, (2002)
47. *W. K. Choi, S. K. Kang, and D. Y. Shih*, A study of the effects of solder volume on the interfacial reactions in solder joints using the differential scanning calorimetry technique, *J. Electron. Mater.*, Vol. 31, No. 11, p. 1283 – 1291, (2002)
48. *W. K. Choi, S. K. Kang, Y. C. Sohn, and D. Y. Shih*, Study of IMC morphologies and phase characteristics affected by the reactions of Ni and Cu metallurgies with Pb-free solder joints, *Proceedings of the 53rd Electronic Components and Technology Conference*, New Orleans, USA, p. 1190 – 1196, (2003)
49. *Y. C. Sohn, J. Yu, S. K. Kang, D. Y. Shih, and T. Y. Lee*, Study of spalling behavior of intermetallic compounds during the reaction between electroless Ni-P metallization and lead-free solders, *Proceedings of the 54th Electronic Components and Technology Conference (IEEE Cat. No.04CH37546)*, Las Vegas, NV, USA, p. 75 – 81, (2004)
50. *W. Paik, Y. D. Jeon, and M. G. Cho*, Interfacial reactions and bump reliability of various Pb-free solder bumps on electroless Ni-P UBMs, *Proceedings of the 54th Electronic Components and Technology Conference (IEEE Cat. No.04CH37546)*, Las Vegas, NV, USA, p. 675 – 682, (2004)
51. *T. C. Chiu, K. Zeng, R. Stierman, D. Edwards, and K. Ano*, Effect of thermal aging on board level drop reliability for Pb-free BGA packages, *Proceedings of the 54th Electronic Components and Technology Conference (IEEE Cat. No.04CH37546)*, Las Vegas, NV, USA, p. 1256 – 1262, (2004)
52. *E. Kirkendall, L. Thomassen, and C. Uphergrove*, Rates of Diffusion of Copper and Zinc in Alpha Brass, *Trans. AIME*, No. 133, p. 186 – 203, (1939)

53. *M. Date, T. Shoji, M. Fujiyoshi, K. Sato, and K. N. Tu*, Impact reliability of solder joints, Proceedings of the 54th Electronic Components and Technology Conference (IEEE Cat. No.04CH37546), Las Vegas, NV, USA, p. 668 – 674, (2004)
54. *D. Mis (Unitive, Inc.)*, presented at the Peaks in Packaging Conference (Semiconductor International), October 10, 2003; see www.unitive.com
55. *S. K. Kang, D. Y. Shih, and D. Leonard*, presented at the 2005 TMS Annual Meeting, San Francisco, February 13–17, 2005; see www.tms.org
56. *Y. Kariya, N. William, C. Gagg, and W. Plumbridge*, Tin pest in Sn–0.5% Cu lead-free solder, JOM, Vol. 53, No. 6, p. 39 – 41, (2001)
57. *D. W. Henderson, T. Gosselin, S. K. Kang, W. K. Choi, D. Y. Shih, C. Goldsmith, and K. Puttlitz*, U.S. Patent 6,805,974, October 19, 2004
58. *S.Y. Sokolov*, The ultrasonic influence on chemical reactions, J. of Solid State Physics, No. 3, p. 176, (1936)
59. *G. Schmid, L. Ehret*, Die Wirkung intensiven Schalls auf Metallschmelzen, Z. Elektrochem., Vol. 43, No. 11, (1937)
60. *H. Seeman*. Metallforschung mit Ultraschall, Metall-Wirsch., No 5, (1936)
61. *V.I. Danilov, E.E. Plushnik, B.M. Teverovsky*, Crystallization of piperylpiperidine in ultrasonic field, J. of Solid State Physics, Vol. 9, No. 1, p. 55, (1939)
62. *V.I. Danilov, E.E. B.M. Teverovsyi*, Crystallization of organic substances in ultrasonic field, Journal of Solid State Physics, Vol.10, No. 11, p. 55, (1940)
63. *A.P. Kapustin*, Ultrasound influence on crystallization kinetics, AN USSR, Moscow, 106 p., 1962
64. *L.D. Rozenberg*, Physical principles of the ultrasound technology, Moscow, Nauka, 686 p., 1970

65. *I.L. Aptekar, D.S. Kameneckaya*, Pressure impact on new phase nuclei sites formation, J. of Physics of Metals, Vol. 14, No 2, p. 316, (1962)
66. *D. P. Cullen*, "Avoiding Microvoids," Assembly (on-line magazine), September 2005.
67. NPL Release Report on Effect of Voiding on Lead-Free Reliability, NPL Press Release, National Physical Laboratory, Teddington, UK, September 30, 2005
68. IPC-610 standard, Rev. D, "Acceptability of Electronic Assemblies," February 2005
69. *Wickham, M., M. Dusek, L. Zou and C. Hunt*, Effect of Voiding on Lead-Free Reliability, NPL Report DECP MPR 033, National Physical Laboratory, Teddington, UK, April 2005
70. *Raiyo Aspandiar*, Voids in solder joints, SMTA Northwest Chapter Meeting, September 21th 2005
71. *J. W. Jang, J. K. Lin, D. R. Frear, T. Y. Lee, and K. N. Tu*, Ripening-assisted void formation in the matrix of Pb-free solder joints during solid-state aging, J. Mater. Res., No. 22, p. 826 – 830, (2007)
72. <http://www.micro.magnet.fsu.edu/primer/anatomy/reflected.html>
73. <http://www.olympusmicro.com/primer/lightandcolor/birefringenceintro.html>
74. *J.I. Goldstein*, Scanning Electron Microscopy and X-Ray microanalysis. 3 ed., New York Springer, 2003
75. *P.J. Goodhew, J. Humphreys, R Beanland*, Electron Microscopy and analysis, 3 ed., London: Taylor and Francis, 2001
76. <http://www.x-raymicroanalysis.com/x-ray-microanalysis-explained/pages/main/main.htm>
77. <http://www.ebsd.com/ebsd-explained/>
78. *I.P. Golyamina*, Ultrasound, Moscow, Soviet Encyclopedia, 401 p., 1979

79. *W. Zhai, Z.Y. Hong, W.J. Xie*, Solidification characteristics of Pb-Sb hypereutectic alloy within ultrasonic field, Chinese Science Bulletin, Vol. 52, No. 6, p. 844 – 848, (2007)
80. *R. J. Fields and S. R. Low*, Physical and mechanical properties of intermetallic compounds commonly found in solder, Metallurgy Division NIST, 2002
81. *T. Siewert, S. Liu, D.R. Smith, J.C. Madeni*, Database for Solder Properties with Emphasis on New Lead-free Solders, National Institute of Standards and Technology & Colorado School of Mines, Colorado, 2002
82. *K.S. Kim, S.H. Huh, K. Suganuma*, Effects of intermetallic compounds on properties of Sn–Ag–Cu lead-free soldered joints, J. Alloys Compd., No. 352, p. 226 – 236, (2003)
83. *W.B. Pearson*, A Handbook of Lattice Spacings and Structure of Metals and Alloys, vol. 2, Pergamon Press, London, 1958
84. *Donald W. Henderson, James J. Woods, Timothy A. Gosselin and Jay Bartelo*, The Microstructure of Sn in near eutectic Sn-Ag-Cu alloy solder joints and its role in thermomechanical fatigue, J. Mater. Res., Vol. 19, No. 6, p. 1608 –1612, (2004)
85. *Frear, D. Grivas, J.W. Morris Jr.*, The effect of Cu₆Sn₅ whisker precipitates in bulk 60Sn-40Pb solder, J. Electron. Mater., Vol 16, No. 2, p. 181 – 186, (1987)
86. *Jicheng Gong, Changqing Liu, Paul P. Conway, Vadim V. Silberschmidt*, Evolution of CuSn intermetallics between molten SnAgCu solder and Cu substrate, J. Acta Mater., Vol. 56, No. 16, p. 4291 – 4297, (2008)
87. *T. Laurila, J. Hurtig, V. Vuorinen, J.K. Kivilahti*, Effect of Ag, Fe, Au and Ni on the growth kinetics of Sn–Cu intermetallic compound layers, J. Microelectron. Reliab., No. 49, p. 242 – 247, (2009)

88. *K. Nogita, C.M. Gourlay, and T. Nishimura*, Cracking and Phase Stability in Reaction Layers between Sn-Cu-Ni Solders and Cu Substrates, *J. Electron. Mater.*, Vol. 61, No. 6, p. 45 – 51, (2009)
89. *Robert H. Esser, A. Dimoulas, N. Strifas, A. Christou, N. Papanicolau*, Materials interfaces in flip chip interconnects for optical components; performance and degradation mechanisms, *J. Microelectron. Reliab.*, No. 38, p. 1307–1312, (1998)
90. *Kaye & Laby*, Tables of Physical and Chemical Constants, Longmans, Green & Co, London, 1968
91. *Tim Wong and A.H. Matsunaga*, Ceramic Ball Grid Array Solder Joint Thermal Fatigue Life Enhancement, Proceedings: NEPCON West Conference, Anaheim, CA, (February 28 – March 2, 1995)
92. *D.R. Frear, S.N. Burchett, H.S. Morgan, and J.H. Lau*, eds., The Mechanics of Solder Alloy Interconnects, Van Nostrand Reinhold, New York, 1994, p. 60
93. *Vianco P. T.*, Sandia National Laboratories, 2001
94. *H.L.J. Pang, K.H. Tan, X.Q. Shi, Z.P. Wang*, Microstructure and intermetallic growth effects on shear and fatigue strength of solder joints subjected to thermal cycling aging, *Mater. Sci. Eng.*, No. A307, p. 42 – 50, (2001)